A System for High Strain Rate Interruptible Tensile Tests

Author: Malcolm Thomas

Supervisor: Dr Reuben Govender

Co-Supervisor: Dr Trevor Cloete

Dissertation submitted for full requirement of MSc degree
in the Department of Mechanical Engineering
Faculty of Engineering and the Built Environment
University of Cape Town

April 2024

Declaration

I, Malcolm Thomas, hereby:

(a) grant the University of Cape Town free license to reproduce the above thesis in whole or in part, for the purpose of research;

(b) declare that:

(i) the above thesis is my own unaided work, both in concept and execution, and that apart from the normal guidance from my supervisor, I have received no assistance.

(ii) neither the substance nor any part of the above thesis has been submitted in the past, or is being, or is to be submitted for a degree at this University or at any other university.

I know the meaning of plagiarism and declare that all the work in the document, save for that which is properly acknowledged, is my own. This thesis/dissertation has been submitted to the Turnitin module (or equivalent similarity and originality checking software) and I confirm that my supervisor has seen my report and any concerns revealed by such have been resolved with my supervisor.

I am now presenting the report for examination for the degree of M.Sc. Mechanical Engineering.

Signed by candidate

M. R. Thomas

25 March 2024

Acknowledgements

I begin by thanking my primary supervisor, Dr Reuben Govender, for being a mentor throughout this degree. He always had valuable input, even beyond the context of my research. His experience with Hopkinson bar techniques helped me out countless times. If I ran into a problem, the chances are that Dr Govender had encountered the issue before, and had a solution in mind.

A thank you also goes out to Dr Trevor Cloete, who co-supervised this project. In a project such as this, his vast knowledge of high strain rate testing, and experience in mechanical design was much appreciated.

Thank you to the Mechanical Engineering workshop staff for the huge role they played in making this project happen. Some parts of this project required a very high level of machining skill, and Pierre Smith and his team were able to make it happen, time and time again.

Thank you to all of my BISRU colleagues, past and present, for always being there to answer any queries, and to play darts during loadshedding. Every one of them played a part in creating a great work atmosphere, that made all the long hours in the lab seem short.

I express my utmost appreciation to my family and friends, who provided me with their ongoing support and encouragement throughout the course of this degree.

I gratefully acknowledge financial support from the US Air Force Office of Scientific Research, via grant FA8655-21-1-7012 which provided a bursary towards my tuition expenses and funded experimental costs. Any opinions, findings and conclusions or recommendations expressed in this material are those of the author(s) and do not necessarily reflect the views of the U.S. Department of Defense.

Abstract

The Split Hopkinson Pressure Bar (SHPB) is a widely used piece of equipment used for measuring a material's response to high strain rates. High strain rate data is critical for exhaustive characterisation, due to the sensitivity of materials to the rate at which they are strained. The principle limitation of conventional SHPB is that there is limited control of the ultimate deformation of specimens, because specimens are rarely recoverable after having undergone a single loading event. For this reason, microstructural investigations on SHPB specimens offer limited value, as the specimen was loaded repeatedly.

In the MSc, a tensile SHPB (TSHB) was designed with momentum trapping to conduct interruptible tests on specimens. This configuration makes use of tandem momentum traps, allowing for the system to be fully trapped without the need for precisely preset gaps, or tight control over striker speed. A pull-off design of tubular tensile striker was used alongside the tandem momentum trapping, in a novel configuration allowing the input bar to remain supported over its entire length. The fir-tree design of dynamic tensile specimen fixture was utilised.

Thorough preliminary measurements of the wave propagation properties of the hardware are taken. Strain gauge calibration tests were then conducted, followed by a rigorous commissioning process. This involved fine-tuning trap impedances and verification of the complex critical subsystems. As the commissioning process progressed, emergent flaws were rectified, and a standard operating procedure was established to ensure the reliable performance of said subsystems.

The operation of the TSHB was demonstrated by a series of experiments on DOMEX 550 specimens. The recorded loading history is compared to the measured length of recovered specimens as verification of the interruptibility of tests using this apparatus. These specimens are also compared to those tested under the same conditions, but without the interruption, further demonstrating the effectiveness of the developed system.

Contents

List of Figures

List of Tables

Glossary of Terms

BISRU:	Blast Impact and Survivability Research Unit
CNC:	Computer Numerical Control
EDM:	Electro-Discharge Machining
FDM:	Fused Deposition Modelling
HSR:	High Strain Rate
ID:	Inside Diameter
Lagrange Diagram:	A plot of time versus location, used to analyse the propagation of stress waves
OD:	Outside Diameter
PLA:	Polylactic Acid
SLA:	Stereolithography
SHPB:	Split Hopkinson Pressure Bar
TSHB:	Tensile Split Hopkinson Bar

Chapter 1

Introduction

1.1 Background

The thorough characterisation of engineering materials is essential in constructing representative material models. These form an important part of modern engineering, as they define material response for computational simulations, such as finite element models. High strain rate (HSR) data is an integral part of a material model, as many mechanical material properties, such as ductility and yield strength, vary depending on strain rate [1]. Knowledge of the HSR behaviour of materials is especially valuable in fields such as automotive crashworthiness, defence, and anti-terrorism since impacts are expected in these applications which involve rapid material deformation. Furthermore, manufacturing processes, such as high-speed wire drawing and shot peening, can be optimised with the ability to predict material behaviour at various strain rates.

The Split Hopkinson Pressure Bar (SHPB) is an elegant and versatile apparatus [2] that is commonly used to conduct material tests in the high strain rate region, i.e. 10^2 /s to 10^4 /s [3]. This apparatus is subjecting specimens to compressive, tensile, shear, or combined loading. When using a SHPB, there is a tendency for the specimen to be exposed to unintended repeated loading due to stress wave reflections in the pressure bars. This consequence is especially prominent with a Tensile Split Hopkinson Pressure Bar (TSHB), as specimens are fixed to the pressure bars. This additional loading creates a mismatch between the loading history calculated from the initial set of waves, and that experienced by the specimen. The total strain, and strain rate after the initial loading are not within full control.

In quasi-static tests, the experiment can be halted simply by stopping the machine. This is because there is closed-loop control of the deformation, and also because the experiments are conducted slow enough to stop accurately, with negligible inertial effects in the

machine. This is not the case in dynamic experiments, as there is no closed-loop control, with no opportunity for operator intervention as the tests take a matter of microseconds. In addition, there are large inertial effects that make the apparatus reluctant to stop suddenly. If SHPB experiments were able to be halted and intact specimens recovered having only undergone a prescribed strain, there would be significantly more value in conducting microstructural investigations on specimens after testing. There is therefore a clear need for a reliable method of interruption for these tests, so that specimens can be recovered without having been reloaded.

1.2 Aims and Objectives

This project aims to design, build, and commission a Tensile Split Hopkinson Pressure Bar apparatus in the Blast Impact and Survivability Research Unit (BISRU) laboratory. It shall be capable of conducting dynamic tensile tests on a range of materials, that can be interrupted after the first loading wave to allow specimen recovery at a specified deformation. This shall be achieved by means of meeting the following objectives:

- Investigate the existing methods of dynamic specimen recovery, pulse generation, and specimen mounting.
- Develop a set of design requirements, and a system that meets these requirements.
- Draught, manufacture, and assemble the system
- Take preliminary measurements, calibrate and commission the system
- Verify the operation of the system, thus proving the design requirements have been met, and that the apparatus is capable of fulfilling its function for future research.

1.3 Scope and Limitations

This project included material testing as verification that the apparatus functions as designed. However, detailed characterisation of a specific material was not part of this MSc project scope.

In order to control total strain, and strain rate, of a specimen independently, this SHPB will require multiple strikers of varying length. Since this project strictly covers the commissioning and proof of concept, and this can be achieved with a single striker, only one striker was manufactured.

Tensile specimens were not manufactured for the purposes of this project. Instead, surplus specimens from a previous project at BISRU were utilized. Since these specimens were

thoroughly designed and developed by previous researchers, their role in this project will be limited to a review.

Work on dispersion effects and their correction shall not be a focus in this project. An existing Python script [4] will be utilised to correct for the first-mode Pochhammer-Chree effects of dispersion.

1.4 Thesis Outline

The chapters in this thesis are structured as follows:

2. Literature Review
   The literature relevant to this project is summarized, and concepts pertaining to TSHB testing are emphasized:
   - The context and development of the TSHB
   - Existing striker designs
   - Methods of dynamic tensile specimen mounting
   - The development of dynamic specimen recovery
   - The background behind one-dimensional dispersion correction
3. Design of the Tensile SHPB
   The requirements for TSHB, as well as the design decisions involved in the various parts and assemblies are described. Calculations driving the design, specifications of parts, and modes of operation of the apparatus are also included.
4. Preliminary Measurements and Calibration
   This chapter outlines the measurement methodologies and results necessary for design calculations and setting up the apparatus for testing. These measurements would be good practice for initial set up of any SHPB apparatus and include:
   - Verification of bar material properties
   - Pressure bar calibration
   - Quasi-static tensile tests
5. Commissioning
   The processes, specific to this apparatus, involved in bringing it to a working condition, are described: This includes tests used to match the impedance of the momentum traps, as well as .
   - Matching of the impedances of the momentum traps
   - Verification of the operation of critical subsystems

- Ironing out of issues that arose in the abovementioned tasks

6. High Strain Rate Tensile Tests
   This chapter outlines the verification tests of the full apparatus, specifically demonstrating that HSR tensile tests can be conducted and interrupted in a controlled manner. This included a series of tests where the momentum trapping system was disengaged to demonstrate uninterrupted tests.

7. Discussion and Concluding Remarks
   The results of previous chapters are discussed and the outcomes of the project are presented:

   - Reflection on the design process
   - Functional performance assessment
   - Component specific concerns

8. Recommendations
   Areas for further improvement are highlighted.

Chapter 2

Literature Review

In this chapter, the existing literature that is relevant to this project is discussed. Firstly, the context of HSR tensile testing is outlined, and brief historical account of the development of the TSHB is described. Secondly, the various approaches to strikers and specimen mounting associated with TSHB testing are reviewed. Thirdly, methods of interrupting SHPB tests are explored, with particular emphasis on momentum trapping. Finally, an introduction is provided to the dispersion correction approach that will be used moving forward in this project.

2.1 High Strain Rate Testing

In many modern fields of research, numerical simulations play a large role in predicting how materials and structures respond to loading. Constitutive material models are a fundamental part of these simulations, as they describe the way that the material behaves. Many material properties, such as ductility and yield strength [5], and ultimate tensile strength (UTS) [6], vary depending on the strain rate. Figure 2.1 displays how the stress-strain curves of copper differ depending on the strain rate that the test was conducted at. In static or quasi-static scenarios, any point in the material is in a state of static equilibrium, but in dynamic scenarios, the time taken for stresses to propagate in the material must be considered [7]. There are also inertial effects within the material itself due to the high acceleration. These effects can be minimised through good specimen design, however, due to the strain rate sensitivity of materials, quasi-static testing alone is not sufficient in investigating the way in which a material behaves. Tests need to be conducted over a range of strain rates. HSR testing is especially relevant to models for ductile metals, as such materials are found in motor vehicles [8], armour steels, and a range of weaponry. These applications often see impact rates of strain.

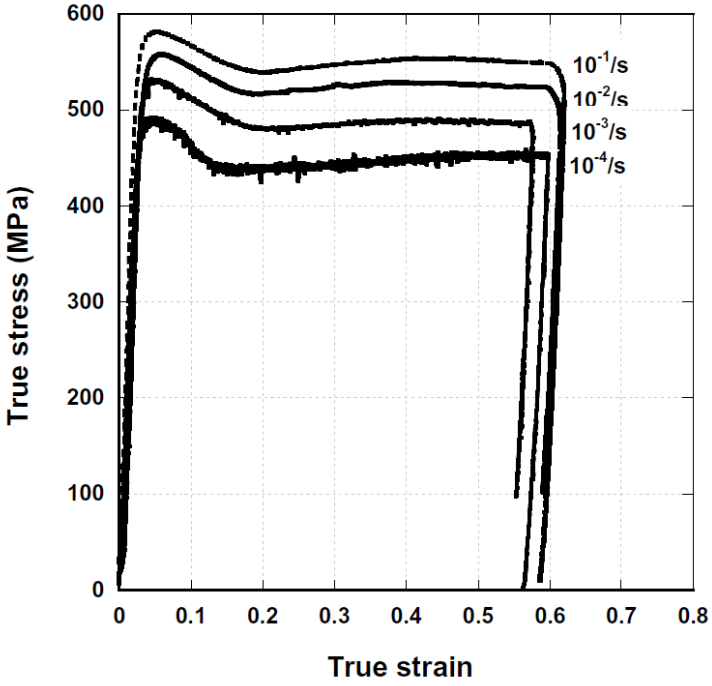

Figure 2.1 Compressive stress-strain curves of cryo-rolled copper at various strain rates [9]

If the fracture model of a material is to be characterised exhaustively, HSR tests cannot only be done in compression. For anisotropic materials, such as wood or composites, it is trivial to justify the need for tensile testing, as such materials have distinct failure modes for tension and compression. In order to fully characterise the fracture of an isotropic material, it is necessary to test the material in various combinations of tension or compression, and shear. Studies have shown that triaxiality [10, 11], and the Lode angle [12, 13] have a strong influence on the fracture response of isotropic materials to various stress states [14]. Triaxiality is the ratio of hydrostatic to flow stress, which affects the material's compressive strength and deformation characteristics [15, 16]. The Lode angle, defined as the deviation of the stress state from uniaxial conditions, and related to the flow stress, provides a more detailed picture of the material behaviour. Testing in tension, compression, and shear allows for the examination of how Lode angle and triaxiality variations impact the material's response [17], particularly relevant in scenarios with multiaxial stress states. For this reason, there is a need for tensile, compressive, and shear tests at varying strain rates.

2.2 The Split Hopkinson Pressure Bar

A popular method used to analyse a material's response to loading at high strain rates is a Hopkinson Pressure Bar (HPB). The SHPB is named after Bertram Hopkinson, who introduced the apparatus in his 1914 study [18]. He used a long metal bar to study the propagation of stress waves produced as a result of impact loading. The idea was further developed by the likes of Landon and Quinney [19] in 1923, and Davies in 1948 [20, 21].

In 1949, Kolsky [22] presented a modification to the apparatus that is still used today. The bar was divided in in two, and a test the test specimen was placed in between them. It became known as the Split Hopkinson Pressure Bar, or SHPB, but is often referred to as a Kolsky bar. Peroni [23] explains that the SHPB, being grounded in the theory of elastic wave propagation, is not adversely affected by these waves, as is the case with other testing methods. Arrangements can typically subject test specimens to compression, tension, torsion, or shear [24], and is regarded as a key step in validating material models at high strain rate [25]. Compressive and tensile arrangements will be discussed further as they hold relevance to the techniques explored in this research.

2.2.1 The Compressive SHPB

The standard SHPB is designed to subject a specimen to a compressive stress wave. Figure 2.2 below shows a typical compressive arrangement. As defined by Gray [1], a standard compressive SHPB consists of two long, uniform bars supported radially, but free to slide in the axial direction. These pressure bars, known as the incident and transmitted bars, are also referred to the input and output bars respectively. They lie end-to-end with one another, as shown in Figure 2.2, and a test specimen is mounted in between them. During a test, the free end of the input bar is impacted with a striker. This causes a compressive stress pulse to move down the bar, through the specimen, and into the output bar. Strikers are typically propelled by compressed gas. Strain signals of the propagating waves are recorded at a point on both the input and output bars [26]. When these signals are shifted to the specimen faces, the loading conditions of the specimen can be inferred.

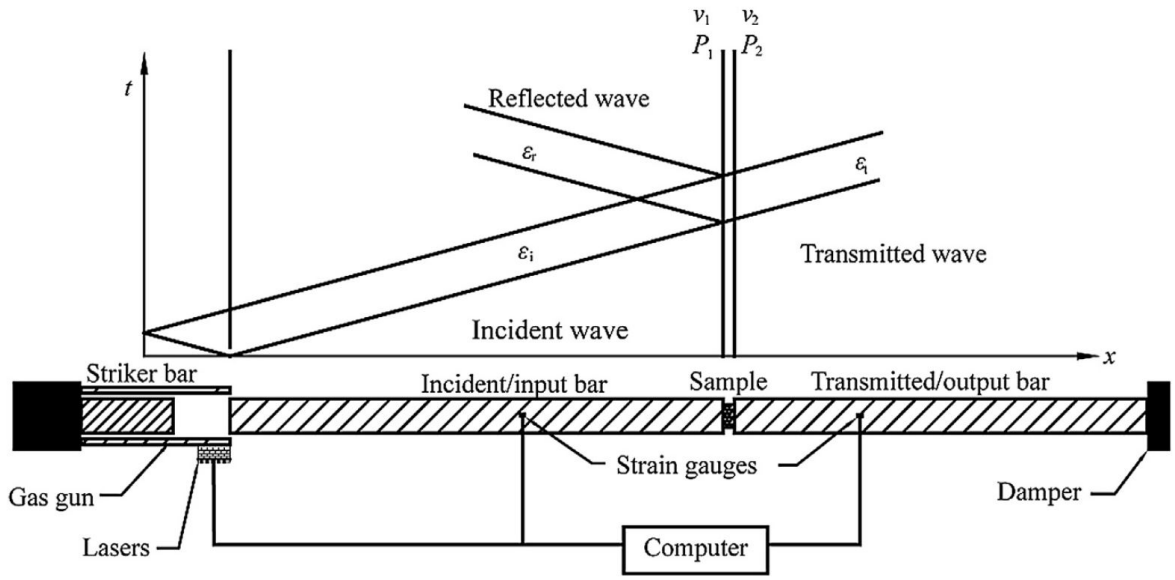

Figure 2.2 Split Hopkinson Pressure Bar, with Lagrangian X-T diagram, as illustrated by Xia *et al.* [27]

2.2.2 The Tensile SHPB

As mentioned in Section 2.1, tensile tests are imperative to do alongside compressive tests for the characterisation of a material's behaviour. In order to make a tensile SHPB (TSHB), the simple compressive arrangement is to be altered. According to Nicholas and Bless [28] the method of creating the stress pulse, specimen geometry, and the way in which the specimen is attached to the pressure bar, are what sets a TSHB apart from a compressive one. Naturally, the TSHB tends to be more complex than a SHPB.

2.2.2.1 Yoke Method

The first version of the TSHB emerged in 1960, developed by Harding *et al.* [29]. The weighbar and inertia bar shown in Figure 2.3b, play the roles of the traditional input and output bar respectively, and are free to slide within each other. The two are connected rigidly only by the specimen via a yoke. Tests are conducted by impacting the end of the weighbar (on its top end in Figure 2.3b) with a striker, and recording the transmitted strain history on the inertia bar using a set of strain gauges [30].

To conduct a set of tests, the elastic test assembly shown in Figure 2.3a was initially used to establish the input conditions. In this test assembly, the specimen and inertia bar are replaced by a uniform elastic bar [30]. The input conditions are measured via strain gauges on the elastic bar and are unique to the impact parameters. By knowing that specific impact parameters produce particular input conditions, those same input

conditions are inferred when applying identical parameters to the specimen test assembly. Once the output parameters are obtained from the test, a strain history of the specimen can be determined.

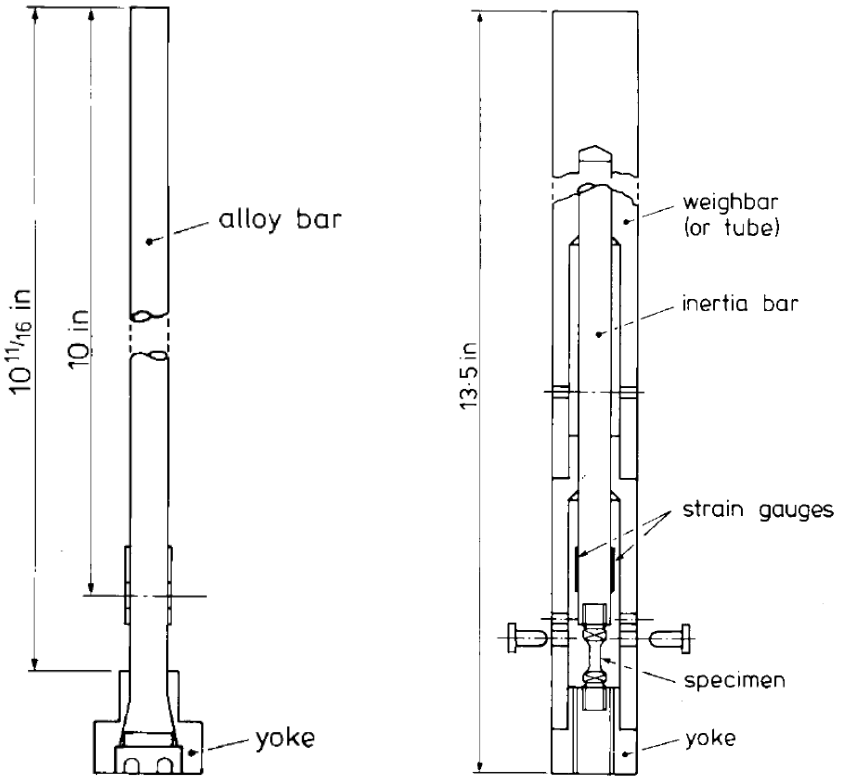

(a) Elastic test assembly **(b)** Specimen test assembly

Figure 2.3 Yoke design of TSHB designed by Harding *et al.* [29]

This test method therefore relied on striker velocity being a highly repeatable and precisely controlled parameter, which it was not. This increased the degree of uncertainty in the results. The bulky yoke introduced further concerns about this method. Due to the significant mass of the yoke on the load path between the weighbar and the specimen, it was not possible to show force equilibrium in the specimen throughout its loading. Wu and Gorham [31] explains that establishing force equilibrium across the specimen interfaces is important, as it ensured that inertial and wave propagation effects are small enough to neglect.

2.2.2.2 Top Hat Method

Another method, developed by Lindholm and Yeakley [32] in 1968, involved substituting the output bar in the standard compressive SHPB for one that takes the form of a hollow tube. The specimen is given a top hat shape, with slots milled into the wall of the specimen, creating four parallel gauge sections. The specimen fits over the end of the input bar, as seen in Figure 2.4, and is located within the output bar.

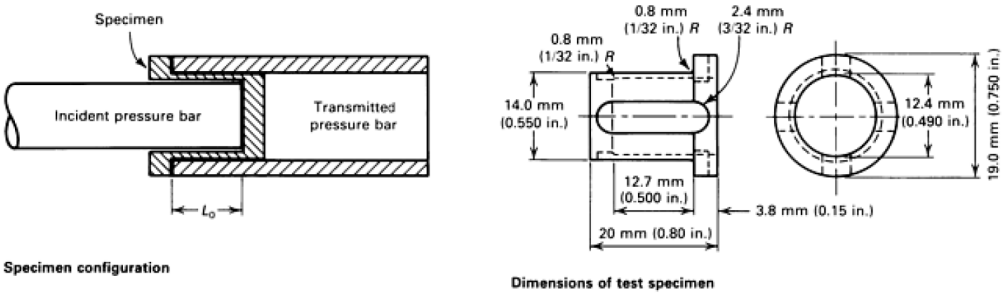

Figure 2.4 Top hat tensile specimen designed by Lindholm and Yeakley [32]

This arrangement means that the specimen can be loaded in tension, while still sending a compressive stress pulse through the pressure bars themselves. This is referred to as a load inversion [33], and is advantageous as creating a compressive pulse is requires a less elaborate arrangement than creating a tensile one. It also allows for tensile SHPB tests to be conducted with a standard compressive apparatus, by changing only the output bar [1].

The downside is the intricate specimen geometry, as it makes test results challenging to analyse. The top hat method involves the gauge section being hidden within the output bar, preventing the use of high speed video, or any measurement techniques where a line of sight of the specimen is required. Furthermore, the top hat shape means the loading direction is not coincident with the centroid of the gauge section, which introduces unwanted eccentric loading [2]. Another disadvantage is that the process of manufacturing specimens involves more complex machining, where tolerances are critical. In addition, the internal corners of the specimen will always have finite radii from the lathe tool [34], affecting bar contact, and introducing transient conditions as the specimen is loaded and unloaded.

2.2.2.3 Indirect Loading Method

In 1981, Nicholas *et al.* [35] proposed an alternative technique to subject a specimen to a dynamic tensile load. The apparatus is similar to a conventional compressive SHPB, with only the region around the specimen differing. A tensile specimen is threaded into the ends of the pressure bars, with a split collar located around it. The collar has a close fit with the ends of the bars as seen in Figure 2.5. Similar method were used in studies by Ellwood *et al.* [36] and Haugou *et al.* [37].

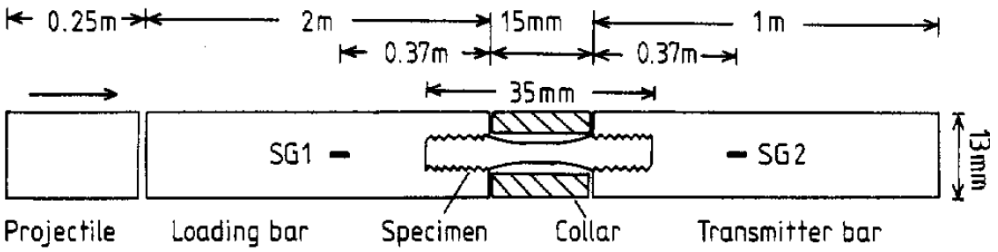

Figure 2.5 Indirect tensile loading method, as used by Ellwood *et al.* [36]

This method is known as indirect loading, as it is the reflection of the transmitted wave that loads the specimen, and not the incident wave. The input bar is struck in compression, and the incident wave travels through the input bar. At the specimen location, the incident wave is transferred into the output bar via the collar, ideally leaving the tensile specimen unaffected. The transmitted wave reflects off the free output bar end as a tensile stress wave, returning to the specimen. The collar, unable to transfer tension, is unloaded and allows the specimen to be loaded in an unrestricted fashion. Figure 2.6 illustrates the wave propagation expected in this arrangement.

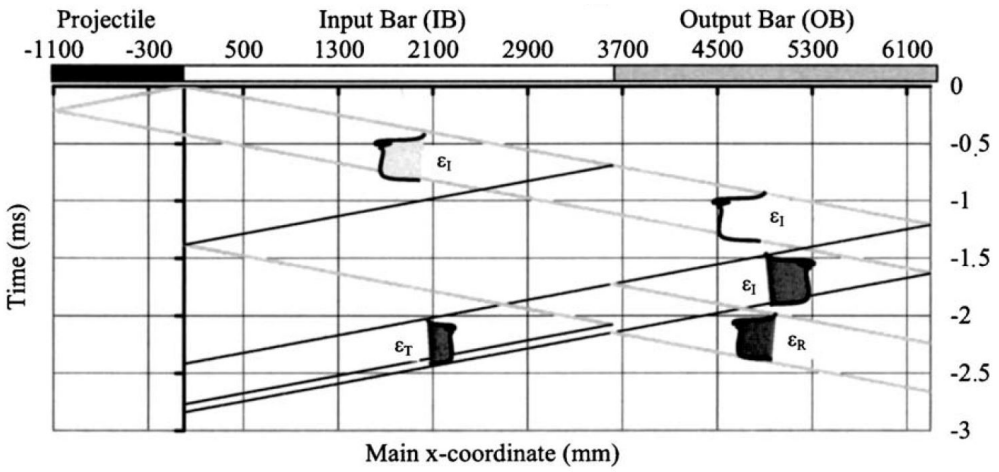

Figure 2.6 Lagrangian X-T diagram for the indirect loading method, as shown by Haugou *et al.* [37]

In an ideal situation, the specimen will only experience elastic compressive strain due to the incident wave [28], however, practically, some undesired compressive pre strain tends to occur [1]. Peroni *et al.* [23] stated that this system tends to introduce noise in the signals due to the residual oscillations generated by the passage of the compression incident wave. Bar length and strain gauge positions are of particular importance, as superposition of any waves over the signal of interest is undesirable. The interference of reflected waves can be seen on the Lagrange diagram in Figure 2.6. This effect was found to be highly problematic, when a project by Watermeyer [38] at BISRU in 2004 used this indirect method. Watermeyer also found that the apparatus was incapable of fracturing ductile metal specimens due to strain limitations, meaning that a full stress strain curve could not be produced in a single test, as stated by Downey [39]. This limitation is also noted by Lindenfeld and Partom [40]. In addition, as was the case with the top hat method described in Section 2.2.2.2, there is no line of sight of the specimen, limiting the measurement techniques that can be employed.

Nicholas [41] notes that the tight fit of the collar against the pressure bars is vital if the interface is to transfer the compressive incident pulse without disrupting the wave significantly. Watermeyer [38] found that achieving adequate contact at the interfaces between the collar and bars is virtually impossible. These components needed to be perfectly aligned and the surfaces parallel to one another in order to cleanly transmit a pulse. The difficulty of that, together with the inherent mismatch of impedance between the bars and the collar created significant spurious reflections [38]. This approach was moved away from, as these issues make it challenging to extract useful data.

2.2.2.4 Preload Tension Method

Albertini and Montagnani [42, 43] proposed the disparate preload tension TSHB. This is often call the direct tension method in literature. Staab and Gilat [3] implemented this technique in 1991. When using this method, instead of creating a pulse from the kinetic energy of a striker, it is created from elastic potential energy stored in a portion of the input bar. The is done by clamping the bar, and applying direct tension at the end of the bar [3]. The test is initiated by releasing the clamp, causing a tensile pulse to propagate through the originally unstressed portion of the input bar towards the specimen [44]. A diagram of this method is shown below in Figure 2.7. This technique has been utilised by studies in a wide range of applications [45, 46, 47, 48, 49]. This arrangement offers the advantage of longitudinal compactness, by omitting a striker bar and its associated launching apparatus [46]. Consequently, the stress waves generated can have longer durations compared to the total length of the apparatus. This is made possible by the absence of striking hardware, which allows for longer pressure bars to be accommodated.

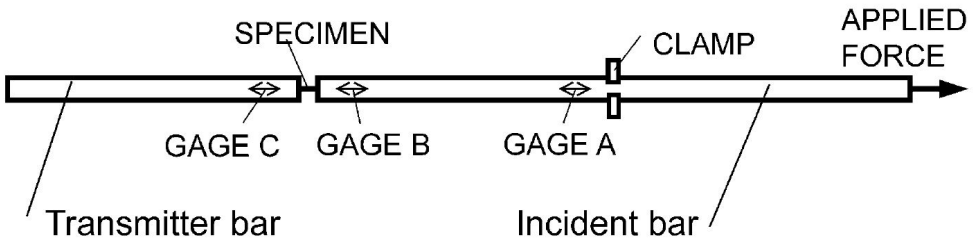

Figure 2.7 Preload tension method by Staab and Gilat [3], as depicted by Gilat [50]

According the Mancini *et al.*, a limitation is that the incident pulse has half the stress magnitude of that in the preloaded section. Essentially, this means that the incident stress can never be greater that half of the yield strength of the bar. Additionally, the shape of the incident pulse depends on the rapidity of the release of the tensile wave, and consequently it is challenging to create a cleanly rising stress pulse [51]. Various clamp designs have been developed to address this, the most notable being by Albertini *et al.* [52] and by Baumann *et al.* [53]. This method is used by researchers, however most have pursued alternative configurations.

2.2.2.5 Tensile Striker Method

The most commonly used method is that of making an incident stress wave using an impact from a striker [54], as shown in Figure 2.8. The striker is typically located around the input bar, and is fired away from the specimen. The striker impacts a flange (the anvil in Figure 2.8) on the end of the input bar, creating a tensile incident stress pulse. This stress pulse propagates to and loads the specimen in direct tension. Figure 2.8 depicts this configuration for TSHB experiments.

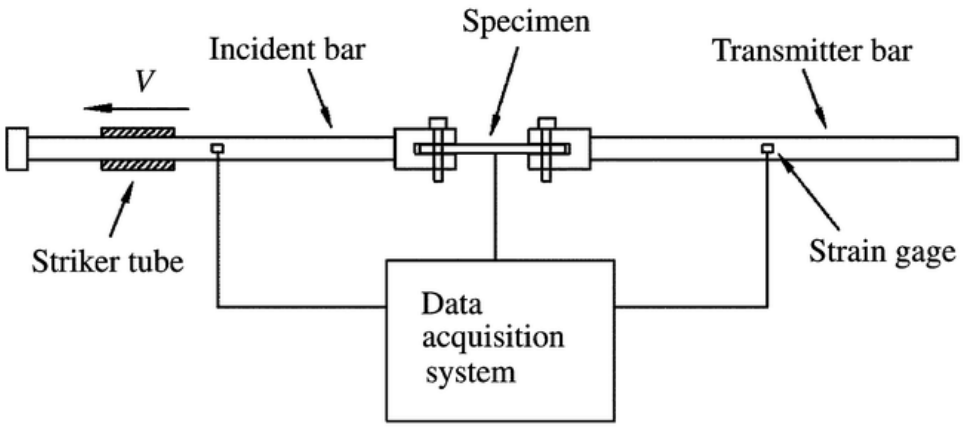

Figure 2.8 Tensile striker design of TSHB, adapted from Xu *et al.* [55]

The advantages of this system is that it does not rely on reflections, load inversion, or input bar preload, and therefore the aforementioned limitations of these methods are avoided. No problematic noise is expected, as was the case with the indirect loading method. This is because the specimen is strained by the incident wave and does not have to wait for a reflection from the free end of the output bar. The incident wave can be adjusted easily by modifying the striker geometry or using pulse shaping techniques. This control is not offered as simply by the aforementioned methods. Further details surrounding striker design and specimen mounting are discussed in Sections 2.3 and 2.4 respectively.

2.3 Tensile Striker Designs

The trademark characteristic of the method discussed in Section 2.2.2.5, is the tensile incident stress wave, created by a tensile striker impact. Tensile strikers tend to be more complex than their compressive counterparts. Various designs have been adopted as the TSHB developed further. These designs are described in the sections below.

2.3.1 Tubular Striker

The tubular striker is the most widely used construction [56, 57, 58, 59, 60, 61], and its implementation is depicted in Figure 2.9. The tube sits around the loading bar and is propelled by means of compressed gas against an impact flange [62]. The loading bar is often neglected to device length constraints, and the impact flange is attached directly onto the input bar. The axisymmetry of the impact face between the striker and the impact flange allows for evenly distributed forces around the perimeter of the flange. This reduces the formation of any transverse waves in the input bar, which would introduce additional stress oscillations in the incident wave.

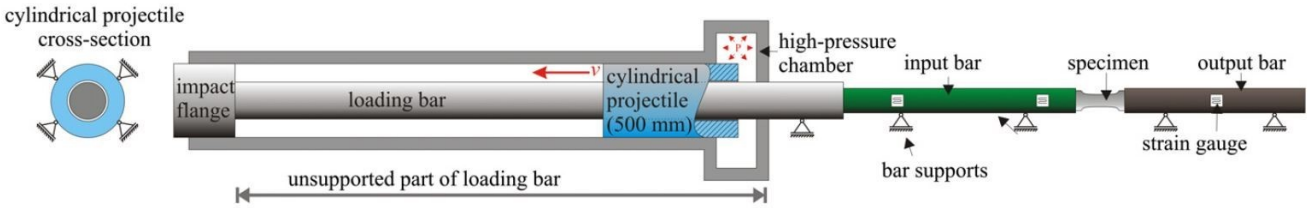

Figure 2.9 Diagram showing the use of a tubular striker on a conventional TSHB [62]

Gerlach [62] expresses however that the design renders most methods of pulse shaping highly inconvenient due to access. The is because the impact flange being surrounded by the gas gun, as seen in Figure 2.9. Furthermore, when a dedicated loading bar is not used, a portion of the input bar remains unsupported. The unsupported length of the bar will be equal to the sum of the striker length, and the striker run-up distance. Input bar sagging can reduce the signal quality significantly, and can touch and drag on the striker if this effect is severe [62].

2.3.2 U-shaped Striker

In 2012, Gerlach *et al.* [62] implemented a tensile striker that has a U-shaped cross section, as shown in Figure 2.10. Neumayer *et al.* [63] later implemented a similar design. This shape of striker was used primarily so that the input bar could be supported in the vicinity of the striker. The gap in the underside of the striker provides access for the additional bar supports, which allows for fewer stress oscillations in the generated pulse [62]. This prevents bar sag, which in turn improves the quality of the input signals, and ensures there is no striker contact made with the input bar. This design also provides for better access to the impact flange, allowing various pulse shaping techniques to be employed [62]. Furthermore, longer strikers can be accommodated as the input bar support is unaffected by the striker.

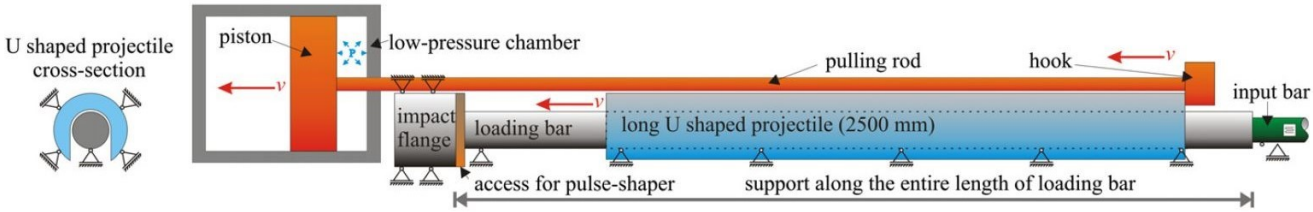

Figure 2.10 Diagram showing the use of a U-shaped striker on a conventional TSHB [62]

A disadvantages to the U-shaped design is that a large portion of the input bar remains inaccessible to the user without the removal of the striker. Access is often required for maintenance. The support hardware of this striker is more complex than that of a tubular one, as rotational motion about its centre axis must be restrained. This is to prevent the striker interfering with the input bar supports. In addition, the impact face is not axisymmetric, as it was with the tubular striker in Section 2.3.1, creating an uneven distribution of the impact forces.

2.3.3 Pull-off Striker

In 2007 at BISRU, Downey [39] developed a new type of tensile striker. In theory, this design was the same as the tubular strikers used in previous work, except the body of the striker was offset, located partially around the gun barrel, instead of only around the input bar [15]. This design is shown in Figure 2.11.

When fired, compressed air is pushed into the striker via holes in the walls of the plugged barrel. This pressure acts on the left-hand flange of the striker, drawing it back towards the gun until the flange on the right-hand-side impacts the flange on the input bar. This

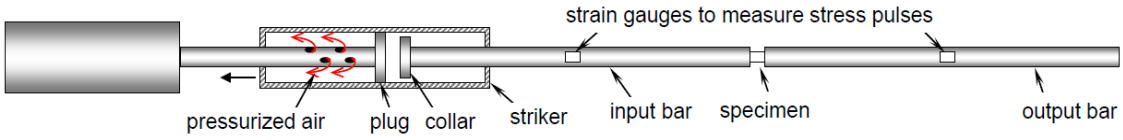

Figure 2.11 The pull-off striker designed by Downey [39]

generates a tensile incident pulse in the bar, similar to other methods. This design of striker is advantageous over others as it allows the input bar to be supported nearly over its entire length, which is key factor lacking from the conventional tubular strikers outlined in Section 2.3.1. It allows for better access to the input bar, and the impact face is axisymmetric, both of which are issues for the U-shaped strikers described in Section 2.3.2. Prior to this dissertation, the Downey striker configuration was used for all published TSHB experiments at BISRU, including the work by Weyer [15] in 2018, and Curry [64] in 2017.

2.4 Tensile Specimen Mounting

Under the umbrella of the TSHB design mentioned in Section 2.2.2.5 that uses a tensile striker, there have been a wide variety of methods to secure the test specimens to the pressure bars. The mounting of a tensile specimen is more challenging than that of a compressive specimen [65], as the connection must transfer tensile forces, and cannot simply be placed in between the bar faces as it is in compressive tests. Some of the specimen mounting arrangements used in previous studies are documented in this section.

2.4.1 Positive Methods

The first method of tensile specimen mounting discussed involves a form of positive engagement connecting the specimen to the rest of the apparatus. A common method is to secure the specimen using dowel pins that pass through cross drilled holes in both the specimen and its fixtures, as displayed in Figure 2.12a. The fixtures are connected to the pressure bars via a threaded connection. Such fixture have been used in studies such as the one by Xu *et al.* [55] in 2012. Peroni *et al.* [23] used cross-pins to hold tensile specimens, in conjunction with a collar in the indirect loading method discussed in Section 2.2.2.3. Owens and Tippur [66], as well Moreira *et al.* [67] have experimented with form-fit specimens, that slot into the fixtures directly instead of using cross-pins. This design is shown in Figure 2.12b.

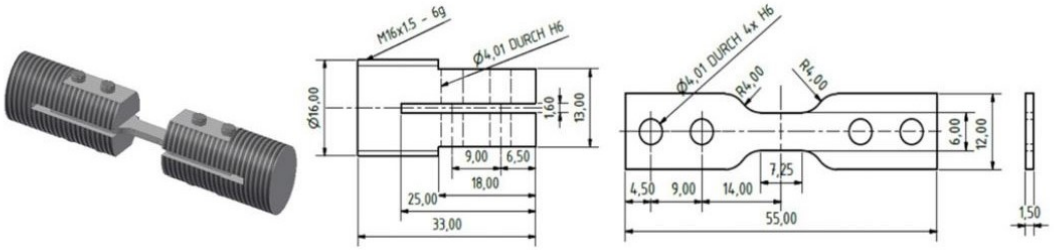

(a) Cross-pin design of mounting

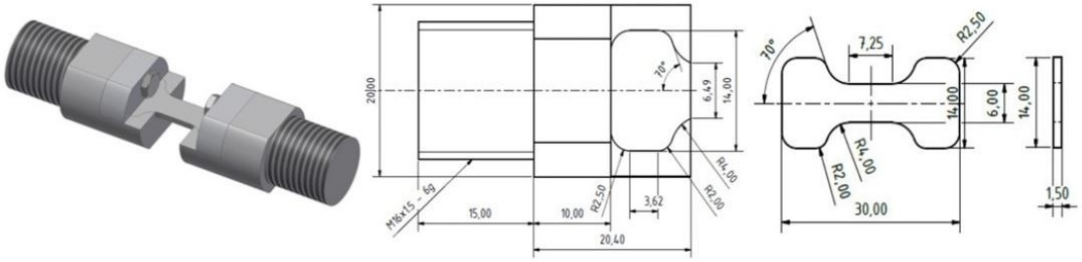

(b) Form-fit design of mounting

Figure 2.12 TSHB setup incorporating tensile specimen mounting using positive methods [65]

Despite the capability of withstanding high tensile loads, and its ease of assembly, the method has distinct drawbacks. The specimen is loaded via holes, which concentrate stresses and could lead to plastic deformation within the mounting region [65]. The inherent play due to the clearance between the specimen, pins, and fixture introduced significant noise in the signals [68]. The fixtures and pins themselves have significant mass, which lowers the rate of loading of the specimen due to inertial effects [65]. The inconsistent mechanical impedance between the bar and the specimen. This adversely affects the propagation of stress waves, and can invalidate the data [67].

2.4.2 Friction Methods

Other methods involve using friction, or a clamping mechanism to hold specimens. Some mechanisms, as seen in Figure 2.13, are simple, such as the method used by Smerd *et al.* [58], or by Huh *et al.* [57]. Both of these styles involve the cutting of a slot into the end of the pressure bar, and clamping the specimen by means of bolts. The clamping friction is said to bear the load, rather than contact between the transverse bolt and the corresponding hole in the specimen. These methods are mostly associated with sheet specimens [69].

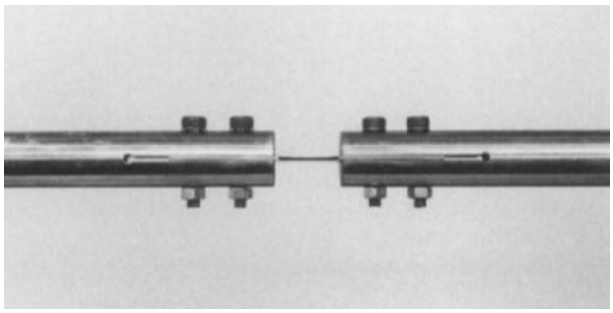

Figure 2.13 Specimen clamping system used by Huh *et al.* [57]

Leblanc and Lassila [70] developed a more sophisticated specimen clamping fixture in 1993, which was later improved on by Koh *et al.* [71]. These designs both use wedge mechanisms to multiply the clamping force on the specimen, and are picture in Figure 2.14.

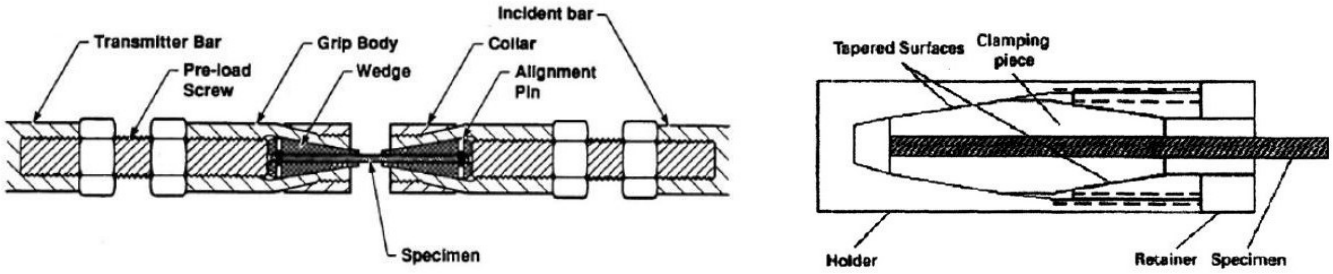

(a) Clamp design used by LeBlanc and Lassila [70] **(b)** Clamp used design by Koh *et al.* [71]

Figure 2.14 Further specimen clamping techniques

These wedge techniques have received criticism as the wedges to protrude from the bar ends, interfering with the gauge region of the specimen [72]. With reference to friction methods in general, minimising the chance of slipping (which would invalidate results completely), necessitates a large clamping force [58]. The end effects on the gauge section of the specimen increase proportionally with clamping force [57]. In addition, to provide adequate force, the fixture hardware must be bulkier and heavier, disrupting the propagation of the stress pulse. A large discontinuity in the mechanical impedance is also introduced, and the associated drawbacks are the same as described in Section 2.4.1. Ganzenmüller [69] designed a clamp to address the impedance issue, by keeping the cross sectional area of the fixtures uniform. The impedance of the clamp however is still greater than that of the bars, and spurious waves are introduced in the signals. Huh *et al.* [57] note that in their findings, 4 % of the incident energy is lost in the grip. This is likely due to slippage as a result of strain mismatch between the clamp and specimen. Force equilibrium for such specimens has not been shown in any of the mentioned studies, and it is improbably that they achieve this.

2.4.3 Use of Adhesive

A tensile dynamic specimen can also be mounted using an adhesive. Eskandari and Nemes [73], as well as Gómez-del Río *et al.* [68] implemented designs where specimens were glued into fixtures, which were in turn threaded into the pressure bars. Haugou *et al.* [37] incorporated bonded specimens into the indirect loading approach outline in Section 2.2.2.3. Alignment is critical when glueing the specimen into the fixtures, as the bending preloads should be avoided. Gómez-del Río *et al.* used a jig, pictured below in Figure 2.15, to ensure proper alignment.

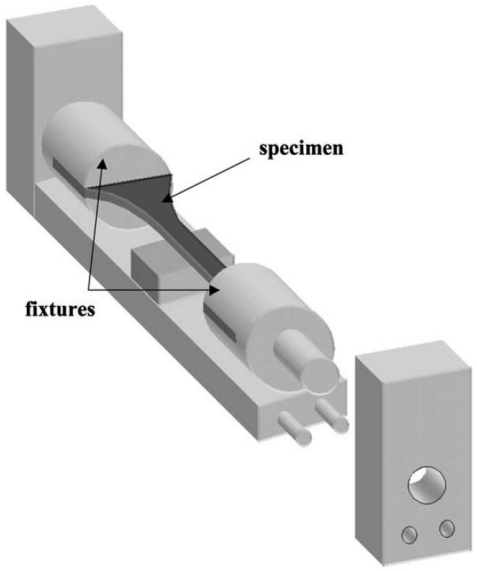

Figure 2.15 Specimen design by Gómez-del Río *et al.*, secured in a alignment jig for glueing [68]

As is the case for the aforementioned designs that incorporate fixtures in between the specimen and the bar, the additional mass and impedance mismatch pose issues. To address this, simplified methods have been used in studies [74, 75, 76, 77, 78], by glueing the dumbbell-shaped sheet specimens directly into slots on the ends of the pressure bars. This is depicted in Figure 2.16. Peirs *et al.* [79], as well as Verleysen and Degrieck [80, 81] later used a similar method.

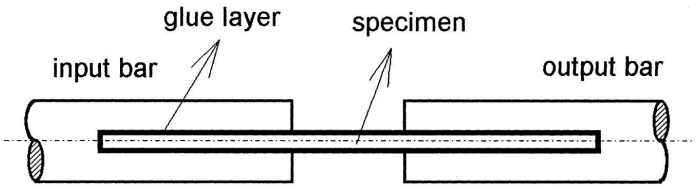

(a) Glued connection of the specimen with the pressure bars

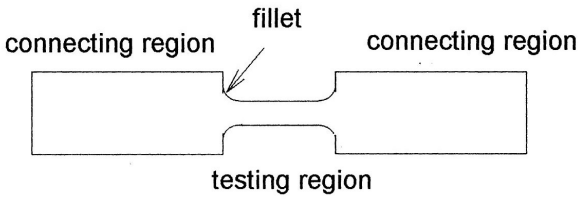

(b) Dumbbell-like flat specimen

Figure 2.16 Diagram of the improved configuration using adhesive, as used by Wang and Xia [77]

These joints provide the best quality and consistency of force equilibrium across the specimen, of all the aforementioned methods. Verleysen *et al.* [82] claim in their 2009 study, that "equilibrium was established in the the early stage of loading", but the data was not presented. The simplified arrangement pictured in Figure 2.16 performed especially well in this regard due to its desirable consistency of mechanical impedance in the clamped region.

Adhesively bonded joints do inherently introduce the need to characterise the glue material itself, and particularly to assess the strain rate dependency of its mechanical properties. Studies have been conducted to confirm such characteristics, such as that done by Lißner *et al.* [83] in 2018. Glued joints were tested over a range of strain rates under tension, shear, and combined loading. Both the specimen and the slots in the bars or fixtures needs to be machine to a small tolerance, as the thickness of the glue layer needs to be correct and consistent. The clearance between slot and specimen needs to be small enough to reduce compliance in the glue layer, but not too tight as to scrape the glue off the specimen upon installation. In order for tests to be run the specimen needs to be carefully aligned and glued into place. The glue then takes time to cure, often up to 24 hours. After testing is complete, the specimen is removed from the bars. This is commonly done by burning them out. This entire process is laborious and time-consuming. For this reason, a single test can typically be conducted per day, meaning this method is not compatible with routine testing [84].

2.4.4 Use of a Threaded Connection

A direct threaded connection between the specimen and the pressure bars has also been experimented with. This specimen design is displayed in Figure 2.5 in Section 2.2.2.3 on the indirect loading method, as utilised by Nicholas [41] and Ellwood *et al.* [36]. In most cases, the specimen has external threads on its ends, which fastened into the internal threads in the pressure bar ends [67].

Bowden [85] used an adaptation of this method that, with the use of an adhesive, can be used to test sheet specimens. This configuration is shown in Figure 2.17. Although glueing is involved with connecting the specimen to the threaded bar adaptors, the adaptors can be mass manufactured and allow for routine testing, unlike the traditional adhesive techniques. Ross *et al.* [86] presented a variation of this concept to accommodate specimens that are unsuited to threads, such as those made of composite materials. This arrangement is displayed in Figure 2.18.

Since straight cut threads are used, they include clearance between the male and female parts. When loaded, the take up of play in the joints can be misinterpreted as specimen strain, influencing the validity of the results [87]. Furthermore, straight cut threads have a tendency to loosen as a result of the stress pulse, which introduces further uncertainty

in the acquired data. There is also a tendency for the first couple of threads to bear the majority of the load. Figure 2.19 from a study by Nguyen *et al.* [88] displays this effect. This concentration of stress can lead to unwanted localised plastic strain in the threads.

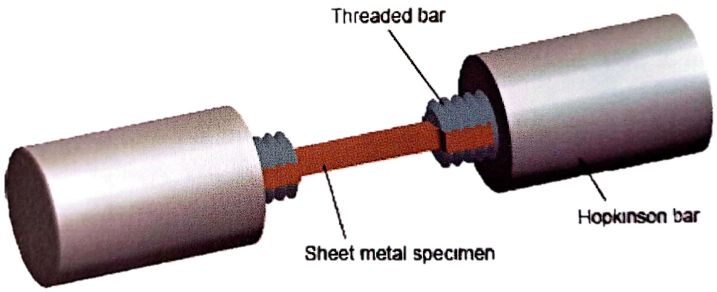

Figure 2.17 Adaptation of the threaded design used by Bowden [85] for sheet specimens, taken from the study by Downey [39]

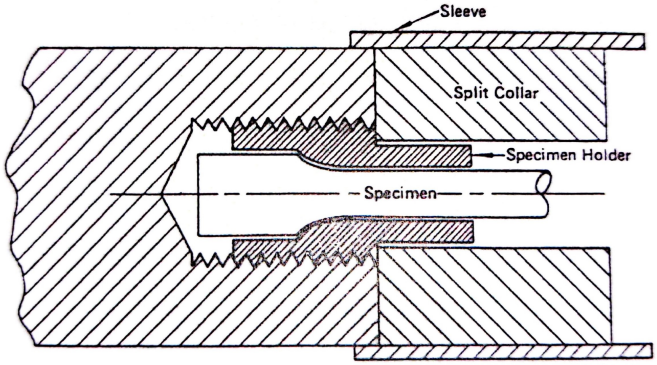

Figure 2.18 Adaptation of the thread design used by Ross *et al.* [86] for composites, applied to the indirect loading method

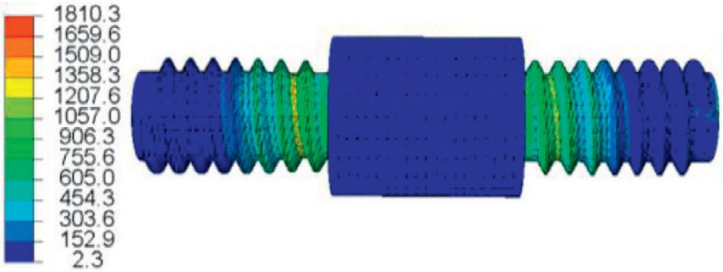

Figure 2.19 Von-Mises stress distribution for a threaded specimen, in MPa [88]

2.4.5 Fir-tree Specimen and Clamp Fixture

BISRU currently makes use of a specimen mounting arrangement called the fir-tree fixture. The concept was conceived by Dr Trevor Cloete and initially implemented by M. Yende [89] in 2010. N. Cele [90] improved on its in 2011 by further refining the fir-tree profile. The tensile specimen, shown in Figure 2.20, is cut from a sheet stock. The ends of the specimen resemble a fir-tree, with its overall conical shape, and toothed edges. These 'teeth' are referred to as lobes. The specimen, along with its clamps, form the fixture.

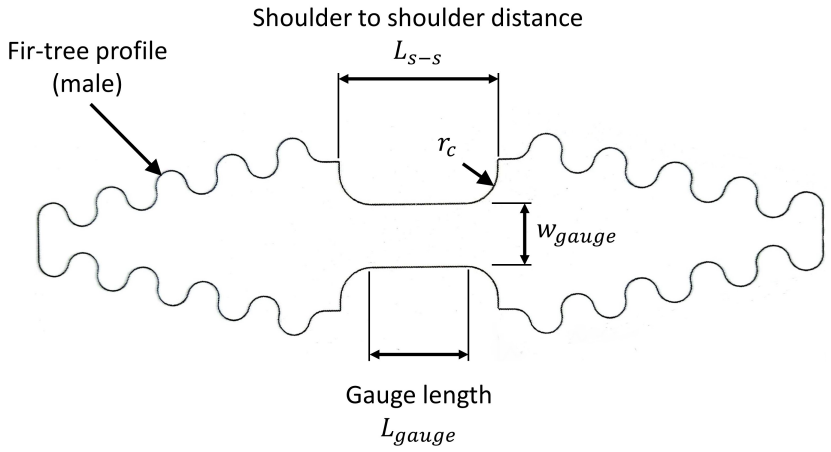

Figure 2.20 Fir-tree tensile specimen design, adapted from Yende [89]

This fixture is symmetric in that it has identical clamps mounting each end of the specimen. Each clamp is made out of a pair of clamp halves that, when placed together, encapsulate the profile on the end of the specimen, forming a cone. The outer surface of this cone is threaded to fit with the ends of the pressure bars. The fixture is secured by tightly screwing the clamp into the bar, using a custom pinned tool which acts on the pin holes in the face of the clamp. This assembly is illustrated in Figure 2.22.

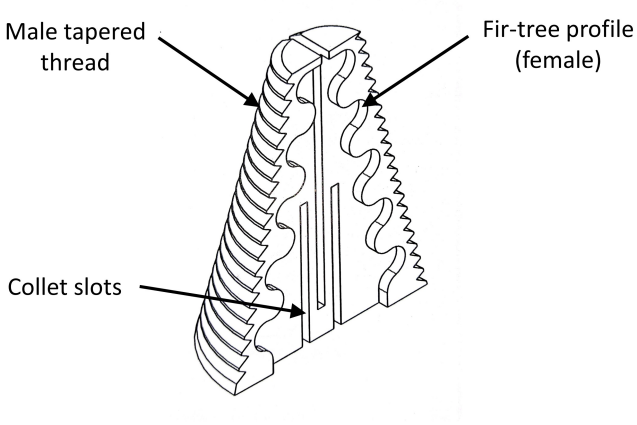

Figure 2.21 Fir-tree specimen clamp half, adapted from the drawing by Yende [89]

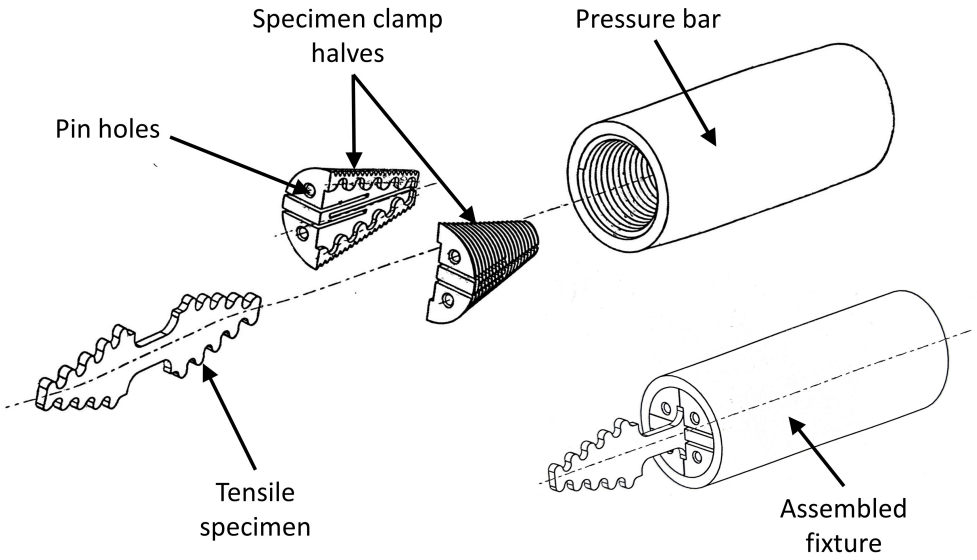

Figure 2.22 Assembly of the fir-tree fixture design, adapted from the drawing by Yende [89]

Each clamp half has a set of collet slots cut through its centre. These slots give the two clamp quarters the flexibility to converge or diverge. The effect of this is that, when threaded into the end of a bar, the four quarters of each clamp come together to grip the specimen. This functions similarly to a four-jaw chuck. Furthermore, the compliance introduced by the collet slots allow the specimens to click into the clamp halves and not

fall apart during handling. The aforementioned features all contribute to a pleasant user experience. The clamp halves are made of titanium to minimise the mass of the fixture while maintaining strength and stiffness. Furthermore, pressure bars in TSHB setups tend to be aluminium, and since the clamps are made of titanium, the dissimilarity reduces the potential for binding of the threaded mating surface [84].

The following are key features of this fixture:

- It is self-centring. Due to the conically threaded fixtures, once tightened, the input bar, specimen and output bar will all be coaxial.
- The specimen is held both by means of positive engagement from the fir-tree lobes, and by clamping force supplied by the tapered threads. For this reason, there is no concern of friction slip.
- There is little to no play or backlash in the fixture.
- The specimens can be cut using a variety of techniques including EDM.
- Specimens are cheap to manufacture.
- Specimens installation and removal is a fast and simple process. No glueing is required, making the fixture appropriate for routine testing.
- Due to the tapered shape of each clamp, an arriving stress wave sees a gradual change in mechanical impedance. A sudden change would result in a large portion of the incident wave being reflected before it reaches the bar end.
- The conical shape of the clamps and specimen allow for smoother transfer of load, as the cross sectional area of the bar, clamp, and specimen changes gradually. This reduces the effect of the stress concentrations found in straight threaded fixtures [84].
- On each lobe of the specimen, the peak radius is marginally bigger than that of the corresponding trough radius in the clamp, and vice versa. This ensures that force is only transmitted on the flat sections of the profile, on either side of each lobe. This further reduces stress concentrations, minimising the possibility of plastically deforming the specimen in the clamped region [84].
- The taper angle of the clamp threads means that once inserted, each clamp can be fully tightened in as little as 1.5 rotations. This saves the inconvenience of rotating pressure bars with strain gauge leads attached, which is troublesome when using straight threaded specimen designs.

- The load on the tapered threads is distributed more evenly than that when using straight threads.
- The load on the lobes of the fir-tree specimen is evenly distributed.

There are a few imperfections to note about this design:

- A given set of clamps is designed with a specific specimen thickness with a small variation. When it comes to specimen thickness, the clamps are not a one-size-fits-all solution. For that reason, a set of clamps are needed in order to accommodate all thicknesses of specimen.
- There is a limit on the size and configuration of specimens.
- Although the clamps are once off parts, the manufacturing process is intricate. The order of machine operations is critical. Furthermore, the small features with tight tolerances require a highly experienced machinist.
- The pinned tool currently being used to tighten the fixture into the bars is static, and does not allow for the converging of the pin holes on the clamp as it is tightened.
- The load transfer from the pressure bar to the clamp to the specimen, although efficient and smooth, will never be as ideal as the glued methods of specimen mounting mentioned in Section 2.4.3.

At BISRU, this method of tensile specimen mounting is favoured due to its multitude of advantages. A set of clamps already exist for a range of common specimen thicknesses.

2.5 Dynamic Specimen Recovery

Nemat-Nasser *et al.* [91, 92] noted that the classical Hopkinson bar technique is "limited to obtaining the dynamic stress-strain relations to failure". In other words, a traditional SHPB experiment results in the specimen being loaded multiple times and consequently the specimen deforms sufficiently to fracture. This is explained in detail below, using the Lagrange diagram of a standard TSHB in Figure 2.23 as an example.

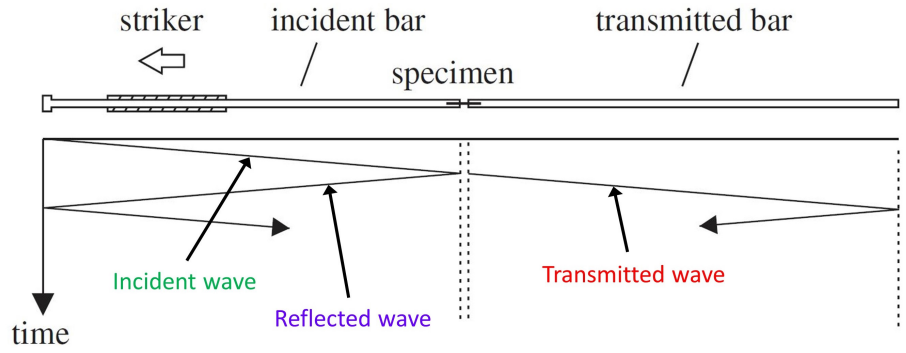

Figure 2.23 Lagrangian X-T diagram of a standard TSHB, adapted from the diagram by Isakov *et al.* [93]

When the tensile incident wave reaches the specimen, a portion of it will be reflected back into the input bar as a compressive wave. This is due to the sudden decrease in mechanical impedance as the wave enters the specimen. This reflected wave will reflect again off the striker end as a tensile wave, and will potentially reload the specimen. Simultaneously, the transmitted portion of the wave will reflect off of the free end of the output bar, and will return to the specimen as a compression wave. As a result, for a single test, the specimen will be subjected to multiple waves of unintended loading, after the prescribed one [93]. If a specimen fails completely, it, in most cases, cannot experience the repeated loading. It can then be removed and analysed on the microstructural level, as there is a known loading history behind that specimen [91]. This is not the case for an intact specimen, as the subsequent reflected waves will have further loaded the specimen, creating a mismatch when comparing loading history to physical post-test analysis [94].

There is however a need to be able to thoroughly analyse intact, or unbroken specimens. Being able to recover these specimens is required in order to piece together the "microstructural evolution" [93] of the material. This may be done by examining the specimen using techniques like electron microscopy [95]. If the SHPB test can be interrupted with the specimen only having experienced the prescribed single loading period, then this is achievable. The requirement simplifies to being able to protect the specimen from any stress waves beyond the intended one.

2.5.1 Strain Limiting Fixture

In other studies [96], stoppers have been tested as a means of limiting the total compressive strain of a specimen, and to take the load from subsequent compressive pulse one such a strain is reached [91]. Equivalent methods have been explored for tension [97, 98, 99, 100], using a stopper frame to protect the support the tensile specimen. An example of this method is depicted in Figure 2.24, and was designed by Lezcano *et al.* [97]. The frame length can be adjusted using a thread, to alter the allowable strain on the specimen.

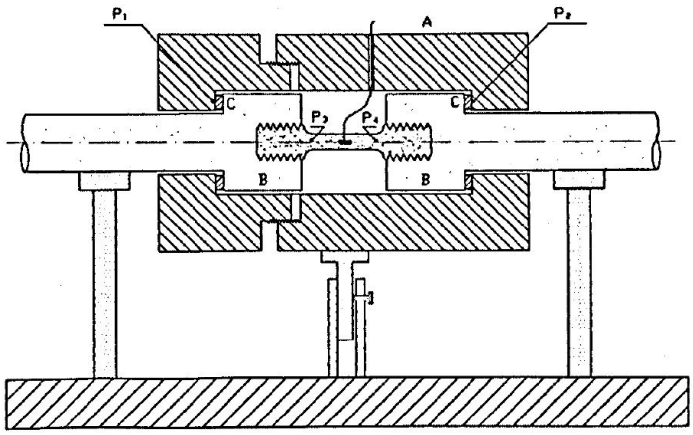

Figure 2.24 Adjustable stopper frame designed by Lezcano *et al.* [97] to protect tensile specimens against reloading

This method of dynamic specimen recovery is limited to certain specimen materials, as those with a low strain to failure render this technique ineffective. The sensitivity to flushness of the experimental setup is once again present. The stopper fixture itself is compliant and is incapable of bringing the bar ends to a dead stop once the desired specimen strain is reached. Since the bars are being forcibly halted, this method gives rise to significant additional stress waves that can obscure the unloading behaviour of the specimen, similar to the indirect method mentioned in Section 2.2.2.3. Furthermore, this strain limiting fixture can only protect the specimen from further strain in one direction. The tensile stopper frame shown in Figure 2.24, for example, cannot protect the specimen from a compressive pulse reflected off a bar end. This approach proves unreliable for recovering dynamic specimens, with its drawbacks far outweighing any potential benefits.

2.5.2 Momentum trapping

A more commonly approach is to use momentum trapping. Utilised first by Nemat-Nasser *et al.* [91] in 1991, this technique prevents any stress waves from reflecting off of the free ends of the pressure bars. This means that the specimen would be protected against significant reloading. The basic concept is that an extra bar is added, which allows a

stress wave to enter it, but not to exit again. This traps the energy in a member that is then isolated from the system.

2.5.2.1 Single Trap Tensile Configuration

First implemented by Nemat-Nasser *et al.* [91] in 1991, the momentum trapped configuration of TSHB is illustrated in Figure 2.25. The striker is tubular, as was the case with the TSHB described in Section 2.2.2.5, and is fired away from the specimen against a flange on the input bar. A trap bar lies end to end with the pressure bar, with a preset gap between the two. The output bar too has a flange on its end, and is surround by a tubular momentum trap designed to capture the transmitted wave [101]. This output trapping method was adopted from that used by Lataillade *et al.* [102].

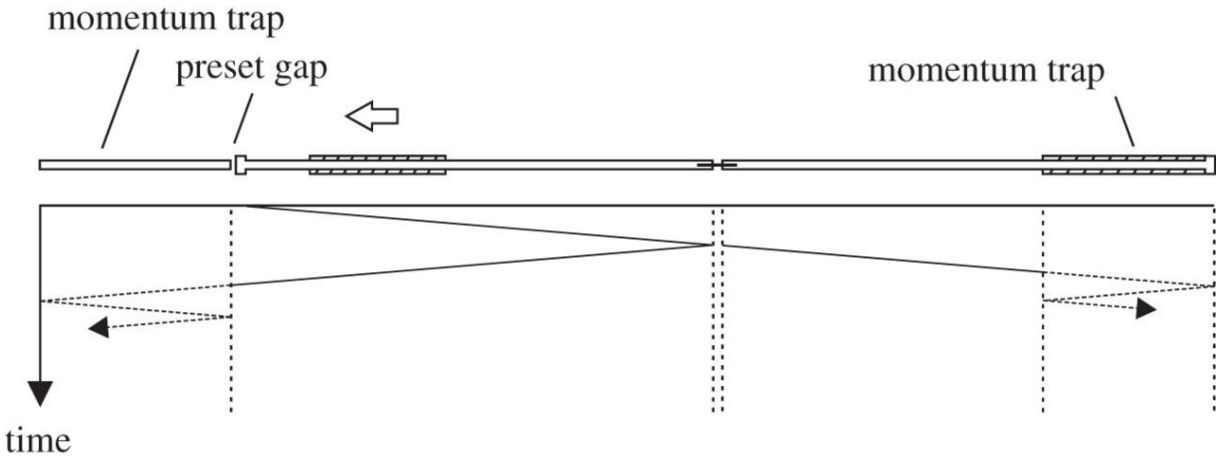

Figure 2.25 Momentum trapping for a TSHB using the single trap method by Nemat-Nasser *et al.* [91], as shown by Isakov *et al.* [93]

Upon striker impact, the preset gap closes, and a tensile wave propagates towards the specimen. The reflected compressive wave returns, and passes into the momentum trap on the input side, which is now in contact with the input bar. The transfer of this stress wave is optimised by matching the mechanical impedances of the two bars. The wave then reflects off the free end of the input momentum trap as a tensile wave, but is unable to re-enter the input bar, as the boundary cannot transfer tensile loads [91]. The reflected wave is therefore trapped and isolated. Simultaneously, the tensile transmitted portion of the wave continues to the end of the input bar, where it is transferred into the tubular momentum trap as a compressive wave. When reflected off of the free end of the output trap as a tensile wave, it is unable to re-enter the output bar, as that interface cannot transfer tensile loads from the trap. The transmitted wave is therefore also trapped and isolated. The tensile specimen has now only been subjected to the single, intended loading.

It is mentioned that when using the single trap method, a gap between certain components needs to be set prior to each test. In each case, this gap is set so that hardware is in the perfect position to trap the reflected wave when it returns. Consider Figure 2.25, the standard trapping configuration by Nemat-Nasser for tensile testing. If the gap does not exist or is too small, a portion of the energy of the striker impact would immediately create a compressive pulse in the momentum trap, which would reflect off its end as tensile, and separate the trap from the input bar before the reflected wave returns. Contrarily, if the gap is too large, the input bar may not have moved enough to be in contact with trap when the reflected wave returns. In both of these cases, the reflected wave will not be able to pass entirely into the momentum trap. If the gap is not closed fully, the specimen will be reloaded with a pulse that may be shorter in duration, but will be of similar magnitude to the reflected wave [103]. This result is illustrated in Figure 2.26.

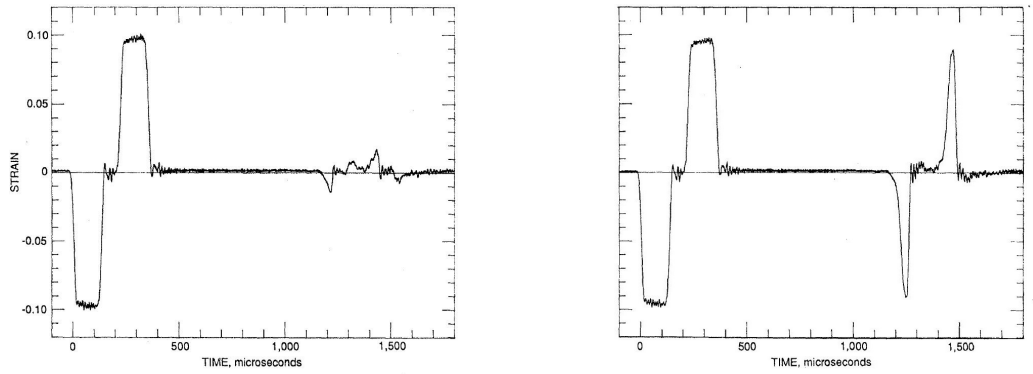

(a) Adequately trapped reflected pulse; gap was well set

(b) Poorly trapped reflected pulse; gap was too large

Figure 2.26 Comparative plots by Nemat-Nasser *et al.* [91] illustrating the importance of precise gap setting

If the gap is set perfectly, the momentum trap will lay in close contact with the input bar before the reflected wave returns. The gap needs can be calculated, but ultimately always requires trial and error [91]. The ideal gap size varies according to striker speed, and is estimated to have a tolerance of 50 μm [104]. Striker speed is difficult to control precisely and predictably, as it relies on the striker launching apparatus performing identically every time, which is not typically the case. Furthermore, setting a gap to a small tolerances is challenging, this method requires considerable operator experience to implement correctly and consistently [105]. Gap setting is therefore a problematic endeavour, leading the quality of results with this method to be highly sensitive to experimental procedure.

2.5.2.2 Tandem Trapped Compressive Configuration

In 2012, Prot *et al.* [105] used a configuration to remedy the issue of gap setting. Referred to as the tandem trapping technique, Prot and Cloete [106] described this configuration as "able to provide a single specimen loading event, without the need for any preset gaps". The tandem trapping solution was first used to conduct compressive tests on cancellous bone. A diagram of the configuration used by Prot *et al.* [105] is shown in Figure 2.27. There are now two momentum traps on the input side, both of which are of matching impedance to the input bar.

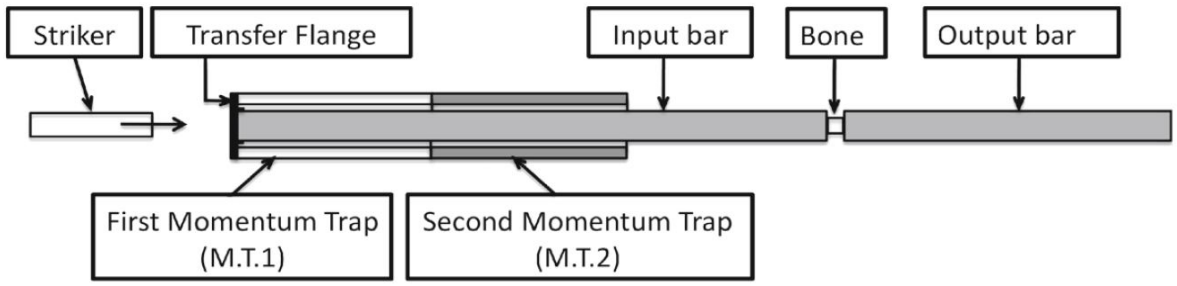

Figure 2.27 Compressive tandem trapping method designed by Prot and Cloete [106]

There is now no preset gaps, and all traps and bars are in physical contact. With reference to Figure 2.27 and its naming convention, M.T.2 is what replaces the need for a preset gap. When the striker impacts the transfer flange, compressive stress pulses are simultaneously sent down the input bar, and down the stack of tubular momentum traps. Since the traps are closely impedance matched, there is minimal reflection at the interface between M.T.1 and M.T.2, and the wave in M.T.1 passes into M.T.2 in its entirety. When it reached the free end of M.T.2, it is reflected as a tensile wave, but cannot re-enter M.T.1 as the interface does not support tension. M.T.2 then separates from M.T.1, leaving M.T.1 in contact with transfer flange.

When the tensile reflected wave returns from the specimen interface, it passes from the input bar into M.T.1 via the transfer flange, loading M.T.1 in compression. As was the case with the interface between M.T.1 and M.T.2, the effectiveness of the stress transfer depends on M.T.1 and the input bar being closely impedance matched. The stress wave in M.T.1 reflected off its free end as a tensile wave, and cannot re-enter the input bar. M.T.1 then separates from the transfer flange and input bar, isolating the reflected wave.

This is the same result that the gap setting method aims to achieve, but is more reliable, is independent of striker speed, and does not rely on the skill or 'touch' of the user [106]. A downside to this method is that part of the incident wave amplitude is lost, as the

impact has to load the input bar and trap stack simultaneously [93]. This means that a higher striker speed, or higher impedance striker, is required to achieve the same loading conditions as a test using the method by Nemmat-Nasser *et al.*.

2.5.2.3 Tandem Trapped Tensile Configuration

In 2014, Isakov *et al.* [93] adapted the tandem trapping concept to be used on a tensile configuration. The bar layout was based off of the trapping system previously utilized [91, 103, 107], but now made use of the tandem trapping solution by Prot and Cloete [106]. The bar layout, along with a Lagrangian X-T diagram is displayed in Figure 2.28.

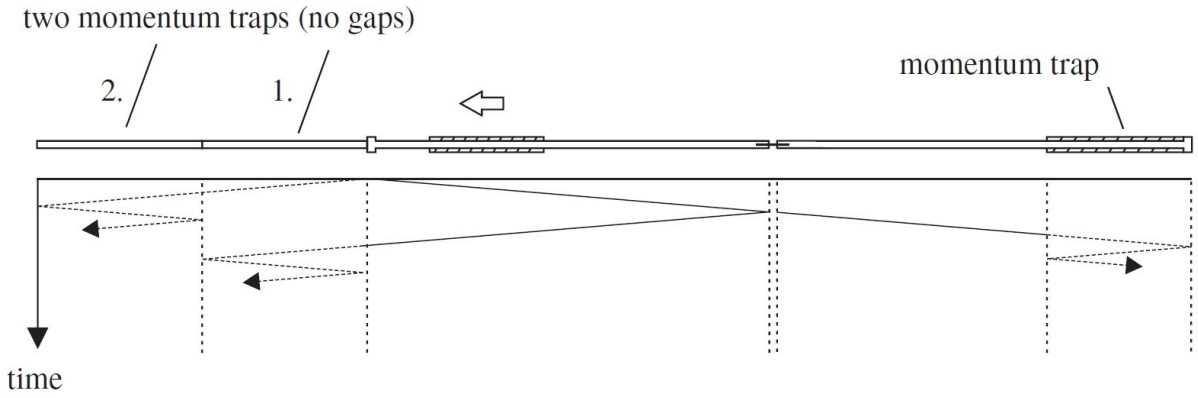

Figure 2.28 Tensile tandem trapping method designed by Isakov *et al.* [93]

Similarly to how the tandem trapping worked in Section 2.5.2.2, trap 2 is responsible for capturing the compressive wave put into the traps stack from the initial striker impact. This leaves trap 1 in close contact with the input bar. When the compressive reflected wave returns from the specimen interface, it passes into trap 1, reflects as a tensile wave, and is unable to re-enter the input bar. If trap 2 was not there, trap 1 would separate upon striker impact and would not be able to capture the reflected wave later on. This removes the need for gap setting one the input side [93]. The trapping on the output side operates identically to the mode described in Section 2.5.2.1.

As mentioned in Section 2.5.2.2, the success of the tandem trapping method relies heavily on how closely the impedances of each tandem trap match to each other, and to the input bar. At any point when a stress wave has to cross and interface, there will be a small portion of the wave that is reflected due to slight impedance mismatch, face imperfections, improper contact, or bar misalignment. Minimising these unwanted reflections is critical if trap 1 is to remain in contact with the input bar after the strike. Impedance mismatch can be addressed by adjusting bar diameters, a process described in Section 5.1. Face imperfections can be remedied via grinding or lapping processes, such as that outlined in

Section 5.3. Lastly, a high degree of bar alignment can be achieved by using methodologies such as that described in Appendix A.

2.6 Wave Dispersion

In SHPB testing of any kind, an important consideration to make is that stress waves are dispersive when propagating along the pressure bars [108]. The velocities at which different frequency components of a pulse propagate varies [109], as displayed in Figure 2.29.

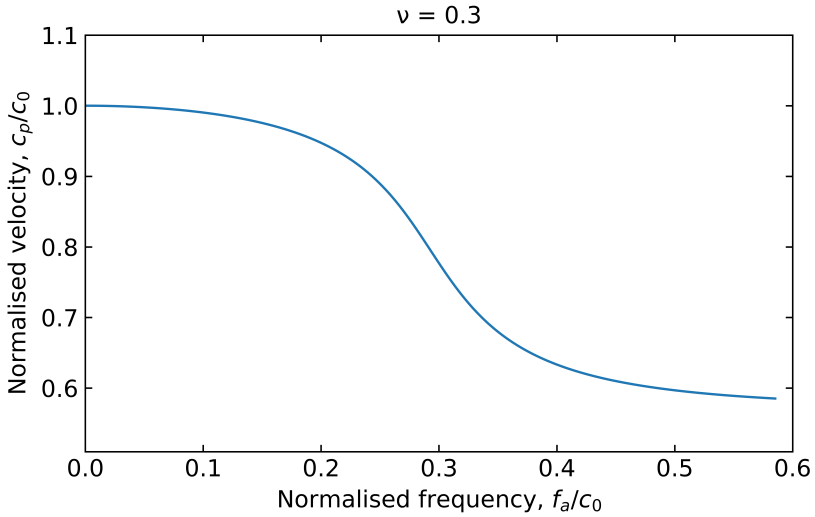

Figure 2.29 Plot of the first root of Bancroft's equation, adapted from a Python code by Van Lerberghe and Barr [4], expressing the variability of phase velocity as a function of frequency

This causes the shape of a stress pulse to change depending on how far it has to travel. Figure 2.30 illustrates this effect. In order to correct for these effects, the velocites of the series of frequency components in a bar must be known [110]. Pochhammer [111] and Chree [112] developed a solution relating the c_p, the phase velocity to the frequency of that particular phase. Bancroft [113] later expressed C_p as a function of the fundamental wave velocity c_0, Poisson's ratio v, frequency f, and the radius of the bar [109]. This allows c_p to be known as a function of frequency f for a particular bar. Davies [21] described how this data, together with Fourier theory, can be used to correct for the effects of wave dispersion in SHPB experiments. Discrete Fourier methods, are now used in studies [114, 115, 116, 117, 118] to attain corrected signals from raw digital SHPB data.

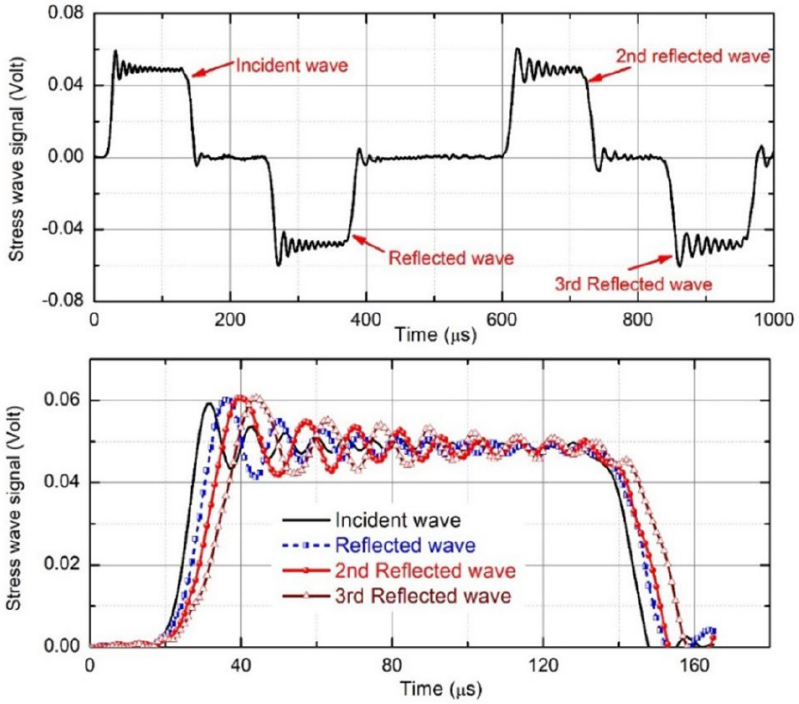

Figure 2.30 Comparative plot of how dispersion affects pulse shape as a function of distance travelled, as shown by Miao *et al.* [87]

Van Lerberghe and Barr [4] developed a Python script that solves for the first root of Bancroft's equation, attaining the phase velocity versus frequency data. The raw recorded data from an SHPB test is then moved to the frequency domain from the time domain using a fast Fourier transform (FFT). Now being in the frequency domain, each frequency component can be shifted by the prescribed distance, according to its associated phase velocity. From there, the shifted data can be moved back to the time domain using the inverse fast Fourier transform (IFFT). For a given pressure bar and material, this code takes the strain gauge data and shift distance as inputs, and outputs the shifted signal, having accounted for dispersion effects.

2.7 Closing Remarks

This chapter has outlined the literature relevant to the task of designing a momentum trapped TSHB. The apparatus historify had been described, and approaches to striker designs, dynamic specimen recovery and dispersion correction have all been summarised. The background knowledge acquired by conducting this literature review proved invaluable moving into the design and commissioning phases of this project.

Chapter 3

Design of the Tensile SHPB

This chapter describes the process of designing the TSHB apparatus. It begins with a set of requirements for this design. This outlines the performance metrics, features, constraints and standards that governed the decisions made in designing the parts and sub-assemblies that make up the final product.

All design considerations and decisions are described throughout the rest of this chapter. Supplementary design material, the full bill of materials, and the engineering assembly drawings may be found in Appendices C, K, and L respectively.

3.1 System Requirements

3.1.1 Functional Requirements

Table 3.1 *Functional requirements of the TSHB*

Requirement	Metric	Value	Rationale
RQ1	Striker velocity	0 - 15 m/s	To produce the required strain rate in the specimen
RQ2	Specimen strain rate	200 /s to 1000 /s	To produce be able to strain a specimen at a desired rate
RQ3	Specimen strain	0 to 0.25	To be capable of straining ductile metals until failure

Requirement **RQ4** : The TSHB shall be capable of producing useful results for material characterisation.

Requirement **RQ5** : Both pressure bars shall be momentum trapped, preventing the specimen from being loaded repeatedly.

Requirement **RQ6** : The TSHB shall utitlise the existing fir-tree tensile specimen and fixture.

Requirement **RQ7** : The TSHB shall include means of measuring and recording striker speed.

3.1.2 Operational Requirements

Table 3.2 *Operational requirements of the TSHB*

Requirement	Metric	Value	Rationale
RQ8	Reset time	Max 5 minutes	Apparatus shall be capable of routine testing

Requirement **RQ9** : In the event of leakage to atmosphere or between pressure chambers, the gas gun shall not fire.

Requirement **RQ10** : The gas gun shall be able to be disarmed and depressurized without firing.

Requirement **RQ11** : The reset of the apparatus shall be a simple process, and shall not depend on the skill of the operator.

3.1.3 Constraints and Standards

Table 3.3 *Constraints and Standards applicable to the TSHB*

Requirement	Metric	Value	Rationale
RQ12	Diameter	Max 210 mm	Device, including the gas gun, must be compatible with height of existing bar supports
RQ13	Total length	Max 9.0 m ± 20 cm	Device must fit on existing bed
RQ14	Working gas pressure	Max 10 bar	To ensure compatibility with current pneumatic supply and equipment

3.1.4 Serviceability Requirements

Requirement **RQ15** : The TSHB shall make use of tool sizes currently used in the lab, else a dedicated custom tool shall be made.

Requirement **RQ16** : All serviceable parts shall be standard sizes and widely available.

Requirement **RQ17** : Metal parts shall be aluminium for corrosion resistance, ease of machining, and handling.

3.2 Bar Layout

The design process began with an analysis of the expected trajectories of the stress pulses. In doing so, an understanding of the required striker, pressure bar, and momentum trap lengths was acquired. Figure 3.1 displays a Lagrangian X-T plot for the proposed system, with all lengths finalised.

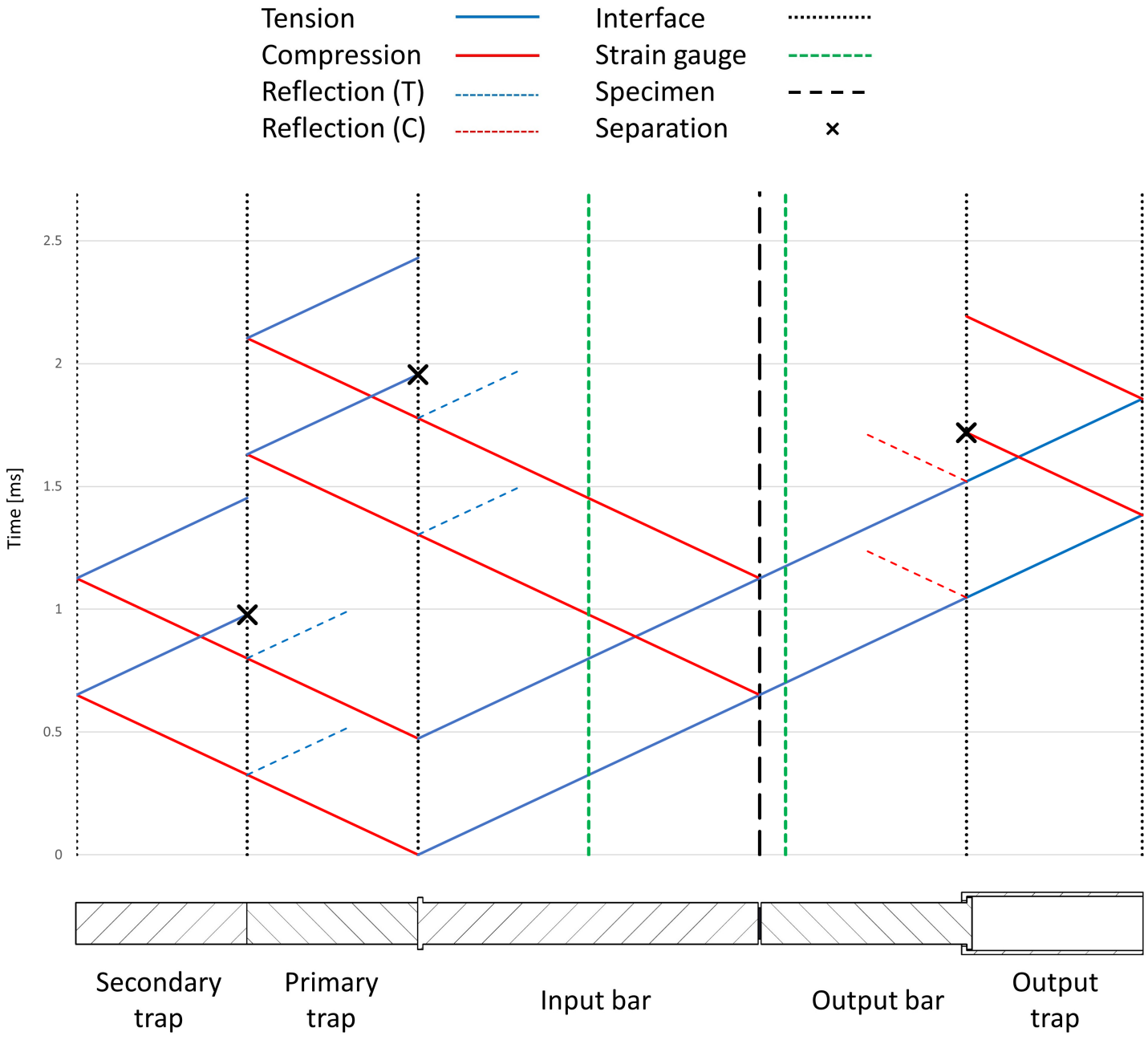

Figure 3.1 Lagrangian X-T diagram of the proposed TSHB configuration

For readability, all components are placed in-line with each other. The displayed bar configuration is an equivalent system to the one that shall be used, which is shown in Figure 3.2. There are two parallel plots present. These represent the leading and trailing end of the stress pulses, and require consideration in order to prevent superposition of signals.

As a starting point, the input bar will have a length of 3300 mm. It will be strain gauged in the middle, at 1650 mm, to minimise boundary effects from either end. A striker length of 1200 mm was chosen, as it is approximately one third of the length of the input bar. It is important that the striker length is slightly less than half the length of the input bar, in order to avoid superposition of the incident and reflected pulses at the input bar's strain gauges. To refer to the input bar gauges and the Lagrange diagram in Figure 3.1, it can be observed that there is a delay between the end of the incident pulse and the start of the reflected pulse. This indicates that these pulses should not be superimposed, and can be independently detected by the input gauges.

Each tandem trap, as well as the output trap, shall have a 1650 mm length. As this is longer then the striker length, all traps should be capable of trapping the full pulse. The trailing end of a captured pulse must have entered the trap bar before the leading end has reflected back, which would separate the trap from the pressure bar. This is apparent when studying the Lagrange diagram diagram in Figure 3.1. Lastly, the output bar is set to a length of 2000 mm, to fit within the limits of the existing SHBP bed, and is strain gauged at 220 mm from the specimen end. Superposition on the output bar gauges is not a concern. Although some reflection is expected from the end of the output bar due to slight impedance mismatch and the mass of the output flange, the position of the output gauges ensure that the portion of the signal containing the transmitted wave remains unobscured. In addition, the output gauge position is constrained by the fact that the output trap tube will locate round the output bar in the implemented configuration, and it is unwise to have a strain gauge and its lead wires between these parts. The length of the various elements or summarized below in Table 3.4.

Table 3.4 *Lengths of striker, pressure bars, and momentum traps*

Component	**Length [mm]**	**Configuration ◇**
Striker	1200	Nested
Input bar	3300	End-to-end
Output bar	2000	End-to-end
Primary momentum trap	1650	End-to-end
Secondary momentum trap	1650	End-to-end*
Output momentum trap	1650	Nested
Total bed length [mm]	8600	

◇ Nested: Does not contribute to total bed length
◇ End-to-end: Contributes to total bed length
* See Section 3.7.1 for details on tandem trap configuration

Since the total bed length of the apparatus is 8.6 m, Requirement RQ13 on bed length is met. Since the existing beds are 9 m long, there is surplus space that can be used for bar stoppers, and allows for more room to work. Figure 3.2 displays a labelled diagram of how the TSHB will be configured.

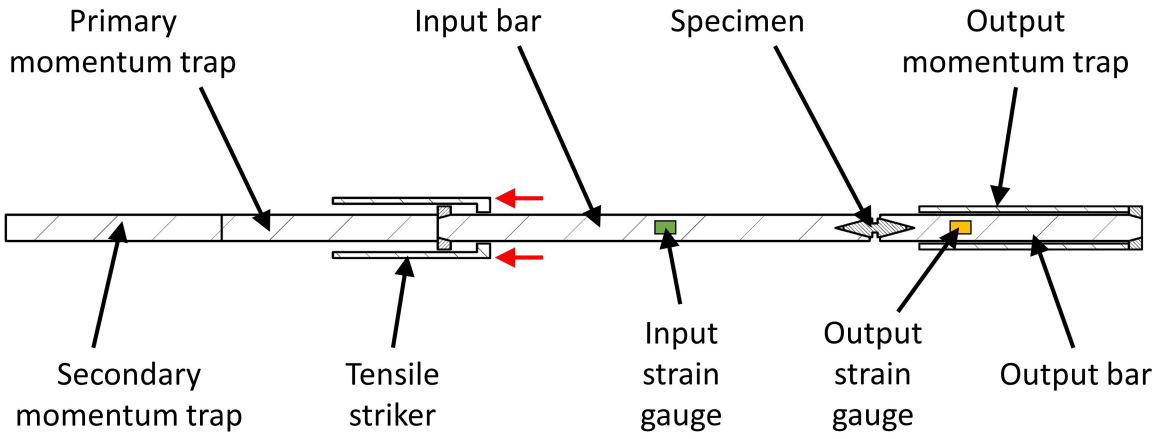

Figure 3.2 Bar layout of the TSHB, as it was be implemented

3.3 General Design Considerations

Several factors were common considerations for the detailed designs of all components, namely:

- **Availability of stock:** All materials and components needed to be sourceable from a local (South African) supplier, in reasonable quantities.
- **Cost:** Components and materials requiring purchase must be available at a reasonable cost.
- **Sizing:** This design of TSHB relies heavily on components running concentric and within each other. Concentric mates need to fit within each other and have enough clearance for adequate support between them.
- **Machinability:** Long boring operations are highly impractical and inaccurate and should be avoided. Tubing should be kept at the stock ID as far as possible.

3.4 Striker

This design will make use of a pull-off type of striker, similar to the one designed by Downey [39] as described in Section 2.3.3. This type of tensile striker was selected as it provides opportunity for the input bar to be supported along almost its entire length. This is because the body of the striker is not primarily located around the input bar. Contrasting traditional tubular strikers, this additional support allows for cleaner and higher quality signals to be recorded on the input bar strain gauges [62]. In addition, access the input bar for inspection and maintenance is improved. The pull-off striker has performed well in prior BISRU studies [15, 119].

Note in Figure 2.11 from Section 2.3.3 that the gun barrel pushes air in the left end of the striker, which acts on an internal flange in order to propel the striker. Since the tandem momentum traps now need to lie end-to-end with the input bar, the gun barrel cannot be located in the same place. The new design of pull-off striker will therefore be propelled by an external flange as shown in Figure 3.3.

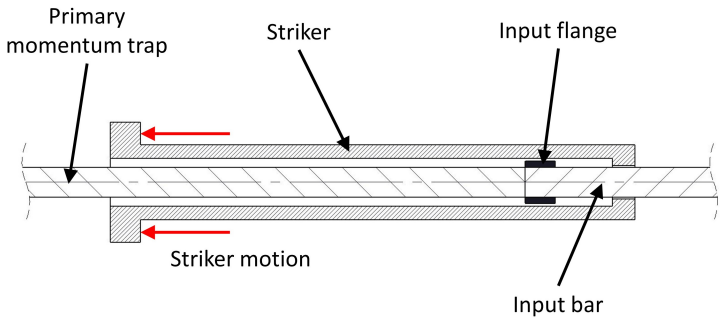

Figure 3.3 Cross section of the proposed pull-off striker

A detail drawing of the assembly is shown in Figure 3.4. The striker is made up of a 1200 mm long AA6061 aluminium tube, with an OD of 38.2 mm and wall thickness of 3.3 mm. The specific cross section was chosen such that it would fit comfortably around the primary momentum trap and isolator sleeve (described in Section 3.8) and within the gun barrel. It was also sized such that its mechanical impedance is less than the sum of that of the input bar and primary trap. This is to ensure that the striker rebounds after impact. Two acetal (POM) pressure collars are shrunk fit onto the outside of the tube. These polymer collars act as guide bushings to centre the striker within the barrel, while allowing sliding, and also to provide a surface on which the gas pressure can act on when the gun is fired. Acetal was chosen as a material in order to minimise the mass of the collars, as these masses on the striker body will alter the shape of the incident pulse. There are two collars so that the striker can be supported near its end, and at the same time minimise the volume that the compressed gas has to expand into before the striker starts to move.

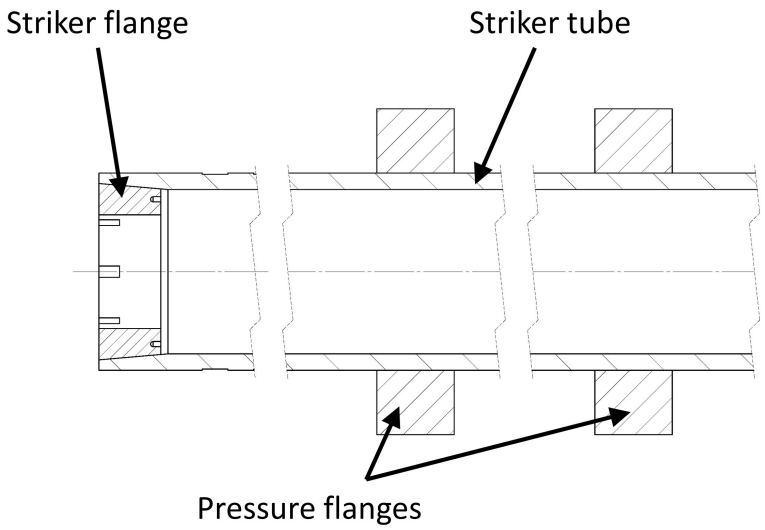

Figure 3.4 Cross section of the striker assembly

An internal flange is then screwed into the other end of the striker. This will impact a collar on the input bar assembly, to transfer momentum from the striker, and is illustrated in Figure 3.5. The striker flange was manufactured from Ti-6Al-4V titanium alloy to minimise mass and maximise stiffness and strength. Strength verification for both the striker tube and striker flange can be found in Appendix B.

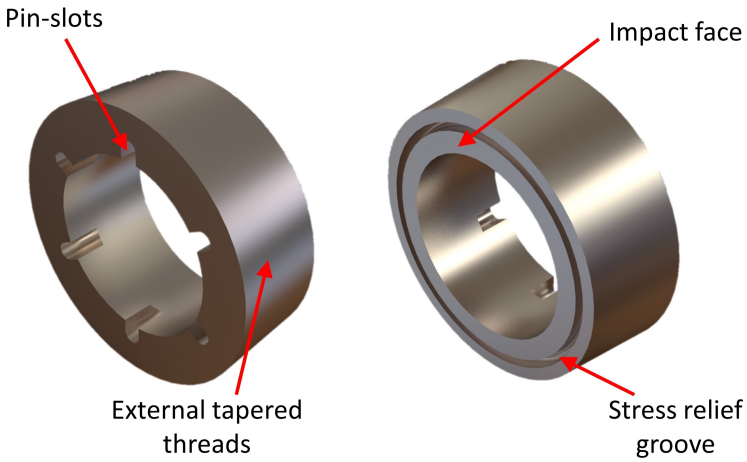

Figure 3.5 Isometric view of the striker flange

The external face of the flange has tapered threads that match with internal threads on the striker tube. The length of the flange is 12 mm, which, according to a study by Shin *et al.* [120], is acceptable given the pressure bar diameter. The bore in the centre is sized to clear the input bar, and let trapped air escape quickly enough when the striker is fired. A

groove is cut on the impact face to relieve the first couple of threads from excessive stress upon impact. Lastly, pin-slots are milled into the external face of the flange to allow the flange to be tightened into the tube using a tool. This tool is described in Section C.5.1.

3.5 Gas Gun

Since the striker designed in Section 3.4 lies within the gas gun's barrel, instead of around it like in the Downey design, a new gun design is required. The primary function of the gas gun is to use pressurized gas to propel the striker. The complexity with this gun arises from the fact that bars need to be able to pass all the way through it. This means that the gun and all its parts are of annular nature.

3.5.1 Conceptual Design

The conceptual design of this gas gun was devised by Dr Trevor Cloete. Figure 3.6 shows a simplified diagram of the gun's internal workings.

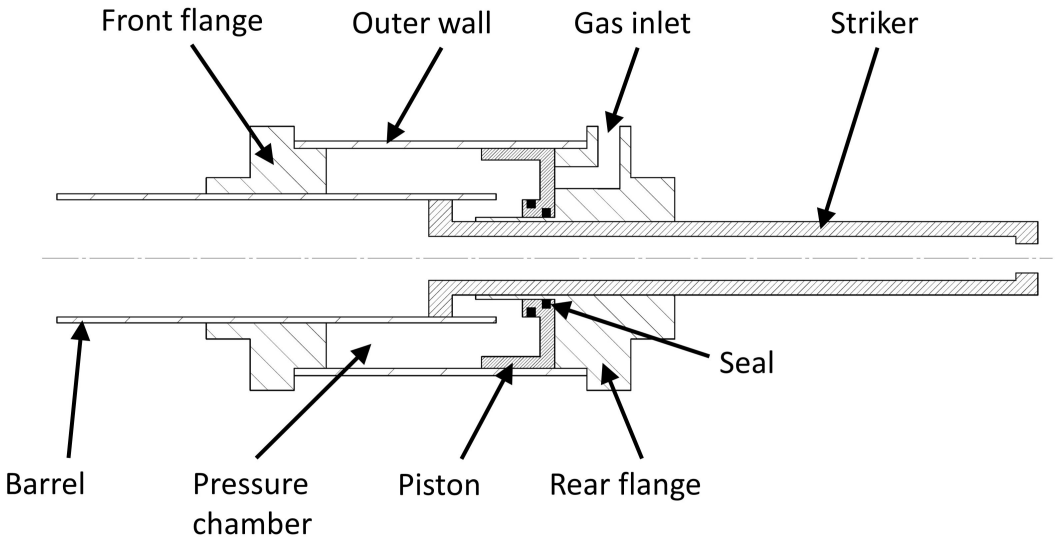

Figure 3.6 Cross section of the gas gun in its idle state

The outer wall of the pressure chamber, as well as the barrel and end flanges do not move at all during operation. The piston is free to slide axially (left and right in Figure 3.6) within its limits. The mating surface between the outside of the piston and the outer wall is machined to have a tight clearance fit, but does not have a seal of any kind. The striker is also free to slide axially within the barrel. It can be noted that there remains an unobstructed passage through the centre of the gun, in which the tandem momentum traps shall lie. Figure 3.6 shows the gun in its idle state. This is how it it sits when not in use.

3.5.2 Mode of Operation

To charge the gun, preparing it to for firing, pressurised gas is applied at the gas inlet port. Figure 3.7 shows how this gas flows directly into the control chamber, pushing the piston up against the barrel, and plugging it. The two seals prevent any gas from escaping into the barrel. Because the outer surface of the piston does not have a seal, gas can slowly leak through the small clearance between the piston and outer wall into the pressure chamber, until its pressure is equal to that of the control chamber.

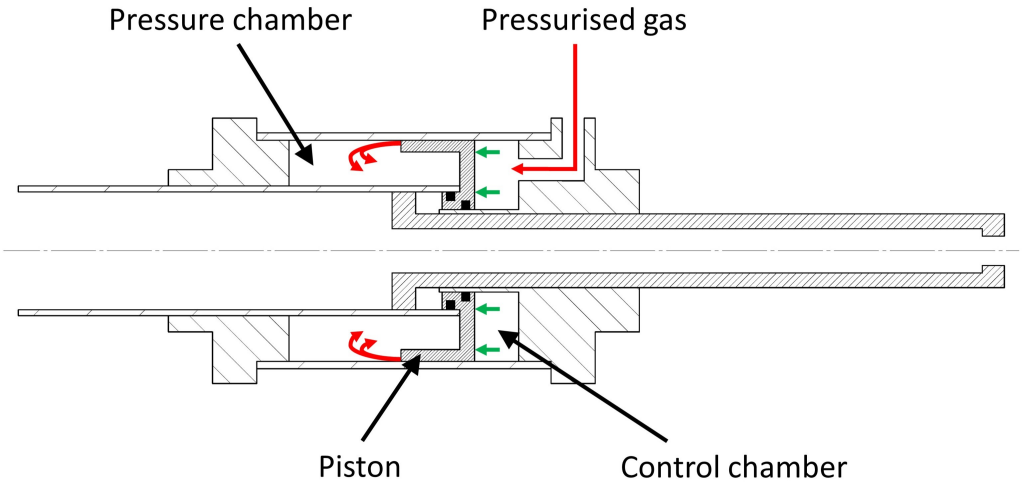

Figure 3.7 Cross section of the gas gun in its armed state

The piston remains firmly against the barrel in this state. Although the pressures are equal on either side, more area is exposed on the right hand side, creating a resultant force to the left. This area mismatch is a strong safety feature against accidental firing, as it's not possible to fill the pressure chamber to a higher pressure than that of the control chamber side. At this stage, the gun is ready to fire.

To fire, the control chamber is rapidly vented to atmosphere. The gas in the pressure chamber cannot escape back around the piston very quickly. Hence the control chamber pressure rapidly drops to atmospheric pressure, resulting in a net force that rapidly pushes the piston to the right. This unplugs the end of the barrel, suddenly giving the pressurised gas from the pressure chamber a flow path into the barrel. This rush of gas propels the striker.

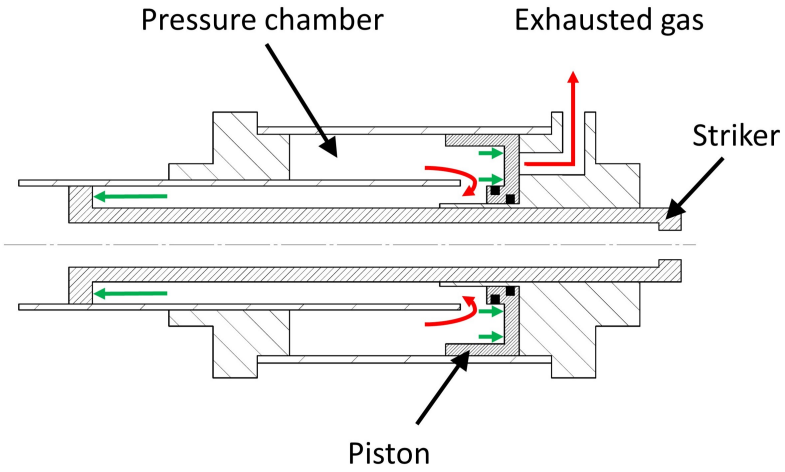

Figure 3.8 Cross section of the gas gun in its fired state

3.5.3 Detailed Design

From the conceptual design described above, the gas gun was then developed into a design that could be implemented to meet the requirements. The details surrounding the features and functions of the various gas gun components are outline in this section.

3.5.3.1 Construction

The conceptual design displayed in Figure 3.6 was developed into the assembly shown in Figure 3.9.

End flanges and pressure tube

The largest components in the gas gun assembly are the front and rear flanges, and the pressure tube. Together these components make up the exterior of the gun. The pressure tube was sourced as pneumatic cylinder barrelling, and is said to be hard anodized aluminium alloy. As a conservative estimate, the alloy was assumed to be a 6000 series aluminium with a T6 temper, and a yield strength of 276 MPa was used in calculations. This stock was selected as it was available to purchase in a small quantity, and its ID comes precisely bored and honed to 160 mm. Its wall thickness is 4.2 mm. The machining on the tube was minimised, and complex features were allocated to the end flanges where possible. The end flanges were machined from 6063 T6 aluminium round stock.

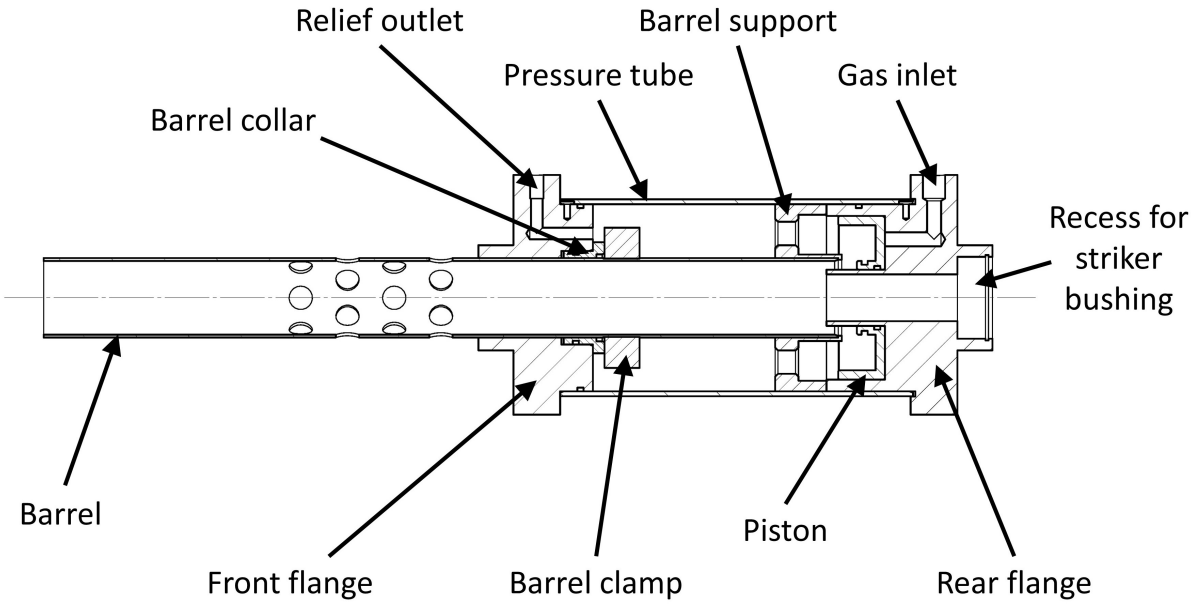

Figure 3.9 Cross section of the detailed gas gun assembly

The following features were included in the design of these components:

- A locational clearance fit was specified between the pressure tube and the bosses of the end flanges. This ensures tight concentricity is maintained throughout the gun, while still being easy to assemble and disassemble.
- Nitrile O-rings were used to seal the aforementioned mates. To constrain the O-rings, grooves were cut into the bosses of the flanges.
- Collinear keyways were milled into the ends of the pressure tube. Corresponding dowel holes were drilled in the end flanges and PLA pins were pressed in. These ensure that the flanges align angularly when the assembly is tightened down. Polymer pins were chosen, as their sole function to aid assembly alignment, and they must not be load bearing during operation. Any significant force on them should break the pins rather than damage the pressure tube. Steel dowel pins were avoided for this reason.
- Lead-in tapers for the O-rings were machined at each end of the pressure tube.
- The two gas ports were positioned so that they exit the flanges on their circumference and not their ends. This ensures that the pneumatic supply tubes emerge radially, rather than axially, to avoid interfering with moving components during the TSHB operation. Push-in pneumatic fittings with $90 degree$ swivels were used to direct the air supply lines from the control board.

- The end flanges are held together using six steel ties, which take the form of M12 threaded rods with nuts at each end. The largest diameter of the flange was sized so that there was enough material on the flange for the tie rods to pass through the flange and clear the pressure tube. A diameter of 210 mm was decided for the end flanges. Since these flanges on the gas gun are the largest diameter of the TSHB, Requirement RQ12 on apparatus diameter has been satisfied. Each tie rod has a nut welded to it at one end. The seat in slots cut in the front flange such that the nut and threaded rod cannot turn. The tie rod holes on the rear flange are counterbored to fit an 18 mm socket. When the nut is threaded on to the rear end of the tie rod, it can be tightened only using one tool. This removes the laboriousness of tightening threaded rods with a spanner on each end.
- As an extra precaution that the flanges do not interfere with the bed, a flat surface was machined onto the bottom of each flange. These features also prevent the gun from rolling away when being stored or serviced on a workbench.
- A recess was bored into the rear end of the rear flange, which houses the striker bushing. This bushing, paired with the POM pressure collars on the striker in Section 3.4, support the striker. This bushing is of the PTFE-in-brass design, which is described in Section C.2 in Appendix C. The bushing is retained by a 70 mm internal circlip, a groove for which is cut into this bore.
- Bosses were included on the outward facing ends of the flanges. These allow the gun to be mounted to the SHPB bed using the supports described in Section C.3 an Appendix C.

Piston

The piston plays a critical role in this assembly as it is the component that controls the flow of compressed gas into the barrel when the gun is fired. The piston was machined from 6063 T6 aluminium round stock, and incorporates the following design features:

- The piston has a close sliding fit with the rear flange, on both its ID and OD, as well as with the barrel tube.
- Concentricity and roundness for both the rear flange and piston were closely monitored. The parts mate with each other concentrically on two separate surfaces simultaneously. There is potential for the parts to bind if they were out of specification. The piston needs to freely slide in and out of the rear flange, at any angular position.
- Nitrile O-rings were used to seal the inner mate with the rear flange, and the mate with the barrel tube. These two sealed surfaces form the plug the obstructed the barrel prior to firing. Grooves were cut into the piston the constrain these O-rings.

Barrel tube and support

The barrel sub-assembly is made up of the barrel tube, the barrel collar, and the split collar clamp. The barrel is manufactured from similar pneumatic piston stock to the pressure tube, with its OD being 68 mm and wall thickness 2.5 mm. This particular cross section was highly influenced by availability. The aluminium collar houses the sealing elements for where the barrel mates with the front flange. The clamp, functions as a removable shoulder in the barrel tube, through which axial forces are transmitted It is described in further detail in Sections 3.5.3.2 and 3.5.3.3. The barrel is supported within the gun by the pressure tube, via an annular support. This support, made from 6063 T6 aluminium, holds the barrel end concentric with the piston that plugs it during operation. The barrel support also forms part of the load path of the assembly preload force, which too is described in Section 3.5.3.2.

The following features were included in the design of these components:

- The barrel collar was sized to have locational clearance fits with both the barrel tube and with the front gun flange.
- Nitrile O-rings were used to seal the aforementioned mating surfaces. Grooves were cut into the barrel collar to house the them.
- Venting holes were drilled in the barrel tube. These vents relieve excess pressure after the striker has passed them and reached its desired speed.
- A lead-in taper for the piston O-ring was machined into the barrel tube. Care was taken to smooth this taper thoroughly, as the respective O-ring forms a dynamic seal.
- The annular barrel support has a tight locational clearance fit with the barrel tube and with the pressure tube. The tight tolerance was necessary as concentricity of the barrel and piston was necessary for sealing. If there is misalignment, the piston may not seat inside the barrel end, and a seal will not be made.
- Large holes are drilled and generously countersunk through the barrel support. This will allow gas to freely move past this support the the pressure chamber.

Piston stopper

A component not included in Figure 3.9 is a stopper for the piston. When the gun is fires and the piston rapids retreats into the rear flange of the gun, it is brought to a stop when it collides with the flange itself. It was decided to avoid this metal-on-metal impact, as there are extremely tight tolerance involved with the piston to flange mate, and the

smallest amount of unintended plastic deformation of either parts could cause binding. A stopper ring, displayed in Figure 3.10, was 3D printed from PLA. It fits inside the rear gun flange and behind the piston. Its purpose is simply to cushion the impact, and it is expected to be replaced periodically due to the accumulated deformation.

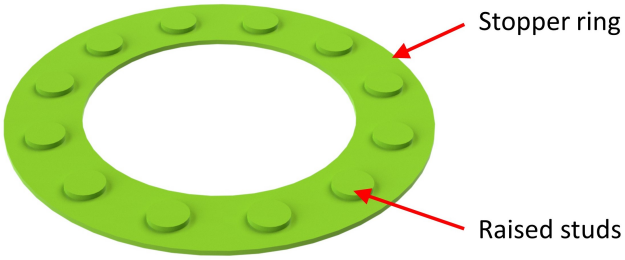

Figure 3.10 Isometric view of the piston stopper

The raised studs on the stopper serve to provide more compliance, further softening the impact. An additional function of this part is that in ensures there is always a gap left behind the piston. When the gun is charged and air is pushed into the control chamber, the pressure is always evenly distributed across the entire rear face of the piston. This reduces the possibility of jamming occurring.

3.5.3.2 Barrel Mounting and Preload Analysis

A complexity arose as to how to secure the barrel in its axial position. The immediate solution was to find a method to rigidly mount it to the front flange. Many common approaches were investigated and rejected:

- Threading was not appropriate. Both the front flange and the barrel are made from aluminium, meaning binding due to the similar materials was a concern. The thin walls of the barrel would only allow for fine threads without compromising their integrity, and fine threads in aluminium do not have large load bearing capacity.
- Welding was not within capability. Welding aluminium is more challenging than steel, and is made significantly harder by the mismatch in thicknesses of the parts. The front flange is very bulky, requiring ample heat, whereas the barrel is highly vulnerable to heat due to its thin walls. Distortion of the barrel's circular cross section, or excessive run-out along the tube's length due to the localised heating were crucial concerns.
- Adhesives were avoided. While a bonded joint is capable of sustaining the axial load, the practical process of adhering the parts together presents challenges. Most

industrial adhesives require application to both surfaces for a thorough bond. Since the mate was located near midway on the barrel, there was a long distance to slide the flange before it is in position, and it was unlikely that a sufficient quantity of glue will remain in the flange bore. It would get wiped onto the barrel as it was slid into place. This would severely compromise the strength of the joint. In addition, it would be a messy process.

- Positive features were not appropriate. Using pins or keys were not an option as the walls of the tube are insufficiently thick to accommodate holes or seats of appropriate depth.

The solution was to design a split collar clamp that grips the barrel tube and transfers the axial force through friction. The compressive preload $F_{preload}$ from the tie rods was then directed through the barrel and clamp. The barrel was then constrained on the piston end by a small internal lip in the bore of the barrel support. This clamp is described in greater detail in Section 3.5.3.3. Figure 3.11 below provides a visualisation of the load path through the gun as the tie rods are tightened.

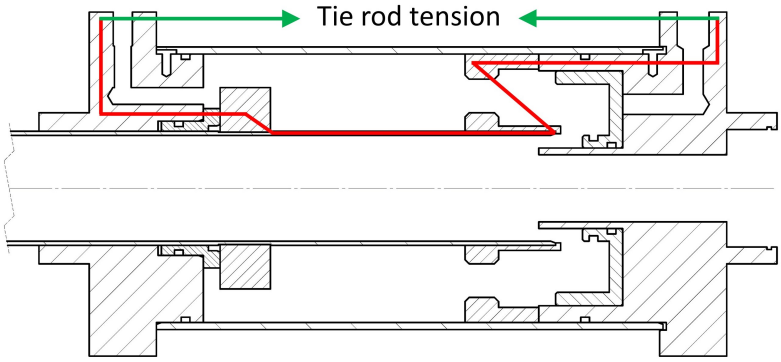

Figure 3.11 Slice section of the detailed gas gun assembly, displaying the load path of the preload forces in the tie rods

The preload force $F_{preload}$ has a maximum, governed by the compressive force that the thin-walled barrel tube can withstand when the gun is in its idle state. In this state, the entirety of $F_{preload}$ is directly down this tube. The area of smallest cross section is on its piston end, where it has an internal lead-in taper for the piston O-ring. The stress-bearing area at that location is 313 mm^2. The maximum value of $F_{preload}$ allowable before the barrel end deforms is therefore 86.5 kN.

The minimum allowable $F_{preload}$ is equal to the force F_{axial} pushing the flanges of the charged gun apart, due to the internal gas pressure. Below this threshold, the components on the load path shown in Figure 3.11 may unload and develop axial play. A conservative

value for F_{axial} is attained using the maximum gas charge pressure of 10 bar, and the entire area of a flange exposed to that air pressure, being 18 300 mm^2. This gives a F_{axial} and minimum $F_{preload}$ of 18.3 kN. A preload force $F_{preload}$ of 20 kN was used, as it is a margin above the minimum allowable value, but not excessively large. It is noted that the consequences of the components on the load path separating due to insufficient preload force, is the leakage of gas pressure, and is therefore not catastrophic. Hence, the value can exist so close to the minimum. Equation 3.1 below shows how an approximate torque specification for the tie rod nuts is calculated.

$$T \approx \frac{1}{n} \cdot K \cdot F_{preload} \cdot d_{thread} \tag{3.1}$$

The number of tie rods is represented by n, the thread friction coefficient by K, and the thread diameter by d_{thread}. These three values are 6, 0.2, and 12 mm respectively. the tie rods require a torques of 8.0 Nm when the gun is assembled. Using a stress area of 84.3 mm^2 [121] for an M12 thread, the preload stress in the tie rods is 39.5 MPa. This gives them a safety factor of 6 which is more than adequate.

3.5.3.3 Barrel Clamp Design

As mentioned in Section 3.5.3.1, the clamp is responsible for the transmission of force between the barrel and front flange. The clamp was manufactured from stainless steel for stiffness, as any deformation of the its bore would translate into non-uniform clamping pressure on the barrel. This could cause the barrel to deviate from a circular cross section. The clamp design is illustrated in Figure 3.12.

The clamp, held together by two M10 bolts, is designed to be able to resist the axial load by the clamping force alone. For additional assurance, a shallow groove, and the width of the clamp, is cut into the barrel tube to provide a positive locating feature preventing the clamp from slipping. Using press fit theory [122], and the properties of the tube and clamp, an interference pressure of 5.5 MPa is required to resist an axial force of 21 kN. By integrating the hoop stress in the split clamp collar over its radial section, it was is found that a hoop force of 5.58 kN is needed. Using Equation 3.1 from Section 3.5.3.2, this time with $n = 1$ and $d_{thread} = 10mm$, the torque specification for the two M10 clamp bolts was found to be 11.2 Nm.

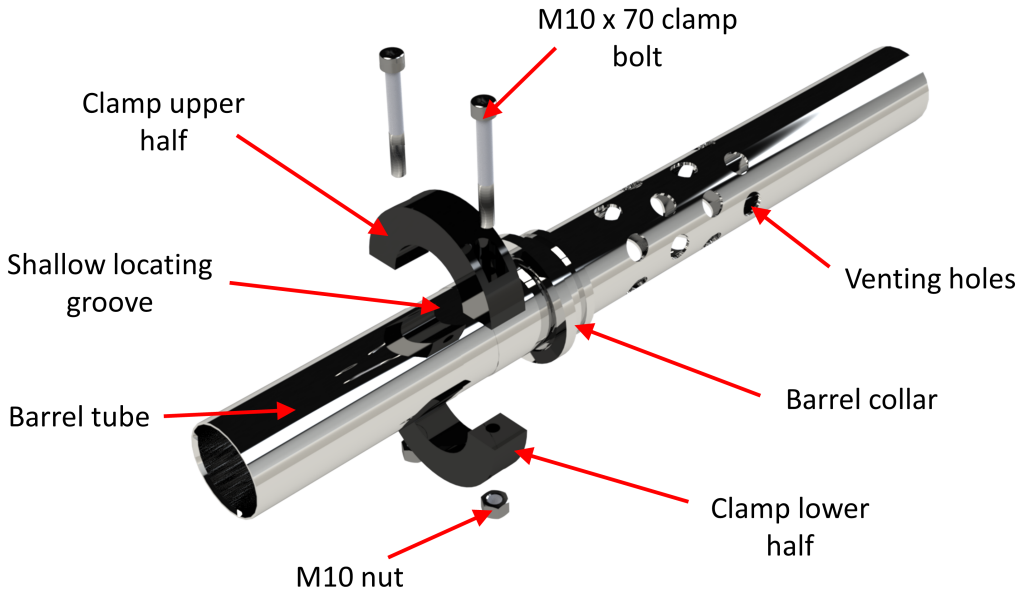

Figure 3.12 Isometric exploded view of the barrel assembly, with clamped collar

3.5.3.4 Considerations as a Pressure Vessel

Next, thick-walled pressure vessel calculation were run to ensure that the pressure tube and barrel tube can withstand their internal and external pressures respectively. These calculations were based off of a 10 bar gun pressure. Both tube stocks were purchased as pneumatic cylinder barrelling. Said cylinders are rated to 10 bar suggesting that a high safety factor is already built in to these components. Axial stress was ignored for the pressure tube, as these forces are opposed by the tie rods and not the tube. Axial stress was also ignored for the barrel tube as the tie rod preload is the only axial force acting on it, and has already been considered. Table 3.5 below summarises the hoop and radial stresses at both the ID and OD of each tube. The lowest safety factor for each diameter is also presented.

Table 3.5 *Safety factors of components subjected to 10 bar of air pressure*

Component	**Direction**	**Stress [MPa]**		**Safety factor**
		At ID	At OD	
Pressure tube	Hoop	19.56	18.56	14.1
	Radial	-1.00	0	276
Barrel tube	Hoop	-14.12	-13.12	19.5
	Radial	0	-1.00	276

The lowest safety factor calculated was 14, indicating that this gas gun design is extremely unlikely to fail due to rupture from over-pressure. These safety factors were calculated at the maximum gas pressure available in the laboratory, ensuring conformity to Requirement RQ14 on working pressure.

This design makes use of six O-rings to seal mating surfaces where needed. Their placements are shown in Figure 3.13.

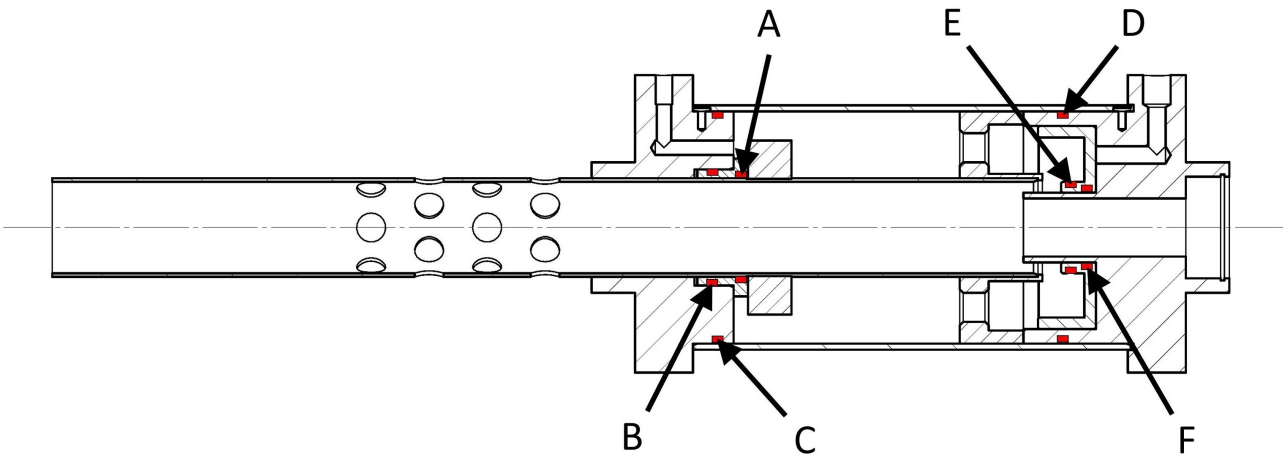

Figure 3.13 Cross section of the gas gun assembly showing O-rings locations

O-rings are designed to be failure points if the pressure somehow exceeds what is expected. Rubber O-rings also can fail due to age. In this gas gun, all O-rings were lubricated well with red rubber grease, both to increase the quality of their seal, and to prolong their lifetime. Table 3.6 summarises the consequences of O-ring failures, indicating that the gas gun design should fail to a safe state as per Requirement RQ9.

Table 3.6 *O-rings and the respective consequences of failures*

O-ring	Effect of failure	Outcome of failure
A, B, C, D	Pressure chamber bleeds to atmosphere	Gun does not fire as control chamber remains at higher pressure
E	Pressure chamber slowly bleeds into the barrel	Gun does not fire, as per above
F	Control chamber slowly bleeds into the barrel	Gun does not fire as the path into the barrel is small *

* Even if the air supply is shut off, the passage around the outside of the piston is far larger than that past O-ring F. This allows the pressure chamber to leak back into the control chamber. The area mismatch on either side of the piston, mentioned in Section 3.5.1, further increases the safety in the event of this failure.

3.6 Pressure Bars

The pressure bars shall be made from 19.05 mm, or 3/4" diameter 7075 T6 aluminium round bar. Aluminium was chosen primarily for its strength-to-density ratio, which allows for high strain rates to be produced at a specimen. In addition, threads cut into 7075 T6 have proven to be more resilient than other alloys or tempers of aluminium. This is imperative, as both the input and output bars make use of threads to transfer loads to and from them. The particular diameter was chosen as it has been used by BISRU for all recent versions of TSHB, and there was bar stock available in storage in the laboratory. This grade of aluminium is a challenge to source in South Africa, should different 7075 T6 bar stock have been chosen.

3.6.1 Input Bar Assembly

The input bar is 3300mm long, with the input flange at one end and a conical threaded socket for the fir-tree clamps at the other. The input flange is the positive feature on the input bar that the striker flange impacts to create the tensile incident pulse. This flange is secured to the bar using a tapered thread, and is displayed in Figure 3.14. Much like the the striker flange in Section 3.4, the input flange has pin-holes to be tightened by using the tool described on Section C.5.1, and also includes a stress relief groove on its impact face. This flange too is manufactured of Ti-6Al-4V alloy and is 12 mm thick. The strength of the input bar and input flange are verified in Appendix B. Since this flange runs inside the striker, there is a bushing that is pressed onto it, and slides in the striker

tube's bore. The shoulder on the outside of the flange serves as a locating feature for this bushing, which was manufactured from acrylic using a resin SLA 3D printer.

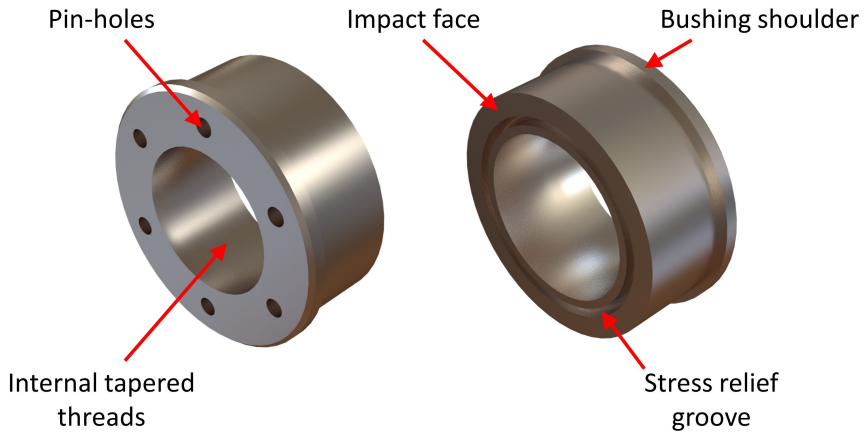

Figure 3.14 Isometric view of the input flange

The far end of the input bar is equipped with a female conical thread to match that of the fir-tree specimen clamps described in Section 2.4.5. These threads are blind and therefore have finite clearance at the deepest part. This clearance was kept to an absolute minimum to reduce any spurious reflections that may result from having an air gap there. The same was the case for this feature on the output bar.

3.6.2 Output Bar Assembly

The output bar was 2000 mm long, and, as was the case with the input bar, the specimen end of the bar is threaded to fit the fir-tree specimen clamps. The far end of output bar is equipped with a Ti-6Al-4V output flange, which is illustrated in Figure 3.15. The role of this flange is to transfer the transmitted stress pulse into the output trap tube. As was the case with the striker flange in Section 3.4 and the input flange in Section 3.6.1, the output flange is fixed to the bar be means of a tapered thread. The transfer face of the flange has a stress relief groove, and the end face has pin-holes so that the pinned tool, outlined in Section C.5.1 in Appendix C, can tighten it.

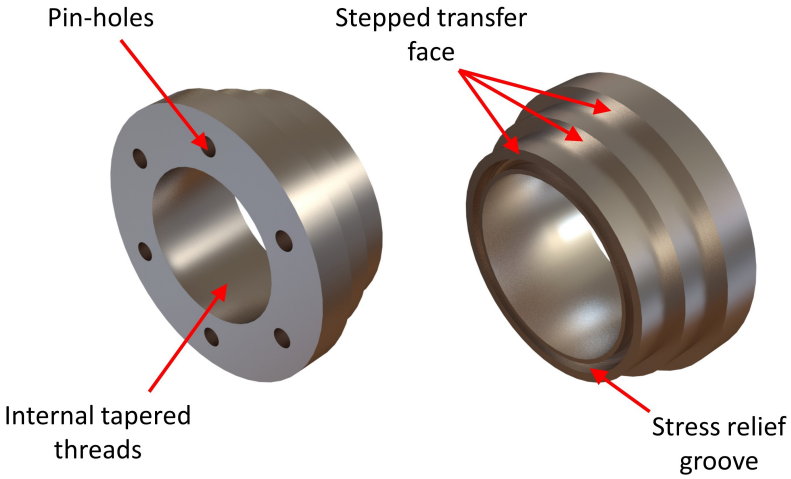

Figure 3.15 Isometric view of the output flange

The transfer face of this flange is broken down into three faces, in a stepped form. These steps were matched to by corresponding geometry on the output momentum trap. This interface was made to be stepped in order to make the boundary more gradual, with the goal of minimising the effects of the impedance change from flange to tube. The diameters of the steps have a tight tolerance to minimise radial play between them and the corresponding bores in the trap tube end.

The output bar is not supported directly at its distal end, but was held by bushings inside the output trap tube. Three thin walled bushings were SLA printed and pressed at regular intervals along the output bar. They have a sliding fit with the bore of the trap tube, allowing for smooth motion between the components.

3.7 Momentum Traps

All three momentum traps were made from aluminium stock to remain consistent with the pressure bars, which eases the process of impedance matching. This is the case because the mechanical properties of the bars and traps are very similar.

3.7.1 Tandem Traps

On the input bar side, the tandem momentum trap method is being used. As explained in Section 3.2, each of the tandem traps shall have a length of 1650 mm. The tandem momentum trapping can be implemented in one of two configurations. The first would be to lay the tandem traps end to end as was described by Isakov [93]. This is shown in Figure 3.16a. An alternative way of configuring the tandem traps is to nest them one inside the other. The primary trap would be a solid bar, and the secondary would take

the form of a tube surrounding it. The secondary trap tube is loaded via a transfer flange, as shown in Figure 3.16b.

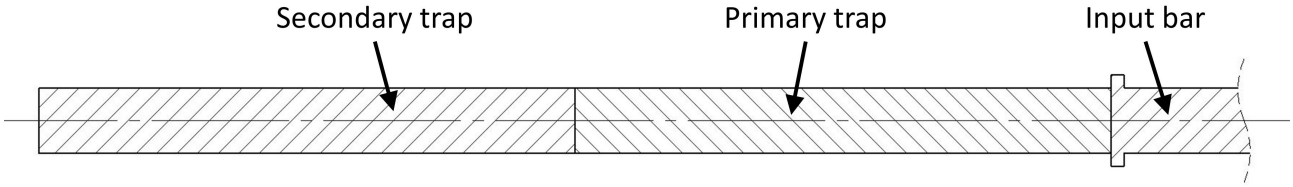

(a) In-line configuration

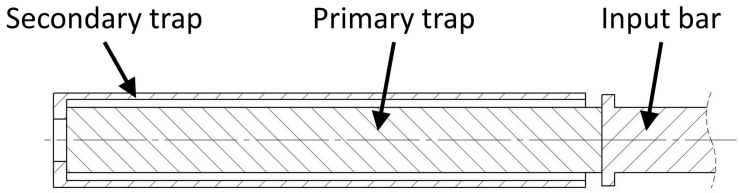

(b) Nested configuration

Figure 3.16 Cross sections comparing the in-line versus nested tandem trap configurations

The in-line configuration has the following benefits:

- The stock is easier to source.
- It is easier to manufacture.
- It is easier to commission, as the traps will simply need to have identical OD in order to be impedance matched.
- It is significantly easier to support.
- The two traps can be made from identical stock, improving the impedance match between them.
- There is no transfer flange to disrupt the movement of a stress wave.
- There is better access to the traps.

While the nested configuration is advantageousness for the following reasons:

- It requires less bed length to achieve the same task.
- It requires fewer external supports.

As seen above, the in-line layout of tandem traps is favourable to use. Its simplicity places it well above the nested layout. While it will use up more bed length, it is still short enough to meet Requirement RQ13. The tandem traps will be identical, and will be manufactured from 20 mm diameter 6082 T6 aluminium round bar. At this diameter this stock has a higher mechanical impedance than that of the pressure bars, which is desirable as they can be turned down to match. The primary trap, once at its final diameter, will have four SLA printed bushings pressed onto it at regular intervals along ts length. These bushing allow it to slide in and be supported by the isolator tube, which is described in Section 3.8. The secondary trap will be supported directly by standard bar supports.

The final part of the tandem trap design was the design of a stopper for the secondary momentum trap. When it separates from the primary trap initially, it had to be stopped from leaving the bed. It also had to remain isolated and cannot rebound off a rigid stopper and impact the primary trap again. A stopper was designed that absorbed the kinetic energy from the secondary trap once isolated from the system, and prevented any significant rebound. A design using putty was used, and is displayed below in Figure 3.17.

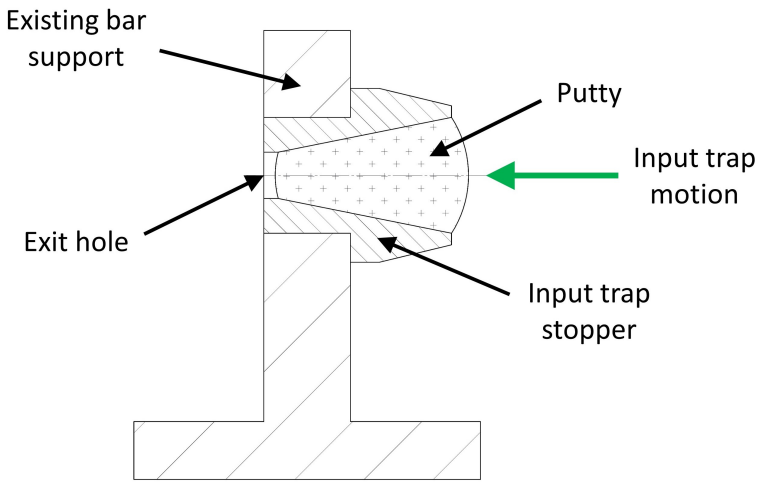

Figure 3.17 Cross section of the stopper for the secondary trap

The stopper takes the form of a conical through hole filled with putty, and is clamped and held in a standard bar support. The stopper is 3D printed in PLA. When the trap bar impacts the stopper, its energy is largely used to extrude putty out the rear exit hole of the stopper, damping the motion. The adhesion of the putty to the bar end prevents any rebound that may still occur. The putty is simply reset every few tests.

3.7.2 Output Trap

The output momentum trap, as per Section 3.2, shall be 1650 mm long, tubular, and shall locate around the the output bar against the output flange. The stock used for this part is 6000 series aluminium tubing, with an OD of 30 mm and a wall thickness of 4 mm. This particular tube section was chosen as its ID is only slightly larger than the diameter of the output bar. This is ideal, as it reduces the flexibility of the output flange, making the flange more effective at transferring the stress pulse. In addition, this tube has a mechanical impedance larger than that of the output bar, again meaning that it can be matched by turning down the OD.

One end of the tube has stepped features cut into it to correspond with those on the output flange outlined in Section 3.6.2. The steps in the tube end are illustrated in Figure 3.18.

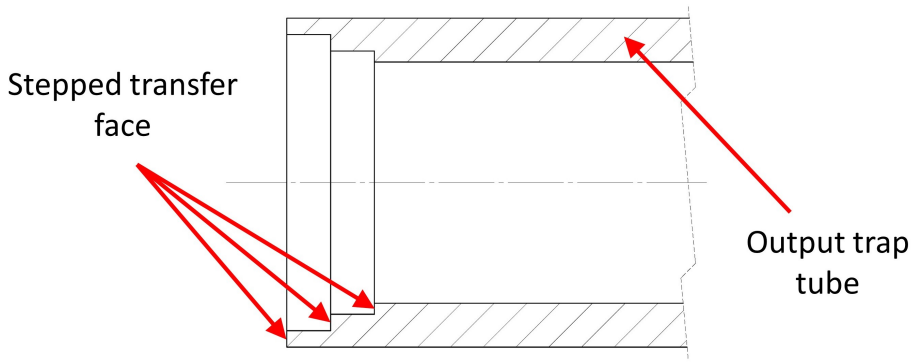

Figure 3.18 Cross section of the steps in the end of the output trap

A stopper mechanism is required for the output momentum trap. This stopper prevents the tube from sliding too far once separated, as this would cause damage to the output strain gauges. A significant rebound off a stopper could result in the the trap impacting the output flange again. As was the case with the stopper described in Section 3.7.1 the function of this stopper is to fully arrest the motion of the trap. Since the output bar must still pass through the stopper unobstructed, a different approach is taken to the input stopper. The method involves catching the trap via a locking taper mechanism. The design is presented in Figure 3.19.

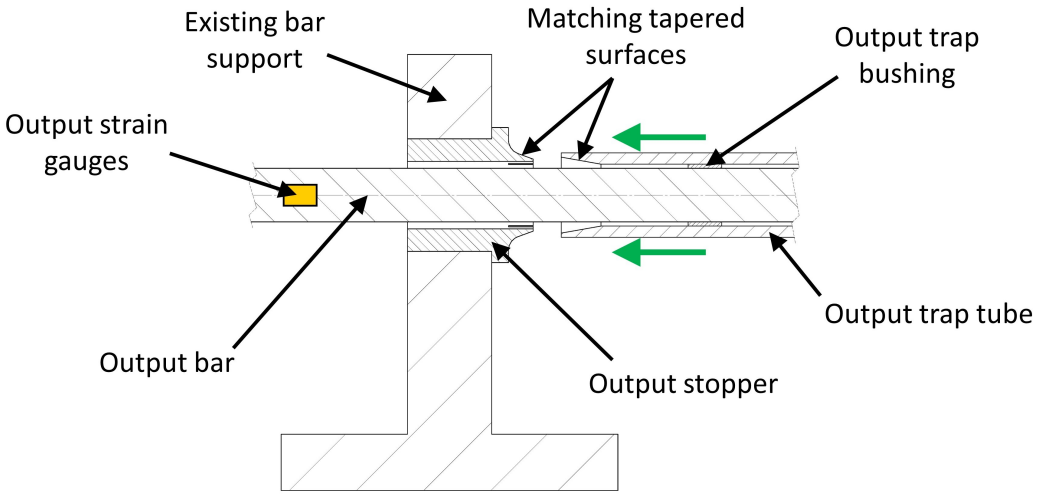

Figure 3.19 Cross section of the stopper assembly for the output trap

The stopper is 3D printed in PLA, and is supported by a standard bar support, and has a bore through which the output bar can run. Enough clearance is given such that the stopper and output bar should never make contact during a test. The stopper is designed with a male taper on one end, with a female counterpart cut into the end of the output trap tube. Collet type slots were placed on the taper feature on the stopper to improve compliance. Upon impact, the kinetic energy is dissipated via friction on the tapered surfaces, as well as by the internal visco-elastic deformation of the PLA material.

3.8 Trap Isolator Sleeve and Compressive Barrel

A potential issue with the design at this point is that the primary momentum trap runs inside the striker tube. With the tandem trapping method, it is imperative that the primary trap stays in perfect contact with the input bar until the reflected wave returns. Since the primary trap is supported by the striker tube, the firing and rapid movement of the striker is highly likely to disturb the trap. To address this another tube was introduced between these two components, surrounding the trap and within the striker tube. The configuration is pictured in Figure 3.20. This tube is fixed rigidly to the SHPB bed via a bar support, and is unable to move axially. Its function is isolate the primary momentum trap from the axial motion of the striker. This part was manufactured from 6082 T6 aluminium tube with an OD of 25.4 mm and a wall thickness of 1.6 mm.

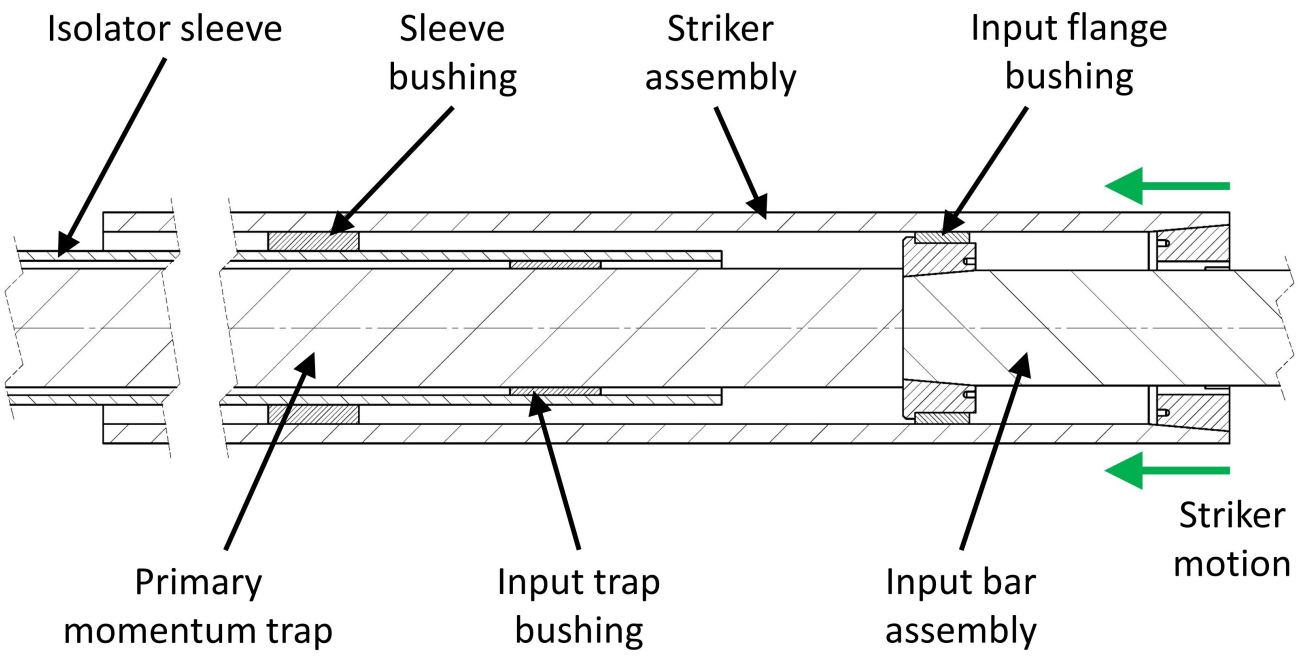

Figure 3.20 Cross section of the location of the isolator sleeve within the apparatus

Many of the tests associated with the calibration and commissioning of this apparatus are conducted in compression as the experimental setup not as intricate. The lack of hardware such as transfer or impact flanges allows for the shape and magnitude of the pulse to be controlled in a simple manner. Normally, this process would involve removing tensile pressure bars from their bed, and installing them in front of a compressive gun to run the required tests. This involves the laborious and time-intensive process of realigning the bars, and disturbing the working tensile configuration. Furthermore, it relies on the availability of a compressive gas gun and unused bed of sufficient length.

During the design of the isolator tube, it was realised that the tube could serve dual functions, and act as a compressive barrel when required. With some minor hardware changes, compressive tests could be run on the same bed, and the pressure bars needn't be disturbed, or be realigned in any way. It is excessive to design a second gas gun for this requirement, so the pneumatic valves on an existing compressive gas gun mounted on an adjacent bed were used. The gas gun on the adjacent bed will be referred to as the blue gun. Hardware was designed so that the blue gun could fire the compressive barrel from its current position via a flexible pneumatic tube.

Venting holes were drilled on the isolator tube, and features to secure a light trap were machined, as described in Section C.4. These features gear it towards its function as a gun barrel. On the rear of the isolator tube, a sleeve mount is attached via an epoxy

adhesive, as the metal is too thin to weld or thread. This mount is held by a standard bar support, and constrains the axial motion of the sleeve. This constraint is required for both functions of this part. The methods of attaching the compressive barrel to the existing blue gas gun, when required, are outline in Section C.1 in Appendix C. All hardware for the compressive arrangements can be set up in less than 10 minutes, and no further bar alignment is needed.

3.9 Pneumatics

For this design of gas gun, the firing of the striker is triggered mechanically via the quick release of gas pressure from the control chamber. A pneumatic circuit was needed to control the charging of the gun, and to fire the striker. This shall be mounted to a control board for ease of use.

The pneumatic control system shall have the following features:

- It must contain an independent pressure regulator. This allows the user to complete a set of tests using the same gas pressure for each.
- The charging pressure must be displayed using a gauge, as an indicator of the pressure in the control chamber.
- The pressure in the pressure chamber must be displayed using a gauge. This can be used to monitor the charging process, and that the gun is operating as it should be.
- The vessel must have a manual dump valve. If the gun should need to be discharged without firing a striker, the gas can be vented to atmosphere directly from the pressure chamber. This is to ensure that Requirement RQ10 on safe disarming is met.
- All components shall be rated to a minimum working pressure of 10 bar, as per Requirement RQ14.

Figure 3.21 below shows the pneumatic circuit used.

The bold lines indicate where ⌀12 mm pneumatic tube shall be used. All other pneumatic lines are ⌀8 mm pneumatic tube. Larger diameter tubes are used in the trigger path, allowing gasses to escape as quickly as possible. All hardware, including valves, gauges, regulator, and vents, shall be mounted into a profiled wooden board using components 3D printed from PLA. The finished product is displayed in Figure 3.22.

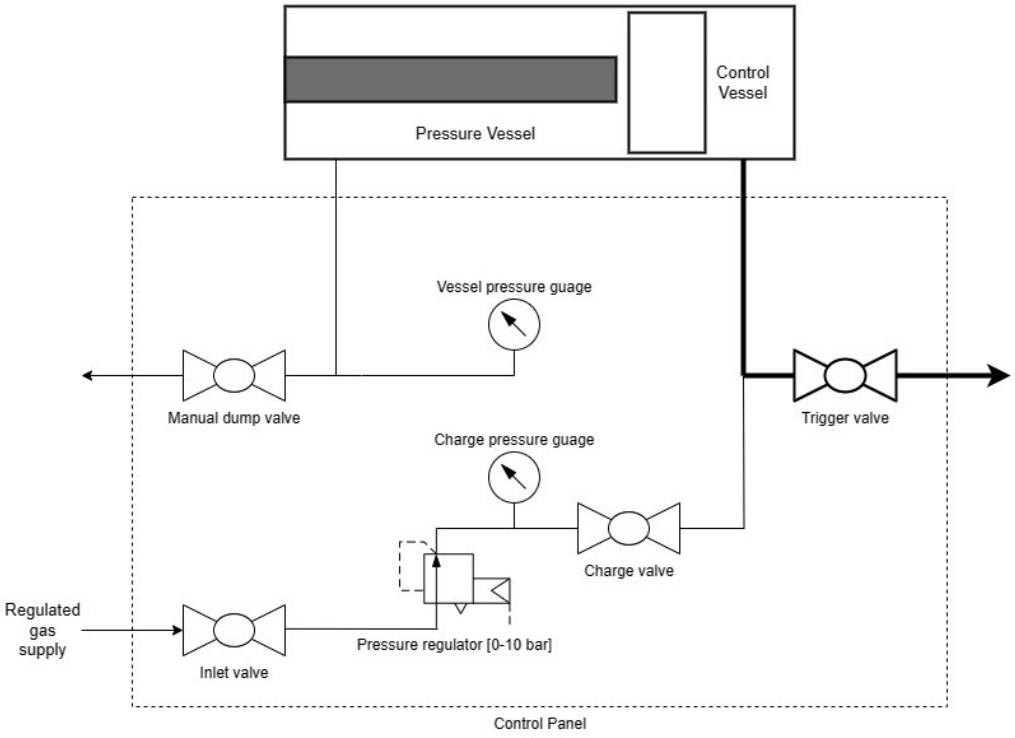

Figure 3.21 Schematic diagram of the pneumatic circuit

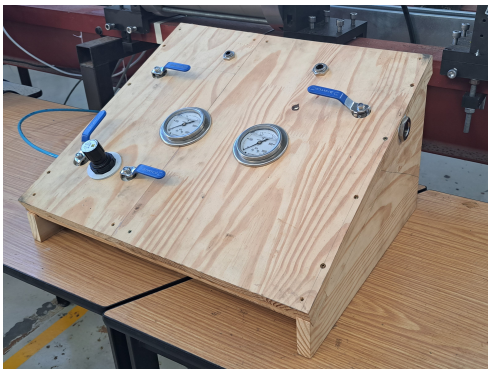

(a) View of the top and externals of the control panel

(b) View of the underside and mounting hardware

Figure 3.22 Photographs of the pneumatic control panel for the gas gun

As seen in Figure 3.22a, the valve handles, regulator knob, and gauge faces all protrude from the top of the panel, with the rest hidden underneath. The bulk of the plumbing is out of sight, but is easily accessible for maintenance should the need arise.

3.10 Striker Speed Sensing

The striker velocity at the moment of impact in an SHPB test, v_0, is an important metric to track, and having a method to measure this value directly is recommended for multiple reasons:

1. During the calibration of the strain pressure bars, experimental maximum stress in the bars is compared and verified against the theoretical value. A value for v_0 is required as an input for the theoretical maximum stress, as used in Equation 4.7 in Chapter 4.

2. When conducting routine SHPB testing, striker velocity is a variable that can easily be controlled and changed between tests. Being knowledgeable of v_0 without having to yet process the strain gauge data can allow for tighter control of testing parameters, such as specimen strain rate.

3. It provides an early indication if the gas gun begins performing suboptimally.

4. It serves as a sanity check for the post-processing stage of SHPB testing.

Two speed sensors need to be developed, as there are different barrels used for compressive and tensile tests. Light trapping is the currently used method at BISRU, and it was used for speed sensing when testing in compression. This is described in detail in Section C.4 in Appendix C.

A light trap would be challenging to implement on the tensile barrel, as the striker is tubular, with other bars running through it. The light beams would not have a clean line of sight to the phototransistors, whether the striker was obstructing or not. Use of a reflective object sensor (ROS) is another method of striker speed sensing. It can be used in a wider range of applications as it is not required to be located at the location of striker impact, and needs access only to one side of the striker. A reflective object sensor (ROS) shall therefore be utilised instead to sense striker speed for the tensile configuration.

BISRU has made use of them in the past to track moving parts, in various applications [123, 124, 125, 126]. Using a ROS necessitates the use of the sensor, its accompanying instrumentation, and a striker equipped with alternating stripes of reflective and non-reflective surfaces of a known pitch . The sensor is comprised of light source and receiver , which typically take the form of an infrared LED and phototransistor. When the LED emits light, it some of that light reflects off of the surface of the striker and enters the phototransistor. The voltage across the photodiode feeds into the instrumentation. This is illustrated in the diagram in Figure 3.23.

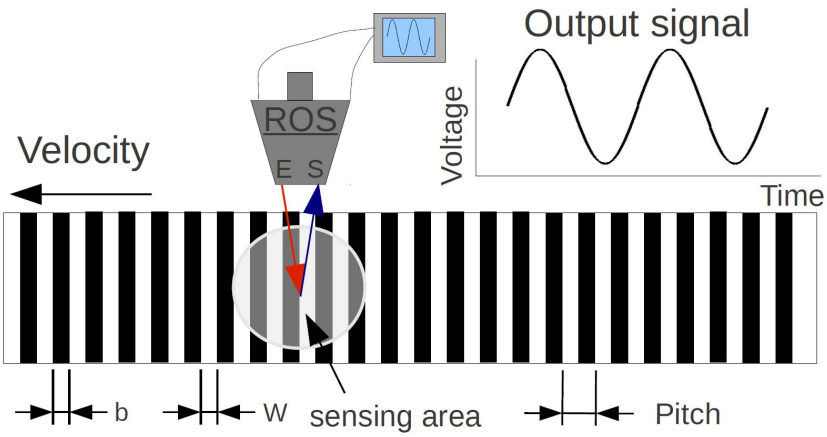

Figure 3.23 Concept diagram of the ROS as a speed sensing device [125]

As the striker moves past the sensor, the ROS instrumentation outputs a voltage signal proportional to how reflective the surface in front of the sensor is. This results loosely resemble a sinusoidal signal, which increases in frequency as the striker accelerates. Using a ROS therefore has the added benefit of being able to record a displacement and velocity history of the striker, instead of only an instantaneous velocity. Figure 3.24 depicts the critical portion of the expected output signal:

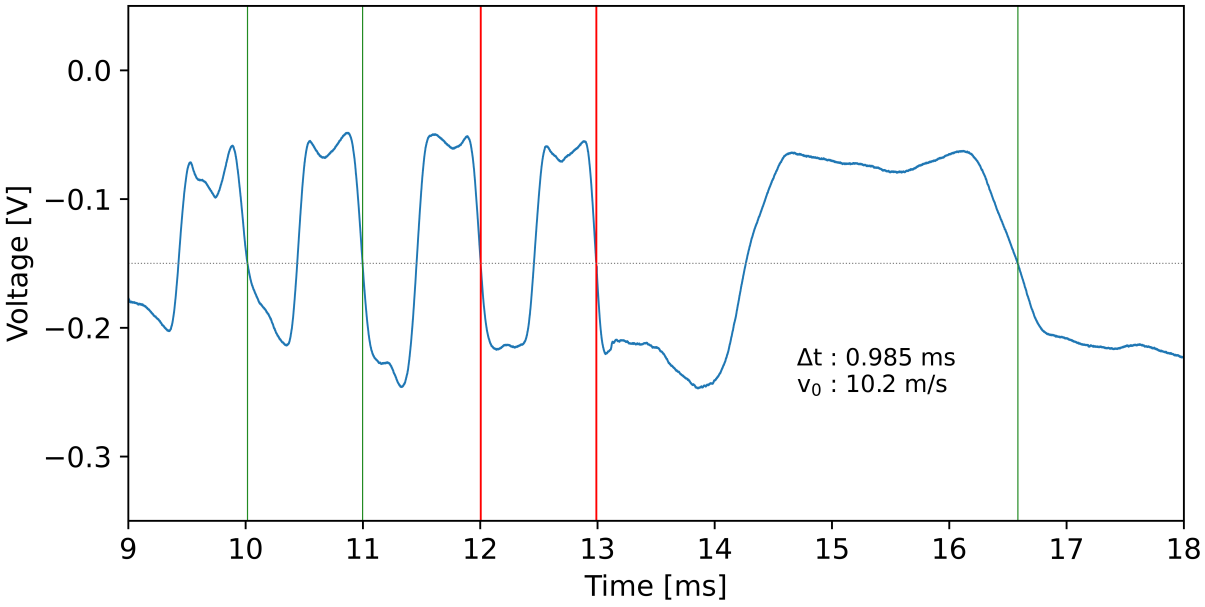

Figure 3.24 Typical voltage signal recorded using a ROS, showing how v_0 is determined

Here the striker appears to impact the input bar at roughly 13.5 ms, where it rebounds at a speed lower that than it impacted with. The period Δt of the last fully formed wave before impact (bounded by the red lines) is used alongside the pitch of the striker stripes to determine the striker velocity v_0 just prior to impact. A mounting fixture for the sensors is the only component that requires a novel design, as it needs to be tailored to this application. The rest of the instrumentation is available at BISRU. The two-piece mounting hardware is assembled and installed as picture in Figure 3.25.

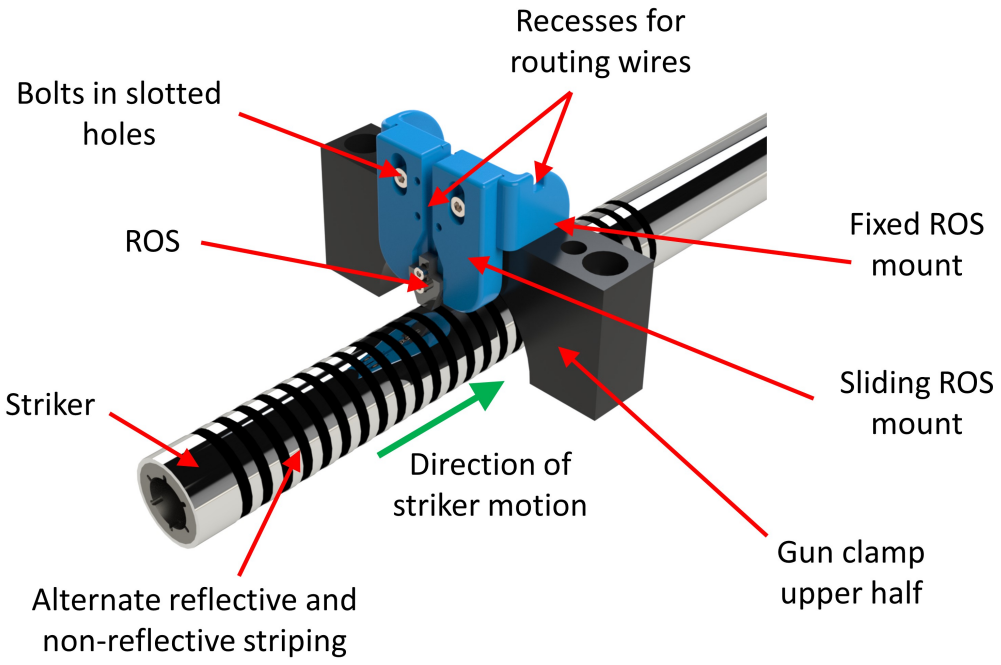

Figure 3.25 Isometric view of the ROS mounting fixture

The fixed mount is bolted onto the top of the gas gun clamp. Mounting slots are used to allow for adjustability along the axis parallel to the striker motion. The sliding mount, equipped with the ROS, is bolted to the fixed mount, again via slotted holes in order to give the ROS vertical adjustability. Adjustment in this direction is required to be able to set the gap between the ROS and the striker surface. This gap should be 3 to 4 mm. Grooves are included for the routing of the wires, as well as holes for securing them. Both parts of the ROS mount shall be 3D printed in PLA. Striker speed is therefore measurable, and Requirement RQ7 regarding this feature is met.

3.11 Closing Remarks

The following requirements were met in addition to those already mentioned:

- Requirement RQ16 was met in the design of this apparatus. All O-rings, bolts, nuts, threaded rods, circlips and bushing materials are readily available and of standard specification. They shall therefore be easy to source should they need to be replaced in the future.
- Requirement RQ17 was met. Almost all metal parts were manufactured from aluminium or titanium alloy, ensuring they do not oxidise, and continue to be sightly over time. In areas where unlike metals mate with each other, surfaces were greased to minimise galvanic corrosion.
- Requirement RQ15 was met. Most of the tools required for the operation and maintenance of this apparatus are exiting in the BISRU laboratory. Where this is not the case, custom tools were made, and are described in Section C.5 in Appendix C.

In this chapter, the design of the momentum trapped TSHB has been described. All important decisions have been justified, and the design in place aims to meet all of the requirements laid out. The parts were then manufactured and ready to move to the next step in the process.

Chapter 4

Preliminary Measurements and Calibration

When conducting any SHB experiments, there are steps to go through in order to verify material properties, and to correctly calibrate the equipment. This chapter outlines the methodology used in preparing the TSHB apparatus for use.

The methodology is summarized below:

1. Density measurements
    - Measured relative to known density of water
    - Conducted on pressure bar stock, input trap stock, and hollow trap stock
2. Elastic modulus measurement
    - Measured by means of a wave speed test
    - Conducted on pressure bar stock, input trap stock, and hollow trap stock
3. Pressure bar calibration
    - Conducted on input and output bars
4. Quasi-static tensile tests
    - Conducted on the specimens to be tested with the TSHB

4.1 Notes

- Both the input and output bar have identical diameters, material density and Young's modulus. Both pieces of stock are 7075 T6 aluminium, and were purchased as part of the same batch.
- The compressive striker used in the strain gauge calibration tests is cut from the output bar stock. For this reason it will be assumed that the striker, input bar, and output bar have identical mechanical impedance.
- The primary and secondary momentum traps that make up the tandem trapping subsystem are cut from the same piece of 6082 T6 aluminium stock. For this reason it will be assumed that they have identical mechanical impedance, but potentially differ from the pressure bars.
- All time shift done on data throughout this chapter are done while correcting for the effects of dispersion, using the existing code [4] mentioned in Section 2.6. This holds true for the Chapter 5 on the commissioning process.

4.2 Verification of Stock Material Properties

For any SHB setup, knowing the precise mechanical properties of the bars being used is critical. These properties dictate the wave speed in the bars, and are used to infer stress values from the strain data recorded from the gauges on the pressure bars. With this TSHB design, the mechanical properties play a key role in the effectiveness of the momentum trapping. Successful momentum trapping relies heavily on efficient transfer of stress waves between bars with minimal reflection or noise. According to one-dimensional wave theory, reflection is minimised when both bars (the bar from which the wave is coming, and the bar into which the wave is going) has matching mechanical impedance. Equation 4.1 shows that mechanical impedance of any bar is comprised of the product of the material density, ρ, the wave speed in that particular material, c, and the cross sectional area of the bar, A.

$$I_m = \rho \cdot c \cdot A \tag{4.1}$$

Wave speed, c, is determined from Equation 4.2.

$$c_{bar} = \sqrt{\frac{E_{bar}}{\rho_{bar}}} \tag{4.2}$$

For this reason, precise values for the density and Young's modulus for all bars are needed. Textbook values, and the values stated by suppliers are not accurate or reliable enough, and will need to be measured experimentally on the exact pieces of stock being used.

4.2.1 Density Tests

The first step is to experimentally determine the density of the various pieces of stock used. The method used [127] utilizes Archimedes' principle of buoyancy to measure the density. This involves comparing the apparent masses of small material specimens, when suspended in air versus when suspended in water.

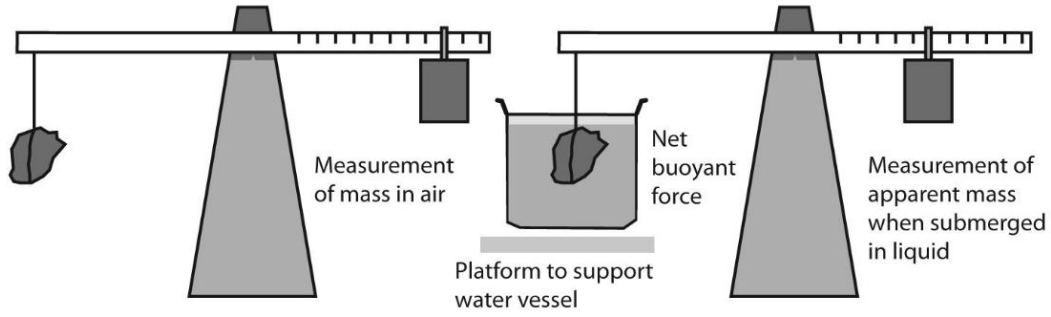

Figure 4.1 Dry versus wet mass measurement [128]

The density of the sample is calculated using Equation 4.3

$$\rho_s = \frac{m_{dry} \cdot \rho_w}{m_{dry} - m_{wet}} \tag{4.3}$$

Where:

ρ_s = Density of sample
ρ_w = Density of water at test conditions, taken as 998.943 kg/m^3 at 16 ° C [129].
m_{dry} = Mass of sample, suspended in air
m_{wet} = Apparent mass of sample, suspended in water

The resulting density values for the stock are shown below in Table 4.1.

These densities have little variation from those published in textbooks or manufacturer specifications, thus verifying the accuracy of these results.

Table 4.1 *Experimentally determined densities for the aluminium stock*

Material	Part	Density [kg/m^3]
7075 T6 Aluminium	Pressure Bars	2811
6082 T6 Aluminium	Solid input traps	2713
6000 series Aluminium	Hollow output trap	2700

4.2.2 Wave Speed Tests

Wave speed is used in SHPB calculations whenever waves are shifted to bar interfaces. Attaining a precise value for the pressure bars contributes directly to the precision of the results. Beyond that, knowing the material density means that Young's modulus can be inferred from wave speed for the purpose of impedance matching. The wave speed test is carried out by impacting an end with a short striker, as displayed in Figure 4.2. For these experiments, and all experiments that follow in this thesis, 120Ω strain gauges of 2 mm gauge length were used on all bars, adhered on opposite side of each bar to account for bending. An amplifier gain of 1000 was used throughout, and tests were sampled at 60 MHz.

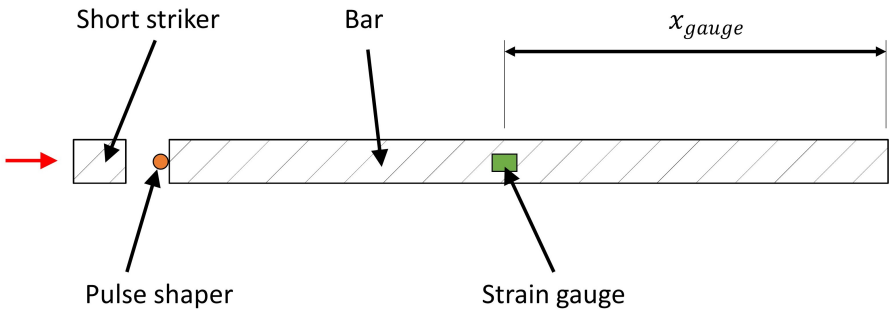

Figure 4.2 Bar layout for wave speed tests

This sends a stress wave down the bar, which reflects off of the free end. A set of strain gauges allow us to record the wave.

In Figure 4.3, we can see that there is a measurable time delay between the incident wave, and the wave that has reflected off of the end of the bar. For a given bar modulus, E_{bar}, and bar density, ρ_{bar}, speed of sound (wave speed), c_{bar} can be calculated using Equation 4.2.

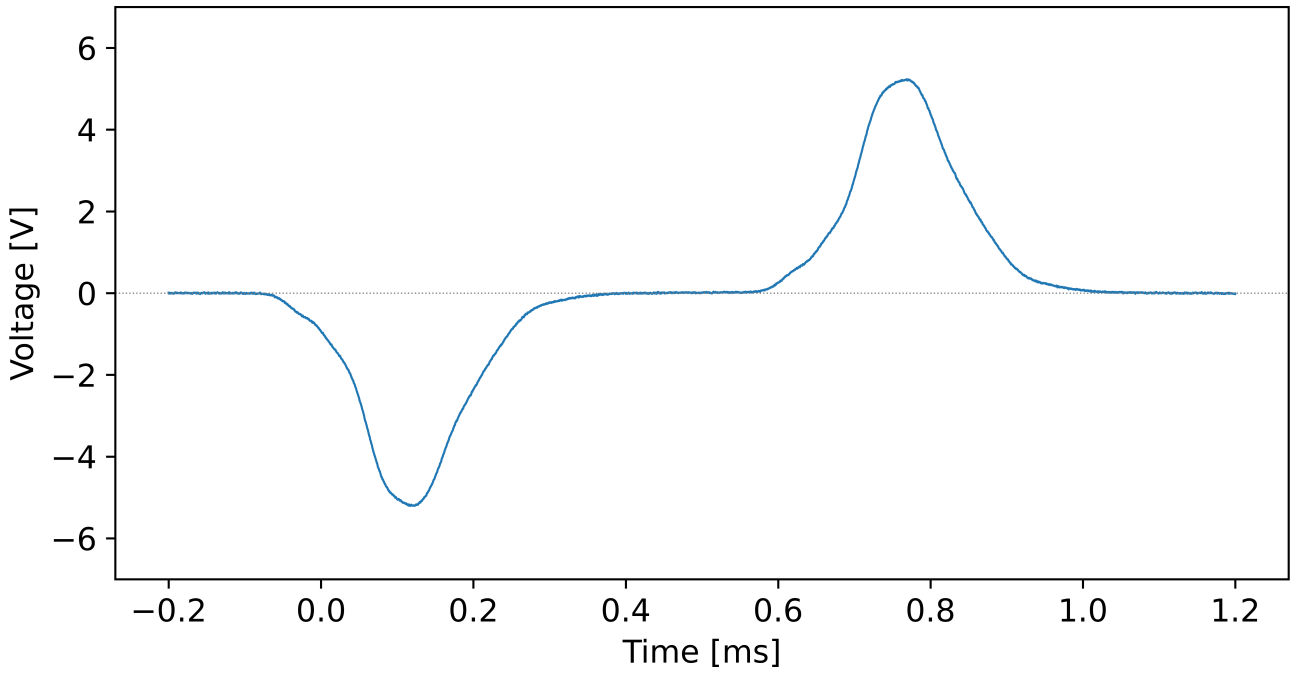

Figure 4.3 Output voltage data from a wave speed test on the input bar

Using that wave speed, and the known distance from the gauges to the bar end, x_{gauge}, the time it takes for a wave to travel that distance can be calculated using Equation 4.4. Note that this will be approximately half of the time difference between the incident and reflected waves, observed by the strain gauges.

$$\Delta t_{gauge} = \frac{x_{gauge}}{c_{bar}} \tag{4.4}$$

Now if the incident wave in Figure 4.3 is time-shifted by Δt_{gauge} to the right, and the reflected wave is time-shifted by Δt_{gauge} the the left, they should align near perfectly as they do in Figure 4.4. Both waves are shifted to the end of the bar, as this is a free surface, where the waves superimpose destructively to equal zero stress. The region of the plot in Figure 4.4 where the relevant waves align is isolated in Figure 4.5.

A third plot is made by summing the two shifted plots. The degree of alignment between the shifted waves is quantified using the root mean square (RMS) method. All data points of the summed plot, within the analysis window (the red lines in Figure 4.5) are squared, summed, and then square rooted to give a single RMS voltage value. This value is an indication how closely the waves align, and therefore how close the modulus used is to the true value. This test is then done for a range of moduli, and the one yielding the

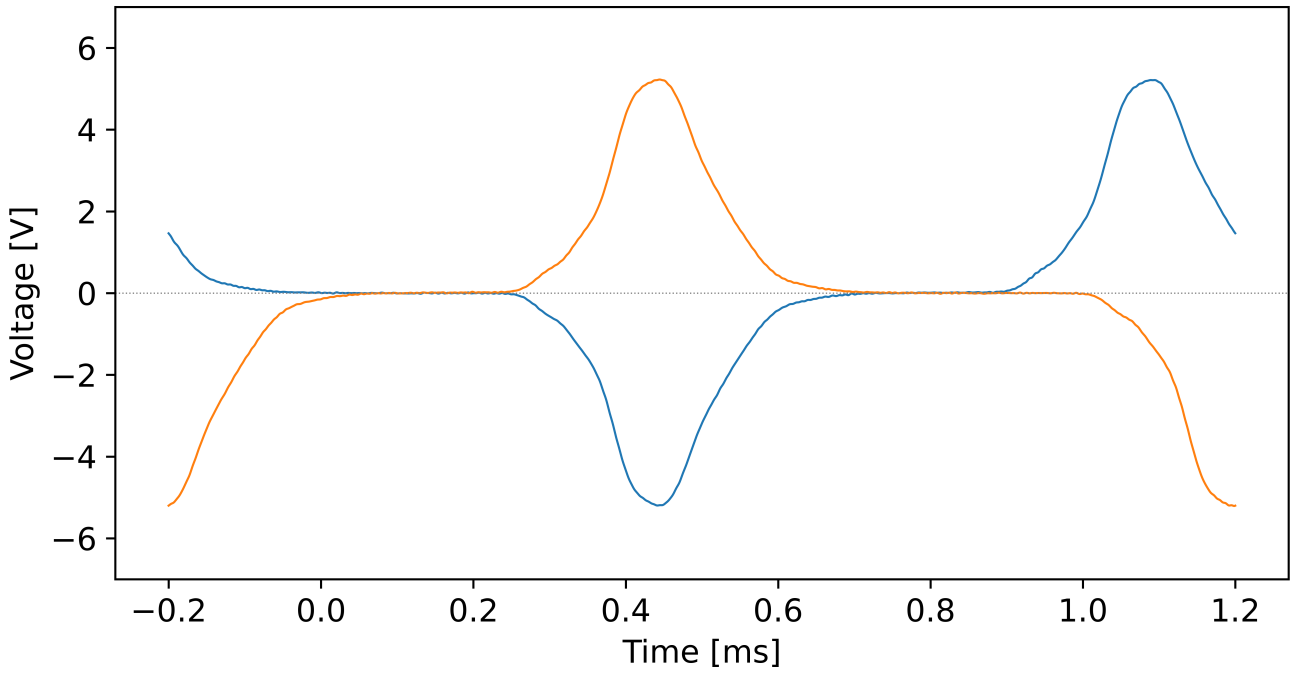

Figure 4.4 Shifted voltage data from the wave speed test on the input bar

lowest RMS voltage value will be the true experimental modulus. Figure 4.6 plots the RMS voltage value as a function of assumed modulus.

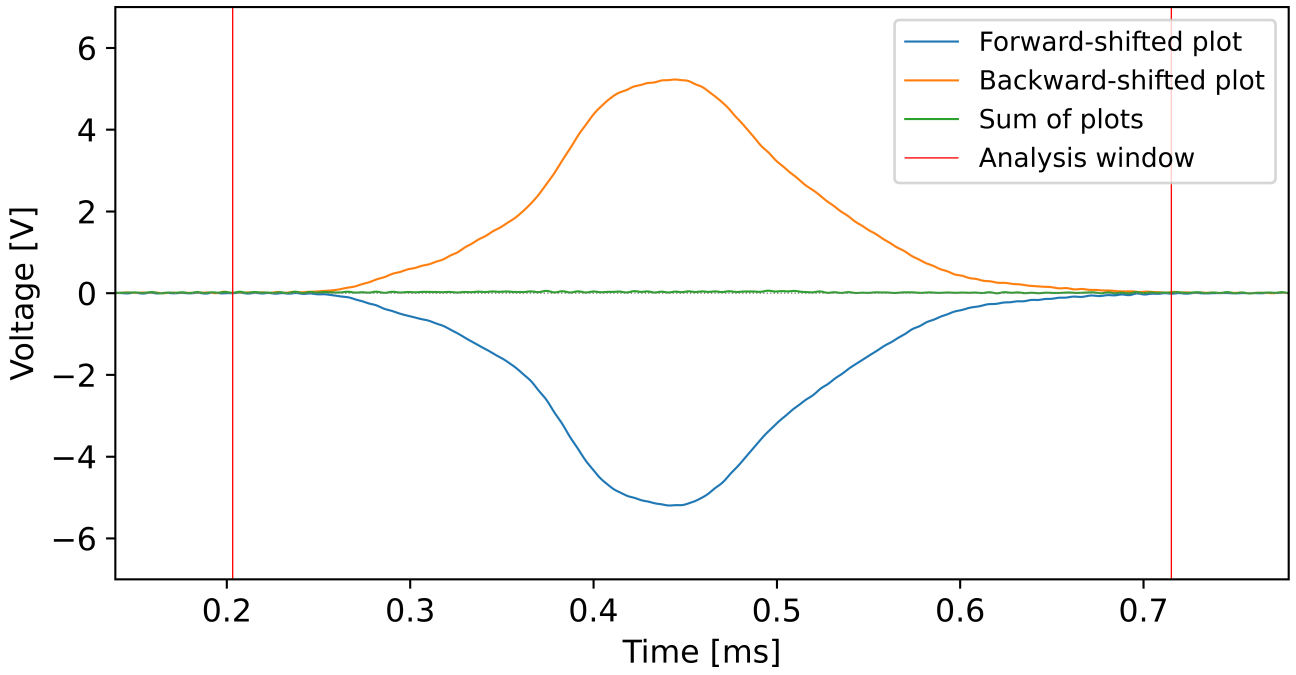

Figure 4.5 Close view of wave alignment from the plot in Figure 4.4

This plot shows that this is an optimization problem, and that a clear modulus value emerges for which the RMS voltage is a minimum. For each of the three materials, ten tests were conducted, with the above steps being completed on each test. The mean of the ten moduli was then taken to be the modulus of the material. The results are displayed in Table 4.2. Extended results may be found in Appendix D.

Table 4.2 *Experimentally determined Young's moduli for the aluminium stock, in GPa*

Material	Minimum	Maximum	Mean	Standard deviation
7075 T6 Aluminium	73.58	73.68	73.63	0.02879
6082 T6 Aluminium	72.67	72.69	72.68	0.008307
6000 series Aluminium	67.81	67.87	67.84	0.01640

For each of the materials the standard deviation was small, indicating that the experimental methods were repeatable across tests. This provides assurance that the calculated mean modulus will be reliable through further experiments. The measured moduli were all close to the expected range, with the modulus of the tube stock being noticeably lower

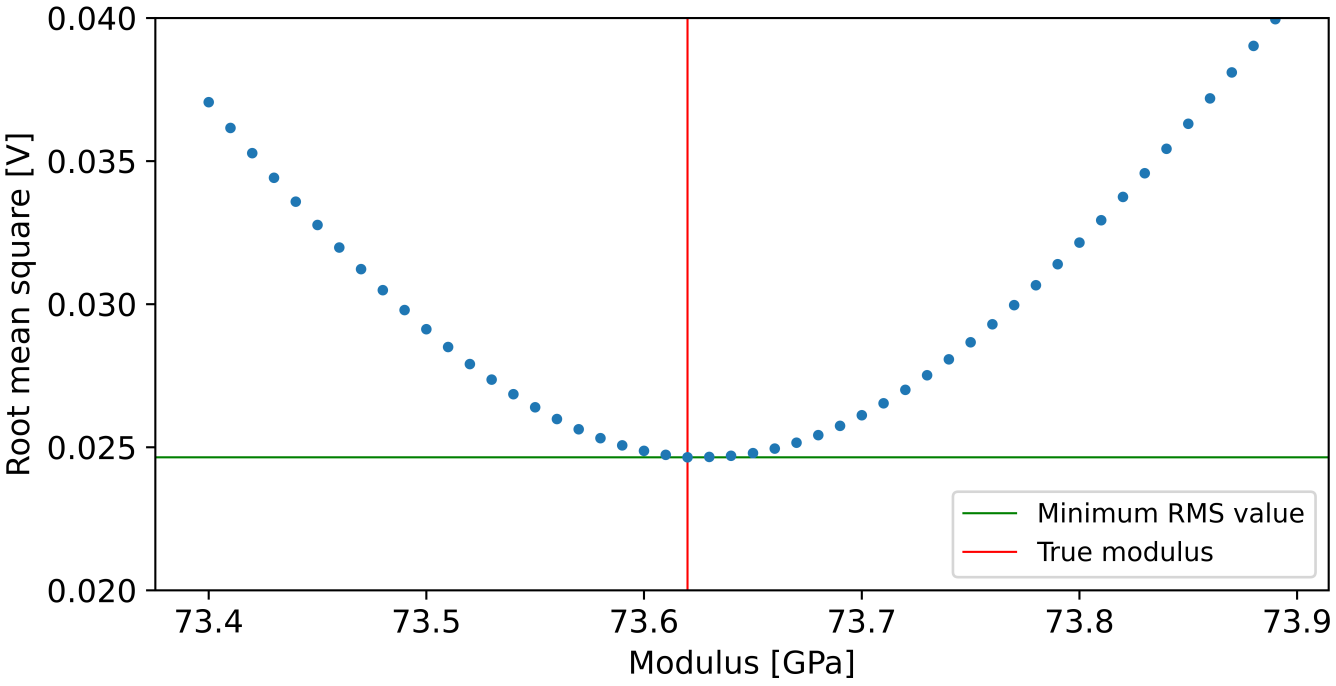

Figure 4.6 RMS error plotted as a function of modulus

than that of the solid bar stock. It was, however, close enough to textbook values to be of no further concern. This does not affect the design, and only points to the tube being manufactured from a different alloy of aluminium to the other bars.

Wave speeds for all three bars are shown in Table 4.3.

Table 4.3 *Experimentally determined wave speeds for the aluminium stock*

Material	Part	Wave speed [m/s]
7075 T6 Aluminium	Pressure Bars	5118
6082 T6 Aluminium	Solid input traps	5176
6000 series Aluminium	Hollow output trap	5013

For wave speed tests, it is highly beneficial to consider the dispersion of the stress pulse. The less dispersion occurs, the better the incident and reflected waves will be able to match when shifted and added to one another. This improves results. Dispersion was dealt with in two ways:

- The stress pulse was smoothed to reduce dispersion as the wave travels down the bar. The pulse was smoothed by sticking a deformable element onto the struck end

of the bar. In this case, the deformable element was 1.5 mm thick gasket paper. This increases the rise and fall time of the pulse, and creates a rounder shape, as seen in Figure 4.3. Dispersion becomes more prominent for waves with steep rises or falls, associated with higher frequency wave components. By creating a wave with more gentle features, the effect of dispersion is substantially reduced.

- The remainder of the dispersion effects were corrected for in post-processing of the data, using existing dispersion correction code [4].

4.3 Strain Gauge Calibration

The stress calibration factor, K, is a constant, specific to a particular bar and gauge pairing, that allows us to define the stress in the bar as a function of the applied and measured voltages across the Wheatstone bridge. In this case, the input and output bars will need calibration. In order to be sure of the calculated K value, the magnitude of the stress wave in the bar was found using two methods, and then compared. Firstly, using strain gauge theory, K may be calculated using Equation 4.5.

$$K = \frac{4 \cdot E_b}{G \cdot k_g} \tag{4.5}$$

E_b is the Young's modulus of the bar, G is the amplifier gain, and k_g is the gauge factor. This formula, being theoretical, assumes ideal conditions, where strain gauges are perfectly aligned, and are equal in resistance. This may not always be the case, and is the reason why K is also acquired experimentally. The bar was struck with a longer, 500 mm striker, producing a flat-topped pulse on the output signal. Minimal pulse shaping was used, as the wave should be as trapezoidal in shape as possible. This is the practice as a plateau voltage needs to be measured off of that wave. Equation 4.6 shows how an experimental stress value is calculated, using the data V_{out}, applied bridge voltage V_{in}, and K.

$$\sigma_{experimental} = K \cdot \frac{V_{out}}{V_{in}} \tag{4.6}$$

Secondly, assuming 1-dimensional wave propagation and conservation of momentum, the peak theoretical stress in the bar may be calculated as a function of striker speed, striker properties and bar properties.

$$\sigma_{theoretical} = v_0 \cdot \frac{A_s \cdot \rho_s \cdot c_s \cdot \rho_b \cdot c_b}{A_s \cdot \rho_s \cdot c_s + A_b \cdot \rho_b \cdot c_b} \tag{4.7}$$

As the striker was cut from the same stock as the bar, Equation 4.7 simplifies to Equation 4.8.

$$\sigma_{theoretical} = \frac{1}{2} \cdot v_0 \cdot \rho_b \cdot c_b \tag{4.8}$$

If these two stress values are close to one another for a given test, it confirms that the value for K is suitable. This test also confirms that no wires are loose, and that the strain gauges have adhered well to the bar and are precisely aligned with the bar axis.

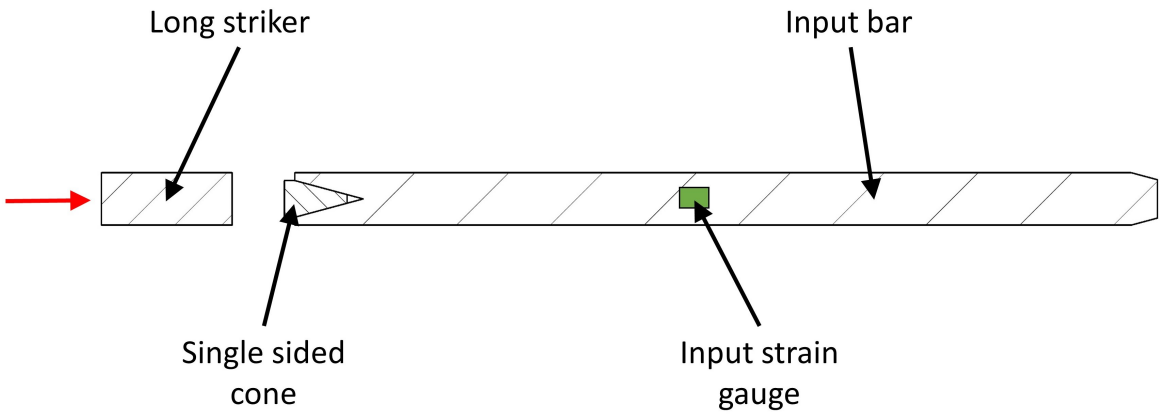

Figure 4.7 Bar layout for strain gauge calibration of the input bar

Figure 4.7 shows the bar layout for the calibration tests of the input bar strain gauges. The layout for that of the output bar gauges was similar. A single sided cone with a male conical thread was fitted into the specimen clamp socket in the bars. This provided a flat surface for the striker to impact, and simultaneously protects the female threads in the bar from damage.

For each of the tests, the output voltage signal was recorded, along with the bridge voltage and striker speed. Figure 4.8 shows a typical output voltage signal from a test on the input bar. The peak output voltage was measured by taking the mean value of the plateau of the wave. The red vertical line show the bounds of the plateau, within which the mean voltage was calculated.

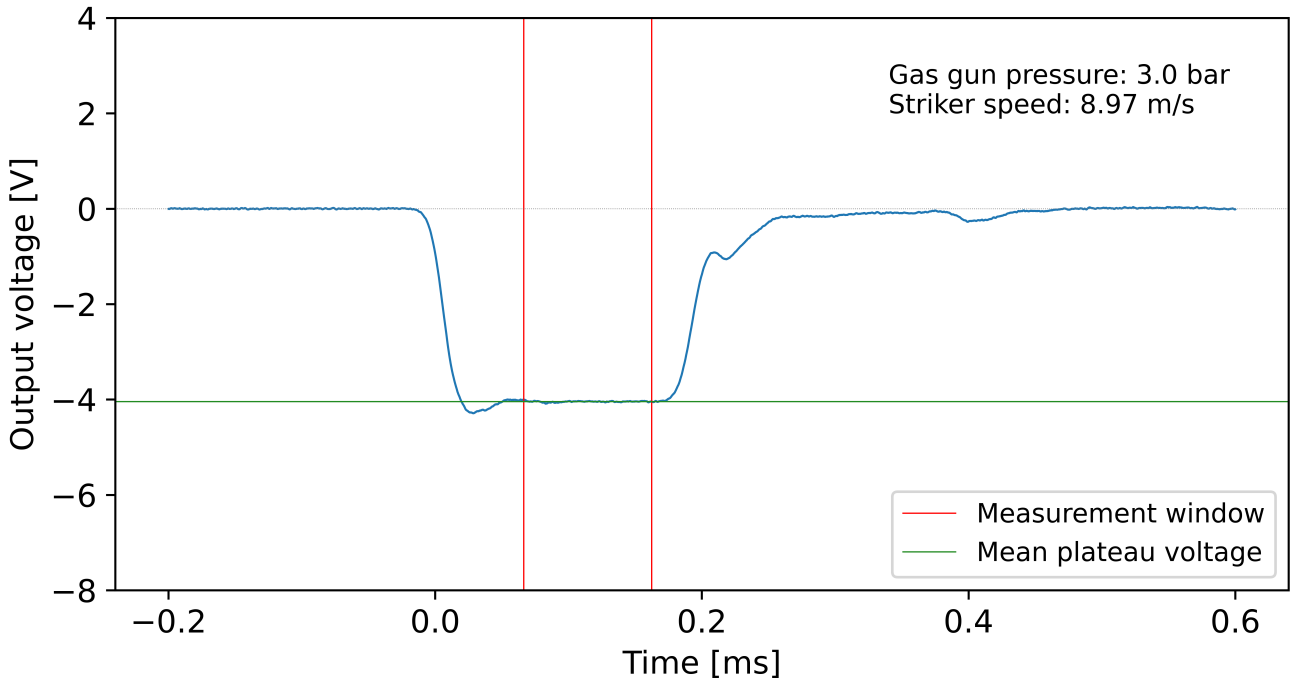

Figure 4.8 Typical output signal from the calibration tests on the input bar

Ten separate tests were conducted for each bar, and their results are summarised in Table 4.4. The extended calibration results may be found in Appendix E.

Table 4.4 *Results for strain gauge calibration*

Theoretical calibration factor $K = 34.57$ MPa V V^{-1}		
Bar	**Mean error between theoretical and experimental bar stress [%]**	**Standard deviation in error [%]**
Input bar	2.40	0.49
Output bar	3.12	0.39

For the input and output bars, the mean error was 2.40 % and 3.12 % respectively. For calibration, 5 % was deemed to be an acceptable error threshold, meaning that the theoretical calibration factor of 34.57 MPa V V^{-1} was acceptable for both bars. Both bars exhibited little variation across the ten conducted tests, with the input and output bar having a standard deviation of 0.49 % and 0.39 % respectively. This demonstrates that the apparatus and experimental setup were repeatable.

4.4 Quasi-static Tensile Tests

The final step of the calibration process is to conduct quasi-static tensile tests of the specimens to be tested. These tests are done so that the material properties attained via dynamic testing, can be verified against those attained under quasi-static conditions. Although this project focuses on developing new experimental hardware and not detailed characterisation of a specific material, specimens will be used to show that the TSHB meets its requirements. These quasi-static tests are being conducted for the purpose of measuring the yield strength for this material, and by extension, verifying which material these specimens are made of. DOMEX 550 should have a yield strength of greater than 550 MPa. As mentioned in Section 1.3, existing tensile specimens from prior BISRU projects were utilised in this project. They were of the 5-lobe fir-tree design discussed in Section 2.4.5. The specimen parameters are described in detail in Section 6.2.

The Zwick Roell 1484 universal testing machine in the Centre for Material Engineering was used for these tests. The configuration of hardware in the machine is described in Appendix F. A 200 kN load cell was used for the force measurement, while an optical extensometer was used to record elongation, via marked tracking points on the specimen gauge section. Four specimens were tested at a strain rate of 0.001 /s and four further tests at 0.1 /s, with all specimens loaded to fracture.

The 0.2 % offset method of determining yield strength was used. For a given test, bounds were established for the linear elastic region of the stress-strain plot. A Young's modulus was then calculated by applying a linear regression to the plot between those bounds. That line was the shifted right by a strain of 0.002 to find the 0.2 % offset yield strength of that specimen, as shown in Figure 4.11.

The engineering stress-strain data for the 0.001 /s series of tests is shown in Figure 4.9, with the measured yield strengths reported in Table 4.5.

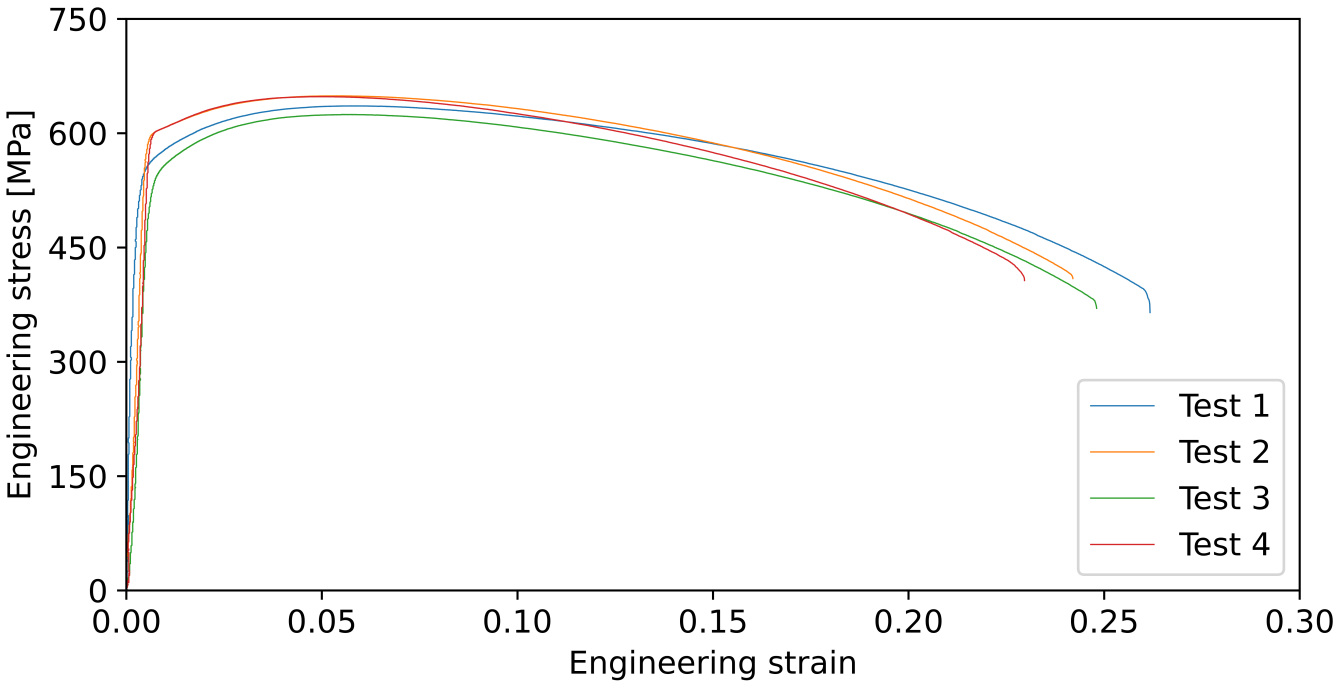

Figure 4.9 Quasi-static stress-strain results, conducted at a strain rate of 0.001 /s

Table 4.5 *Quasi-static yield stress results, conducted at a strain rate of 0.001 /s*

Test number	**Yield Stress [MPa]**
1	550.07
2	601.16
3	543.22
4	603.97
Mean [MPa]	574.61

The results for the 0.1 /s series of test is displayed in Figure 4.10 and Table 4.6.

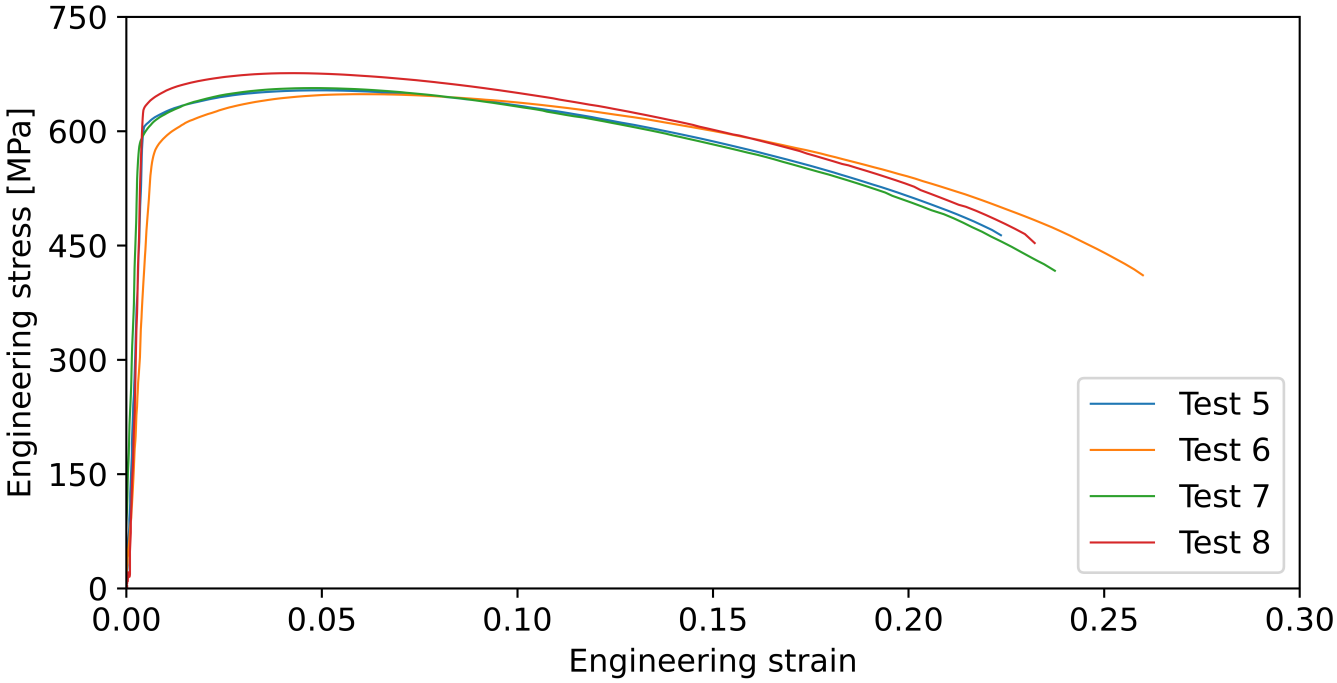

Figure 4.10 Quasi-static stress-strain results, conducted at a strain rate of 0.1 /s

Table 4.6 *Quasi-static yield stress results, conducted at a strain rate of 0.1 /s*

Test number	**Yield Stress [MPa]**
5	616.69
6	587.60
7	606.35
8	641.54
Mean [MPa]	613.05

Both test series attain a yield strength of greater than 550 MPa and significantly less than 700 MPa. Given that these specimens were known to be a DOMEX alloy, the measured yield strength confirms that the exact material is DOMEX 550.

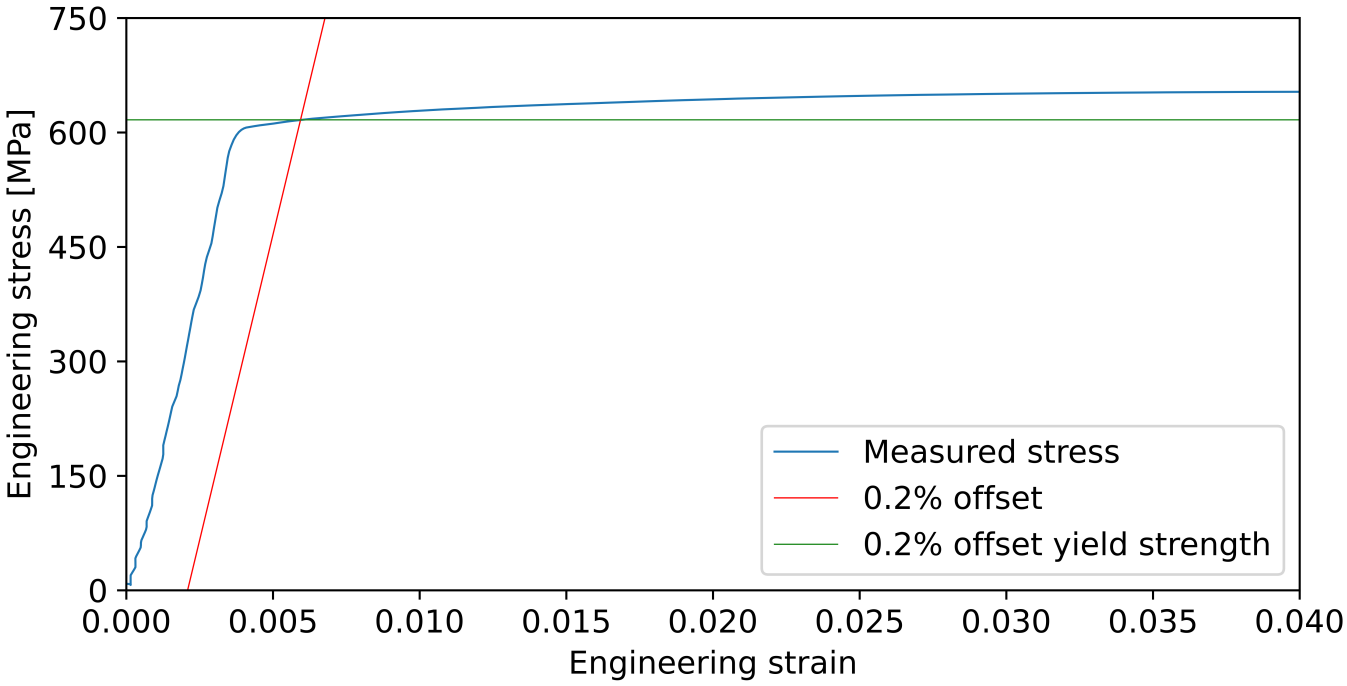

Figure 4.11 Method for calculating the 0.2% offset yield strength, shown for test 5

4.5 Closing Remarks

This chapter has outlined all of the necessary tests and processes that support the work to follow. The relevant material properties are known with great certainty, and have been verified experimentally. Now that the groundwork has been completed, the commissioning of the apparatus can commence.

Chapter 5

Commissioning

There is lot of refinement that needs to happen before the the manufactured parts and assemblies can operate as a functional system. The commissioning process of this new tensile split Hopkinson bar set up has been broken down, in order, below:

1. Impedance matching of solid tandem traps
    - Tuning of traps' OD to in order to match the impedance of the input bar, and to each other
2. Test operation of the tandem trap sub-system
    - Verification in compression
    - Verification in tension
3. Impedance matching of hollow trap
    - Tuning of trap's OD to in order to match the impedance of the output bar

5.1 Impedance Matching the Input-side Traps

The first step is to finalise the diameter of the two momentum trap bars that make up the tandem arrangement on the input side. The goal is that the impedances of the input bar, primary tandem trap, and secondary tandem trap are all as close as possible. This can be done by reducing the trap OD, and thus changing the cross sectional area. An iterative approach was taken to adjust the traps. Tests were run and the trap's performance assessed. The bar OD was reduced accordingly and then the tests would run again. This cycle would gradually approach the ideal diameter for matching the impedance of the traps to the input bar. The two compressive bars that make up the tandem momentum traps have identical diameters and material properties, as they both are turned from the same bar stock. Hence only one trap bar needs to undergo the iterative experimental impedance matching. The second trap bar can be turned down to the same final diameter.

For these tests, the solid trap was placed up against the input bar, and a compressive striker was impacted onto the other end. This bar layout is displayed in Figure 5.1. In order to slightly smooth the shape of the incident wave, masking tape was used on the impacted face of the input bar. Four layers of tape were used, and were replaced for every test. This gave good repeatability of pulse smoothing while being quick and not requiring careful operator actions.

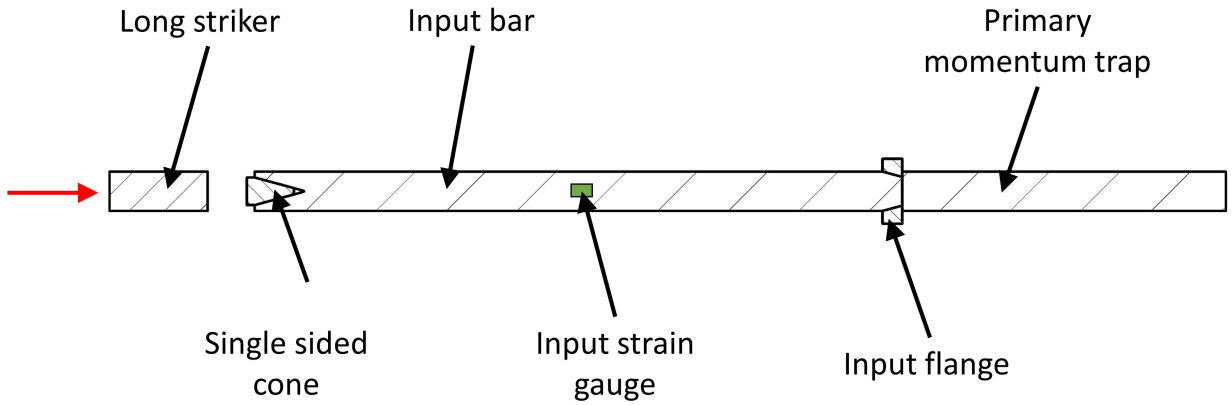

Figure 5.1 Bar layout for matching the solid trap impedance

To replicate the actual testing conditions, the impedance tests were done with the impact flange attached to the input bar. Both bars were given an index mark on their diameter, so that the bars were known to be in their same angular position for all tests. This system was employed for all further tests in the commissioning process. Stress data was recorded using the strain gauges on the input bar. The aim was to minimise the reflected wave, returning from the end of the input bar.

Due to the thread on the end of the input bar, it is challenging to accurately align the ends of the bars. Since bar alignment is critical for the stress wave to be able to efficiently transfer to the trap, a new method for aligning bars was used. This method is outlined in Appendix A.

5.1.1 Test with Trap at Stock Diameter of 20 mm

The trap bar stock was nominally 20 mm diameter, and was used as received in the first round of tests. Ten tests were conducted to account for any anomalies that may present themselves during testing. Figure 5.2 shows a stress plot from one of these initial tests.

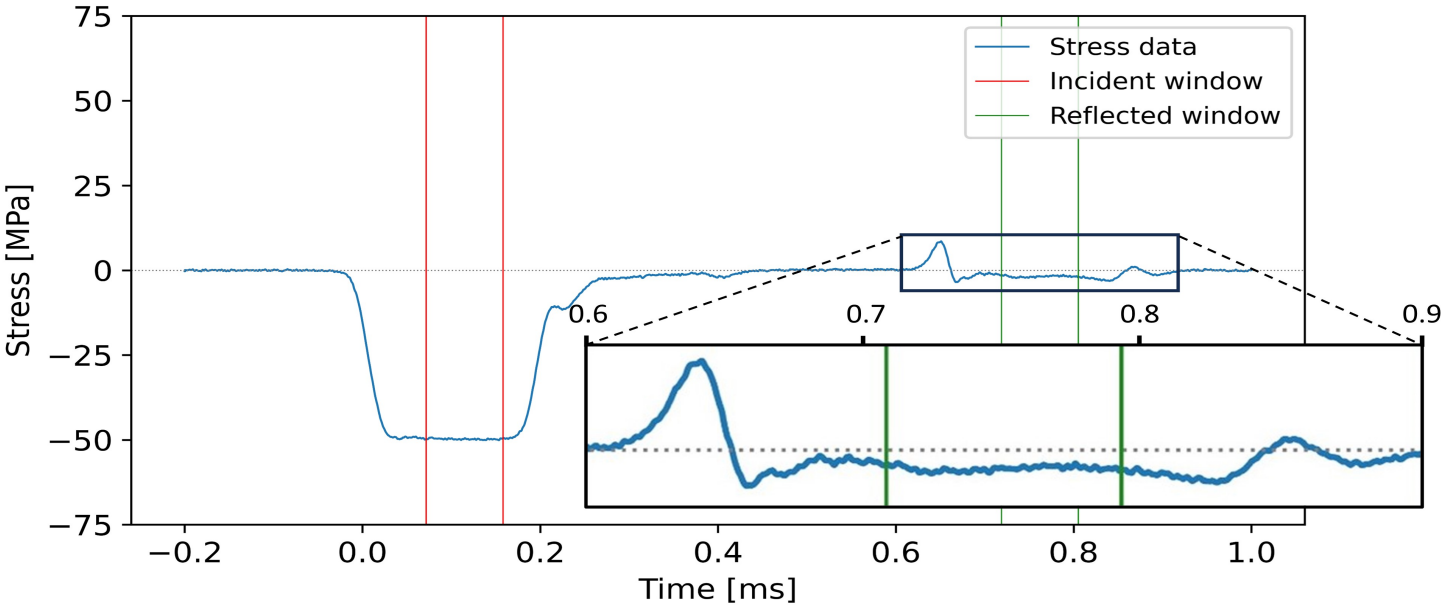

Figure 5.2 Results with the solid trap at 20 mm diameter

The reflected wave, seen more clearly in the zoomed view in Figure 5.2, can be seen to begin with a transient (the 'blip' between 0.6 ms and 0.7 ms), before settling to a stable, non-zero stress. This transient was the result of the mass of the input flange, which was screwed onto the input bar right where the two bars come together.

From each of the tests, an experimental incident stress was measured. This was taken to be the mean stress along the plateau of incident wave. The data between the red vertical lines was used. The same was done with the measured reflected wave, using the data between the green lines. Lastly, a theoretically expected value was calculated for the reflected stress, using bar properties, and was based off of the experimental incident

stress. By comparing the two reflected stress values, it could be verified how closely the tests correlate to the one-dimensional wave propagation theory. The mean values across all tests are shown in Table 5.1, with the extended found shown in Appendix G.

Table 5.1 *Results from tests with the solid trap at 20 mm diameter*

Parameter	**Reflected stress expressed as a fraction of incident stress [%]**	**Error between experimental and theoretical reflected stress [%]**
Mean	3.86	6.61
Standard deviation	0.34	8.69

On average, less than 4 % of the incident wave was returning in the reflection, indicating that most of the stress wave being trapped. The variance of the results between repeated tests was very low. The fact that the incident and reflected waves were both compressive confirms that the mechanical impedance of the trap was higher than that of the pressure bars. With the exception of tests 3 and 4, the experimental and theoretical stresses were very close to one another. This indicates that the interface between the two bars was behaving very close to that expected from the theory of one-dimensional waves. There was most likely an error when setting up tests 3 and 4, such as a small gap or some debris between the bars, which lead to longer time to achieve full contact and proper stress transfer.

Since the bar interface was well aligned and contacting fully in eight of ten experiments, a theoretical final diameter was calculated for the solid trap, using the properties of the bars in question. This final diameter is 19.28 mm. It was decided to turn the trap stock from 20 mm diameter down to 19.60 mm for the next round of tests. A diameter of 19.60 mm is roughly half way to 19.28 mm in terms of area reduction, and re-testing at this halfway point was the conservative option. Material removal from the bars is irreversible and over-shooting the perfect impedance match would result in scrapping the trap bar and starting again with new stock.

5.1.2 Test with Trap at Reduced Diameter of 19.60 mm

The trap bar's diameter was then reduced, and another set of tests were run. A typical stress plot for this iteration of trap bar is displayed in Figure 5.3 and the results are summarised in Table 5.2. Extended results for these tests may be found in Appendix G.

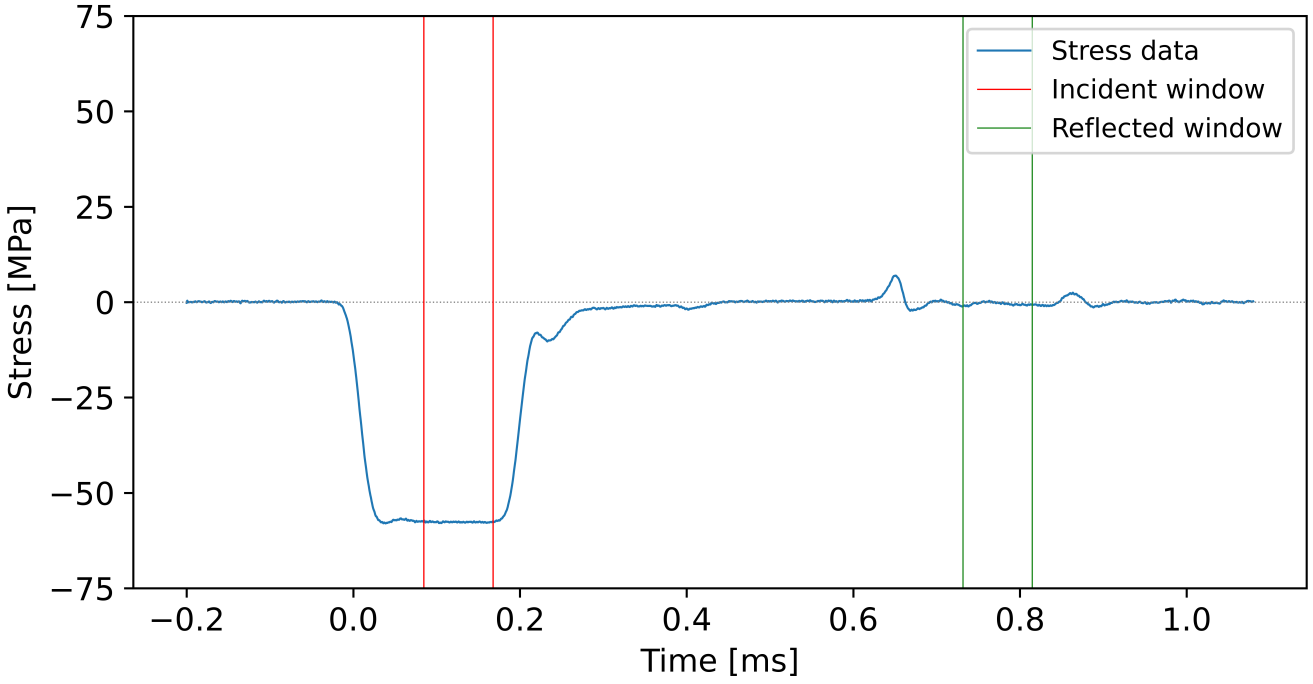

Figure 5.3 Results with the solid trap at 19.60 mm diameter

Table 5.2 *Results from tests with the solid trap at 19.60 mm diameter*

Parameter	Reflected stress expressed as a fraction of incident stress [%]	Error between experimental and theoretical reflected stress [%]
Mean	0.87	46.53
Standard deviation	0.21	12.60

For the 19.60 mm diameter trap, only 1 % of the incident wave is being reflected, meaning that the momentum trap is capturing 99 % of the incident wave. Again, there is very little variance in this result between repeated tests. The experimental and theoretical reflected stress were not correlating as closely in this round of tests. The experimental

reflected stress was 47 % of what the theory says it should be, on average. This suggests that the momentum trap was operating better than expected at this reduced diameter. Since the trap was very close to performing optimally, and there was little room for error, it was decided not to further reduce the trap's diameter. The second solid trap was then manufactured to the same diameter, that being 19.60 mm.

To demonstrate the effectiveness of the momentum trap, Figure 5.4 compares data from one test without any momentum trapping, and one test with a single trap bar of diameter 19.60 mm. All other variable were kept constant.

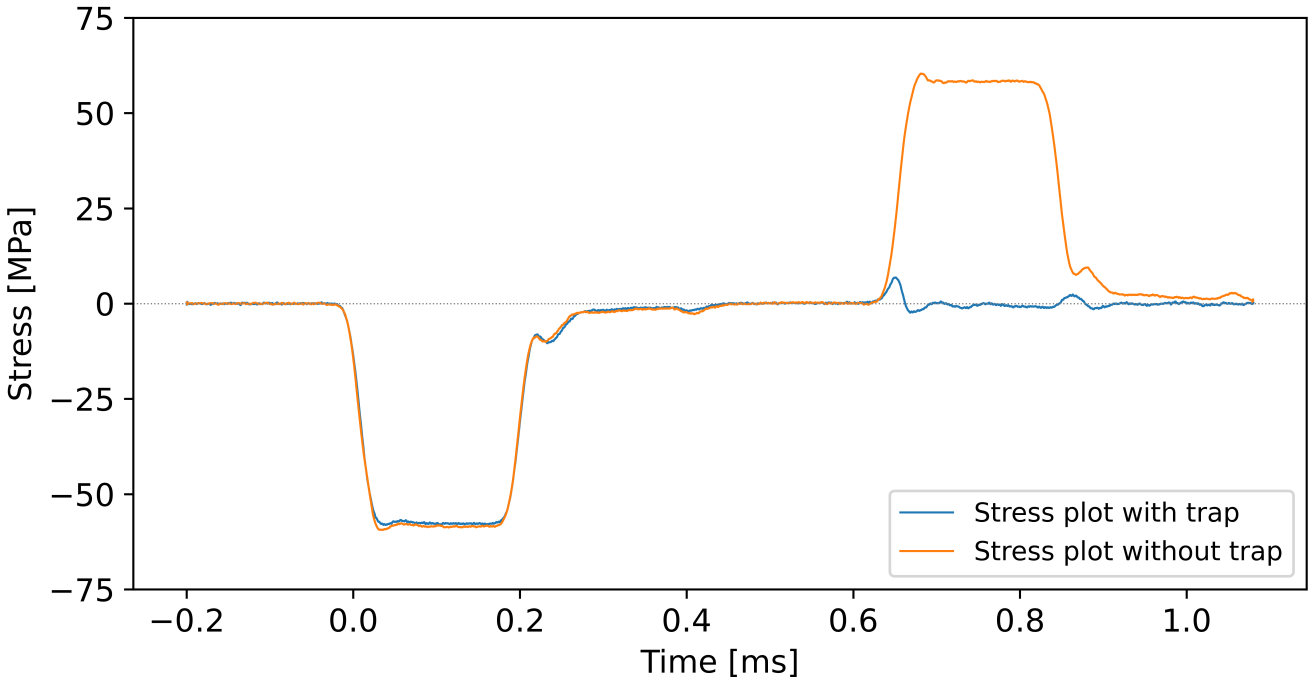

Figure 5.4 Stress plots comparing tests with and without a momentum trap

It can be concluded that the solid trap of 19.60 mm diameter was clearly trapping the vast majority of a compressive pulse from the input bar.

5.2 Verifying the Operation of the Tandem Input-side Traps

Since the two input traps had been impedance matched, the next step was to ensure that they operate well in tandem. The performance of this subsystem is of high importance to the function of this apparatus. The specimen is most vulnerable to reloading from the reflected wave, and this wave is only trapped if both of the tandem traps function properly. Looking at the Lagrange diagram for this TSHB in Figure 3.1 in Section 3.2, it can be seen that the tandem traps' isolated function is to capture two consecutive compressive stress pulses without any user intervention in between.

5.2.1 Two-phase Verification Tests

The operation of the input bar momentum traps was verified in two phases, testing each trap's performance in compression separately. Similarly to the tests in Section 5.1, the input bar will be struck in compression, using four layers of masking tape to smooth the incident wave. Figure 5.5 shows the arrangement of both solid traps in line with the input bar. The contact face between the input bar and the primary trap is referred to as interface 1, and that between the primary and secondary traps is referred to as interface 2.

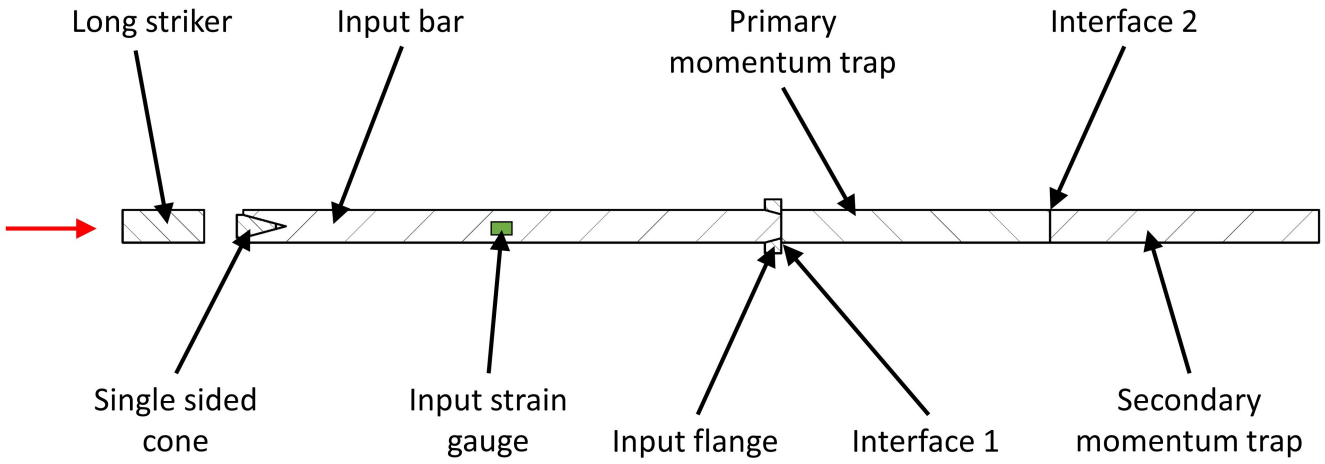

Figure 5.5 Bar layout for the two-phase tandem trap verification tests

If all functions correctly, phase 1 should result in the secondary trap separating from the primary trap, leaving the primary trap in close contact with the input bar. This simulated the compressive pulse that enters the traps as the striker first impacts the input flange. The striker was then reloaded, without disturbing any of the bars or traps.

Phase 2 simulates the traditional reflected compressive wave, and should be captured in the primary trap, as it separates from the input bar.

In order to monitor the contact between the bars, an electrical continuity circuit was created, that makes use of the bars as conductors. Bar separation would create an open circuit, and the timing can be recorded using an oscilloscope. The circuit diagram is shown in Figure 5.6:

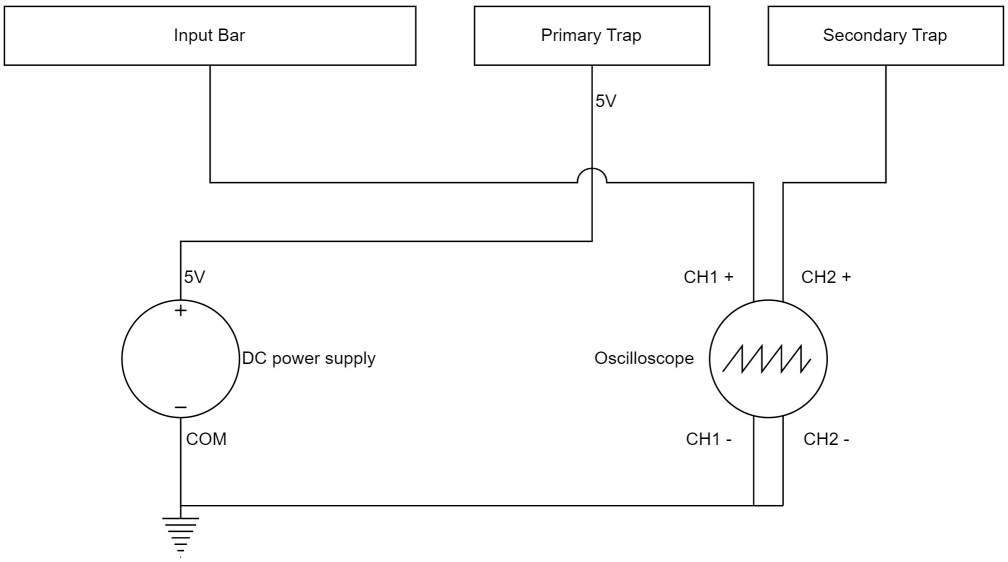

Figure 5.6 Circuit diagram for monitoring contact between bars

The circuit input voltage will be read on the an oscilloscope channel when there is bar contact at the respective interface. An input voltage of 1 V was used in the presented data. Figure 5.7 was the result seen across the initial tests.

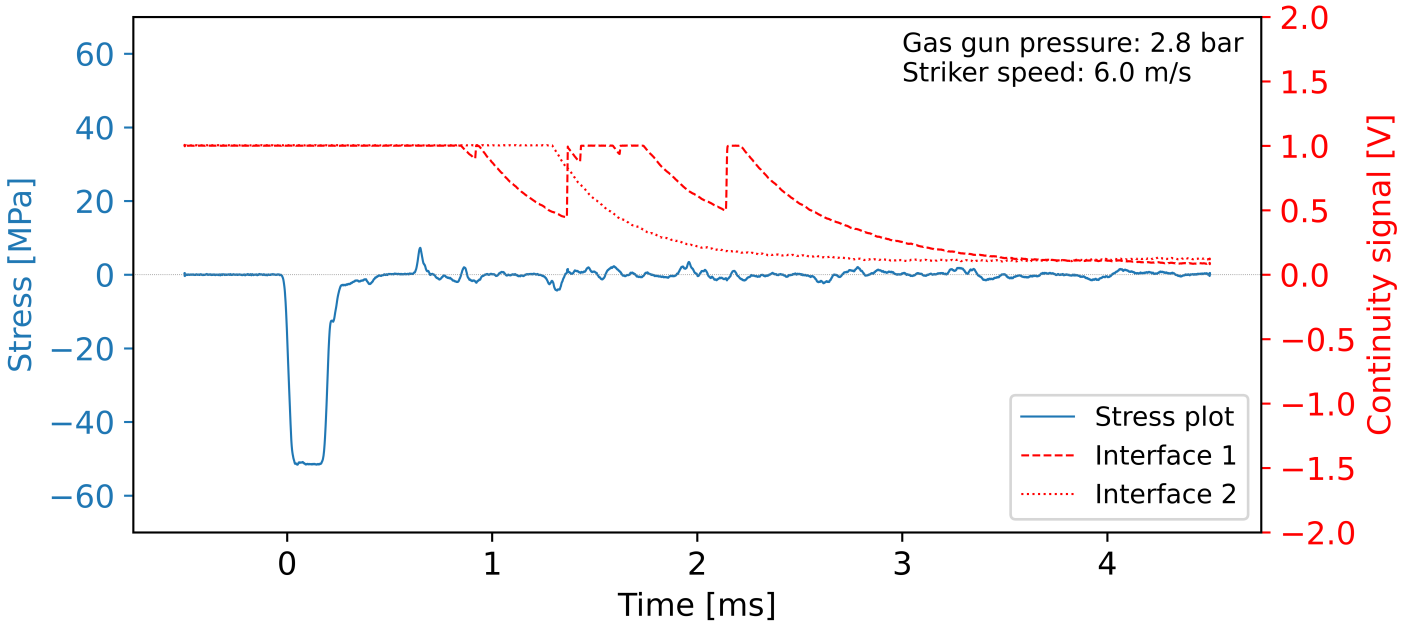

(a) Response to phase 1

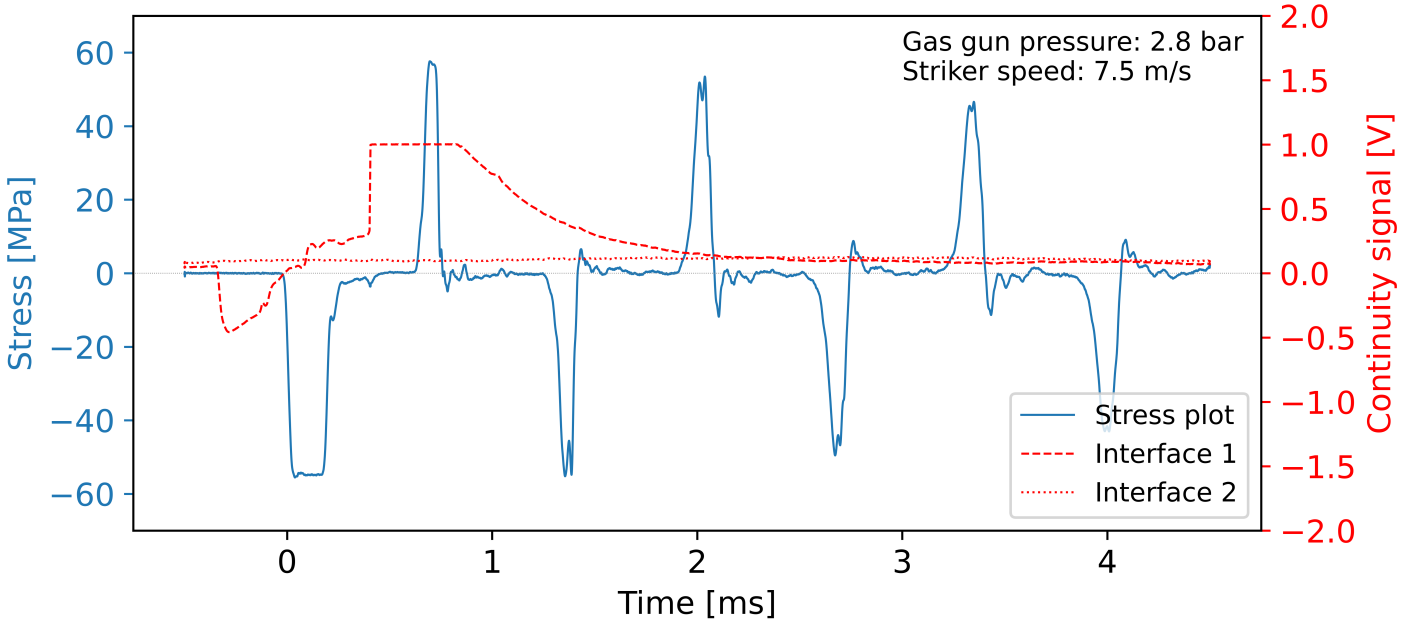

(b) Response to phase 2

Figure 5.7 Results of the initial two-phase tandem verification tests

In Figure 5.7a, it is apparent that interface 1 lost contact in phase 1, while interface 2 separated as intended. In Figure 5.7b, interface 1 was brought back into contact briefly, before finally separating again. There was a notable portion of the stress wave left oscillating in the input bar after that. This data infers that after phase 1, there was a small gap left in between the bars at interface 1, where there should be contact. This was confirmed by measuring a gap of approximately 0.5 mm, using feeler gauges. As a result of that gap, the stress wave in phase 2 could reflect at that interface up until the instant that the gap was closed and contact was made. The portion of the wave that makes it through the traps is capable of significantly reloading a specimen in a tensile test, so this issue needed attention, to ensure that interface 1 remained in contact after phase 1.

The simplest way of keeping contact was to add a small drop of grease between the bars of interface 1, allowing the bars to slightly adhere. The very small adhesion force of the grease could hold interface 1 together in phase 1, when there is not a significant force separating it. The force is small because the secondary trap will have isolated the majority of the stress wave before interface 1 might want to separate. The small adhesive strength of the grease would allow easy separation in phase 2, when the forces are far larger. Vaseline, RB2 grease, red rubber grease, and a tin foil strip were all tested on interface 1 and their results compared. The greases were applied by adding a lentil sized blob onto the end of the input bar. Too little grease may result in inadequate coverage of the bar faces, while too much grease creates unnecessary mess, and places other components at risk of getting contaminated with grease. A wringing action, while pressing the bars together was used, and was stopped once continuity was restored across interface 1. The RB2 grease performed the best, and the most reliably. The results are displayed in Figure 5.8, and the plots for the other tested media may be found in Appendix H.

Figure 5.8a shows that having applied RB2 grease, interface 1 was able to remain in contact after phase 1. The bars are moving relative to one another, shown by the 'drops' along the interface 1 plot, but as seen at the start of Figure 5.8b, the bars come to rest in contact once phase 1 is complete. There was no physical gap, as electrical continuity was present. Interface 2 broke contact when expected, and remained isolated from then on. Since interface 1 was in contact for phase 2, the stress wave was trapped in near ideal fashion. This demonstrated that the traps were sufficiently impedance matched to each other and the input bar, for the traps to function as designed. From this point forward, RB2 grease was applied to interface 1 for every test.

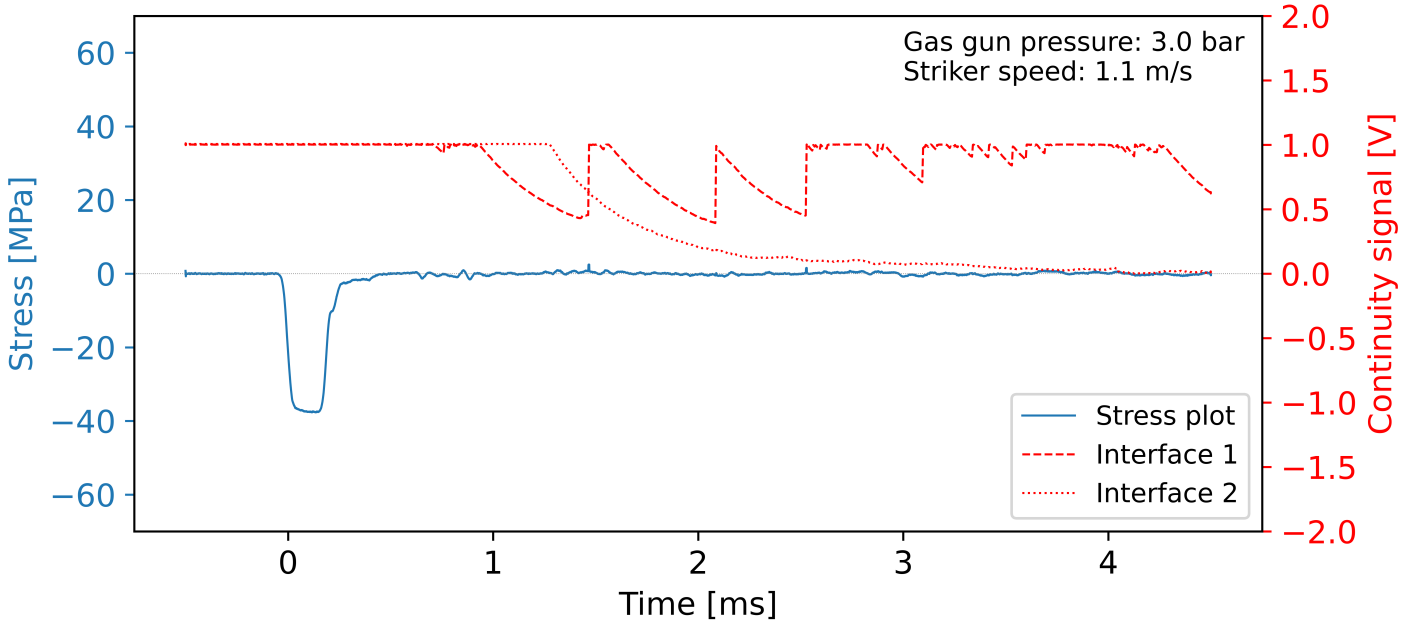

(a) Response to phase 1

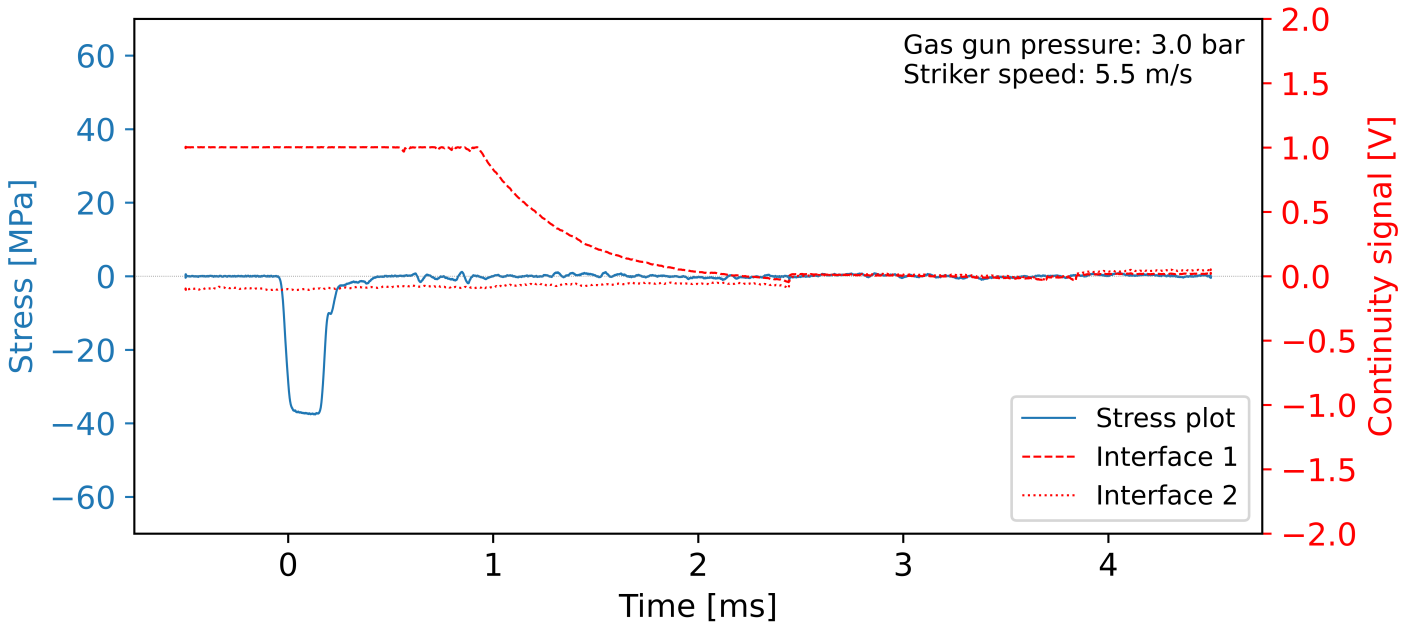

(b) Response to phase 2

Figure 5.8 Results of two-phase tandem verification tests, using RB2 grease on interface 1

5.2.2 One-phase Verification Tests

The next step was to test whether the two phases mentioned in Section 5.2.1 occur as ideally when running them in a single test. During the operation of the TSHB, both phases will happen in quick succession during a test, so it must be verified that it can work in this arrangement too. This step was done using the tensile gas gun and the hollow pull-off striker, which was discussed in Chapter 3. Since these are the first tests run with the tensile gun and striker, they were used to verify their operation, and to fine-tune if necessary.

The bar layout illustrated in Figure 5.9.

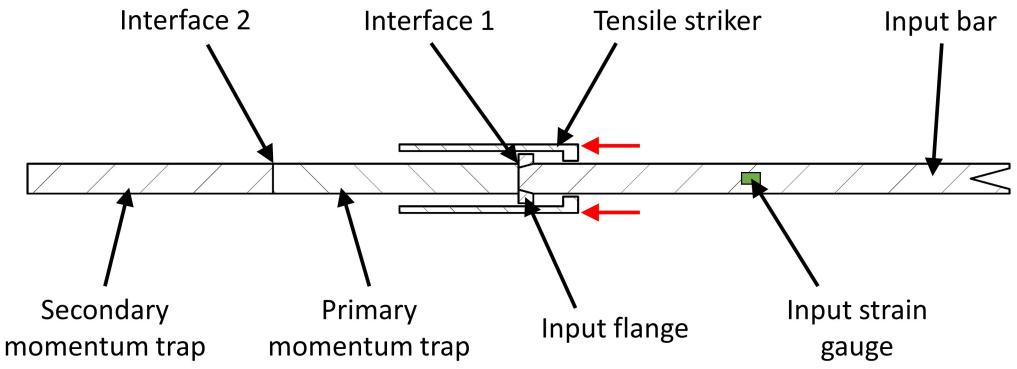

Figure 5.9 Bar layout for the one-phase tandem trap verification tests

The desired outcome was to attain a stress signal with an incident wave, followed by a reflected wave. Beyond those two features the input strain gauges should read as quiet a signal as possible. The results of the initial tests are shown in Figure 5.10.

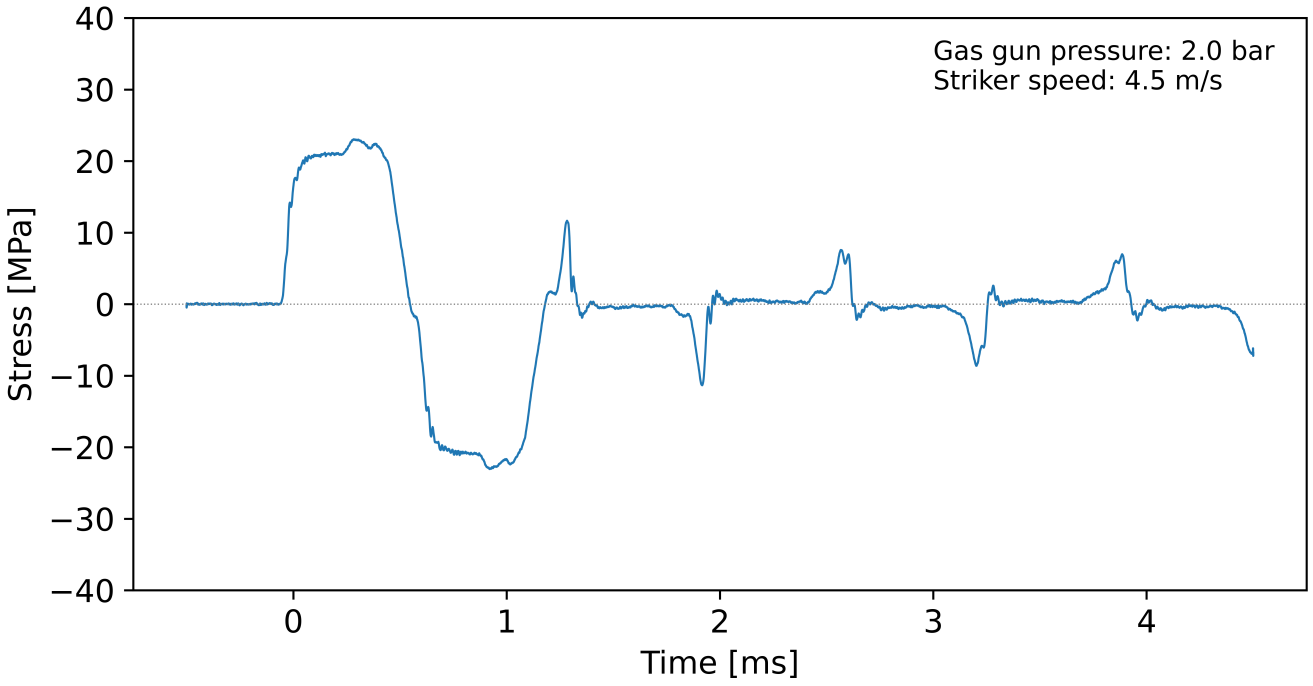

Figure 5.10 Results of the initial one-phase tandem verification test

While this plot displays largely successful momentum trapping, there were apparent issues that required attention:

- There was no separation between the incident and reflected waves. Ideally, this signal should read zero for a short period between these waves. In this plot it is unclear whether there was superposition occurring at the input strain gauges, and if so, it is unclear by how much they were superimposing. The cause was that the incident stress pulse was too long. In Section 3.2, it was calculated that a striker length of 1200 mm should have been short enough to avoid superposition, but the experimental results showed otherwise. The unexpected length of the input pulse was likely due to compliance of the striker flange and input flange. This compliance led to the wave having longer rise and fall times.
- There was a portion of the reflected wave that did not get trapped, and continued to oscillate in the input bar. This is illustrated by the small spikes in the signal beyond the two desired waves. Possible causes for this include misalignment at the interfaces, and again, the pulse being too long. No matter how well the tandem traps work, they are only capable of capturing a finite length of pulse.
- The input wave had two small peaks near the end of its plateau. This was be explained by the masses of the two POM pressure collars on the striker.

The first task was to address the length of the pulse, and to achieve a degree of separation between the incident and reflected waves. Since the compliance of the Ti-6Al-4V flanges can only be changed via a complete redesign of those parts, the simplest way to correct the length of the pulse was to shorten the striker slightly. It was also noted that the incident wave was smooth enough in shape, and therefore no additional pulse shaping is necessary.

The 1200 mm long striker tube was trimmed down to 1100 mm length. The POM collars were lightened by cutting a groove of semicircular cross section into both faces of each collar. Tests were run again and a typical result is shown in 5.11.

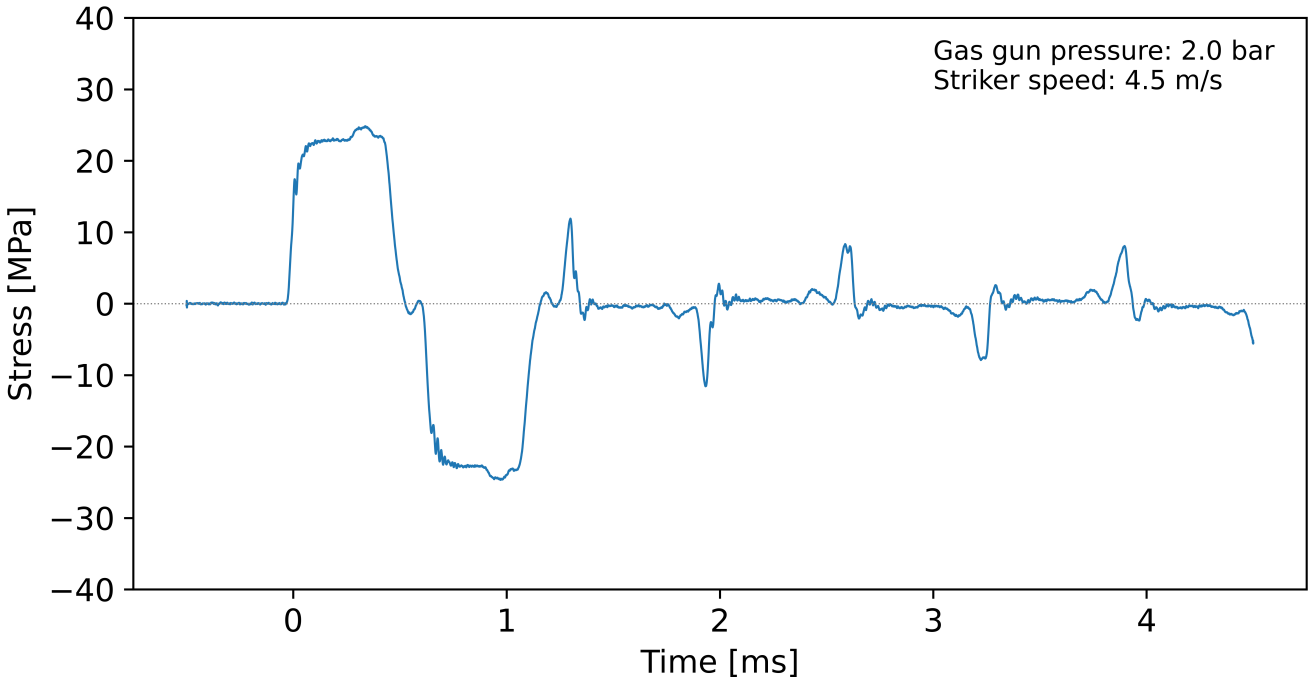

Figure 5.11 Results of a follow-up test, using a 1100 mm long striker

At the 1100 mm striker length, the incident and reflected waves now appear to be separate, but the gauges still do not settle to a zero stress state for any amount of time in between. Although less than before, there is still evidence of the masses of the pressure collars in the shape of the incident wave. The striker length was further reduced, this time to 1000 mm, and more material was removed from the pressure collars. The round grooves in the collars' faces were machined to square grooves, to take away as much mass as possible without compromising the strength of the collar. Tests were run again, and a typical result is shown in Figure 5.12.

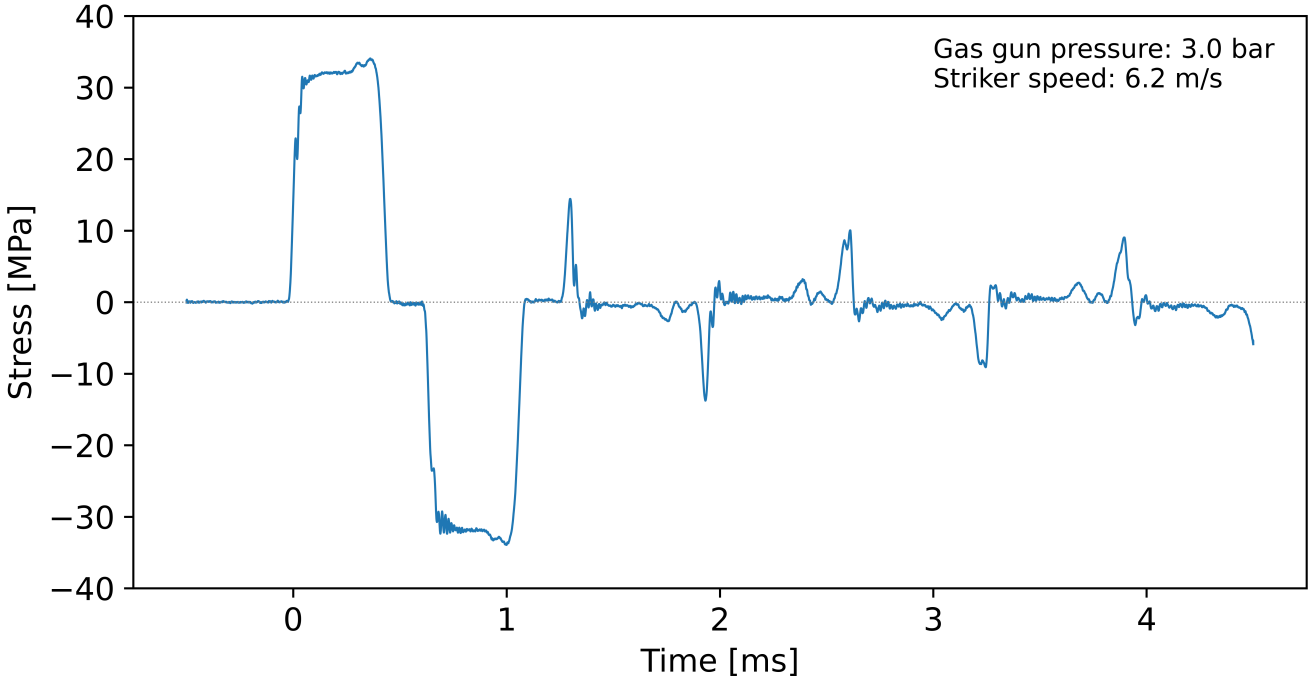

Figure 5.12 Results of a follow-up test, using a 1000 mm long striker

There is now a clear period of zero stress occurring between the two waves, and it was concluded that the striker length was optimal. The incident wave still contains slight peaks near the end of its plateau, but the collars' masses cannot be reduced more without a complete redesign of the part. The collars were deemed as adequate for use moving forward in this project. The remaining spikes towards the end of the signal are undesirable, but will translate to a negligible amount of strain on the specimen compared to what the incident wave will provide. The remaining noise on the signal is purely a result of imperfect contact between bars. The performance of the tandem traps in this configuration was considered adequate to meet the requirements for this project.

5.3 Impedance Matching the Output-side Trap

Lastly, the hollow momentum trap, used to capture the transmitted wave, must be matched to the output bar. This task was done using the tensile gun, with all the bars in final position. The layout of all bars and traps is identical to that of the final testing setup. This is displayed in Figure 3.2 in Section 3.2.

Similarly to how impedance was matched for the input-side traps, a pulse was passed across the interface between the output bar and the output trap tube. The trap's performance was assessed based on how much of the transmitted pulse is reflected off of that

interface. Notched specimens were used for these tests to lower the elongation to fracture. This was done in order to test the output side trapping in isolation. If the specimen remained intact, and the input side traps didn't function as expected, this would result in further loading of the output bar, which could obscure the output trap performance. A stress-time plot for an initial test, with the tube at its stock OD of 30 mm, is shown in Figure 5.13. There are four plots present on these axes, three of them showing the incident, reflected, and transmitted wave. The fourth is the most important for this test, as it is the portion of the transmitted wave that is reflected off of the output bar-trap interface. This was the wave that needs to be minimised in magnitude in order to match the trap to the output bar. In Figure 5.13, all four waves have been shifted to the specimen interface. The magenta lines illustrate the bounds of the waves.

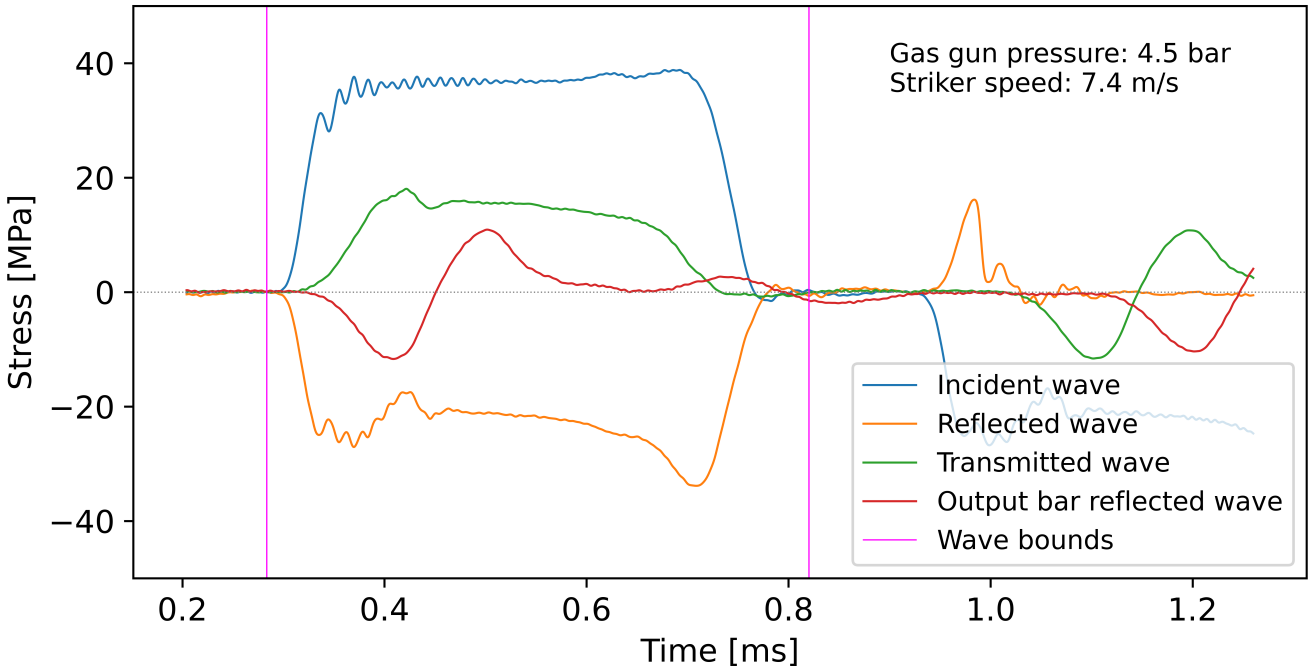

Figure 5.13 Results of an initial output trap test, with all waves shifted to the specimen

Looking at the waves on the green and red plots on Figure 5.13, we ideally want to be able to compare their magnitudes. These two waves, however, have highly dissimilar shapes. The most prominent difference is that the red reflected pulse has a large transient between 0.3 ms and 0.6 ms. This transient portion of the wave shows that some reflection was occurring as the leading edge of the transmitted wave reached the interface. The magnitude of this reflection decreases as the main portion of the wave passes. Since there is a transfer flange here this transient can be expected, simply because of the added mass.

This could also indicates incomplete contact at the interface, that only resolves the further it is loaded.

The mass of the output flange has already been designed to be as lightweight as possible, and that is not easily improved upon. Contrarily, the contact between the flange and the trap tube could be improved without substantial redesign. This interface is broken up into three steps, evident in Figures 3.15 and 3.18 in Chapter 3. Within machining tolerances, it is exceptionally unlikely that all three vertical faces are in contact with the corresponding faces of the hollow output trap. If one step is the slightest bit higher or lower on the flange or tube, the others will not be in contact when the parts are brought together. There may be miniscule air gaps that were allowing potions of the transmitted wave to reflect.

To investigate the contact, engineer's blue was used. The blue was applied to the surfaces of the flange that make contact with the trap tube. It was then screwed onto the output bar and the trap was slid into place as it would be while testing. The flange and trap were wrung together, allowing for the blue to transfer onto the trap where contact was being made. The assembly was then carefully taken apart and the trap tube was inspected.

(a) The output flange with engineer's blue applied

(b) End view of the blue present on the output trap

Figure 5.14 Assessing contact of the parts using engineer's blue

The results in Figure 5.14b confirmed suspicions. Blue was only present on the outer step of the trap, with nearly none present on the other two steps. Therefore only the outer face actually touched the flange. It can also be seen that the blue was not evenly spread around the whole circumference of the outer step. This implies that the flange was not perfectly coaxial with the trap when screwed onto the output bar.

In order to correct the above-mentioned issues, more relief was machined into the internal corners on both parts, and the chamfers on the external corners were enlarged slightly. It was decided that a lapping process would be used to finely shape the parts to one another. It would involve relative rotation between the parts with the presence of an abrasive paste between them. This was achieved by placing the flange on the floor, within the flange tool to ensure it does not rotate. The trap was then placed on top of it vertically, and rotated by hand. Once satisfied, the parts were cleaned and checked with the blue again. The results are shown in Figure 5.15.

(a) End view of the output trap **(b)** Angled view of the output trap

Figure 5.15 Assessing contact of the parts using engineer's blue, after lapping by hand

In Figure 5.15 an improvement can be seen, in that there is blue present on all three steps. Further tests were then run to see how this had affected the performance of the output momentum trapping.

The results from one of these tests are plotted in Figure 5.16, and the magnitude of the transient on the output bar reflected wave has visually decreased. It was noted at this point that although the three steps make contact, the faces were not flat. When fitting the flange to the tube without the output bar present, the flange rocked slightly within the tube. Since the blue was distributed well on each step on the trap in Figure 5.15a, the flange most likely contained the high and low spots responsible for the rocking. The unconstrained nature of the hand lapping meant that coaxiality of the two parts during lapping may have been off, resulting in uneven pressure on the steps on the flange. While turning the trap by hand, the trap may have been moving about a little, and not staying perfectly vertical. This provided opportunity for further improvement of the the performance of the output momentum trapping.

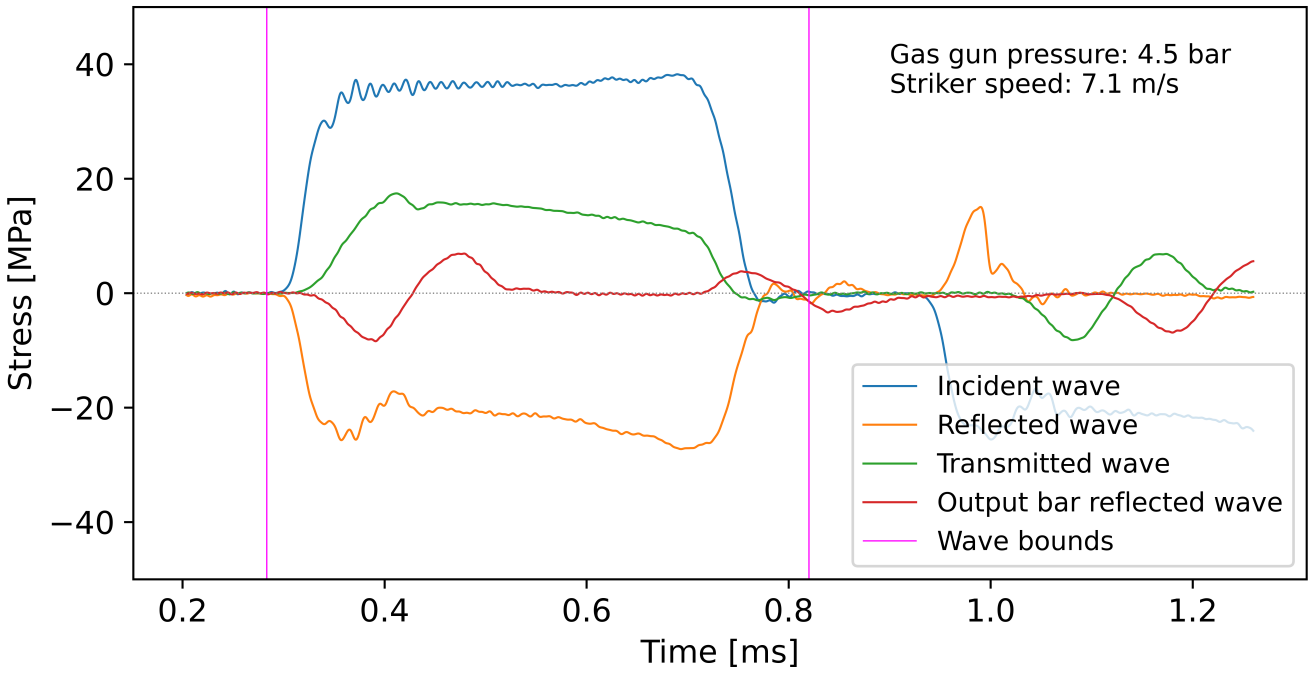

Figure 5.16 Results from a follow-up test, after lapping by hand

The best option was to lap the parts again, this time making an effort to limit the motion of the trap tube to rotation about its centre line. Using a lathe would mean that the chuck could securely hold the trap tube, and also could provide the rotational motion needed for the lapping process. A jig, seen in Figure 5.17a, was used to hold the flange stationary while the tube rotates. The jig incorporates a hole in its end so that a live centre in the lathe's tailstock could hold alignment and apply some axial force while lapping. The flange tool was used to constrain the rotational motion of the flange. This lathe setup is shown in Figure 5.17b.

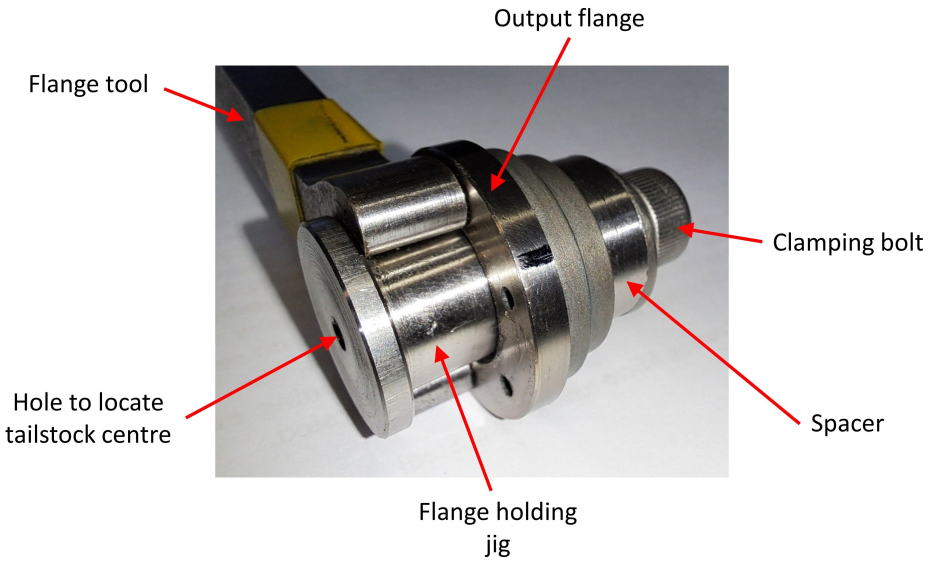

(a) The jig made to hold the output flange

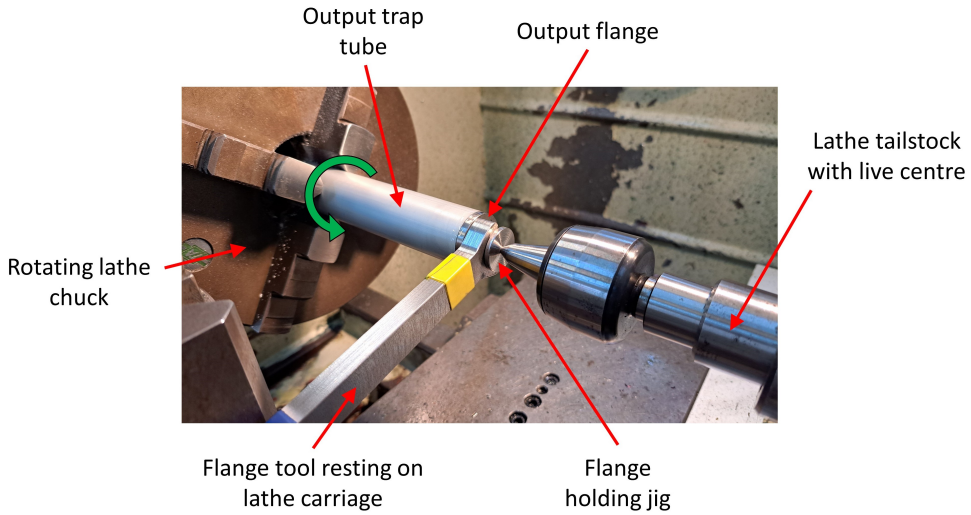

(b) The jig and parts set up in the lathe

Figure 5.17 Arrangement used to lap the parts together in a lathe

After lapping using this method, the contact between the flange and trap was checked again using engineer's blue. This time, the blue was applied to the trap tube, as the results are easier to observe on the external feature of the flange. The result is displayed in Figure 5.18.

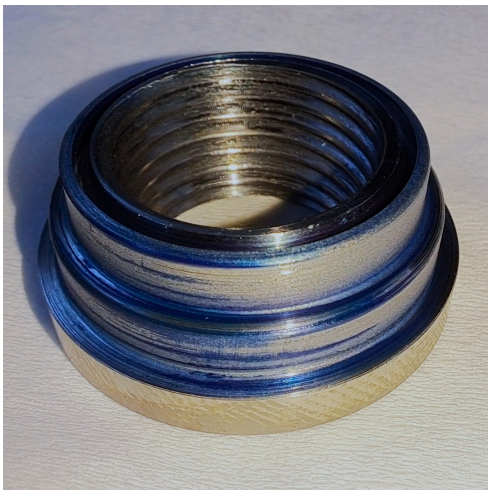

Figure 5.18 Assessing contact of the parts using engineer's blue, after lapping using the flange holding jig

Again we see that the blue is evenly distributed around the circumference of all three steps. Figure 5.19 shows a set of results from the next round of tests.

It was surprising to note that the reflected transient on the output bar had increased slightly, both in magnitude and in duration. Neither of these are desirable as they both lead to the specimen experiencing more strain as result of the output reflection. This method of lapping proved unsuccessful. When the flange is lapped in the setup shown in Figure 5.17, both parts are sitting together in a position that may not be the same position that they sit in when the output bar is present.

This was remedied by lapping one last time, again in the lathe, and using the output bar itself to hold the output flange stationary. All bushings between the output bar and output trap were in place to replicate the experimental setup exactly. Again, the lathe was used to rotate the output trap, and the flange was tightly screwed onto the output bar. The end of the output bar that protrudes from the other end of the lathe spindle was held from rotating using a pair of vice grips, as shown in Figure 5.20b. Axial force was applied to the lapping interface by pulling on the output bar via the vice grips.

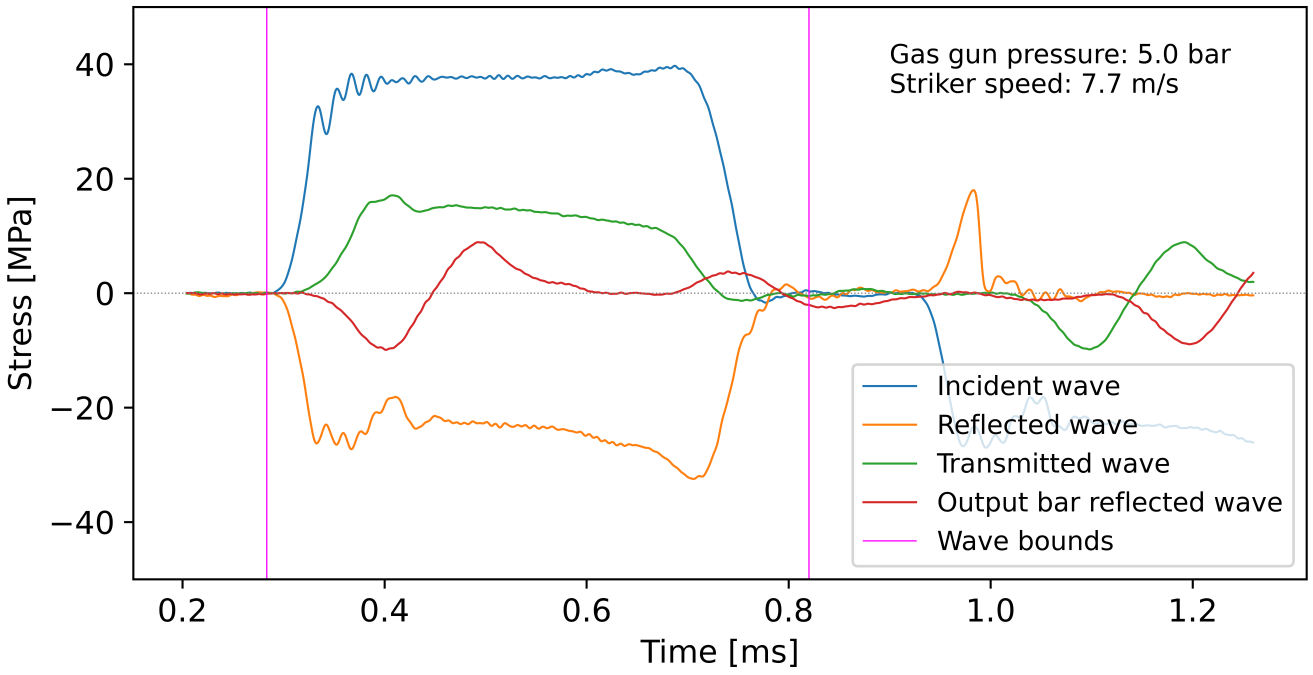

Figure 5.19 Results from a follow-up test, after lapping using the flange holding jig

Having thoroughly lapped the parts using this improved arrangement in the lathe, the contact was checked once again using the blue. Figure 5.21 exhibits that contact continues to occur across the whole surface of each step on the flange.

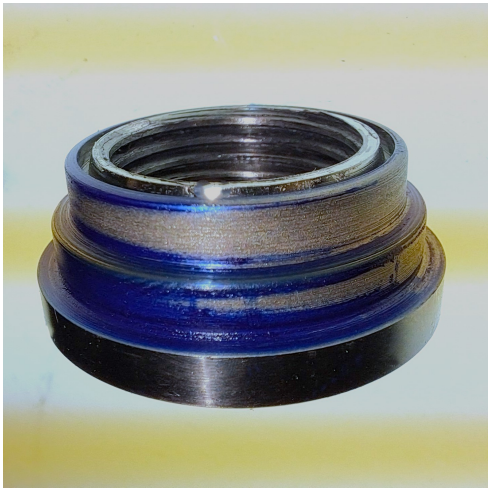

Figure 5.21 Assessing contact of the parts using engineer's blue, after lapping using improved lathe setup

Another round of testing was conducted after lapping the flange and trap together with the output bar in place. Figure 5.22 shows the significant reduction in amplitude of the reflected transient observed on the output bar. It has also decreased in duration. As the transient recorded here was the least prominent compared to all previous test, by a large margin, the lapping process was concluded here. The interface between the output flange and the output had sufficient contact to smoothly transfer a stress wave across it.

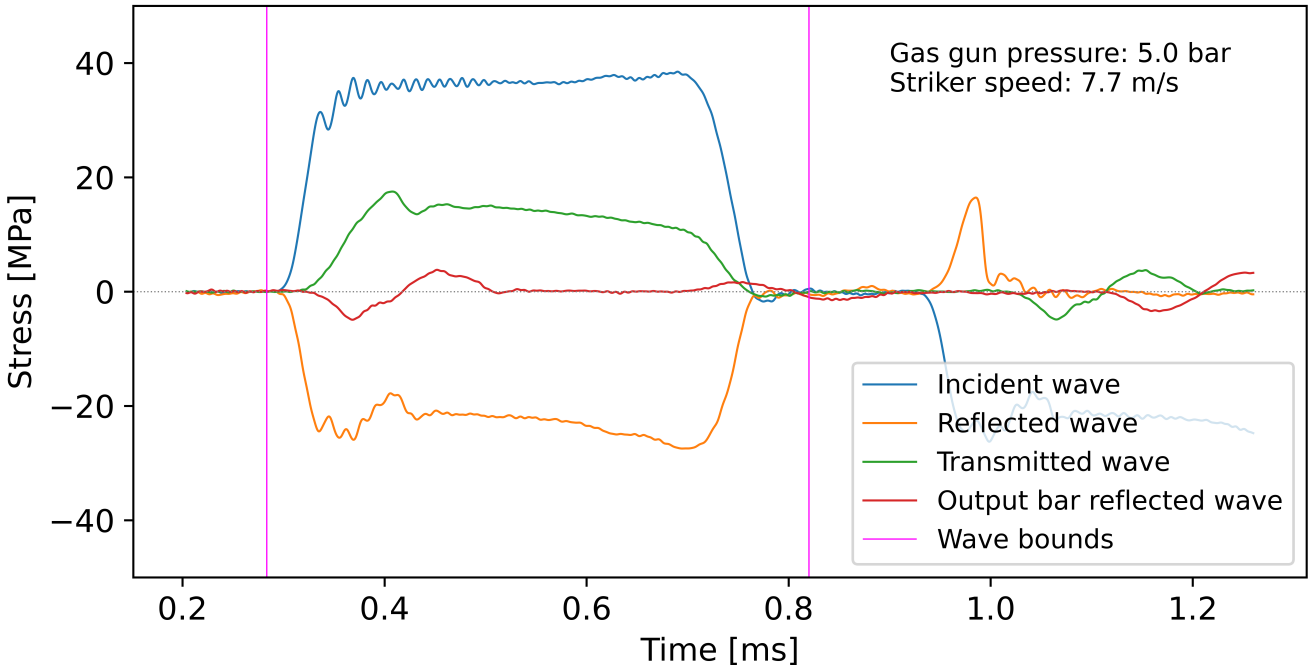

Figure 5.22 Results from a follow-up test, after lapping using improved lathe setup

In Figure 5.22 it can be noted that after the transient, the reflected wave on the output bar settles to a steady stress value between 0.5 ms and 0.7 ms. This steady stress is the plateau stress of the output bar reflected wave, which is the value that must be minimised in order to match the impedance of the output trap to that of the output bar. The stress value here is deemed to be negligible as it barely deviates from zero. Any small stress that does occur as a reflection from the output bar end is insignificant compared to the magnitude of the input wave, and is not capable of significantly further stretching a tensile specimen. This means that the output-side trap has an impedance that is already well matched to the output bar, and no further reduction to its diameter was required.

5.4 Closing Remarks

All subsystems of this apparatus had now undergone the necessary fine-tuning and verification. All momentum traps were adequately impedance matched, and an operating procedure had been developed. The momentum trapped TSHB was ready for tensile testing of specimens.

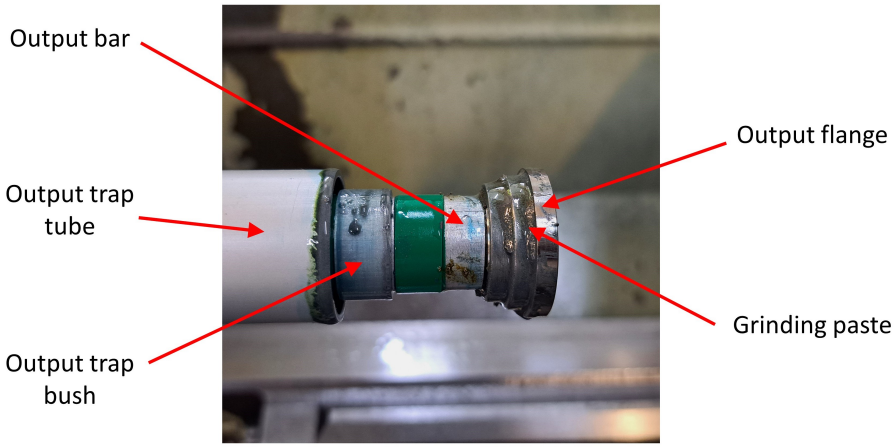

(a) The flange end of the setup

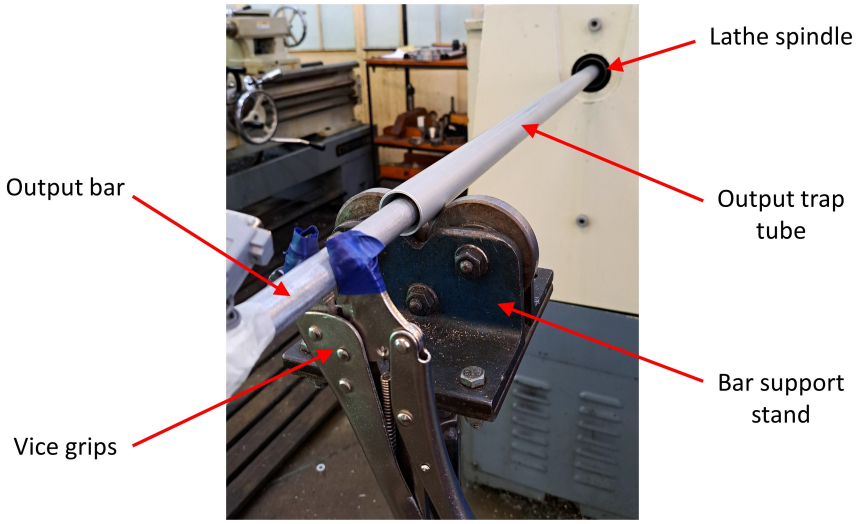

(b) The non-flange end of the setup

Figure 5.20 The improved arrangement used to lap the parts together in the lathe

Chapter 6

High Strain Rate Tensile Tests

Chapters 3, 4 and 5 have described the process of developing an SHB capable of interruptible tensile tests in the HSR region. The following chapter is dedicated to proving that this apparatus meets the functional requirements outlined in Section 3.1.1. This is broken down as follows:

1. **Verification of HSR Tensile Testing Ability**
   • Proving that the apparatus is capable of producing useful data for material characterisation, as per Requirement RQ4.
   • Proving that the apparatus is capable of conducting routine testing, as per Requirement RQ8.
   • Proving that the resetting process of the apparatus between tests is simple and requires little to no "operator's feel", as per Requirement RQ11.

2. **Verification of interruptible testing ability**
   • Proving that the striker can be fired at adequate speeds, as per Requirement RQ1.
   • Proving that the apparatus is capable of subjecting a specimen to the required strain rate, as per Requirement RQ2.
   • Proving that the apparatus is capable of straining a specimen to the point of fracture, as per Requirement RQ3.
   • Proving that test specimens do not strain further than what is expected from the prescribed loading, using full momentum trapping on both bars, as per Requirement RQ5.

3. **Verification of the momentum trap function**
   • Further proving the effect of the momentum trapping, by comparing interrupted tests (using momentum trapping) to uninterrupted tests (with no momentum trapping).

6.1 General Testing Procedure

All experiments in this chapter were conducted under the following conditions:

- No pulse shaping techniques were used.
- Striker speed v_0 was recorded for each test.
- Linear alignment of the bars, traps, flanges and striker was achieved using the method described in Appendix A, and was not tampered with between tests.
- Angular alignment of the bars, traps, flanges and striker was consistent across all tests, and was ensured by index markings.
- The interface between the input bar and the primary momentum trap was cleaned and re-greased for each interrupted test.
- The interface between the input bar and the primary momentum trap was cleaned for each uninterrupted test .
- All time shifts of waves include a correction for dispersion effects. This was done using the existing code by Van Lerberghe and Barr [4].

6.2 Tensile Specimen Parameters

For all tests conducted in this chapter, the specimens used will take on the design of the ten lobe fir-tree, as specified in Requirement RQ6. The specimens used were cut from DOMEX 550 plate using an EDM wire cutting process, and are identical to the ones pictured in Figure 2.20 in Section 2.4.5.

The parameters of the specimens used are outlined below:

$$\begin{aligned} \text{Shoulder to shoulder distance } L_{s-s} &: 10 \text{ mm} \\ \text{Corner radius } r_c &: 1.5 \text{ mm} \\ \text{Gauge length } L_{gauge} &: 7 \text{ mm} \\ \text{Gauge thickness } t_{gauge} &: 2 \text{ mm} \\ \text{Gauge width } w_{gauge} &: 4 \text{ mm} \\ \text{Gauge area } A_{gauge} &: 8 \text{ mm}^2 \end{aligned}$$

The gauge length of the specimens is regarded as the region where the specimen sides are parallel, excluding the corner radii. All dimensions were verified prior to testing.

6.3 Verification of HSR Tensile Testing Ability

The primary function of a TSHB is to conduct HSR tensile tests on materials. This function will be the first to be proven. SHPB calculations will be outlined, along with the approach taken for processing the recorded data. Figure 6.1 exhibits the experimental setup utilised for the verification tests.

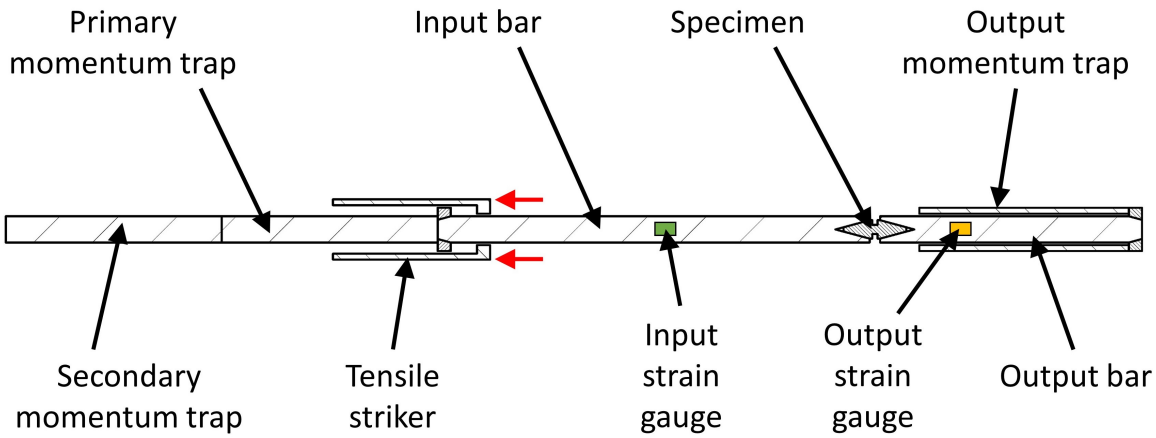

Figure 6.1 Bar layout for interrupted dynamic tensile tests

For this example, the following test parameters were used:

$$\begin{aligned} \text{Gas gun pressure } P &: 5.0 \text{ bar} \\ \text{Striker speed } v_0 &: 12.2 \text{ m/s} \\ \text{Amplifier voltage } V_{amp} &: 7.67 \text{ V} \\ \text{Bridge voltage } V_b &: 2.47 \text{ V} \end{aligned}$$

The gas gun pressure was optimised to obtain a reasonable striker speed to demonstrate the capability of this apparatus effectively. The amplifier voltage was chosen based on the power requirement of the instrumentation, and bridge voltage was chosen to maximise the resolution of the results. This was attained experimentally throughout the calibration and commissioning process. The test was run and the output voltage versus time data is recorded for the input and output channels. The raw voltage data is plotted in Figure 6.2.

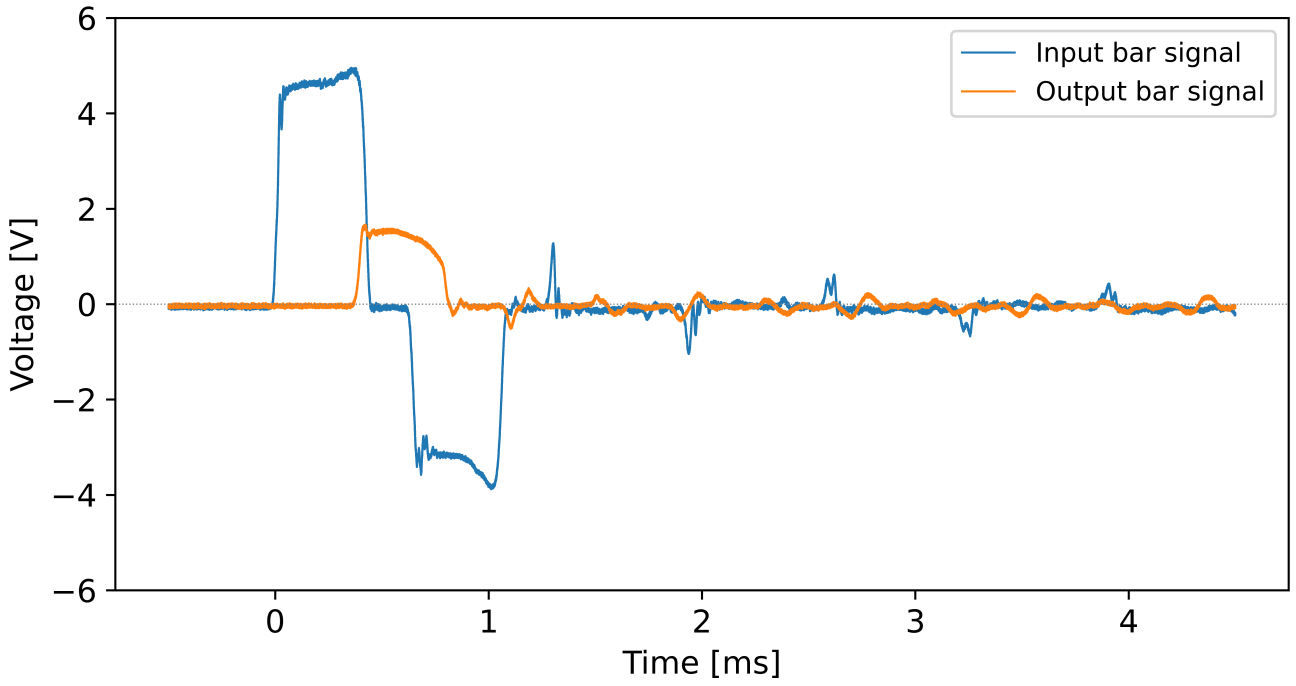

Figure 6.2 Raw output voltage signals from the test

The raw data was then smoothed, and zeroed. Smoothing refers to the reduction of noise in the signal, and was done using a moving average. In this case, the moving average used a window of 0.8 μs. Zeroing alludes to the vertical shift of the data, in order to ensure that the dead time at the start of the signal corresponds to 0 V on the plot.

The processed data is plotted in Figure 6.3.

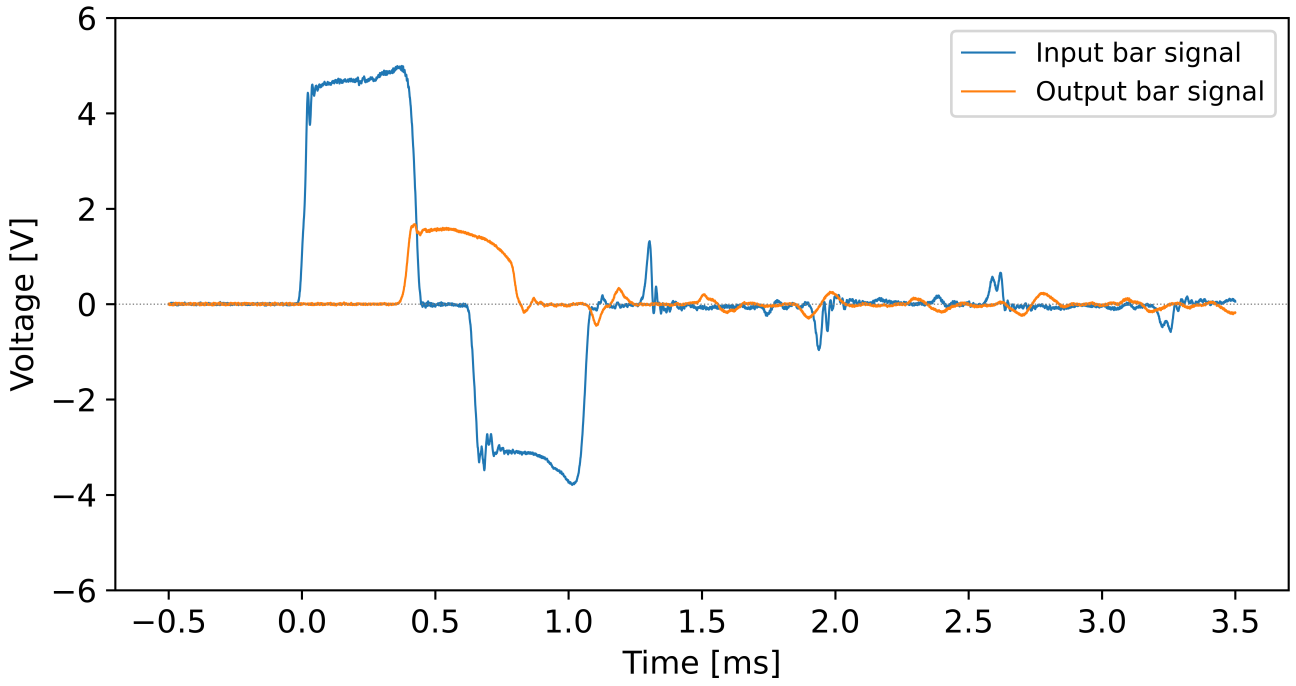

Figure 6.3 Smoothed and zeroed signals from the test

From the cleaned data it can be observed that the specimen is not experiencing significant loading subsequent to that intended from the initial pulses. The voltage signal was then converted to stress, using the calibration factor K and bridge voltage V_b. The incident, reflected, and transmitted waves were then shifted to the specimen end of their respective bars. The three shifted waves are shown below in Figure 6.4, along with the bounds of the analytical region.

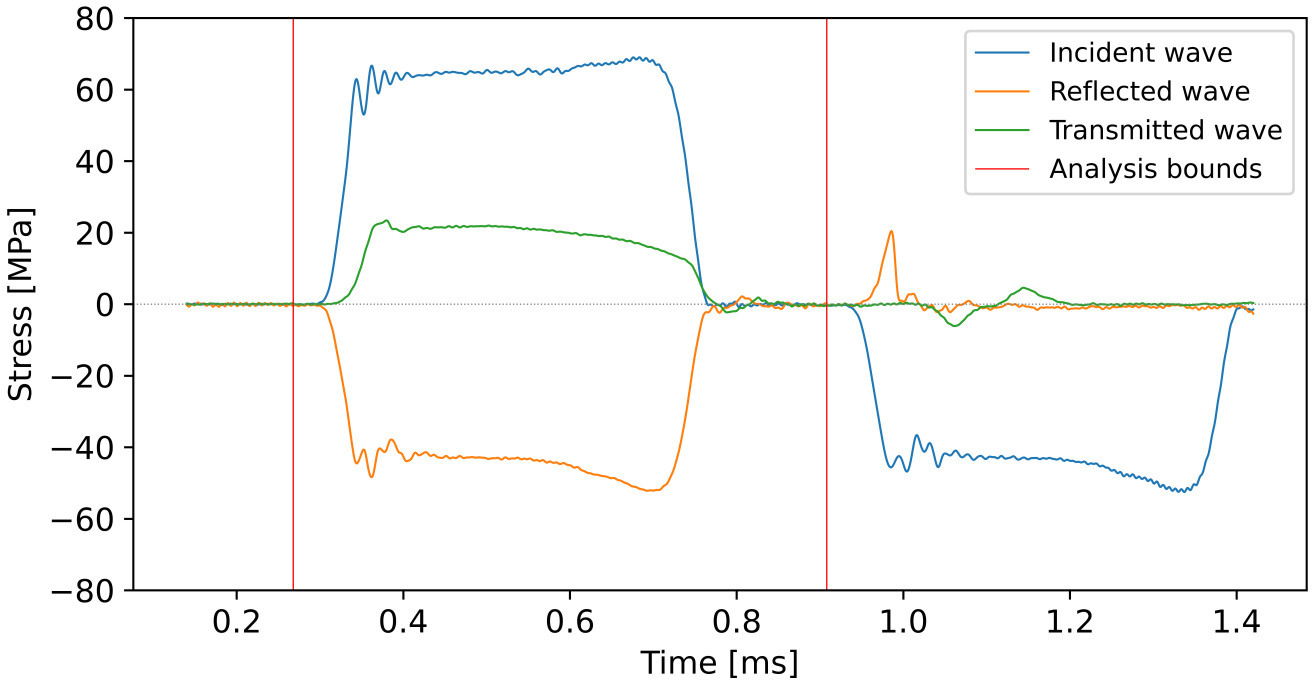

Figure 6.4 Plot of stress waves shifted to specimen end of bars, with analytical bounds shown

The analysis bounds encapsulate the stress waves, providing a start and end point for the data to be analysed. From the stress versus time data for each wave, velocity versus time data was attained for the specimen end of each bar using Equation 6.1 and 6.2:

$$v_{input} = \frac{\sigma_{Inc} - \sigma_{Ref}}{\rho_{bar} \cdot c_{bar}} \tag{6.1}$$

$$v_{output} = \frac{\sigma_{Trans}}{\rho_{bar} \cdot c_{bar}} \tag{6.2}$$

These bar end velocities are plotted in Figure 6.5:

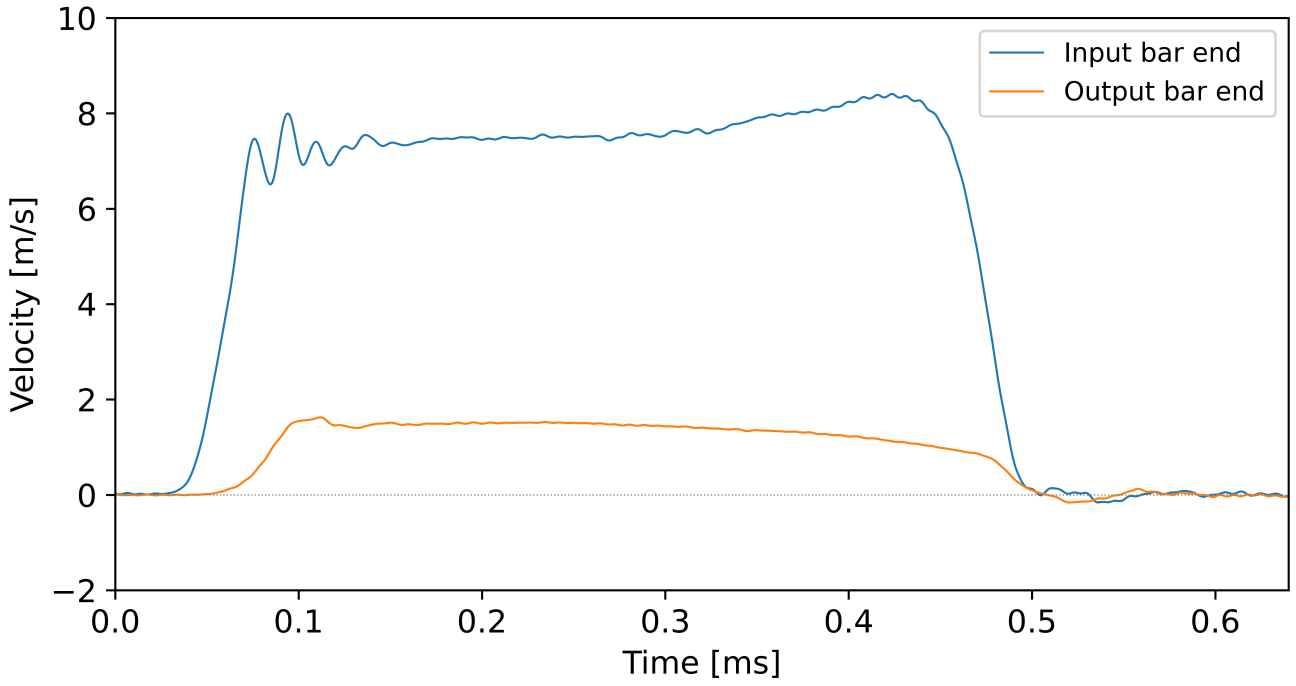

Figure 6.5 Velocity versus time plot of the specimen end of the bars

The velocity time data for the bar ends was integrated with respect to time to attain displacement versus time data for each bar end, as per Equation 6.3:

$$\delta(t) = \int_{t_{start}}^{t_{end}} v(t)\, dt \tag{6.3}$$

Figure 6.6 below illustrates the integrated results:

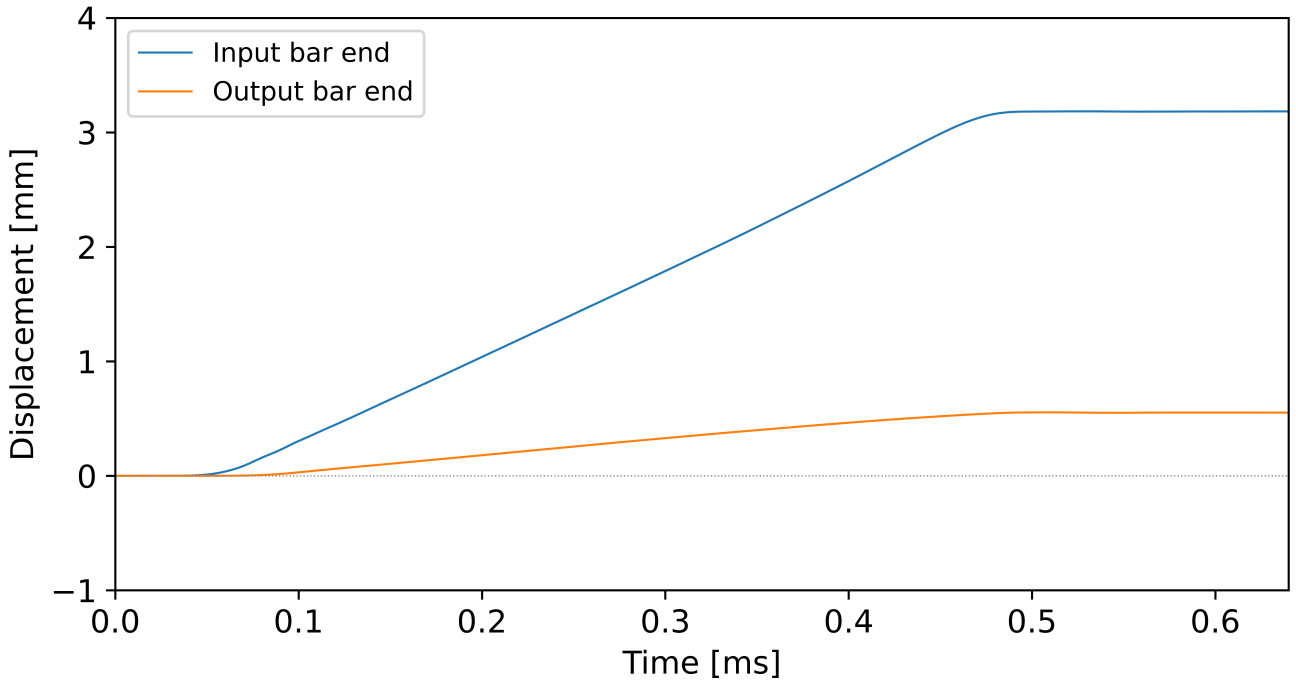

Figure 6.6 Displacement versus time plot of the specimen end of the bars

The stress versus time data at each bar end was converted to force versus time using Equations 6.4 and 6.5. These results are plotted in Figure 6.7 with the purpose of showing force equilibrium between either end of the specimen over the duration of its loading.

$$F_{input} = (\sigma_{Inc} + \sigma_{Ref}) \cdot A_{bar} \tag{6.4}$$

$$F_{output} = (\sigma_{Trans}) \cdot A_{bar} \tag{6.5}$$

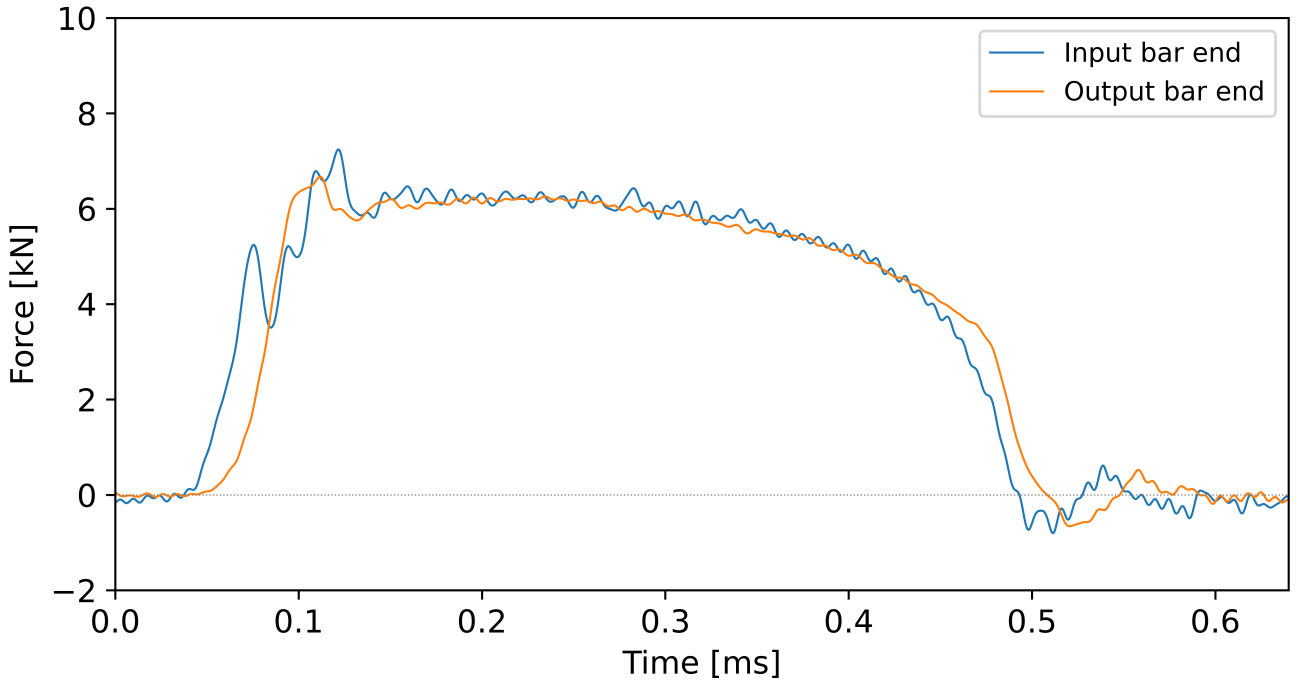

Figure 6.7 Force versus time plot of the specimen end of the bars, showing force equilibrium within the specimen as it is strained

The loading up of the output bar is observed to have a small delay relative to the input bar, which is related to the length of the specimen and the various changes in impedance between the bars, clamps and specimen. This has been observed in previous studies [84, 89, 90], and is the expected behaviour of the fir-tree specimen fixture. Other than the initial load rise, which is ¡10 % of the total loading duration, the input and output bar forces are in good agreement, indicating specimen equilibrium was achieved

The elongation of the specimen was inferred from the bar end displacements and the elongation rate was inferred from the bar end velocities. Tensile force versus elongation of the specimen is plotted in Figure 6.8:

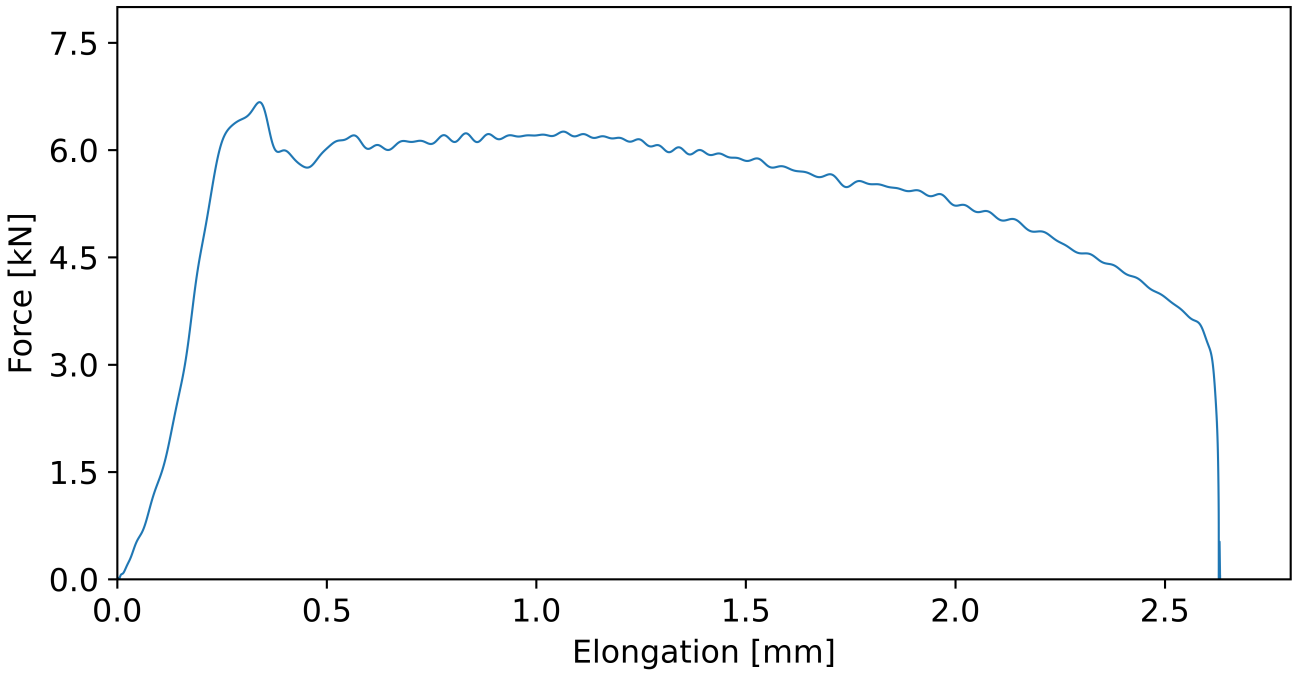

Figure 6.8 Force versus elongation plot of the specimen

Hereafter, all stress and strain refer to engineering stress and engineering strain, and are calculated using the original gauge area and length. The results of the tests are presented below in Figure 6.9, in the form of stress and strain rate, each plotted versus strain.

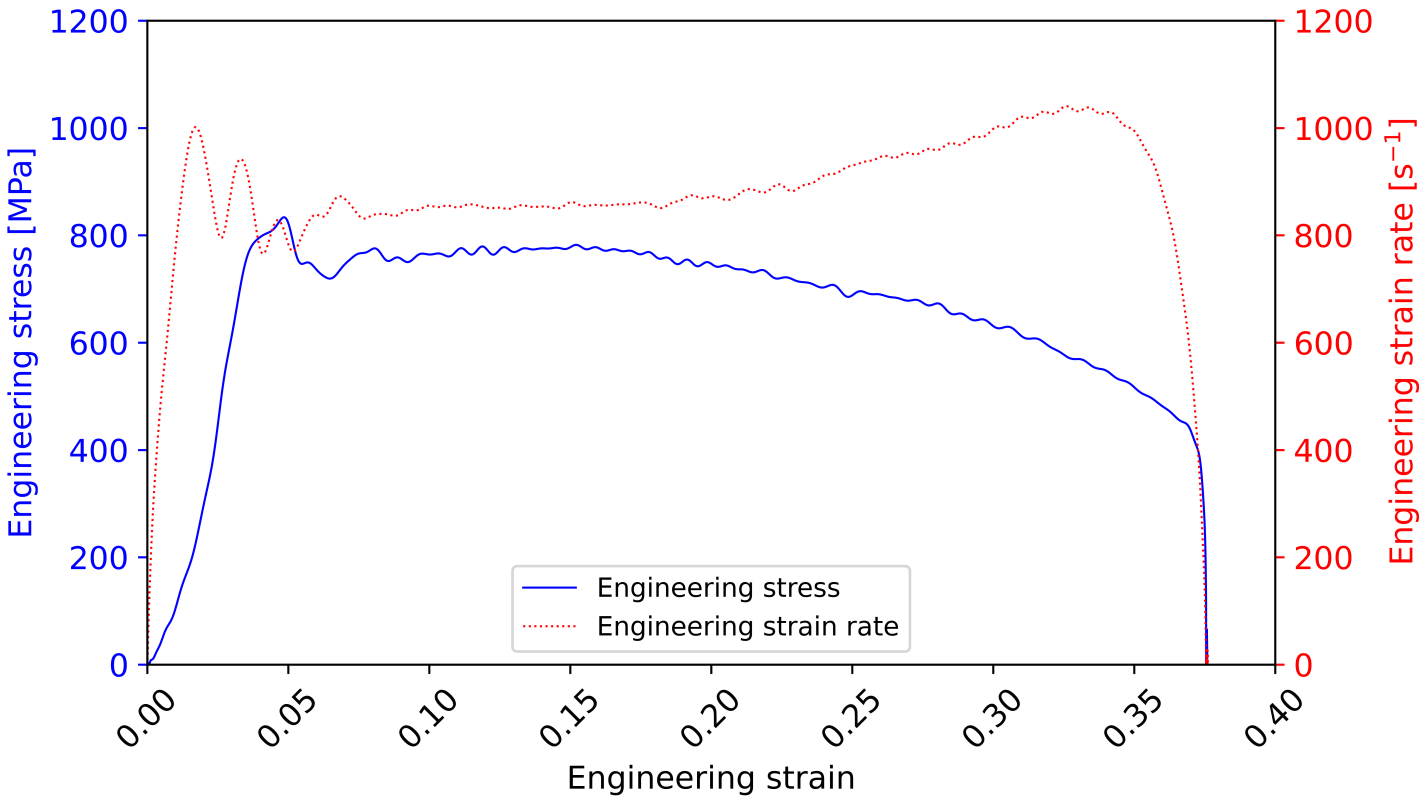

Figure 6.9 Stress and strain rate, plotted as a function of strain

Lastly, the engineering stress versus strain strain data is plotted alongside that acquired using in quasi-static testing. Figure 6.10 shows this comparison:

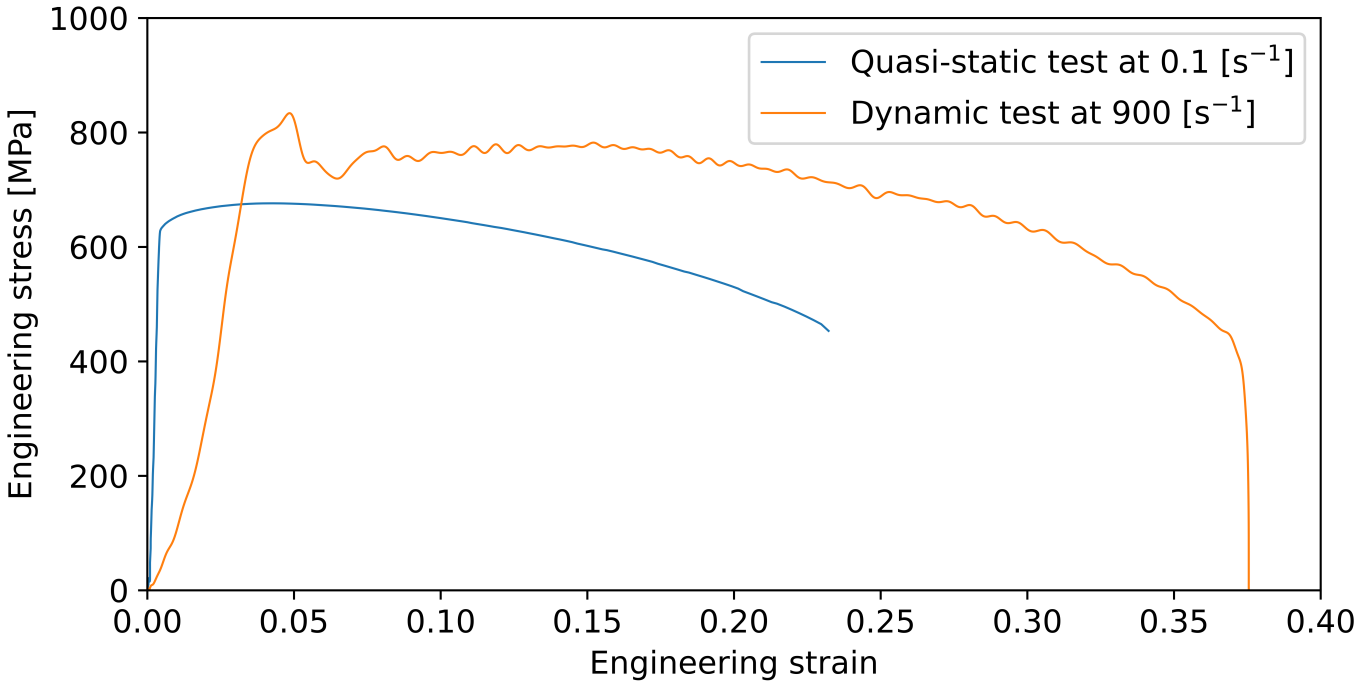

Figure 6.10 Stress versus strain plots, comparing dynamic and quasi-static results

The disparities between the quasi-static and dynamic results are explained by the following:

- The quasi-static tests made use of an optical extensometer, as explained in Section 4.4. Therefore any compliance outside the gauge length was removed from the deformation data, providing a stiffer initial response to loading.
- The plastic response in the dynamic tests is higher, which is expected from steel alloys such as DOMEX 550.

Figure 6.10 verifies that the TSHB and accompanying data processing methods are functional in producing valid stress versus strain data.

Requirement RQ4 has been met, as the TSHB apparatus shown in Figure 6.1 has proven to be capable of acquiring HSR data for purposes of material characterisation. The process of running routine tests was facile, and with practise, tests could be run every 5 minutes. The process of changing over specimens, resetting the striker and momentum traps, and greasing the end of the input bar was simple, repeatable, and required very little 'operator's feel' to do correctly. For these reasons, requirements RQ8 and RQ11 were met.

6.4 Verification of Interruptibility

The aim of this section is to prove that tested specimens, so long as they do not fracture, do not undergo further plastic deformation beyond the prescribed stress wave. A set of tests were done, ranging from purely elastic strain, to slight plastic strain, to necking and fracture. They are labelled according to their respective striker speed, with that being the only variable distinguishing the tests. The engineering stress-strain plot for a range of tests are shown in Figure 6.11. The 'x' markers denote the largest value of strain reached by each test. This corresponds to the point where elastic recovery begins.

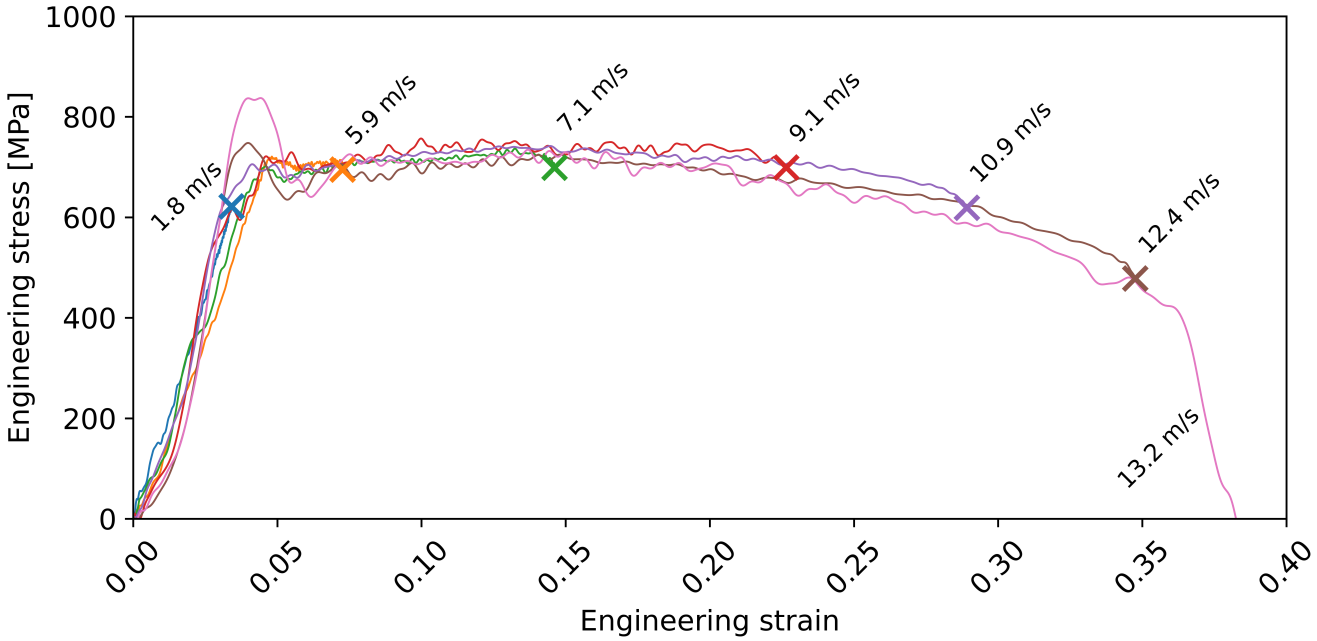

Figure 6.11 Stress versus strain plots for tests at various striker speeds

Figure 6.11 shows how the strain of the specimen varies with the striker speed. This plot also demonstrates that Requirement RQ3 on specimen strain has been met as there are tests where specimens are strained to anywhere between 0 and 0.38, including one that was strained to fracture. From 6.11 can be observed that flow stress does not vary significantly even though ultimate strain does.

Figure 6.12 shows how strain rate varies with the striker speed, for the same tests. This data alone is not enough to show that Requirement RQ2 on specimen strain rate has been met, as only 200 /s to 900 /s was achieved in this set of tests. Although this is lower than the targeted maximum strain rate of 1000 /s, it can be inferred that the TSHB is capable of meeting that requirement, given modest changes to the specimen gauge length and striker speed. This is discussed further in Section 7.2.

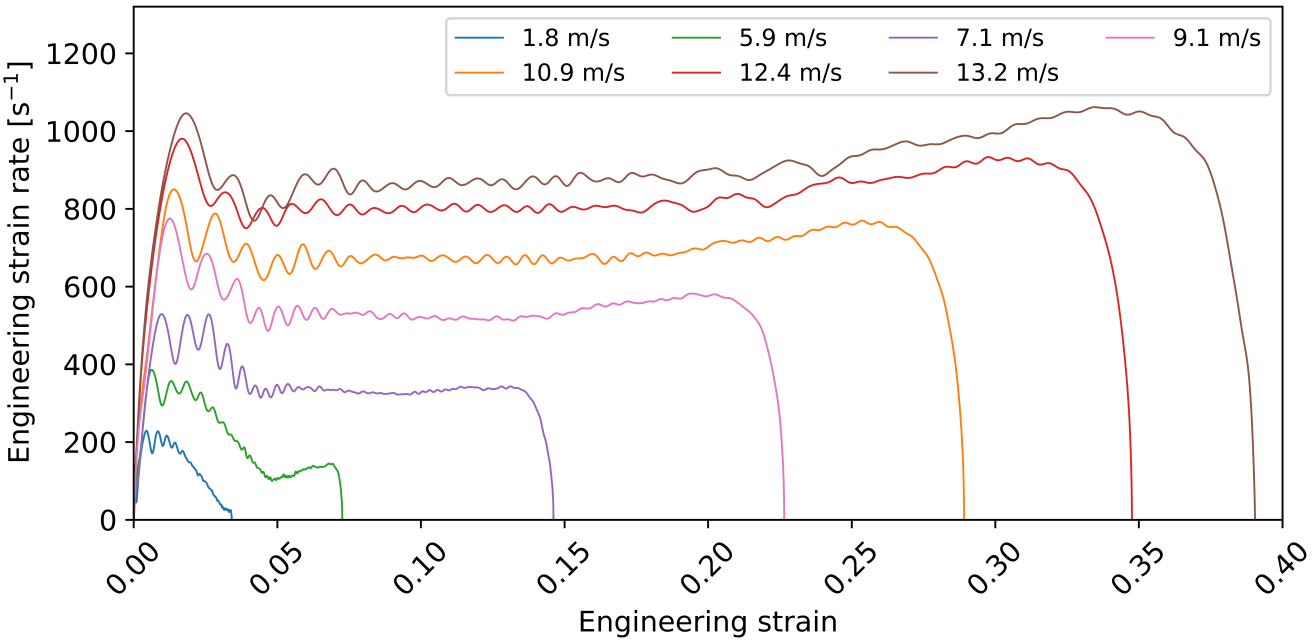

Figure 6.12 Strain rate versus strain plots for tests at various striker speeds

In order to prove that that no unintended subsequent plastic loading of the specimen occurred, the total plastic elongation of the gauge length of the specimens can be attained from the stress-strain data, and can be used to calculate what the gauge length L_{gauge} should be after testing. This can then be verified by measuring the shoulder to shoulder distance L_{s-s} on the physical specimens using a vernier caliper and subtracting two corner radii, as shown in Equation 6.6. If the values are reasonably close, it indicates that the deformation of the specimen is limited to what was captured in the data, and that all waves were adequately trapped after the prescribed loading.

$$L_{gauge,measured} = L_{s-s,measured} - 2 \cdot r_c \tag{6.6}$$

Figure 6.13 shows the stress-strain results again, this time including the elastic recovery of the specimens. The elastic recovery portion of the plots do not extend all the way back to a state of zero stress. To know the total plastic strain of each specimen, these portions of the plots were projected down to the zero stress line using a Young's modulus of 200 GPa, which is standard for most steels. This strain value was then used to calculate an expected L_{gauge} for each test.

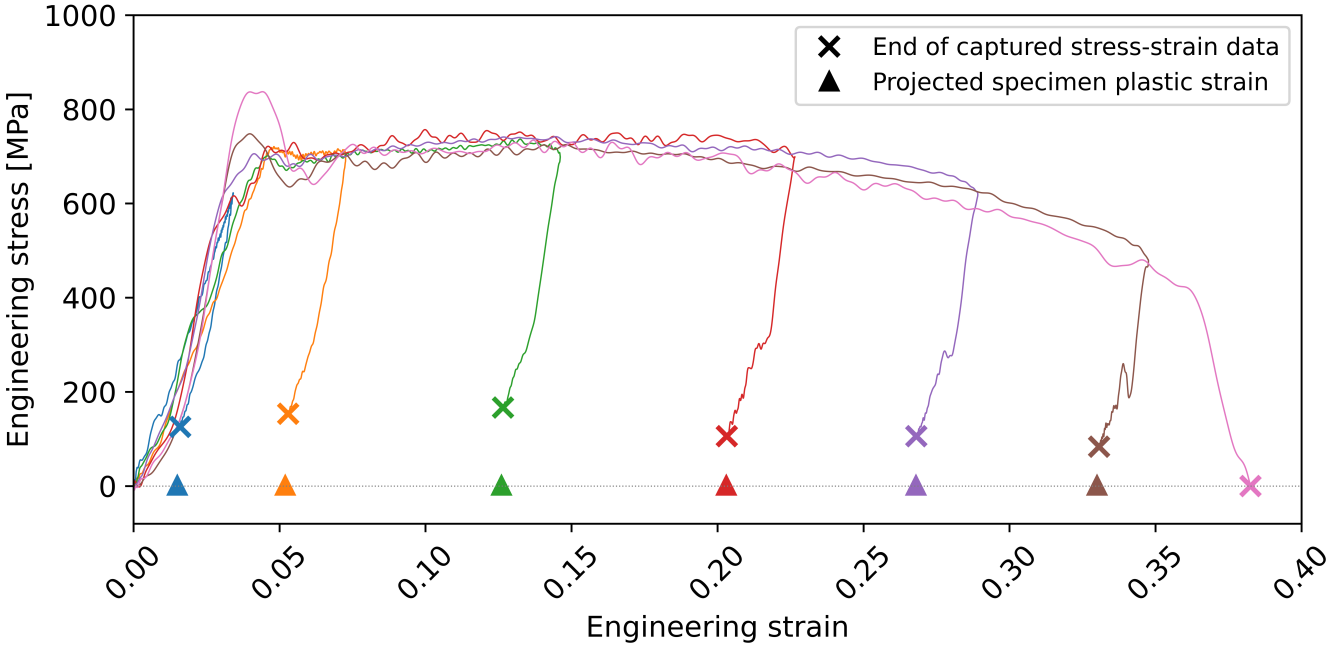

Figure 6.13 Stress versus strain plot, showing elastic recovery, and the projected total plastic strain of the specimen

The specimens from these tests are displayed below in Figure 6.14. It can be noted that, much like the stress-strain data presented in Figure 6.13, the specimens show a gradual increase in plastic strain:

Untested : Unstrained specimen

T1 : Purely elastically strained specimen

T2, T3, T4 : Uniformly strained specimens

T5 : Specimen displaying minor localised strain or necking

T6 : Specimen displaying clear localised strain or necking

T7 : Fractured specimen

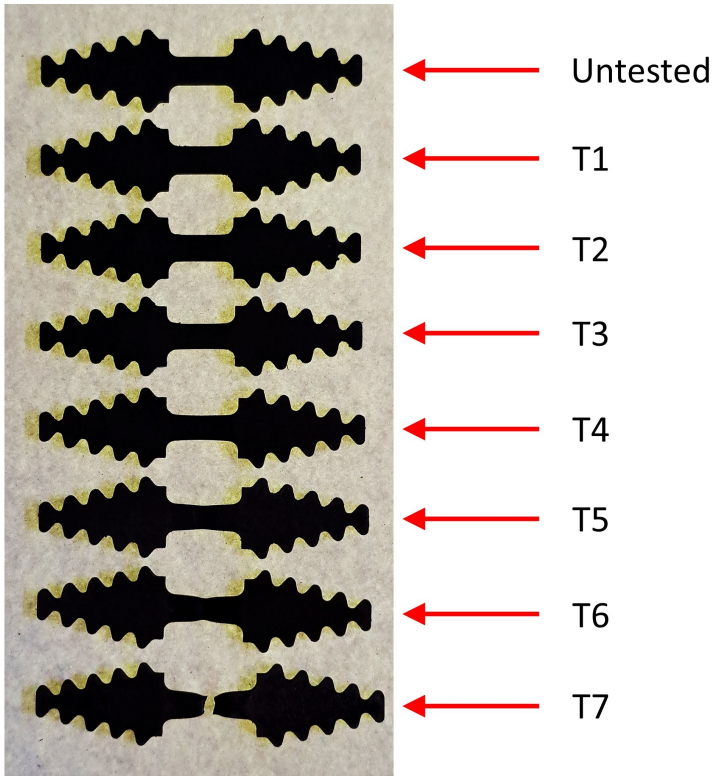

Figure 6.14 Photograph comparing the tested specimens to an untested specimen

The expected value for L_{gauge} calculated from the data, and the measured value from the specimens, are summarised in Table 6.1, along with the error for each test.

Table 6.1 *Results comparing expected to measured post-test gauge lengths*

Test	$\mathbf{v_0}$ **[m/s]**	$\mathbf{L_{gauge}}$ **[mm]**		**Error [%]**
		Expected	**Measured**	
T1	1.8	7.11	7.00	1.55
T2	5.9	7.37	7.20	2.31
T3	7.1	7.88	7.76	1.52
T4	9.1	8.42	8.28	1.66
T5	10.9	8.87	8.76	1.24
T6	12.4	9.31	9.30	0.11
T7 *	13.2	-	-	-
Mean [%]				1.40

* Specimen fractured

The average error for these results sits below 1.5 %, which is a promising indication that the tests are being interrupted successfully. It proves that the specimens do not experience significant subsequent loading after the prescribed pulse, and are therefore not further deformed unknowingly. The error value remains reasonably consistent no matter how far a specimen is strained. Although only by a small margin, the measured gauge length is less than expected for all tests. This can be explained by slack or play in the fir tree clamping fixtures. The expected gauge length would include any shift of the specimen in the fir-tree clamps, or of the clamps in the pressure bars. The current specimen clamp spanner used to install the clamps in the bars, has flaws that limit how tightly the fixture can be secured, which allows for play in the load path. This tooling issue is described in further detail in Section C.5 in Appendix C. The results presented in Table 6.1 are evidence that Requirement RQ5 on interruptibility of tests has been met.

It must be noted that the striker speed of 13.2 m/s in test T7 was achieved using a gas gun pressure of 5.5 bar. Since the gun and air supply is capable of firing at 10.0 bar, it can be inferred that striker speeds of 15 m/s are well within the capability of the gas gun at the current striker run-up of 170 mm. This run-up can be increased if needed, which allows potential for far higher striker speeds, though one should take care as to not damage threads, or yield the striker or bars. Appendix B outlines the limits on striker speed. The target metric on striker speed, set out in Requirement RQ1, although not explicitly proven, is well within the gas gun's capability.

6.5 Momentum Trap Functionality

This section aims to further demonstrate the effect of the momentum trapping, by comparing results of tests conducted with and without them. The bar layout for the interrupted tests was shown in Figure 6.1, and the layout for the uninterrupted tests is shown in Figure 6.15. The primary momentum trap is still in place in this layout, as it contributes to the effective impedance of the input bar at the struck region. If the primary trap was not there, the striker would have higher impedance than the lone input bar and would not rebound on impact. In addition, removing the primary trap would double the magnitude of the incident wave compared to that when including the primary trap. This is because the striker momentum would not be split between the pressure bar and the trap. The primary trap will separate after a single internal wave transit of 0.65 ms. This is much less than the 1.3 ms needed for the wave to transit the input bar. Hence when the reflected wave returns, there will be no trap in contact with the input bar to capture this wave, leaving the system effectively without any momentum trapping.

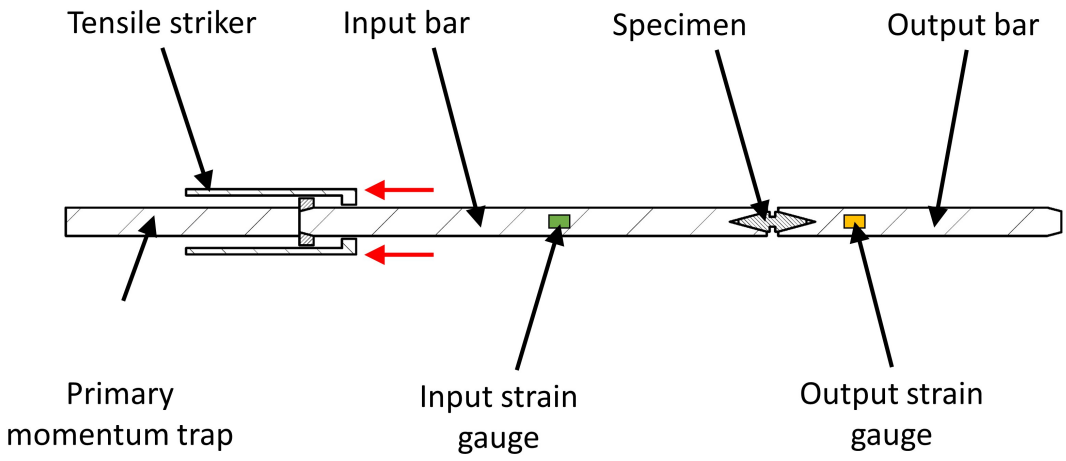

Figure 6.15 Bar layout for uninterrupted dynamic tensile tests

Three pairs of tests were conducted. Each pair used a similar striker speed, with one test being interrupted, and the other not. All other variables were kept consistent. For a visual comparison, Figure 6.16 shows the signals recorded from the first pair of tests, test M1 and test M2. Plots for the other tests may be found in Appendix I.

In the interrupted test in Figure 6.16a, it can be observed that beyond the prescribed incident, reflected and transmitted waves, the signals remain reasonably quiet. This indicates the absence of residual stress waves oscillating up and down either of the pressure bars, which is the desired outcome for the fully momentum trapped configuration.

Figure 6.16b shows the signals from an uninterrupted test, emphasising the effect of the momentum trapping. There is clear evidence of the reflected wave travelling back and forth in the input bar signal. The magnitude of the reflected wave is of significant proportion, and is ≈ 75 % of the magnitude of the incident wave. Similar effects can be observed on the output bar signal, where the transmitted wave continues to reverberate at significant magnitude. These waves load the specimen repeatedly, resulting in further strain and potentially reaching fracture. In Figure 6.16b particularly, it is evident that the reflected portion of the prescribed wave fractured the specimen when it arrived the second time. The oscillating wave on the input bar signal has a sharp change in shape at 1.75 ms, and from that point on, the two signal appear independent of each other. This indicates that the specimen has fractured and that the two bars are no longer attached.

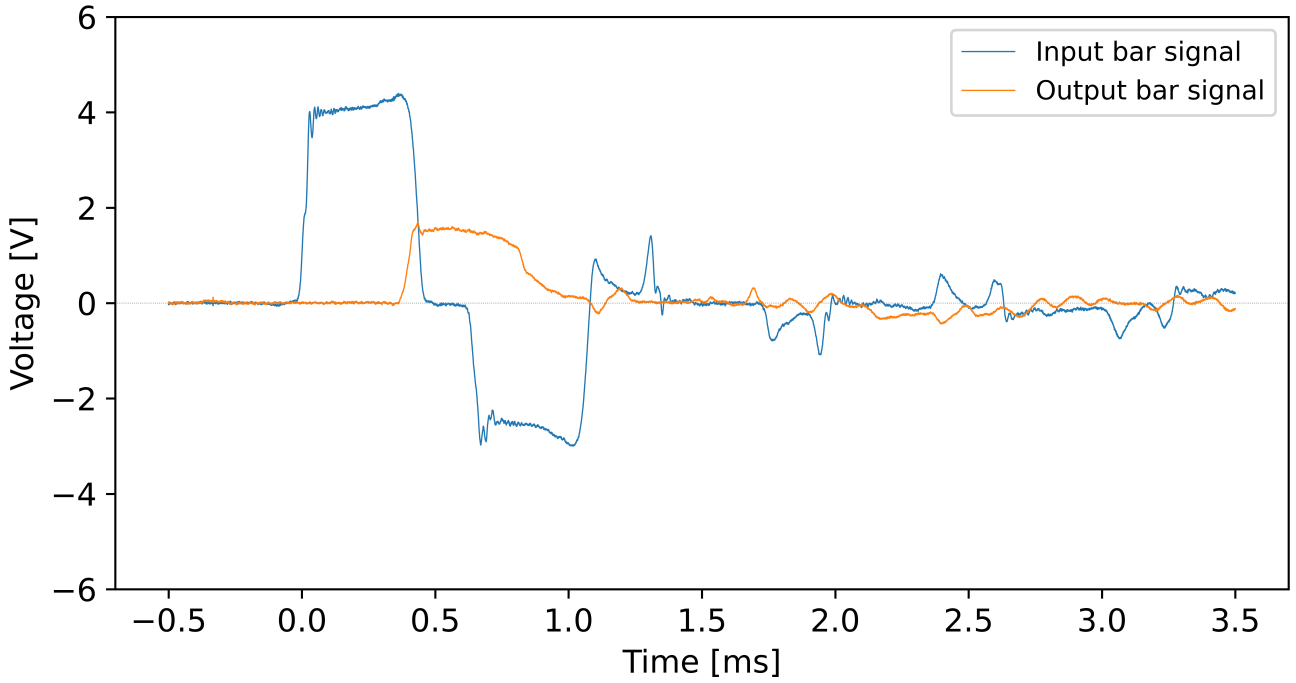

(a) Signals recorded from an interrupted test, M1, using full momentum trapping

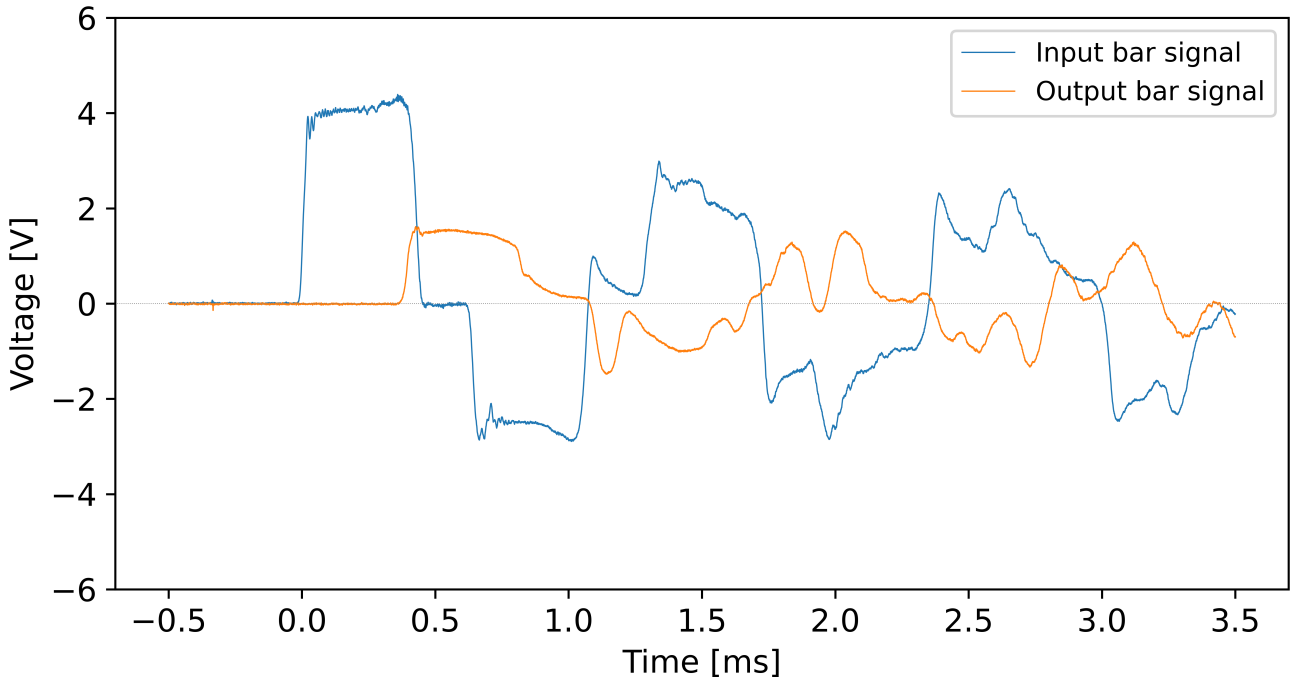

(b) Signals recorded from an uninterrupted test, M2, using only primary momentum trapping

Figure 6.16 Comparison of the recorded signal for interrupted versus uninterrupted TSHB tests, at $v_0 = 10.5$ m/s

Figure 6.17 below shows the resulting stress strain plot for the six tests conducted. This plot illustrates that the whether a TSHB test is interrupted or not, the stress-strain data, prior to unloading and reloading, has very little variation.

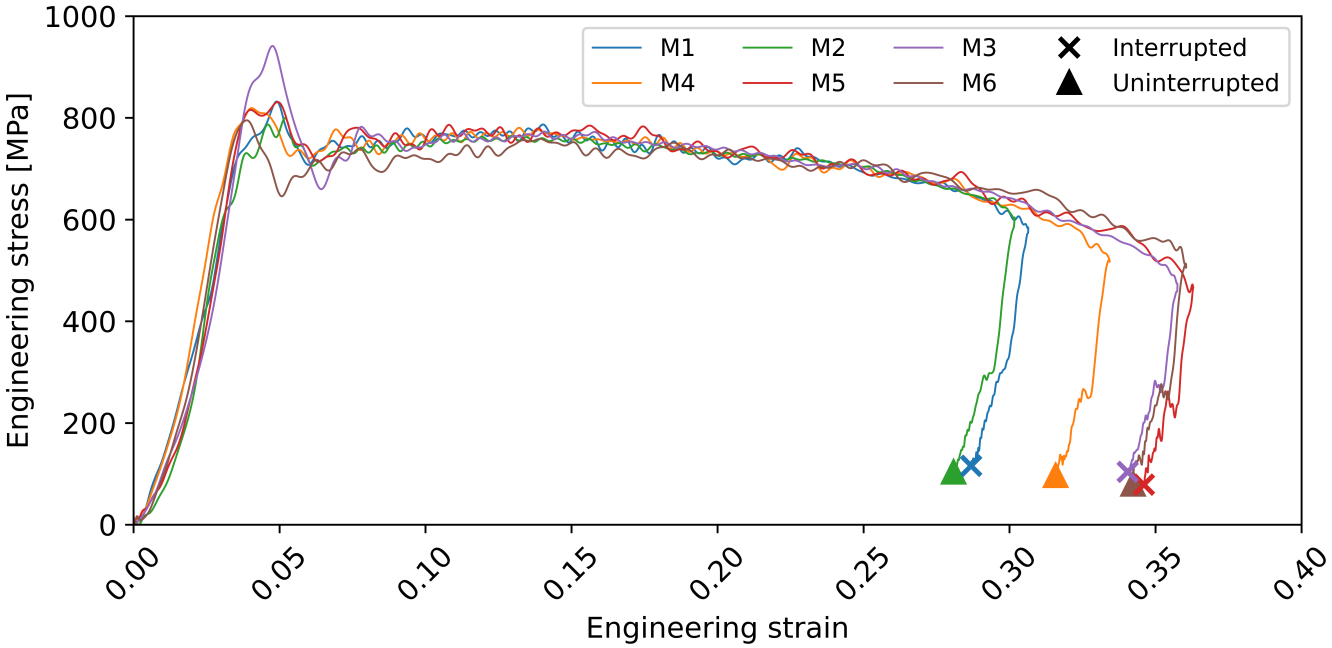

Figure 6.17 Stress versus strain plots, comparing interrupted and uninterrupted tests

The difference is apparent when analysing the specimens post test. Figure 6.18 displays the specimens used in this set of tests, and Table 6.2 summarises the outcomes. Although the stress-strain data agrees between the two types of tests, the specimens from the uninterrupted tests cannot be analysed physically as the stress-strain curves do not represent the full loading history of the specimens, which experienced repeating loading until fracture.

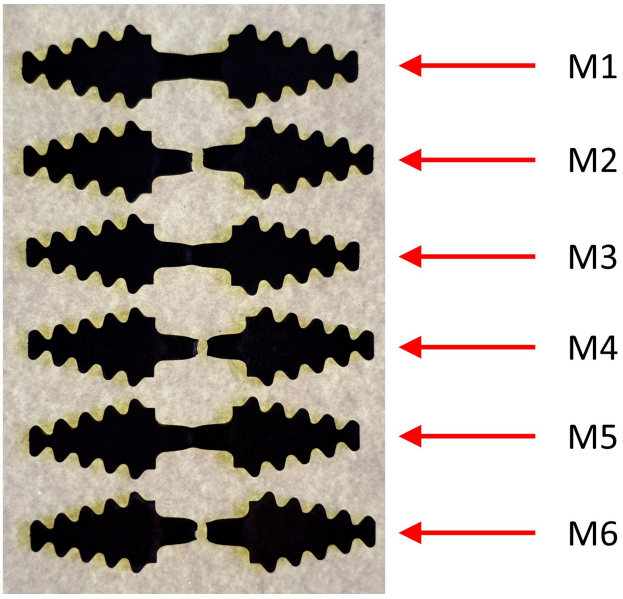

Figure 6.18 Photograph comparing the tested specimens

Table 6.2 *Results comparing expected to actual post-test specimen condition*

Test	v_0 [m/s]	Type	Expected		Actual	
			L_{gauge} [mm]	Condition	L_{gauge} [mm]	Condition
M1	10.7	⋆	9.00	Intact	8.82	Intact
M2	10.5	◇	8.96	Intact	-	Fractured
M3	11.6	⋆	9.38	Intact	-	Intact
M4	11.3	◇	9.21	Intact	-	Fractured
M5	11.9	⋆	9.42	Intact	9.26	Intact
M6	11.9	◇	9.39	Intact	-	Fractured

⋆ Test was interrupted
◇ Test was uninterrupted

6.6 Closing Remarks

The results presented in this chapter underlines the very purpose of having an interruptible TSHB. If one can analyse a strained specimen while comparing to its full loading history, that test yields more applicable data. Specimens strained at high rate to a desired strain may be analysed for microstructure changes and void growth, and this ultimately leads to more representative material models.

Chapter 7

Discussion and Concluding Remarks

This aim of this MSc project was to design, build, and commission a Tensile Split Hopkinson Pressure Bar apparatus in the BISRU laboratory. In this chapter, the final product is assessed, with focus on the quality and comprehensiveness of the design, and it its functional performance.

7.1 Assessment of the Design Process

The design process commenced with extensive investigation into existing techniques for TSHB testing, which encompassed all pertinent concepts. This served as a foundation on which to structure the development outlined in this thesis. Parts and assemblies underwent numerous cycles of design, critique and feedback. Although this meant that the design process was time-intensive, the scrutiny produced a design that functioned exceptionally, and required minimal design revision after initial manufacturing. The calibration and commissioning processes were conducted meticulously, so that issues could be identified and promptly corrected. Each sub-system was verified and fine-tuned to consistently function as intended, so that when the TSHB system was operated in full, the process was seamless and efficient. The are key attributes to the TSHB design:

- **Functionality:** The TSHB fulfils its function as described in Section 7.2 below.
- **Ergonomics:** The apparatus was designed to serve its function consistently without any intricate input from the user. All instrumentation and controls are located together so that the TSHB can be operated from one place. Assembly of the apparatus only requires a small set of standard spanners and hex keys. To facilitate specimen mounting with the fir-tree grips and the attachment of flanges, custom tools were refined.

- **Aesthetics and consistency:** All large components were made from aluminium. 3d printed parts were manufactures in suitable colours, and the gas gun supports were painted black to match the existing bar supports. All wires run the length of the apparatus in cable channelling for neatness and protection.
- **Innovation:** This design incorporates a novel combination of full tandem momentum trapping, a pull-off design of striker, and the fir-tree specimen fixture into a standard TSHB. This integration enhances the functionality, efficiency, and quality of results, setting it apart from existing designs.
- **Safety:** All pressure bearing metal components were designed with generous safety factors. The pressure boundary and pistons were designed to "leak before rupture", ensuring that the most likely failure would leave the gas gun in a safe state.

7.2 Functional performance

The results presented in sections 6.3, 6.4, and 6.5 show that this TSHB apparatus has largely met expectations. Interrupted tests were conducted and verified over a range of strains and the results appeared consistent throughout. The pull-off design of tensile striker, and the fir-tree design of tensile specimen fixture performed well. There are two functional requirements, namely Requirement RQ1 concerning striker speed and Requirement RQ2 concerning strain rate, that have not been met explicitly. These two requirements are closely related, as striker speed dictates particle velocity in the input bar, and that in turn dictates the strain rate experienced by the specimen. If the target striker speed was achieved, then the target strain rate of 1000 /s would also be achieved.

With the DOMEX 550 specimens and striker length used, the threshold on specimen fracture was a strain rate of ≈ 900 /s. While we are able to push the gas gun to higher speeds, it increases the risk of damaging the equipment. At one point during testing, the striker was fired at significantly faster than required to due incorrect pressure setting. The specimen fractured, leaving ample surplus energy in the input bar, which led to the input bar colliding with the isolator tube and damaging it. This is described in Appendix J. It is important to note that the achievable strain rate is also limited by the time it takes the specimen to reach a state of dynamic equilibrium. This was not an issue in the region of strain rate explored in this dissertation.

The targeted upper bound of strain rate could be achieved by altering the configuration in the following ways:

1. The gauge length of the specimens may be reduced.
2. The striker length may be reduced.

Equation 7.1 displays how the strain rate experienced by the specimen is directly proportional to the striker speed, but inversely proportional to the gauge length of the specimen.

$$\dot{\varepsilon} \propto \frac{v_0}{L_{gauge}} \tag{7.1}$$

Therefore, if the specimen gauge length is reduced, higher strain rates can be achieved without necessarily increasing striker speed. There are however limitations as to how small a tensile specimen can be. One is manufacturing constraints, in that is is difficult to machine minute specimens. The other limitation as that as gauge length is decreased, it becomes more challenging to fully control its ultimate strain during dynamic testing. This is a significant drawback, as control over ultimate strain is the primary aim when conducting interruptible tests.

Alternatively strain rate can be increased by simply increasing the striker speed. An additional effect to increasing the striker speed, is that more energy is put into the system. A portion of that energy is dissipated in deforming the specimen, and another portion is transmitted into the output bar. A significant portion of this energy is however left in the input bar in the form of the reflected wave, an excess of which is what caused the damage described in Appendix J. If an increase in striker speed is required, without increasing its kinetic energy, then the striker mass must be decreased. Reducing its cross sectional area is unwise, as it affects the impedance of the striker and therefore its rebound behaviour on impact. In addition a reduction in cross sectional area reduces the magnitude of the incident stress pulse. It is therefore recommended to reduce the striker length. This reduces its mass, allowing it to carry less kinetic energy at higher speeds. Since a shorter striker can safely be fired faster, higher strain rates in the specimen can be achieved. Requirements RQ1 and RQ2 would be able to be met in this case.

An additional benefit to the using shorter strikers, is the ability to independently control the specimen's total strain and strain rate. One can increase strain rate by increasing the striker speed, but that simultaneously increases the total strain on the specimen. Being able to change the length of striker would allow the total strain to be controlled independently. With a set of strikers of varying lengths, and reasonable control on striker speed, the specimen strain and strain rate can both be prescribed for a test. In addition, shorter strikers will allow for tests to be conducted at higher strain rates without damaging the apparatus. Manufacturing a set of shorter strikers would help reach the full potential of the apparatus.

7.3 Component Specific Concerns

There were a few areas in which the designed components or subsystems have a small margin for improvement. These margins, although small, impact the quality of the results produces by the TSHB, are are outlined below.

7.3.1 Deformation of the Striker Tube

The striker flange screws into the inside of the striker tube via a tapered thread. For each test, this flange needs to be removed in order to push the striker tube back and reveal the interface between the input bar the primary momentum trap. This is to re-apply the grease needed for the functioning of the tandem traps. This repetitive tightening and loosening of this flange, together with the large impact loads caused the striker tube the flare out slightly on the striker flange end. This was noticeable as the striker can no longer slide out of the striker bush, and therefore cannot be removed from the rig without persuasion. This deformation will need addressing. If the striker tube can be sourced in a stronger material such as 7000 series aluminium, this would be beneficial.

7.3.2 ROS Performance

The stripes on the striker, added for the ROS to detect, were created using black spray paint. This paint began to wear off quickly during regular usage, despite the painted areas lying in shallow grooves. The striped section of the striker runs inside the striker bush, located in the rear flange of the gas gun. The sliding action here is the primary reason for the chipping and wearing of the painted stripes. Silicone lubricant spray was used here and may have exacerbated the wear. The layer of paint was thick, and this may have made it more susceptible to chipping. Repainting the stripes more conservatively may work better. Other options include adding a clear, matte lacquer over the stripes to protect from wear, or to mask and anodise the stripes onto the tube instead. The quality of the striping is critical for precise striker speed measurement, and so this requires addressing.

7.3.3 Incident Wave Shape

Impact flange compliance

It was noted in Section 5.2.2 that when initially trialling the tensile striker, superposition was evident at the input strain gauges, as the incident pulse was longer in duration than expected. The lengthy rise and fall durations of the wave was responsible for this. The compliance of the striker flange was not accounted for in initial calculations, hence the underestimation of pulse duration. In addition, the compliance inherently smooths the shape of the incident pulse.

Effects of the pressure collars

The pressure collars on the striker serve to support it inside the barrel of the gas gun, as well as to propel the striker when acted on by pressurised gas. The OD of the striker tube is 38 mm and the barrel bore is 63 mm. This means that the collars are bulky, and so they were machined from a polymer (POM) to minimise mass. After the effects of their mass on the shape of the incident wave were still evident, they were lightened further by removing more material from them. These pressure collars were attached to the striker tube by means of a tight shrink fit. Despite the interference fit, they slowly shifted axially down the striker tube over the many tests conducted as part of this project. For this reason, not only are the masses of the collars visible in the shape of the incident wave, but their effect changes over time as they shifted down the tube. In future, a new set of these collars can be designed with low mass in mind from the start, and can rely on ribs to stiffen them. There will need to be some positive features on the striker tube that hold the collars in place.

7.3.4 Primary Momentum Trap Support

Bar alignment is a strong factor in determining how well a wave transfers from one bar into another. Slight misalignment can mean that wave sees a sudden change in impedance if the whole face of a bar is not in contact with the adjacent bar. In addition, if the faces of the contacting bars are not perfectly parallel, parts of the face will make contact before others, once loaded, causing exaggerated transient behaviour on the transmitted and the reflected portion of the wave. The alignment between the input bar and the primary momentum trap is especially crucial, as the tandem trapping system works best when stress wave transfer is unimpeded. The alignment of this interface was carefully done using the method described in Appendix A, and it functioned well during this project.

Consistency, however, was an issue. The input bar was well supported, and had no noticeable play in its bushes. The same could not be said for the primary trap, as it has a more complex support system. It slides inside the isolator tube via a set of bushings. This

static tube is supported by the moving striker, again via a set of bushings. The striker is supported by the gas gun, and slides in yet another set of bushings. The primary trap has three coaxial sets of bushings that secure it to the bed. All of this bushings have clearance, as they need a free sliding fit, and these clearances stack up to give the trap bar a lot of play relative to the bed and to the input bar. A total of 0.23 mm of radial play was measured using a dial test indicator. Although the bars could be accurately aligned during setup, due to this play it could not be guaranteed that they were still aligned at the critical moments during testing.

The support of the input trap is something that can be improved on in future projects. The clearance on all of the bushings may be optimised further, to give minimal play will still allowing sliding to occur freely. Another route that can be explored is to develop a set of flexure bushings to replace some of the plain bushings referred to above. These bushings will serve to keep all bars concentric with little to no play, while giving flexibility in other degrees of freedom to reduce the binding potential associated with the smaller clearances.

7.3.5 Output Flange Design

The output flange posed a big challenge to optimise, and although it performed in a satisfactory manner, there is potential for more improvement. Having a transfer flange between a bar and a momentum trap creates an inherent reflection due to the mass of the flange. This flange may be able to be compacted and lightened while sacrificing minimal stiffness. This may mean changing the stepped interface between flange and trap tube, and replacing it with a spherical interface. These would both allow the flange to be shorter in the axial direction, reducing the mass. A conical or spherical surface would be easier to lap uniformly, and would transfer a stress wave cleanly if lapped well.

7.3.6 Bar Alignment

As mentioned in Section 7.3.4, alignment has a strong influence on the performance. While all bars can be aligned to each other in the vertical and horizontal direction (see Appendix A), alignment in the angular direction (by rotating the bars about their centre axis) is valuable. No bar is perfectly straight. The input and output bars of this TSHB have noticeable curvature when removed from the supports and laid on a flat surface. This creates alignment issues in two ways:

- While the bar supports can be used to hold the bars straight on the bed, there is still radial movement of the bar ends when rotated. This means that no matter how perfectly the bars are initially aligned, if one of the bars rotates, the alignment is lost.
- Bar faces may not be perfectly parallel to each other.

The solution to the first problem would be to keep all bars and traps orientated in the same angular position that they were aligned in. Improvement can be made by optimising the angular position of each bar relative to adjacent bars. With respect to the second problem outlined above, there may be relative angles between bars that bring the faces close to parallel. If this ideal positioning can be found and marked for each interface, then the bar alignment will be correct and consistent throughout testing. This process can be worked through by running a batch of tests, and changing the angles of the bars to see what yields the best results. Alternatively, the use of engineer's blue on the faces of the bars will give a good indication of the uniformity of contact. In this project, the angular alignment of the bars were kept consistent, but not necessarily in their optimum positions.

7.3.7 Output Trap Stopper

The output trap stopper was designed to protect the strain gauges on the output bar from damage. In addition, the aim of the stopper was to arrest the output trap completely, preventing it from rebounding back into the output flange. The design worked, as neither of those occurred, but the stopper accumulated lot of damage, and had to be replaced periodically. Instead of 3D printed PLA, this part should be machined from nylon or POM. These materials are tougher than PLA, which could not handle the repetitive impact loading. The layered nature of 3D printing added additional weakness to the part. Furthermore, this part is annular in nature, and is located around the output bar between the strain gauges and output trap. This makes it laborious to remove when it requires replacement.

7.3.8 Specimen Clamp Spanner

The new specimen clamp spanner, described in C, served as a prototype, and aimed at improving on the existing one. It demonstrated that the machining required is possible, and that a working tool can be produced. This prototype had shortcomings that led to it not being used to install the specimens during testing. These are important considerations to make in the development of the next prototype:

- The flexible arms are too stiff, and take an unreasonable amount of force to deflect at their end. This can be corrected for by cutting thinner arms, or by making the whole tool thinner. The former is recommended as only bending flexibility in one direction is required. Bending in other directions, or torsion of the arms is something to be avoided.
- The pins of the tool don't line up with the holes on the clamps. This issue may come right with an increase in arm flexibility, but it must be noted that the holes on the titanium clamps do not form a perfectly square pattern. It also varies between clamp pairs. This was not realised when designing this prototype.

The previous version of the specimen spanner was utilized in this project. This tool holds the pins rigidly in position and does not accommodate for the contraction and expansion of the fir-tree specimen clamps as they are installed and removed from the pressure bars. This meant that the clamping force from the tapered threads was directed more at the pins on the tool than at the specimen. This loss of clamping force on the specimen introduced minor compliance into the fixture. The compliance is noticeable in Figure 6.8 showing force equilibrium, as there is a small delay in the loading up of the output bar. An improved specimen clamp tool will help reduce this delay, emphasising the importance of furthering the tool's development.

Chapter 8

Recommendations

This chapter summarizes ways in which the apparatus can be improved upon or optimized further in the future.

1. **Redesign of striker sub-assembly:** The issues outlined in Sections 7.3.1, 7.3.2, 7.3.3 all reside in the tensile striker assembly, emphasising the opportunity for refinement of this sub-assembly.
2. **Primary trap support:** Improving the trap support would enhance the performance of the tandem momentum traps.
3. **Refinement of output flange:** The output flange can be can be further improved on, as mentioned in Section 7.3.5, to facilitate stress transfer to the output trap.
4. **Angular bar alignment:** Optimising the angular positions of all pressure bars and momentum traps will minimise reflections at all interfaces.
5. **Output trap stopper:** This part requires refinement, for the reasons outlined in Section 7.3.7
6. **Specimen clamp spanner:** The prototype specimen clamp spanner requires further design iteration, for the reasons outlined in Section 7.3.8.

8.1 Closing Comment

The TSHB described in this thesis is representative of the state of the art. The recommendations mentioned are minor improvements, offering small gains in the performance of the interruptible TSHB. In its current state, this apparatus is fully functional and ready for use in HSR material characterisation.

References

[1] G T Gray III, *Classic Split-Hopkinson Pressure Bar Testing*, ASM International, 2000, URL https://dl.asminternational.org/book/chapter-pdf/480641/a0003296.pdf.

[2] M M Al-Mousawi, S R Reid & W F Deans, "The use of the split hopkinson pressure bar techniques in high strain rate materials testing", *Proceedings of the Institution of Mechanical Engineers, Part C: Journal of Mechanical Engineering Science*, vol. 211, (1997), pp. 273–292, doi: 10.1243/0954406971522042.

[3] G H Staab & AMOS Gilat, "A direct-tension split hopkinson bar for high strain-rate testing", *Experimental mechanics*, vol. 31, (1991), pp. 232–235.

[4] Arthur Van Lerberghe & Andrew D Barr, "dispersion.py - first-mode dispersion correction of a finite arbitrary signal in a cylindrical bar", 2023, URL https://figshare.shef.ac.uk/articles/software/process_SHPB_py_-_A_Python_algorithm_for_stress_wave_dispersion_correction_in_split-Hopkinson_pressure_bar_experiments/21973325.

[5] G T Gray III, "High-strain-rate deformation: Mechanical behavior and deformation substructures induced", *Annual Review of Materials Research*, vol. 42, (2012), pp. 285–303, doi: 10.1146/annurev-matsci-070511-155034.

[6] Wei Wang, Yan Ma, Muxin Yang, Ping Jiang, Fuping Yuan & Xiaolei Wu, "Strain rate effect on tensile behavior for a high specific strength steel: From quasi-static to intermediate strain rates", *Metals*, vol. 8, (2017), p. 11.

[7] Olivier Pantalé & Lu Ming, "An optimized dynamic tensile impact test for characterizing the behavior of materials", *Applied Mechanics*, vol. 3, (2022), pp. 1107–1122, URL https://www.mdpi.com/2673-3161/3/3/63.

[8] J Bouquerel, K Verbeken, J Van Slycken, P Verleysen & Y Houbaert, "Physically based modeling of the mechanical behavior of trip steels", *International Journal of Material Forming*, vol. 1, (2008), pp. 57–60, URL https://doi.org/10.1007/s12289-008-0047-7.

[9] Y M Wang & E Ma, "Strain hardening, strain rate sensitivity, and ductility of nanostructured metals", *Materials Science and Engineering: A*, vol. 375-377, (2004), pp. 46–52, URL https://www.sciencedirect.com/science/article/pii/S0921509303012462.

[10] F A McClintock, "A criterion for ductile fracture by the growth of holes", *Journal of Applied Mechanics*, vol. 35, (1968), pp. 363–371, URL https://doi.org/10.1115/1.3601204.

[11] J R Rice & D M Tracey, "On the ductile enlargement of voids in triaxial stress fields", *Journal of the Mechanics and Physics of Solids*, vol. 17, (1969), pp. 201–217, URL https://www.sciencedirect.com/science/article/pii/0022509669900337.

[12] Yuanli Bai & Tomasz Wierzbicki, "A new model of metal plasticity and fracture with pressure and lode dependence", *International Journal of Plasticity*, vol. 24, (2008), pp. 1071–1096, URL https://www.sciencedirect.com/science/article/pii/S0749641907001246.

[13] Liang Xue & Tomasz Wierzbicki, "Ductile fracture initiation and propagation modeling using damage plasticity theory", *Engineering Fracture Mechanics*, vol. 75, (2008), pp. 3276–3293, URL https://www.sciencedirect.com/science/article/pii/S0013794407003499.

[14] Yuanli Bai & Tomasz Wierzbicki, "A comparative study of three groups of ductile fracture loci in the 3d space", *Engineering Fracture Mechanics*, vol. 135, (2015), pp. 147–167, URL https://www.sciencedirect.com/science/article/pii/S0013794414004196.

[15] M P Weyer, T J Cloete & R A Govender, "Strain rate and triaxiality effects on the dynamic ductile damage of domex 355mc", *The European Physical Journal Special Topics*, vol. 227, (2018), pp. 99–109, URL https://doi.org/10.1140/epjst/e2018-00068-x.

[16] Michael Brünig, Steffen Gerke & Vanessa Hagenbrock, "Micro-mechanical studies on the effect of the stress triaxiality and the lode parameter on ductile damage", *International Journal of Plasticity*, vol. 50, (2013), pp. 49–65, URL https://www.sciencedirect.com/science/article/pii/S074964191300082X.

[17] Yingbin Bao & Tomasz Wierzbicki, "On fracture locus in the equivalent strain and stress triaxiality space", *International Journal of Mechanical Sciences*, vol. 46, (2004), pp. 81–98, URL https://www.sciencedirect.com/science/article/pii/S0020740304000360.

[18] Bertram Hopkinson, "X. a method of measuring the pressure produced in the detonation of high, explosives or by the impact of bullets", *Philosophical Transactions of the Royal Society of London. Series A, Containing Papers of a Mathematical or Physical Character*, vol. 213, (1914), pp. 437–456, doi: 10.1098/rsta.1914.0010.

[19] J W Landon, H Quinney & A W Ewing, "Experiments with the hopkinson pressure bar", *Proceedings of the Royal Society of London. Series A, Containing Papers of a Mathematical and Physical Character*, vol. 103, (1923), pp. 622–643, URL https://doi.org/10.1098/rspa.1923.0084, doi: 10.1098/rspa.1923.0084.

[20] R M Davies, "A simple modification of the hopkinson pressure bar", *Proc. 7th Int. Cong. on Applied Mechanics*, vol. 1, (1948), p. 404.

[21] R M Davies, "A critical study of the hopkinson pressure bar", *Philosophical Transactions of the Royal Society of London. Series A, Mathematical and Physical Sciences*, vol. 240, (1948), pp. 375–457.

[22] H Kolsky, "An investigation of the mechanical properties of materials at very high rates of loading", *Proceedings of the Physical Society. Section B*, vol. 62, (1949), p. 676, URL https://dx.doi.org/10.1088/0370-1301/62/11/302.

[23] Lorenzo Peroni & Marco Peroni, "Development of testing systems for dynamic assessment of sheet metal specimens", *Meccanica*, vol. 43, (2008), pp. 225–236.

[24] M. Bilal Nutkani, Muhammad Abid, Riffat Asim Pasha & Uzair Ahmed Dar, "Indigenous design and development of split hopkinson pressure bar (shpb) test setup for characterization of materials at high strain rates", IOP Publishing Ltd, 2020.

[25] Philip Church, Rory Cornish, Ian Cullis, Peter Gould & Ian Lewtas, "Using the split hopkinson pressure bar to validate material models", *Philosophical Transactions of the Royal Society A: Mathematical, Physical and Engineering Sciences*, vol. 372, (2014), p. 20130294.

[26] Han Zhao & Gérard Gary, "A three dimensional analytical solution of the longitudinal wave propagation in an infinite linear viscoelastic cylindrical bar. application to experimental techniques", *Journal of the Mechanics and Physics of Solids*, vol. 43, (1995), pp. 1335–1348, URL https://www.sciencedirect.com/science/article/pii/002250969500030M.

[27] K Xia, F Dai & R Chen, "Split hopkinson pressure bar tests of rocks: Advances in experimental techniques and applications to rock strength and fracture", 2011, URL https://www.scopus.com/inward/record.uri?eid=2-s2.0-85059475202&partnerID=40&md5=7f21f95901681661501101644d2b7649.

[28] Theodore Nicholas & S J Bless, "High strain rate tension testing", *ASM Handbook.*, vol. 8, (1985), pp. 208–214.

[29] JWEOC Harding, E O Wood & J D Campbell, "Tensile testing of materials at impact rates of strain", *Journal of Mechanical Engineering Science*, vol. 2, (1960), pp. 88–96.

[30] J Harding & L M Welsh, "A tensile testing technique for fibre-reinforced composites at impact rates of strain", *Journal of Materials Science*, vol. 18, (1983), pp. 1810–1826.

[31] XJ Wu & DA Gorham, "Stress equilibrium in the split hopkinson pressure bar test", *Le Journal de Physique IV*, vol. 7, (1997), pp. C3–91.

[32] U S Lindholm & L M Yeakley, "High strain-rate testing: Tension and compression", *Experimental Mechanics*, vol. 8, (1968), pp. 1–9, URL `https://doi.org/10.1007/BF02326244`.

[33] M Dunand, G Gary & D Mohr, "Load-inversion device for the high strain rate tensile testing of sheet materials with hopkinson pressure bars", *Experimental Mechanics*, vol. 53, (2013), pp. 1177–1188, URL `https://doi.org/10.1007/s11340-013-9712-y`.

[34] J Peirs, P Verleysen, J Degrieck & F Coghe, "The use of hat-shaped specimens to study the high strain rate shear behaviour of ti–6al–4v", *International Journal of Impact Engineering*, vol. 37, (2010), pp. 703–714, URL `https://www.sciencedirect.com/science/article/pii/S0734743X09001444`.

[35] Theodore Nicholas, *Dynamic tensile testing of structural materials using a split Hopkinson bar apparatus*, Materials Laboratory, Air Force Wright Aeronautical Laboratories, Air Force, 1980.

[36] S Ellwood, L J Griffiths & D J Parry, "A tensile technique for materials testing at high strain rates", *Journal of Physics E: Scientific Instruments*, vol. 15, (1982), p. 1169, URL `https://dx.doi.org/10.1088/0022-3735/15/11/011`.

[37] G Haugou, E Markiewicz & J Fabis, "On the use of the non direct tensile loading on a classical split hopkinson bar apparatus dedicated to sheet metal specimen characterisation", *International Journal of Impact Engineering*, vol. 32, (2006), pp. 778–798, URL `https://www.sciencedirect.com/science/article/pii/S0734743X05001107`.

[38] Gerald Watermeyer, "Design, build and commission a tensile shpb", 2004.

[39] M. S. Downey, "Design, build and test a tensile split hopkinson pressure bar apparatus", 2007.

[40] Avishay Lindenfeld & Yehuda Partom, "Improving data interpretation from shtb tests on ductile metals", *EPJ Web Conf.*, vol. 183, URL https://doi.org/10.1051/epjconf/201818301006.

[41] Theodore Nicholas, "Tensile testing of materials at high rates of strain", *Experimental Mechanics*, vol. 21, (1981), pp. 177–185, URL https://doi.org/10.1007/BF02326644.

[42] C Albertini & M Montagnani, "Testing techniques based on the split hopkinson bar", 1974.

[43] C Albertini & M Montagnani, "Study of the true tensile stress-strain diagram of plain concrete with real size aggregate; need for and design of a large hopkinson bar bundle", *Le Journal de Physique IV*, vol. 4, (1994), pp. C8–113.

[44] Weinong W Chen & Bo Song, *Split Hopkinson (Kolsky) bar: design, testing and applications*, Springer Science & Business Media, 2010.

[45] M Quik, K Labibes, C Albertini, T Valentin & P Magain, "Dynamic mechanical properties of automotive thin sheet steel in tension, compression and shear", *Le Journal de Physique IV*, vol. 7, (1997), pp. C3–379.

[46] E Mancini, M Sasso, M Rossi, G Chiappini, G Newaz & D Amodio, "Design of an innovative system for wave generation in direct tension–compression split hopkinson bar", *Journal of Dynamic Behavior of Materials*, vol. 1, (2015), pp. 201–213, URL https://doi.org/10.1007/s40870-015-0019-1.

[47] Grégory Haugou, Nicolas Leconte, & Hervé Morvan, "Separation of the elastic waves' system in pre-stretched bar devices", *EPJ Web of Conferences*, vol. 94, URL https://doi.org/10.1051/epjconf/20159401067.

[48] G Haugou, N Leconte & H Morvan, "Design of a pre-stretched tension hopkinson bar device: Configuration, tail corrections, and numerical validation", *International Journal of Impact Engineering*, vol. 97, (2016), pp. 89–101, URL https://www.sciencedirect.com/science/article/pii/S0734743X16303074.

[49] Y Xu, J Zhou, L Farbaniec & A Pellegrino, "Optimal design, development and experimental analysis of a tension–torsion hopkinson bar for the understanding of complex impact loading scenarios", *Experimental Mechanics*, vol. 63, (2023), pp. 773–789, URL https://doi.org/10.1007/s11340-023-00942-1.

[50] Amos Gilat, Robert K Goldberg & Gary D Roberts, "Experimental study of strain-rate-dependent behavior of carbon/epoxy composite", *Composites Science and Technology*, vol. 62, (2002), pp. 1469–1476, URL https://www.sciencedirect.com/science/article/pii/S0266353802001008.

[51] Y Chen, A H Clausen, O S Hopperstad & M Langseth, "Application of a split-hopkinson tension bar in a mutual assessment of experimental tests and numerical predictions", *International Journal of Impact Engineering*, vol. 38, (2011), pp. 824–836, URL https://www.sciencedirect.com/science/article/pii/S0734743X11000790.

[52] Carlo Albertini, Ezio Cadoni & George Solomos, "Advances in the hopkinson bar testing of irradiated/non-irradiated nuclear materials and large specimens", *Philosophical Transactions of the Royal Society A: Mathematical, Physical and Engineering Sciences*, vol. 372, (2014), p. 20130197.

[53] Georg Baumann, Dominik Niederkofler, Christian Ellersdorfer & Florian Feist, "On the development of a release mechanism for a split hopkinson tension and compression bar", *Materials*, vol. 14, URL https://www.mdpi.com/1996-1944/14/24/7609.

[54] J E Field, S M Walley, N K Bourne & J M Huntley, "Review of experimental techniques for high rate deformation studies", *Proceedings of the Acoustics and Vibration Asia*, vol. 98, (1998), pp. 9–38.

[55] Ze-Jian Xu, Yulong Li & Feng-Lei Huang, "Application of split hopkinson tension bar technique to the study of dynamic fracture properties of materials", *Acta Mechanica Sinica*, vol. 28.

[56] W Chen, F Lu & M Cheng, "Tension and compression tests of two polymers under quasi-static and dynamic loading", *Polymer Testing*, vol. 21, (2002), pp. 113–121, URL https://www.sciencedirect.com/science/article/pii/S0142941801000551.

[57] H Huh, W J Kang & S S Han, "A tension split hopkinson bar for investigating the dynamic behavior of sheet metals", *Experimental Mechanics*, vol. 42, (2002), pp. 8–17, URL https://doi.org/10.1007/BF02411046.

[58] R Smerd, S Winkler, C Salisbury, M Worswick, D Lloyd & M Finn, "High strain rate tensile testing of automotive aluminum alloy sheet", *International Journal of Impact Engineering*, vol. 32, (2005), pp. 541–560, URL https://www.sciencedirect.com/science/article/pii/S0734743X05000680.

[59] Robert Gerlach, Sivasubramaniam K Sathianathan, Clive Siviour & Nik Petrinic, "A novel method for pulse shaping of split hopkinson tensile bar signals", *International Journal of Impact Engineering*, vol. 38, (2011), pp. 976–980, URL https://www.sciencedirect.com/science/article/pii/S0734743X11001370.

[60] M R Arthington, C R Siviour & N Petrinic, "Improved materials characterisation through the application of geometry reconstruction to quasi-static and high-strain-rate tension tests", *International Journal of Impact Engineering*, vol. 46, (2012), pp. 86–96, URL https://www.sciencedirect.com/science/article/pii/S0734743X12000395.

[61] G C Ganzenmüller, E Blaum, D Mohrmann, T Langhof, D Plappert, N Ledford, H Paul & S Hiermaier, "A simplified design for a split-hopkinson tension bar with long pulse duration", *Procedia Engineering*, vol. 197, (2017), pp. 109–118, URL https://www.sciencedirect.com/science/article/pii/S1877705817332198.

[62] Robert Gerlach, Christian Kettenbeil & Nik Petrinic, "A new split hopkinson tensile bar design", *International Journal of Impact Engineering*, vol. 50, (2012), pp. 63–67, URL https://www.sciencedirect.com/science/article/pii/S0734743X1200156X.

[63] J Neumayer, P Kuhn, H Koerber & R Hinterhölzl, "Experimental determination of the tensile and shear behaviour of adhesives under impact loading", *The Journal of Adhesion*, vol. 92, (2016), pp. 503–516, doi: 10.1080/00218464.2015.1092387.

[64] Richard Curry, "Response of plates subjected to air-blast and buried explosions", 2017.

[65] Noah Ledford, Hanna Paul, Georg Ganzenmueller, Michael May, Matthias Höfemann, Manuel Otto & Nik Petrinic, *Investigations on specimen design and mounting for Split Hopkinson Tension Bar (SHTB) experiments*, vol. 94, 2015.

[66] A T Owens & H V Tippur, "A tensile split hopkinson bar for testing particulate polymer composites under elevated rates of loading", *Experimental Mechanics*, vol. 49, (2009), pp. 799–811, URL https://doi.org/10.1007/s11340-008-9192-7.

[67] Bernardo S Moreira, Paulo D P Nunes, Carlos M da Silva, António Francisco G Tenreiro, António M Lopes, Ricardo J C Carbas, Eduardo A S Marques, Marco P L Parente & Lucas F M da Silva, "Numerical design of a thread-optimized gripping system for lap joint testing in a split hopkinson apparatus", *Sensors*, vol. 23, (2023), p. 2273.

[68] T Gómez del Río, E Barbero, R Zaera & C Navarro, "Dynamic tensile behaviour at low temperature of cfrp using a split hopkinson pressure bar", *Composites Science*

and Technology, vol. 65, (2005), pp. 61–71, URL https://www.sciencedirect.com/science/article/pii/S0266353804001617.

[69] Georg. C Ganzenmüller, Timo Langhof & Stefan Hiermaier, "A constant acoustic impedance mount for sheet-type specimens in the tensile split-hopkinson bar", *EPJ Web Conf.*, vol. 183, URL https://doi.org/10.1051/epjconf/201818302064.

[70] M M LeBlanc & D H Lassila, "Dynamic tensile testing of sheet material using the split-hopkinson bar technique", *Experimental Techniques*, vol. 17, (1993), pp. 37–42, URL https://doi.org/10.1111/j.1747-1567.1993.tb00274.x.

[71] C P Koh, V P W Shim, V B C Tan & B L Tan, "Response of a high-strength flexible laminate to dynamic tension", *International Journal of Impact Engineering*, vol. 35, (2008), pp. 559–568, URL https://www.sciencedirect.com/science/article/pii/S0734743X07000796.

[72] J M T Holt, "Uniaxial tension testing.", *Materials Park, OH: ASM International, 2000.*, pp. 124–142.

[73] H Eskandari & J A Nemes, "Dynamic testing of composite laminates with a tensile split hopkinson bar", *Journal of Composite Materials*, vol. 34, (2000), pp. 260–273, doi: 10.1177/002199830003400401.

[74] J Harding & L M Welsh, *Impact testing of fibre reinforced composite materials*, University of Oxford Department of Engineering Science, 1982.

[75] Yu Chen, Zhihua Tu & Baochang Yang, "Study of dynamic and mechanical behaviour of sicp/al composite under tensile impact", *Applied Composite Materials*, vol. 2, (1995), pp. 43–50.

[76] Yuanming Xia & Xing Wang, "Constitutive equation for unidirectional composites under tensile impact", *Composites Science and Technology*, vol. 56, (1996), pp. 155–160, URL https://www.sciencedirect.com/science/article/pii/0266353895001395.

[77] C Y Wang & Y M Xia, "Validity of one-dimensional experimental principle for flat specimen in bar–bar tensile impact apparatus", *International Journal of Solids and Structures*, vol. 37, (2000), pp. 3305–3322, URL https://www.sciencedirect.com/science/article/pii/S0020768399000359.

[78] T Rahmaan, A Bardelcik, J Imbert, C Butcher & M J Worswick, "Effect of strain rate on flow stress and anisotropy of dp600, trip780, and aa5182-o sheet metal alloys", *International Journal of Impact Engineering*, vol. 88, (2016), pp. 72–90.

[79] J Peirs, P Verleysen, W Van Paepegem & J Degrieck, "Determining the stress–strain behaviour at large strains from high strain rate tensile and shear experiments", *International Journal of Impact Engineering*, vol. 38, (2011), pp. 406–415, URL https://www.sciencedirect.com/science/article/pii/S0734743X11000054.

[80] Patricia Verleysen & Joris Degrieck, "Measurement of the evolution of the axial strain distribution in hopkinson specimens", *Journal de Physique IV (Proceedings)*, vol. 110, (2003), pp. 501–506.

[81] Patricia Verleysen & Joris Degrieck, "Experimental investigation of the deformation of hopkinson bar specimens", *International Journal of Impact Engineering*, vol. 30, (2004), pp. 239–253, URL https://www.sciencedirect.com/science/article/pii/S0734743X03000691.

[82] Patricia Verleysen, Benedict Verhegghe, Tom Verstraete & Joris Degrieck, "Numerical study of the influence of the specimen geometry on split hopkinson bar tensile test results", *Latin American Journal of Solids and Structures*, vol. 6, (2009), pp. 285Â–298.

[83] Maria Lißner, Enrique Alabort, Borja Erice, Hao Cui & Nik Petrinic, "A rate dependent experimental and numerical analysis of adhesive joints under different loading directions", *The European Physical Journal Special Topics*, vol. 227, (2018), pp. 85–97, URL https://doi.org/10.1140/epjst/e2018-00070-x.

[84] Matthew Weyer, "An experimental and theoretical study on the effect of strain rate on ductile damage", 2016.

[85] Andrew Scott Bowden, "Experimental and numerical study on the effect of strain rate to ductile damage", 2009.

[86] C A Ross, W H Cook & L L Wilson, "Dynamic tensile tests of composite materials using a split-hopkinson pressure bar", *Experimental techniques*, vol. 8, (1984), pp. 30–33.

[87] Yinggang Miao, Bing Du, Chenbo Ma, Haitao Hu & Qiong Deng, "Some fundamental problems concerning the measurement accuracy of the hopkinson tension bar technique", *Measurement Science and Technology*, vol. 30, (2019), p. 055009, URL https://dx.doi.org/10.1088/1361-6501/ab01b5.

[88] Khac-Ha Nguyen, Hee Cheol Kim, Hyunho Shin, Yo-Han Yoo & Jong-Bong Kim, "Numerical investigation into the stress wave transmitting characteristics of threads in the split hopkinson tensile bar test", *International Journal of Impact Engineering*, vol. 109, (2017), pp. 253–263, URL https://www.sciencedirect.com/science/article/pii/S0734743X16310661.

[89] Mbuso Yende, "Design, build and test a tensile specimen fixture for a split hopkinson pressure bar apparatus", 2010.

[90] Nkululeko Humphrey Cele, "Redesign, build and test a tensile specimen fixture for a split hopkinson bar (shb) apparatus", 2011.

[91] Sia Nemat-Nasser, Jon B Isaacs & John E Starrett, "Hopkinson techniques for dynamic recovery experiments", *Proceedings of the Royal Society of London. Series A: Mathematical and Physical Sciences*, vol. 435.

[92] Sia Nemat-Nasser, "Introduction to high strain rate testing", *ASM handbook*, vol. 8, (2000), pp. 427–428.

[93] Matti Isakov, Stefan Hiermaier & Veli Tapani Kuokkala, "Improved specimen recovery in tensile split hopkinson bar", *Philosophical Transactions of the Royal Society A: Mathematical, Physical and Engineering Sciences*, vol. 372.

[94] M V Hosur, J Alexander, U K Vaidya & S Jeelani, "High strain rate compression response of carbon/epoxy laminate composites", *Composite Structures*, vol. 52, (2001), pp. 405–417, URL `https://www.sciencedirect.com/science/article/pii/S0263822301000319`.

[95] Shishay Amare Gebremeskel, Neelanchali Asija, Aryan Priyanshu, Hemant Chouhan & Naresh Bhatnagar, "Design customization and development of split hopkinson pressure bar for light and soft armour materials", *Global Journal of Researches in Engineering A: Mechanical and Mechanics Engineering*, vol. 14, (2014), pp. 62–75.

[96] K.-H. Hartmann, H.-D. Kunze & L W Meyer, "Metallurgical effects on impact loaded materials", 1981, URL `https://doi.org/10.1007/978-1-4613-3219-0_21`.

[97] R González Lezcano, Y E Essa & J L Pérez-Castellanos, "Numerical analysis of interruption process of dynamic tensile tests using a hopkinson bar", EDP sciences, 2003, pp. 565–570.

[98] Y El-Saeid Essa, J López-Puente & J L Pérez-Castellanos, "Numerical simulation and experimental study of a mechanism for hopkinson bar test interruption", *The Journal of Strain Analysis for Engineering Design*, vol. 42, (2007), pp. 163–172, doi: 10.1243/03093247JSA206.

[99] Ma Dongfang, Chen Danian, Wu Shanxing, Wang Huanran, Hou Yanjun & Cai Canyuan, "An interrupted tensile testing at high strain rates for pure copper bars", *Journal of Applied Physics*, vol. 108, (2010), p. 114902, URL `https://doi.org/10.1063/1.3516475`.

[100] X. Yang, X. Xiong, Z. Yin, H. Wang, J. Wang & D. Chen, "Interrupted test of advanced high strength steel with tensile split hopkinson bar method", *Experimental Mechanics*, vol. 54, (2014), pp. 641–652.

[101] J P Fowler, M J Worswick, A K Pilkey & H Nahme, "Camage leading to ductile fracture under high strain-rate conditions", *Metallurgical and Materials Transactions A*, vol. 31, (2000), pp. 831–844.

[102] J L Lataillade, M Delaet, F Collombet & C Wolff, "Effects of the intralaminar shear loading rate on the damage of multi-ply composites", *International Journal of Impact Engineering*, vol. 18, (1996), pp. 679–699, URL `https://www.sciencedirect.com/science/article/pii/0734743X9500059J`.

[103] S Huang, Rong Chen & K W Xia, "Quantification of dynamic tensile parameters of rocks using a modified kolsky tension bar apparatus", *Journal of Rock Mechanics and Geotechnical Engineering*, vol. 2, (2010), pp. 162–168, URL `https://www.sciencedirect.com/science/article/pii/S1674775515300391`.

[104] Joost Van Slycken, "Advanced use of a split hopkinson bar setup application to trip steels", 2007.

[105] M Prot, T J Cloete & S Pattofatto, "Dynamic compression and recovery of cancellous bone for microstructural investigation", *EPJ Web of Conferences*, vol. 26, (2012), p. 03003.

[106] Marianne Prot & Trevor John Cloete, "A tandem momentum trap for dynamic specimen recovery during split hopkinson pressure bar testing of cancellous bone", *Journal of Dynamic Behavior of Materials*, vol. 2, (2016), pp. 50–58.

[107] Wen Huang, Zhong Wei Huang & Xiao Qing Zhou, "Loading and unloading split hopkinson tension bar technique for studying dynamic microstructure evolution of materials", *Advanced Materials Research*, vol. 160, (2011), pp. 891–894.

[108] Herbert Kolsky, *Stress waves in solids*, vol. 1098, Courier Corporation, 1963.

[109] R Govender A., T Cloete J. & G Nurick N., "A numerical investigation of dispersion in hopkinson pressure bar experiments", *J. Phys. IV France*, vol. 134, (2006), pp. 521–526, URL `https://doi.org/10.1051/jp4:2006134080`.

[110] Hyunho Shin, "Pochhammer–chree equation solver for dispersion correction of elastic waves in a (split) hopkinson bar", *Proceedings of the Institution of Mechanical Engineers, Part C: Journal of Mechanical Engineering Science*, vol. 236, (2022), pp. 80–87.

[111] L Pochhammer, "Beitrag zur theorie der biegung des kreiscylinders.", .

[112] C Chree, "The equations of an isotropic elastic solid in polar and cylindrical coordinates their solution and application", *transactions of the Cambridge Philosophical Society*, vol. 14, (1889), p. 250.

[113] Dennison Bancroft, "The velocity of longitudinal waves in cylindrical bars", *Physical Review*, vol. 59, (1941), pp. 588–593, URL `https://link.aps.org/doi/10.1103/PhysRev.59.588`.

[114] D A Gorham, "A numerical method for the correction of dispersion in pressure bar signals", *Journal of Physics E: Scientific Instruments*, vol. 16, (1983), p. 477, URL `https://dx.doi.org/10.1088/0022-3735/16/6/008`.

[115] J M Lifshitz & H Leber, "Data processing in the split hopkinson pressure bar tests", *International Journal of Impact Engineering*, vol. 15, (1994), pp. 723–733, URL `https://www.sciencedirect.com/science/article/pii/0734743X94900119`.

[116] S T Marais, R B Tait, T J Cloete & G N Nurick, "Material testing at high strain rate using the split hopkinson pressure bar", *Latin American Journal of Solids and Structures*, vol. 1, (2004), pp. 219–339.

[117] Andrew Tyas & Dan J. Pope, "Full correction of first-mode pochammer-chree dispersion effects in experimental pressure bar signals", *Measurement Science and Technology*, vol. 16, (2005), pp. 642–652.

[118] Sam E Rigby, Andrew D Barr & Max Clayton, "A review of pochhammer–chree dispersion in the hopkinson bar", *Proceedings of the Institution of Civil Engineers - Engineering and Computational Mechanics*, vol. 171, (2017), pp. 3–13, doi: 10.1680/jencm.16.00027.

[119] Richard Curry, "Implementation of viscoelastic hopkinson bars", 2011.

[120] Hyunho Shin, Jae-Ha Lee, Jong-Bong Kim & Sung-Ik Sohn, "Design guidelines for the striker and transfer flange of a split hopkinson tension bar and the origin of spurious waves", *Proceedings of the Institution of Mechanical Engineers, Part C: Journal of Mechanical Engineering Science*, vol. 234, (2019), pp. 137–151, doi: 10.1177/0954406219869984.

[121] Robert C Juvinall & Kurt M Marshek, *Fundamentals of machine component design*, John Wiley & Sons, 2020.

[122] W.H. Dornfeld, "Presscylinder: Stresses in thick-walled cylinders", 2004.

[123] Richard Peter Merrett, "Dynamic response of aluminium foams", 2011.

[124] R A Govender, G S Langdon, G N Nurick & T J Cloete, "Impact delamination testing of fibre reinforced polymers using hopkinson pressure bars", *Engineering Fracture Mechanics*, vol. 101, (2013), pp. 80–90, URL `https://www.sciencedirect.com/science/article/pii/S0013794412003256`.

[125] Melchior Stander, "Development of an intermediate strain rate compression testing machine", 2014.

[126] Andrew Roginsky, "An experimental investigation into the anisotropic behaviour of bovine femoral cortical bone", 2017.

[127] "How to determine metal density", 2017, publisher: Canadian Conservation Institute (CCI).

[128] Summit measurement LLC, "How do i measure density?", URL `https://www.summitmeasurement.net/Articles.asp?ID=243`.

[129] Roger Walker, "Mass, weight, density or specific gravity of water at various temperatures", 2015.

[130] M F Spotts, "Mechanical design analysis", 1964.

Appendices

Appendix A

A general method for bar alignment

In any SHB setup, it is important that all bars lay concentric to one another. This is particularly important at the bar ends, where two or more bars are in contact. The concentricity of the bar ends can have a large influence on how effectively stress can be transferred across that boundary. Bar are supported near their end by clamps, as shown in Figure A.1, and alignment can be achieved by adjusting the clamps vertically and horizontally until the optimum position is reached.

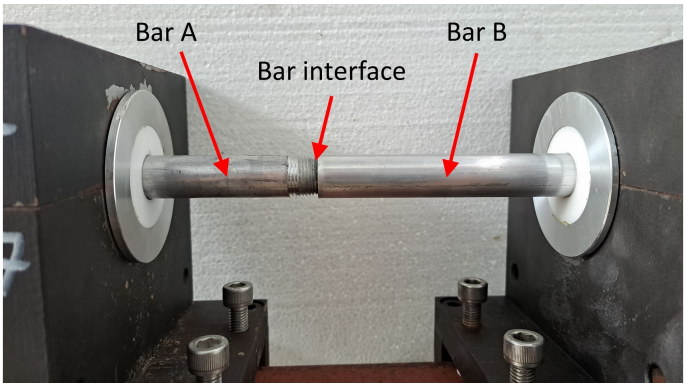

Figure A.1 Bars placed end-to-end

When the bars in question are of equal diameter, alignment can be assessed by tracing a finger over the bars, and feeling for a step. Since a very small discrepancy can be picked up by feel, this is a sufficient method of alignment. As seen in Figure A.2, the conical threads on bar A will make it impossible to align the bars by feel. To add to this, the bars are of different diameters. In this case, the standard method is not sufficient, and a different approach is required.

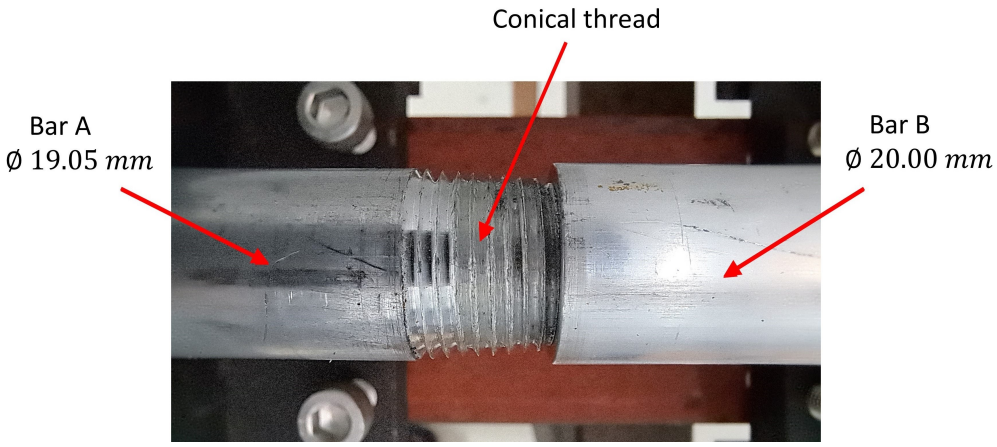

Figure A.2 Close view of the bar ends

Assessing Bar Run-out

Before aligning bars, it is good practice to assess the run-out at the bars ends. Run-out refers to how far a bar deviates from its ideal centre axis. The equipment required is:

- A dial indicator
- A stand for the indicator, with a magnetic base

Run-out can be tested by rotating the bars, with a dial indicator resting on their outer surface, as seen in Figure A.3. In this case, bar A was bent, so the support for that bar was moved very close to the bar end. Run-out was measured to be significantly less in this configuration.

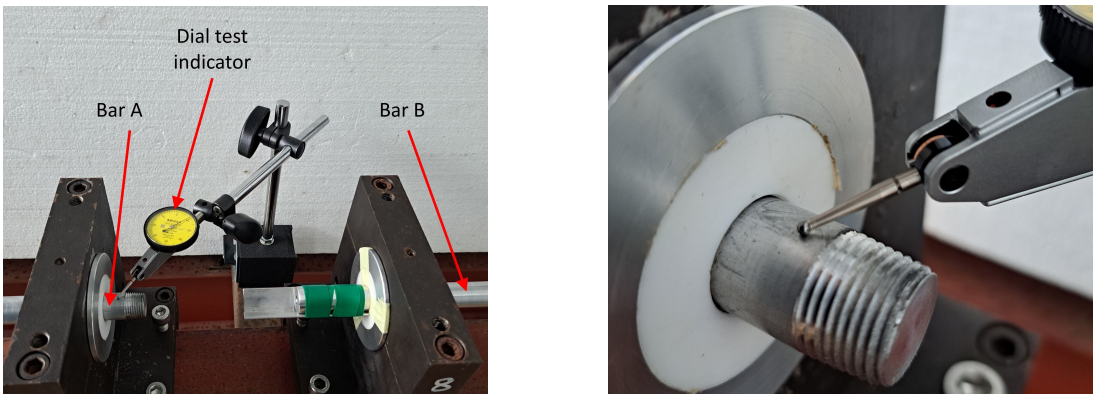

(a) The indicator setup **(b)** Testing height of top surface

Figure A.3 Quantifying run-out using a dial test indicator

If run-out is excessive, the quality of bar alignment will change if one of the bars is rotated. If needed, this can be overcome by marking and maintaining the angular position of the bars. This will ensure that bars are always in the same angular position relative to one another.

Aligning the Bars

A new alignment method was suggested by Dr Reuben Govender, and was used in this project. This method works for bars of unequal diameters, as well as for bars with cut features near the ends. The equipment required is:

- A 100mm long piece of right angle aluminium extrusion that is straight, as seen in Figure A.4a. The side length of the section should be approximately equal to the diameter of the larger bar.
- Insulation tape or cable ties
- A set of feeler gauges

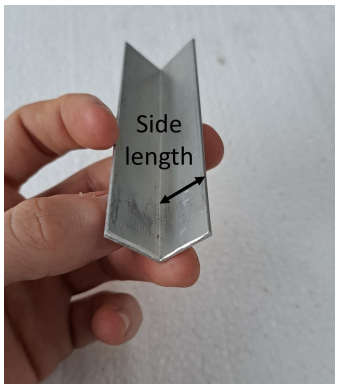

(a) Right angle aluminium extrusion

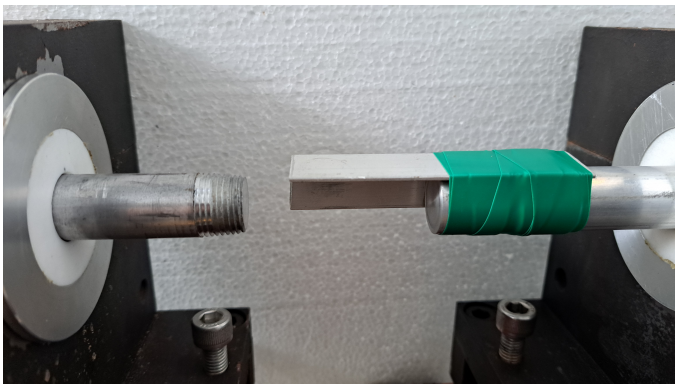

(b) Right angle aluminium extrusion taped firmly to the larger diameter bar

Figure A.4 The arrangement used for bar alignment

Firstly, make rough adjustments by eye. Secondly, firmly attach the right angle aluminium extrusion to the larger diameter bar, with half of it protruding as shown in Figure A.4b, and bring the two bars end-to-end.

Vertical and horizontal alignment will be adjusted separately, one at a time. Position the bars such that the gap between the top of the thinner bar, and the aluminium section, can be measured using the an appropriate feeler gauge (or a combination of gauges). Rotate the bars again such that the equivalent gap can be measured on the underneath of the

thinner bar. Adjust the clamps vertically, until the upper gap is equal to the lower gap. The comparative measurements of the upper and lower gaps can be seen in Figures A.5a and A.5b respectively.

(a) Measurement of the upper gap

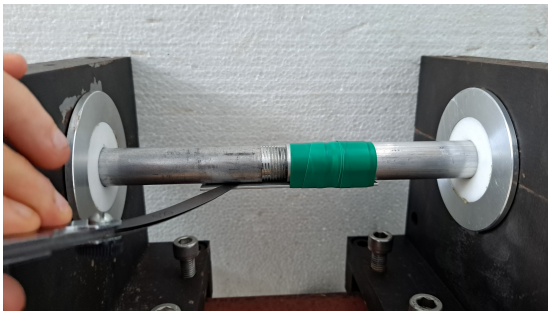

(b) Measurement of the lower gap

Figure A.5 Comparative measurement made for vertical bar alignment

Once vertical alignment has been achieved, use a similar method to align the bars horizontally, this time by comparing the gaps on either side of the bars. These measurements are shown in Figure A.6. Once the bars have been aligned both vertically and horizontally, remove the piece of aluminium extrusion. The degree of alignment achieved when using this method is more than adequate for producing reliable test results.

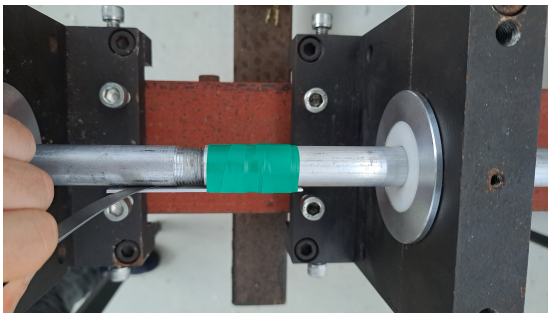

(a) Measurement of the right side gap

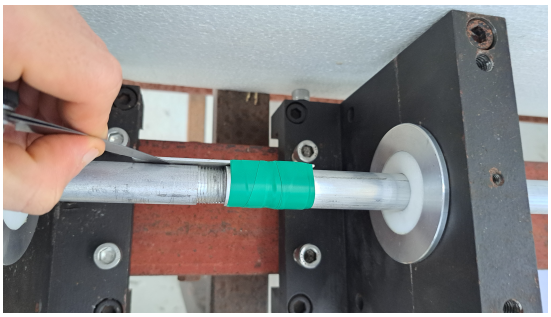

(b) Measurement of the left side gap

Figure A.6 Comparative measurement made for horizontal bar alignment

Appendix B

Limitations on Striker Speed

In SHPB testing, there are limits to the loading conditions that a given apparatus can produce. A practical interpretation of this is to consider the striker speed. As striker speed is raised, there comes a point where a component will fail. The aim of this section to to where the apparatus will fail first, and at what striker speed. It also will verify that the components in question are adequate for the task at hand.

The following ten failure points will be analysed:

- Failure of the input bar in uniaxial tension
- Failure of the striker tube in uniaxial tension
- Failure of the flange attachment threads, via both compressive bearing stress and shear stress (stripping) on the following components:
    - ⋆ Striker flange
    - ⋆ Striker tube
    - ⋆ Input flange
    - ⋆ Input bar

Using one-dimensional wave theory [130], and the material properties of the tensile striker (subscript s) and input bar (subscript b), the stress in the input bar due to the impact can be calculated using Equation B.1.

$$\sigma_b = v_0 \cdot \frac{\rho_b c_b \rho_s c_s A_s}{\rho_b c_b A_b + \rho_s c_s A_s} \tag{B.1}$$

This stress can be used along with bar geometry to attain the force applied by the striker upon impact, F_i. For force equilibrium at the point of impact, this force is equal to that

in the striker, as well as in the threads on the striker and input flanges. Equations B.2 and B.3 can be used to calculate the bearing and shear stresses in the threads. Since these threads are tapered, an average value was used for all diameters, and the stresses were from there assumed to be straight threads.

$$\sigma_{bearing} = \frac{4 \cdot F_i \cdot p}{\pi \cdot L \cdot ({d_{major}}^2 - {d_{minor}}^2)} \tag{B.2}$$

In Equation B.2, p is the thread pitch, L is the length of the threaded portion of the part, and d_{major} and d_{minor} are the average major and minor diamters of the thread.

$$\sigma_{shear} = \frac{F_i}{\pi \cdot d_{root} \cdot L} \tag{B.3}$$

In Equation B.3, d_{root} is the root diameter of the thread. For external threads, d_{root} is d_{minor}, and for internal threads d_{root} is d_{major}. Safety factors were calculated for axial stress in the input bar and striker, as well as for both failure modes for each or the four parts mentioned above. Tables B.1, B.2, and B.3 present these safety factors for striker speeds of 10 m/s, 20 m/s and 30 m/s respectively. At $v_0 = 30$ m/s, the safety factor on tensile stress in the striker tube is 1.03, indicating that failure is likely to occur at that region of striker speeds. No experiments in this project exceeded a striker speed of 15 m/s, indicating that no safety factor was ever lower than 2.0 during typical operating conditions.

Table B.1 *Table of critical safety factors, at v_0 = 10 m/s*

Item	**Failure mode**		**Safety factor at v_0 = 10 m/s**
Input bar	Uniaxial tension		8.42
	Threads	Bearing stress	6.31
		Shear stress	6.8
Striker tube	Uniaxial tension		3.10
	Threads	Bearing stress	6.30
		Shear stress	5.36
Input flange	Threads	Bearing stress	14.1
		Shear stress	12.7
Striker flange	Threads	Bearing stress	22.1
		Shear stress	18.2

Table B.2 *Table of critical safety factors, at v_0 = 20 m/s*

Item	**Failure mode**		**Safety factor at v_0 = 20 m/s**
Input bar	Uniaxial tension		4.21
	Threads	Bearing stress	3.16
		Shear stress	3.40
Striker tube	Uniaxial tension		1.55
	Threads	Bearing stress	3.15
		Shear stress	2.68
Input flange	Threads	Bearing stress	7.05
		Shear stress	6.35
Striker flange	Threads	Bearing stress	11.1
		Shear stress	9.12

Table B.3 *Table of critical safety factors, at v_0 = 30 m/s*

Item	**Failure mode**		**Safety factor at v_0 = 30 m/s**
Input bar	Uniaxial tension		2.81
	Threads	Bearing stress	2.10
		Shear stress	2.27
Striker tube	Uniaxial tension		1.03
	Threads	Bearing stress	2.10
		Shear stress	1.79
Input flange	Threads	Bearing stress	4.70
		Shear stress	4.23
Striker flange	Threads	Bearing stress	7.38
		Shear stress	6.08

Appendix C

Supplementary Design Material

The following appendix describes the design of components used in this project, that are not pertinent to the design requirements outlined in Section 3.1.

C.1 Compressive Barrel Air Supply

When compressive tests are required, the sleeve cap, installed with a push-in pneumatic fitting, is threaded into th sleeve mount by hand. A 12 mm diameter pneumatic tube then plugs into the fitting, supplying compressed gas from the blue gun when firing. This assembly on the rear of the sleeve is shown in Figure C.1.

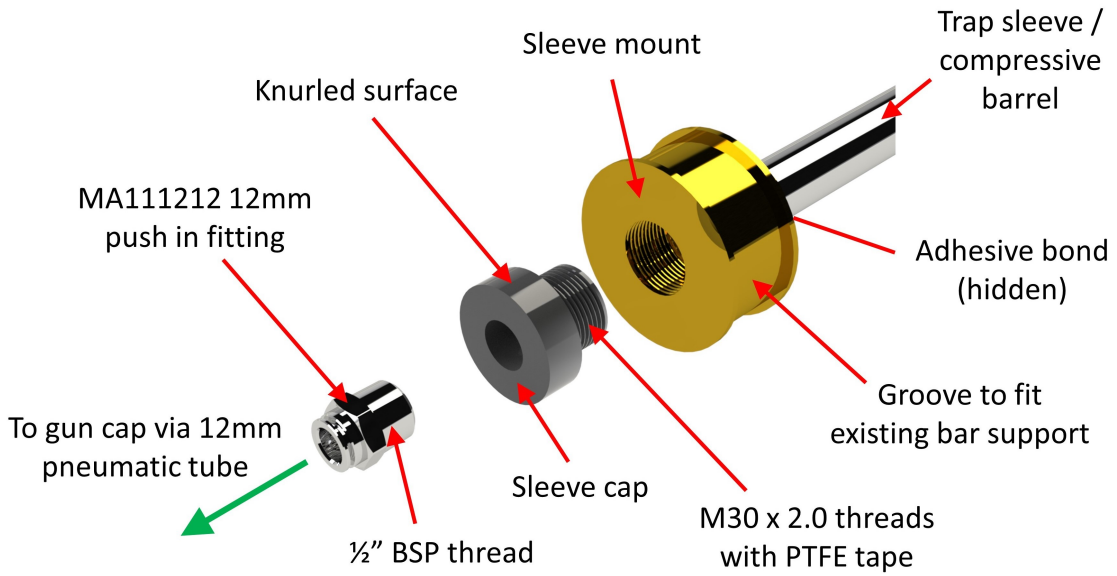

Figure C.1 Isometric exploded view of the isolator and compressive barrel hardware

When the isolator sleeve is being used as a compressive barrel, the gas is supplied via a flexible pneumatic tube originating from the blue gas gun. The blue gas gun feeds compressed air into the tube when fired, by means of the gun cap assembly. This is pictured below in Figure C.2. The gun cap replaces the barrel of the blue gun, and it held in place using the existing barrel retention nut. The flexible tube is attached to this assembly via a push-in pneumatic fitting.

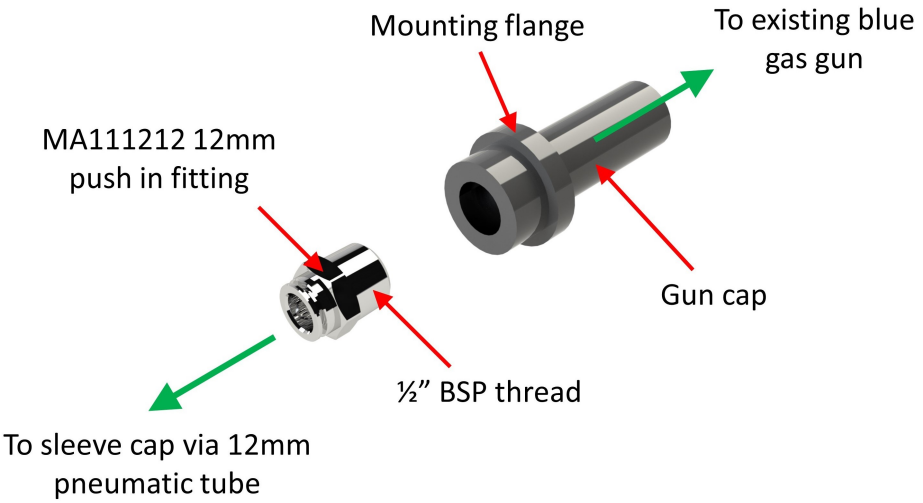

Figure C.2 Isometric exploded view of the gun cap assembly for use on the existing blue gas gun at BISRU

C.2 Bar Bushings

Existing bar supports were use to hold and align the bars and traps of this system. All bar supports required bushings to be made, which are tailored to the bars. At BISRU the tried and tested style of bar bushing is the PTFE-in-brass design. It is made up of a PTFE inner, that is pressed into a brass outer. The brass outer is clamped in the bar support, while the bar sits inside a bore in the PTFE inner. The PTFE is used as a bushing material, as it has very low friction and low impedance. The brass outer was added to protect the softer PTFE against damage when installing or removing the bushings from the bar support. Brass, being cheaper than PTFE, was the a more cost-effective method to fill the annular space when using a small diameter bar in a support with a large bore. In this project, 6000 series aluminium was used in place of brass as it is yet more cost effective. The press fit of the two bushing elements was supplemented by flared ends on the inner, and corresponding chamfers on the bore of the outer. This positive engagement further dissuades the inner from slipping out. A typical bar bushing assembly is picture in Figure C.3.

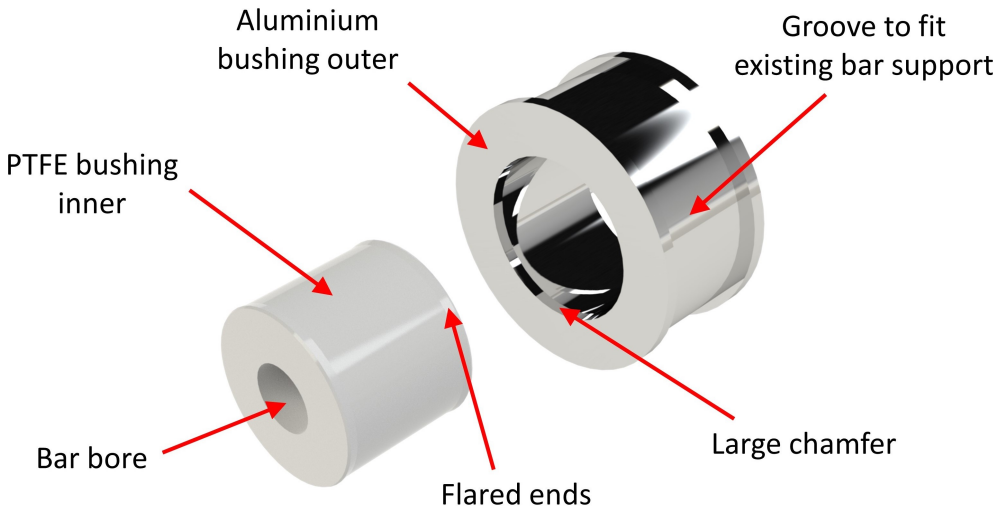

Figure C.3 Exploded view of a bar support bushing

The thermal expansion coefficient of PTFE is 120 m m^{-1} $°C^{-1}$ is large compared to that of the aluminium bushing outers. This causes issues with bar fitment over the temperature range that can be expected in the laboratory. Temperature effects are accounted for by having a summer and winter set of bar bushings for this apparatus. All bushings require an accurately located, but free sliding fit on their respective bars. Since the boring of the PTFE inners was largely tuned by feel, the winter bushing bushing set was machined on a cold day, and the summer set on a hot day. This ensures that the bar bushings can perform optimally across a range of temperatures. Table C.1 below summarizes the sizes and quantities of the bar bushings required.

Table C.1 *Required bushing sizes, quantities, and fitting condition*

Bar	**Diameter [mm]**	**Quantity**	**Fitting conditions**	
			Fit	**Temperature***
Input bar	19.05	4	Sliding	C
		4	Sliding	H
Output bar	19.05	1	Sliding	C
		1	Sliding	H
Secondary trap	TBD, $\leq$ 20.00	2	Sliding	C
		2	Sliding	H
	20.00	2	Sliding	C
Output trap	TBD, $\leq$ 30.00	2	Sliding	C
		2	Sliding	H
	30.00	2	Sliding	C

* H = $\geq$ 24°C, C = $\leq$ 16°C

C.3 Gas Gun Supports

Since the gas gun is of novel design, it requires two supports to be manufactures to secure it to the bed, and align it appropriately. As seen in Figure C.4, the support takes a very similar form to the existing bar supports, where the gun is clamped in a split bore and is secured by bolts. Alignment pins are used in conjunction. The base of the support stands on four vertical jacking screws, and has four horizontal one on its side. These eight jacking screws allow the support to be aligned. There is a bed clamp that runs underneath the SHPB bed below the support. Through the use of bolts, this allows the supports to be firmly secured to the bed.

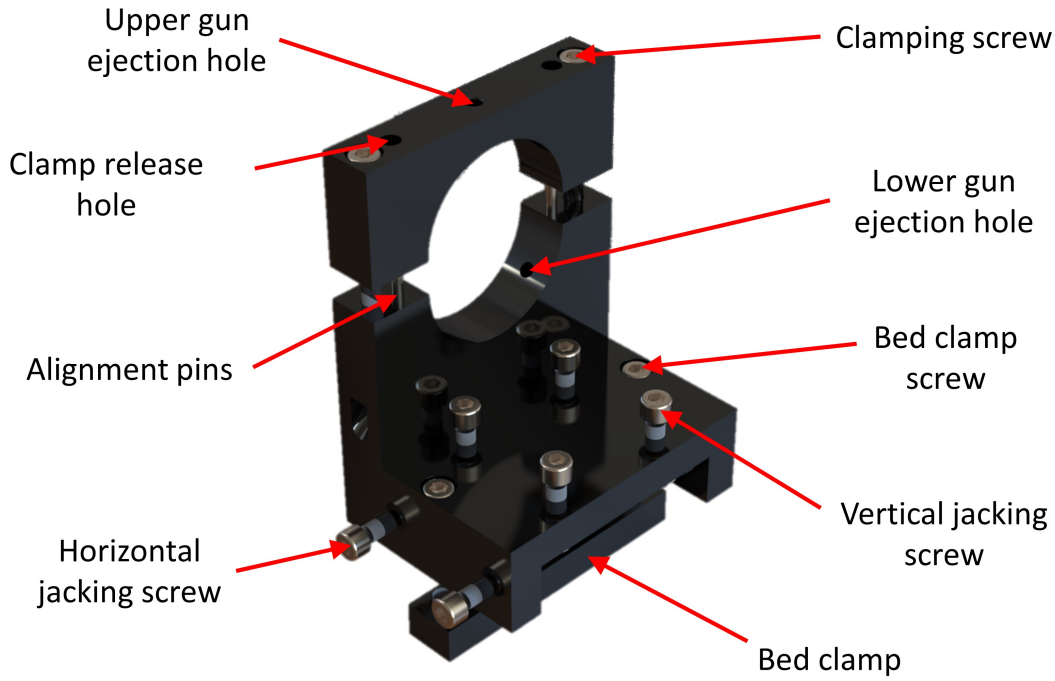

Figure C.4 Isometric view of the gas gun support

Additional features were added beyond those mentioned above. The vertical member of the support assembly is placed on one side of the clamp base. This is due to the large diameter gas gun end flanges that sit lower than the support base. This improves access to jacking screws. The bed clamp, that runs underneath the SHPB bed below the support, incorporates threaded holes. Through the use of bolts, this allows the supports to be firmly secured to the bed. Previously this had been done using nuts thread rods, which introduces the need for a 17 mm spanner. Now the entire clamp can be operated with one tool, that being an 8 mm Allen key. Small feet were 3D printed in PLA for the end of each jacking screw. This was done to prevent damage to the painted SHPB beds when

the jacking screws are tightened or when the support is slid along the bed. These were added to all bar supports used. The PLA feet add some compliance to the jacking screws, which made the alignment process simpler. This compliance was reduced once the bed clamp was tightened sufficiently, so the supports retained their rigidity for testing. The rest of the modifications were features added to ease the process of removing the gun from the support. These features are all labelled in the cross-section in Figure C.5.

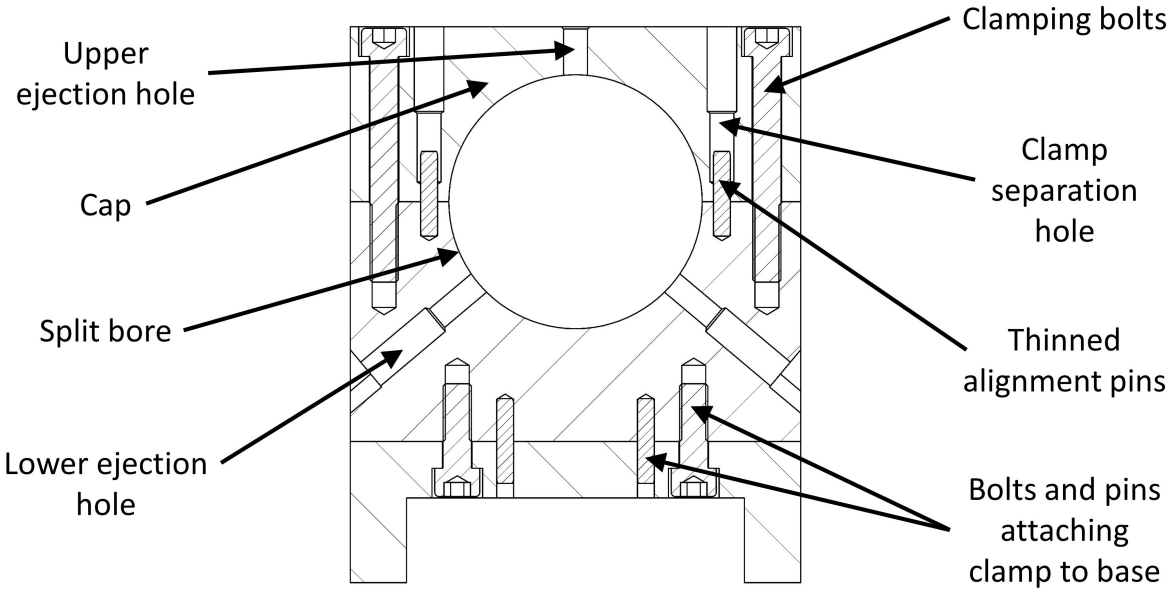

Figure C.5 Cross section of the gas gun clamp design

Once the clamping bolts have been removed, the cap remains tightly bound around the bore of the gun. The pressed-fitted alignment pins also prevent it from lifting off. The clamping bolts can be screwed into the threaded clamp separation holes. When tightened, they press on the tops of the alignment pins, separating the cap from the rest of the clamp. Pressing on the alignment pins themselves ensure that they remain pressed into the lower half of the clamp, and not in the cap. The top portion of the alignment pins have been ground to a slightly reduced diameter, so that once the clamp had separated far enough, the pins only fit loosely on the dowel holes of the cap, and it can simply be lifted off by hand.

Now that the clamp is separated, it is highly probable that the gas gun's mounting feature remains jammed in the bore of either the lower half of the clamp, or of the cap. If the gun remains stuck in the lower half, the clamping bolts can be screwed into the lower ejection holes to push the gun out. Alternatively, if the gun sticks in the bore of the cap, the upper ejection hole can be used. The improves the usability of the gun supports, as preserves the hardware as no hammering is required to separate the components.

C.4 Light Trap

Conventional light trapping shall be used for the compressive tests, as it is simplest to implement. As the striker reaches the end of the barrel, it passes through the trap, sequentially breaking two beams of light. These beams are typically emitted by infrared LEDs, and received on the opposite side of the trap by phototransistors. The time difference Δt between these instances is acquired using an oscilloscope. Knowing the physical distance Δx between the light beams, the striker velocity, v_0, just before impact can be calculated using Equation C.1.

$$v_0 = \frac{\Delta x}{\Delta t} \tag{C.1}$$

This method effectively uses the strikers average velocity of the last Δx of travel before it impacts the input bar. Since compressive gas gun barrels in this application typically have venting holes, the striker is usually no longer accelerating when it passes the light trap as there is no longer significant gas pressure driving it. The striker is moving at close to constant velocity at this point, and so using this metric of an average velocity is representative of v_0. Disadvantages of the this style of speed sensing include that the light trap must be located very close to the point of impact with the input bar, which wan get in the way. In addition, the beams of light must remain unobstructed before the striker arrives, and so nested striker arrangements pose difficulty.

The light trap body is the only component that requires a redesign, as the remaining hardware and electronic instrumentation exists at BISRU. It will be attached to the end of the compressive barrel when such tests are being conducted, and therefore needs to correspond closely with the dimensions and features. A labelled diagram of the new body design is displayed in Figure C.6.

The light trap body takes the form of a hollow cylinder, which fits snugly over the end of the barrel. Two through-holes allow for the mounting of the infrared LEDs and phototransistors. These holes need to align with the through-holes on the barrel end, as the light needs to be able to pass through the path of the striker. The key and end flange provide locating features for the rotational and axial positions respectively, ensuring that the holes can be aligned quickly and easily when installing the trap on the barrel. The barrel end and its features are displayed in Figure C.7.

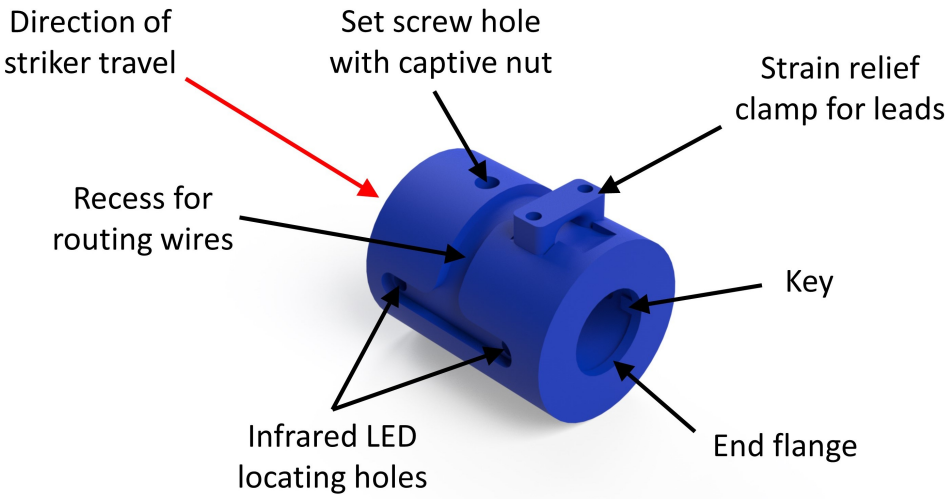

Figure C.6 Isometric view of the compressive light trap body

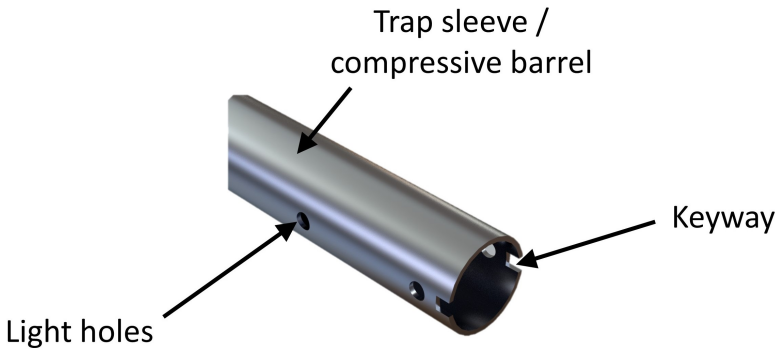

Figure C.7 Isometric view of the compressive barrel end

A hole, with provision for a captive nut, allows the light trap to be secured to the barrel by means of a set screw. Wire recesses, as well as a strain relief clamp are included to protect delicate wiring against knocks and tugs. The light trap body shall be 3D printed in PLA.

C.5 Custom Tooling

The design has made use of off-the-shelf fasteners, and requires standard tools for all maintenance and operations. The exceptions are the tightening of the three titanium flanges, and the tightening of the fir-tree specimen clamps. As described in Section 2.4.5, the current fir-tree tightening tool is problematic. These tools will complete the tooling aspect of this apparatus, ensuring that Requirement RQ15 on tooling is met. The design of these two custom tools are described below.

C.5.1 Flange Spanner

The tensile SHB outlined in this report makes used of three titanium flanges, namely:

1. The input flange on the input bar.
2. The striker flange, which impacts the input flange to create the tensile stress pulse.
3. The transfer flange on the output bar, which passes the stress wave into the output momentum trap.

All of these flanges screw to their parent sub-assemblies by means of a 5° tapered thread with pitch of 1.5 mm. A custom tool was designed to be used to tighten them. The tool has two sides, as shown in Figure C.8, each with protruding pins that act on holes in the various flanges, shown in Figure C.9. One end has the pins positioned 23 mm apart, and the other, 25 mm. This is done because the striker flange is larger than the other two, making it impossible to standardise the pitch circle diameter of the pin holes across all three flanges.

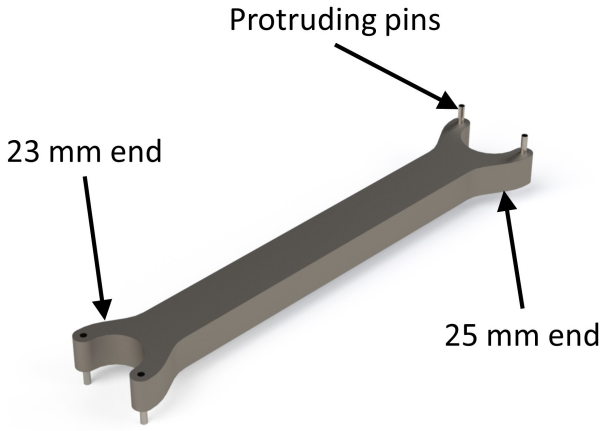

Figure C.8 Isometric view of the flange tool

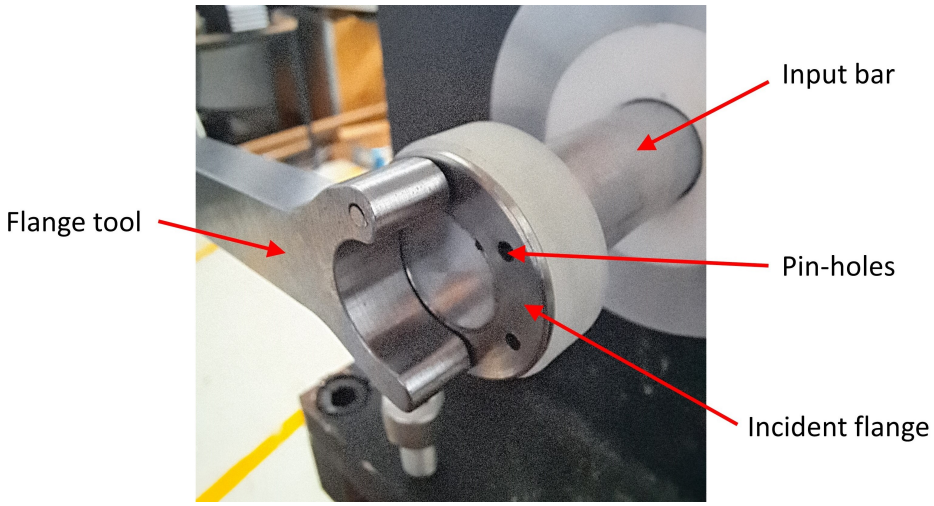

Figure C.9 Photograph of the tool securing the input flange

The length of the tool is such that the average human is unable to over-tighten any flanges using this tool. The tool body was manufactured from K110 tool steel. This material choice was made to ensure that the pressed pins remain secured over time and use, as well as to prevent excessive corrosion.

C.5.2 Specimen Clamp Spanner

Due to the collet-like nature of the fir-tree specimen clamping fixture described in Section 2.4.5, the dimensions of the conical clamps will change as it is tightened into the female threads on the pressure bars. It has been noted in past projects [89] that have used this clamp that the holes used to tighten the fixture, using a tool, are becoming damaged. As the fixture gets tightened, the four holes move closer together. This is a problem, as the pins in the current tool are fixed, and cannot move. This creates additional stress on these small holes. This problem will addressed by designing a new tool that can be used to tighten the clamps.

The new tool must incorporate the following features:

- The pins on the tool shall be able to move to follow the position of the holes on the clamps.
- The tool shall prevent over-tightening
- The tool shall be able to be manufactured using the machines available in the mechanical workshop at UCT.
- Using the tool shall be an easy process

The proposed design, conceptualised by Dr Trevor Cloete, is shown below in Figure C.10.

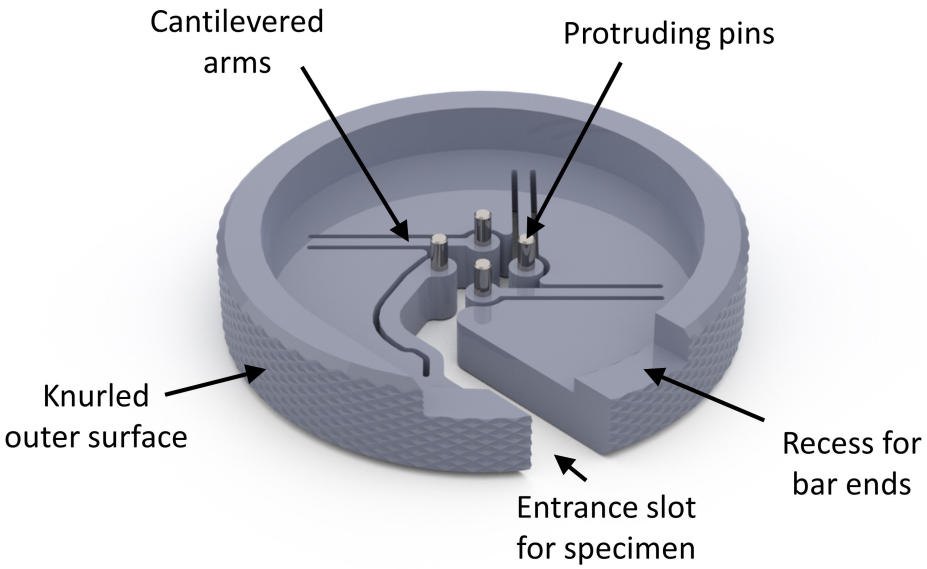

Figure C.10 Tool for installing the specimen clamps

The critical part of the design was the sizing of the cantilevered arms that support the pins. These arms are what provide the pins with the required flexibility to stay aligned, as well as the strength to tighten the fixture. The length, width, and thickness of the arms were estimated to give the tool suitable properties. These dimensions can be optimised in later iterations. An added benefit to the flexible arms is that there is allowance for machining inaccuracies, both in the tool and in the clamps. The diameter of the tool is sized such that the average human is unable to over tighten the clamping fixtures. The knurl provides for a better grip. As was with the flange tool, K110 tool steel was used. The tool can be manufactured using, at most, a lathe, a manual milling machine, and an EDM wire cutter.

This tool was manufactured as a first prototype. It requires further revision, which falls outside of the scope of the project due to time constraints. The exiting tool was used for experiments in this project.

Appendix D

Wave Speed Test - Extended Results

Table D.1 *Extended results for Young's modulus across ten wave speed tests for the 7075 T6 aluminium bar stock*

Test number	**Modulus [GPa]**
1	73.62
2	73.62
3	73.61
4	73.58
5	73.61
6	73.66
7	73.68
8	73.62
9	73.66
10	73.65
Maximum [GPa]	73.68
Minimum [GPa]	73.58
Mean [GPa]	73.631
Std. Dev. [GPa]	0.02879

Table D.2 *Extended results for Young's modulus across ten wave speed tests for the 6082 T6 aluminium bar stock*

Test number	**Modulus [GPa]**
1	72.67
2	72.68
3	72.67
4	72.69
5	72.68
6	72.69
7	72.69
8	72.69
9	72.68
10	72.67
Maximum [GPa]	72.69
Minimum [GPa]	72.67
Mean [GPa]	72.68
Std. Dev. [GPa]	0.008307

Table D.3 *Extended results for Young's modulus across ten wave speed tests for the aluminium tube stock*

Test number	**Modulus [GPa]**
1	67.84
2	67.85
3	67.85
4	67.87
5	67.85
6	67.84
7	67.83
8	67.82
9	67.83
10	67.81
Maximum [GPa]	67.87
Minimum [GPa]	67.81
Mean [GPa]	67.84
Std. Dev. [GPa]	0.01640

Appendix E

Pressure Bar Calibration - Extended Results

Table E.1 *Extended input bar calibration results*

Calibration factor K = 34.57 MPa V V^{-1}					
Test	**Bridge voltage [V]**	**Striker speed [m/s]**	**Experimental stress [MPa]**	**Theoretical stress [MPa]**	**Error [%]**
1	2.06	7.35	-54.802	-52.892	3.49
2	2.20	8.97	-63.538	-64.514	1.54
3	2.20	6.80	-48.038	-48.934	1.87
4	2.98	8.23	-57.901	-59.204	2.25
5	2.69	7.35	-51.702	-52.892	2.30
6	2.79	6.78	-47.526	-48.768	2.61
7	2.89	5.97	-41.829	-42.945	2.67
8	2.89	6.43	-45.107	-46.259	2.55
9	2.89	7.55	-53.062	-54.289	2.31
10	2.89	6.25	-43.912	-44.958	2.38
Mean error [%]					3.12
Standard deviation in error [%]					0.39

Table E.2 *Extended output bar calibration results*

Calibration factor K = 34.57 MPa V V^{-1}					
Test	**Bridge voltage [V]**	**Striker speed [m/s]**	**Experimental stress [MPa]**	**Theoretical stress [MPa]**	**Error [%]**
1	2.65	7.27	-50.597	-52.315	3.40
2	2.70	5.75	-40.147	-41.341	2.97
3	2.63	5.57	-38.557	-40.074	3.94
4	2.64	7.33	-50.948	-52.698	3.44
5	2.64	10.15	-70.936	-73.028	2.95
6	2.36	8.66	-60.429	-62.280	3.06
7	2.36	9.57	-67.213	-68.835	2.41
8	2.52	7.94	-55.418	-57.090	3.02
9	2.50	6.02	-41.998	-43.333	3.18
10	2.52	10.20	-71.403	-73.401	2.80
Mean error [%]					2.40
Standard deviation in error [%]					0.49

Appendix F

Experimental setup for Quasi-static Tensile Tests

Figure F.1 shows how the hardware was arranged on the Zwick Roell 1484 universal testing machine in the Centre for Material Engineering. In Figure F.1a, the static top end of the specimen is attached to the Zwick via the load cell. The lower end of the specimen is then attached to the moving crosshead of the machine, as shown in F.1b.

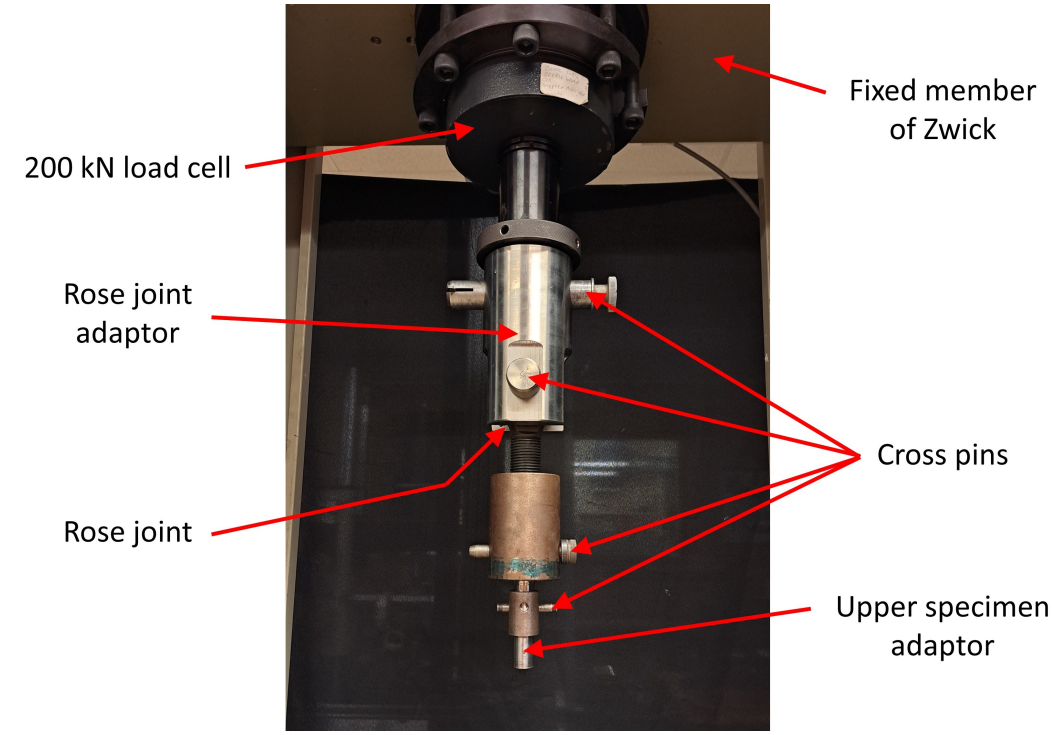

(a) Top (fixed) end of setup

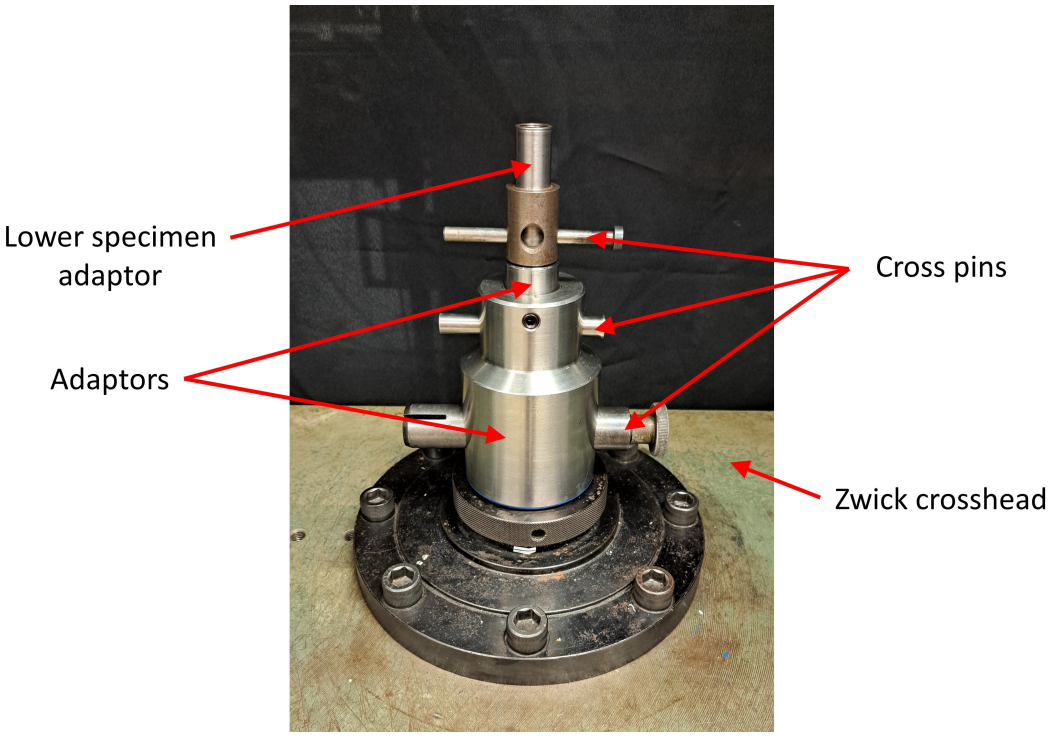

(b) Bottom (moving) end of setup

Figure F.1 Experimental setup in the Zwick

Appendix G

Impedance Matching the Solid Input-side Traps - Extended Results

Table G.1 *Extended results from the solid trap impedance test with 20 mm trap diameter*

Test	Incident stress [MPa]	Reflected stress [MPa]	Reflected stress [%]	Theoretical reflected stress [MPa]	Error [%]
1	-78.808	-2.969	3.77	-2.879	3.13
2	-48.769	-1.729	3.55	-1.782	2.97
3	-40.646	-1.920	4.72	-1.485	29.29
4	-36.464	-1.583	4.34	-1.332	18.84
5	-64.730	-2.471	3.82	-2.365	4.48
6	-68.173	-2.565	3.76	-2.490	3.01
7	-49.731	-1.842	3.70	-1.817	1.38
8	-42.627	-1.527	3.58	-1.557	1.93
9	-61.980	-2.259	3.64	-2.264	0.22
10	-61.539	-2.268	3.69	-2.248	0.89
Mean fraction [%]			3.86	**Mean error [%]**	6.61
Standard deviation in fraction [%]			0.34	**Standard deviation in error [%]**	8.69

Table G.2 *Extended results from the solid trap impedance test with 19.60 mm trap diameter*

Test	**Incident stress [MPa]**	**Reflected stress [MPa]**	**Reflected stress [%]**	**Theoretical reflected stress [MPa]**	**Error [%]**
1	-57.639	-0.466	0.81	-0.942	50.53
2	-59.668	-0.515	0.86	-0.975	47.18
3	-54.381	-0.527	0.97	-0.889	40.72
4	-69.884	-0.742	1.06	-1.142	35.03
5	-41.942	-0.344	0.82	-0.685	49.78
6	-38.059	-0.180	0.47	-0.622	71.06
7	-61.690	-0.714	1.16	-1.008	29.17
8	-61.710	-0.568	0.92	-1.009	43.71
9	-68.535	-0.769	1.12	-1.120	31.34
10	-36.632	-0.199	0.54	-0.599	66.78
Mean fraction [%]			0.87	**Mean error [%]**	46.53
Standard deviation in fraction [%]			0.21	**Standard deviation in error [%]**	12.60

Appendix H

Two-phase Tandem Trap Verification Tests

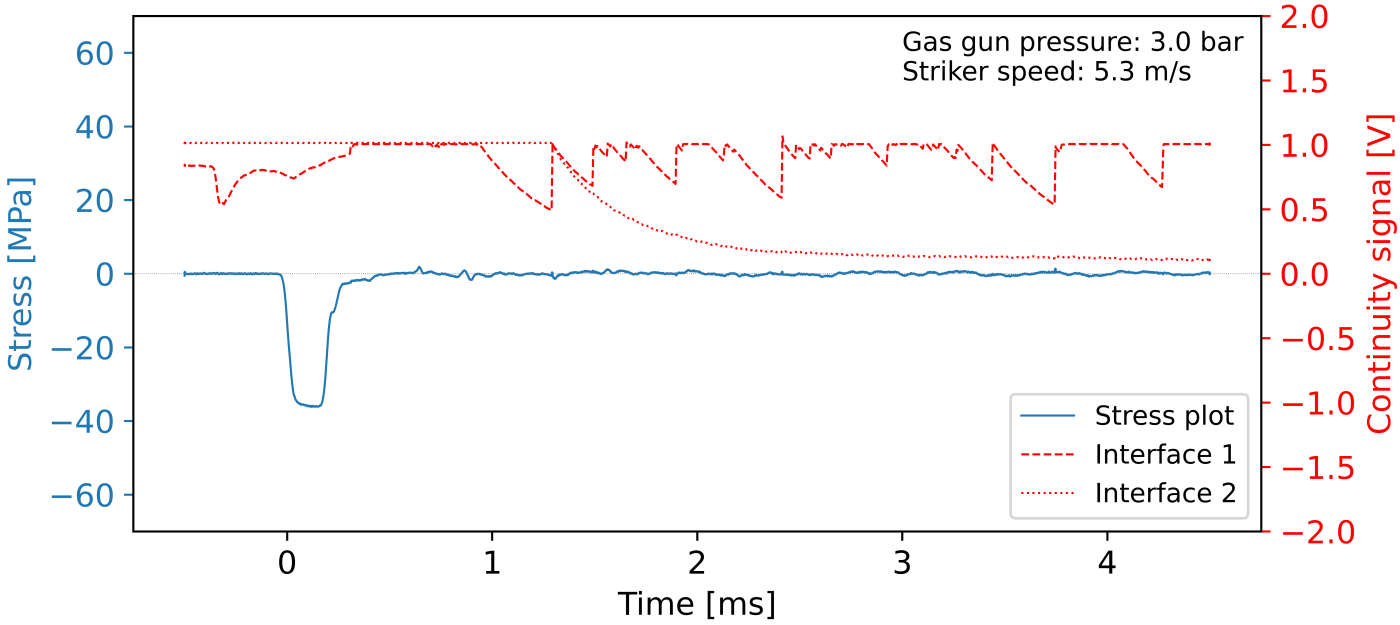

(a) Response to phase 1

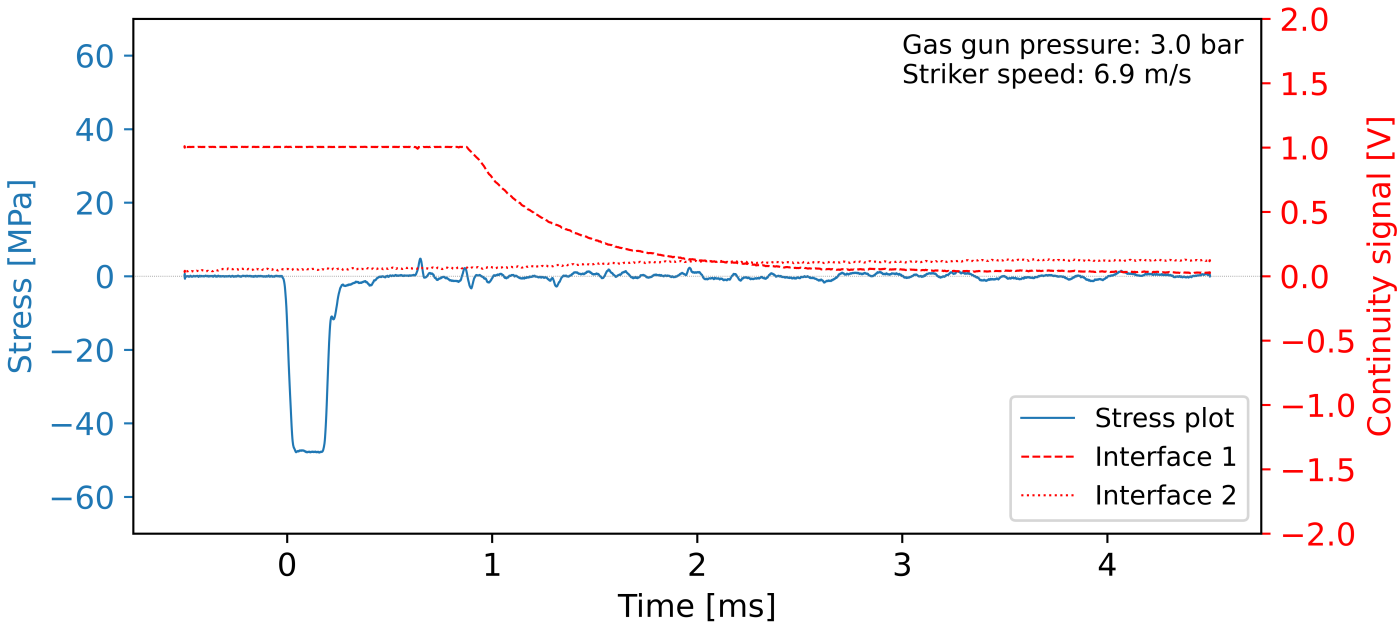

(b) Response to phase 2

Figure H.1 Results of two-phase tandem verification tests using Vaseline on interface 1

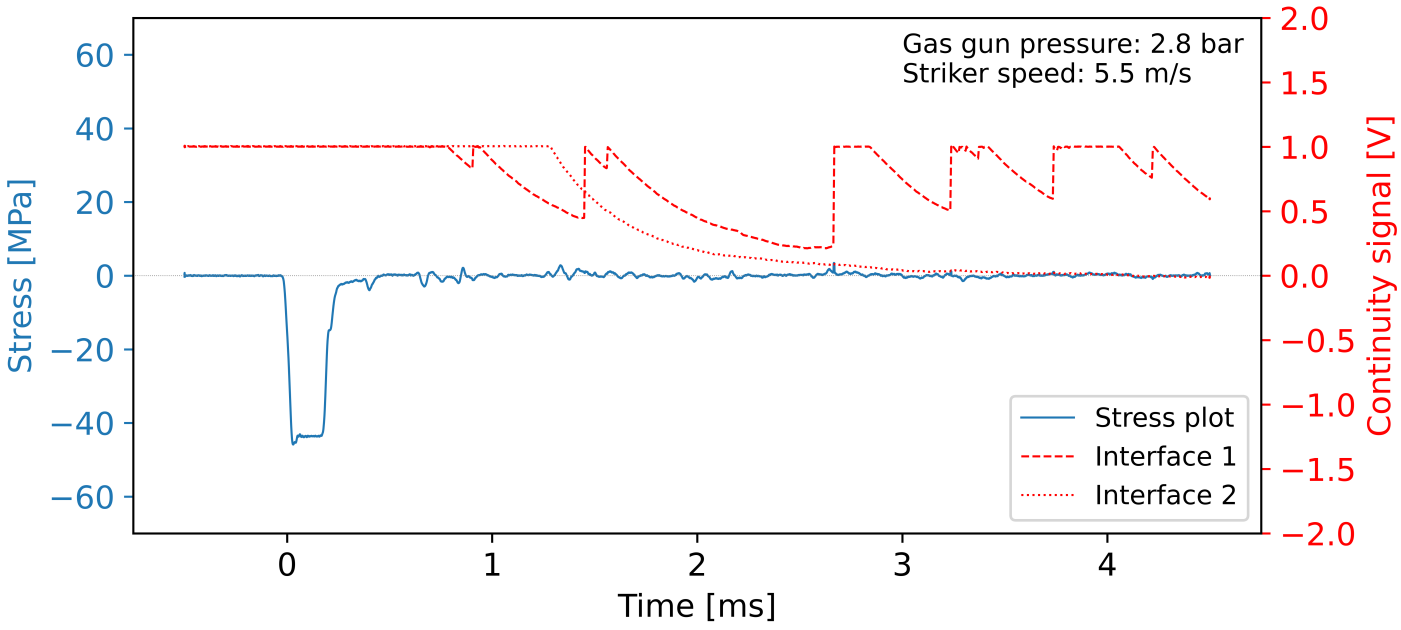

(a) Response to phase 1

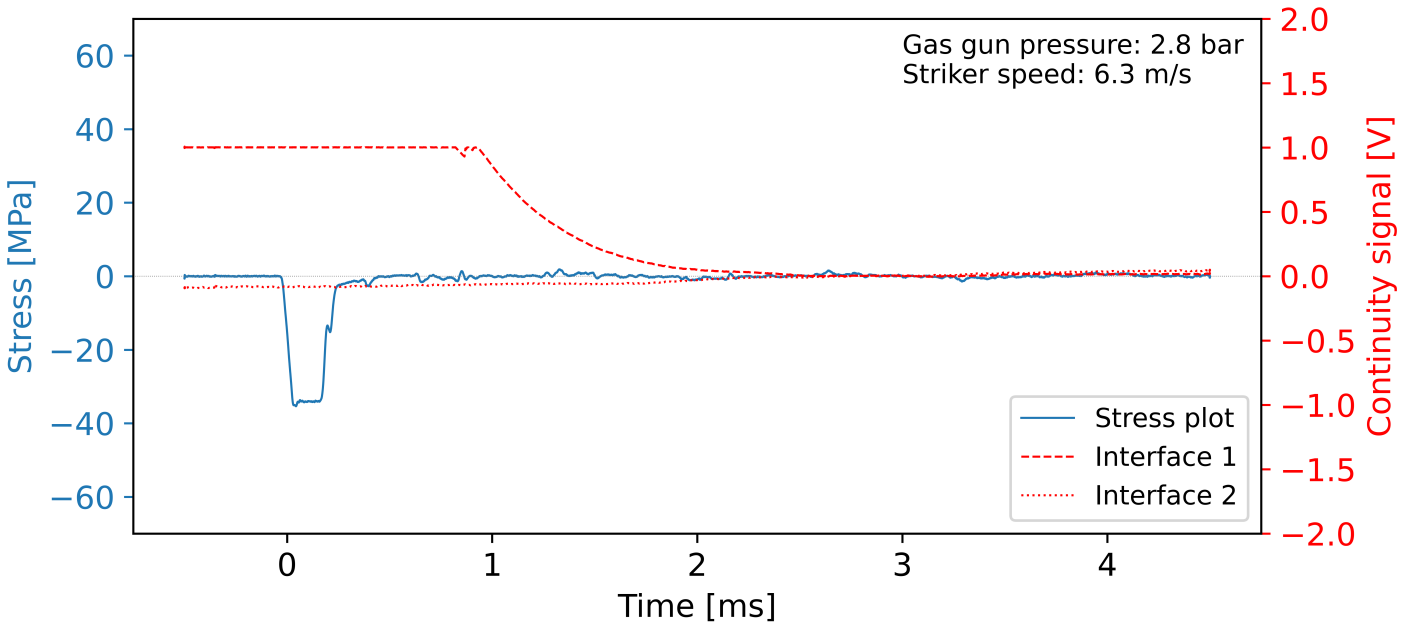

(b) Response to phase 2

Figure H.2 Results of two-phase tandem verification tests using red rubber grease on interface 1

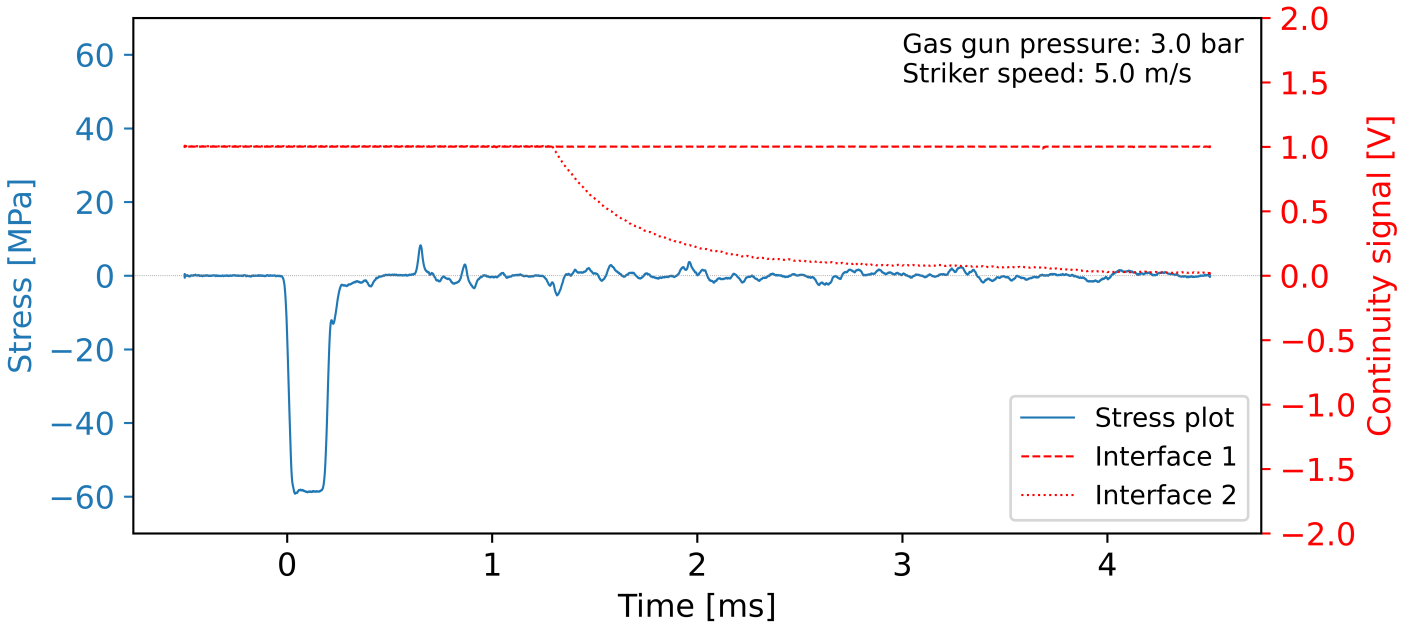

(a) Response to phase 1

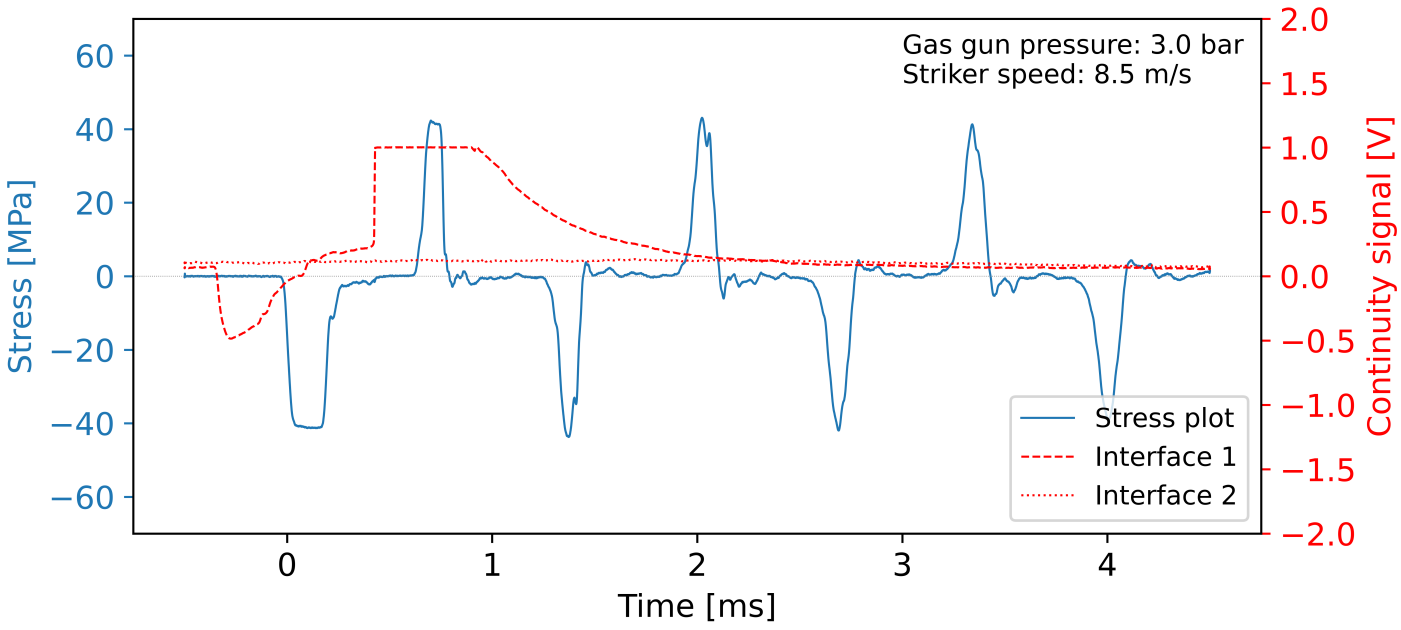

(b) Response to phase 2

Figure H.3 Results of two-phase tandem verification tests using aluminium foil on interface 1

Appendix I

Momentum Trap Functionality - Further Signal Plots

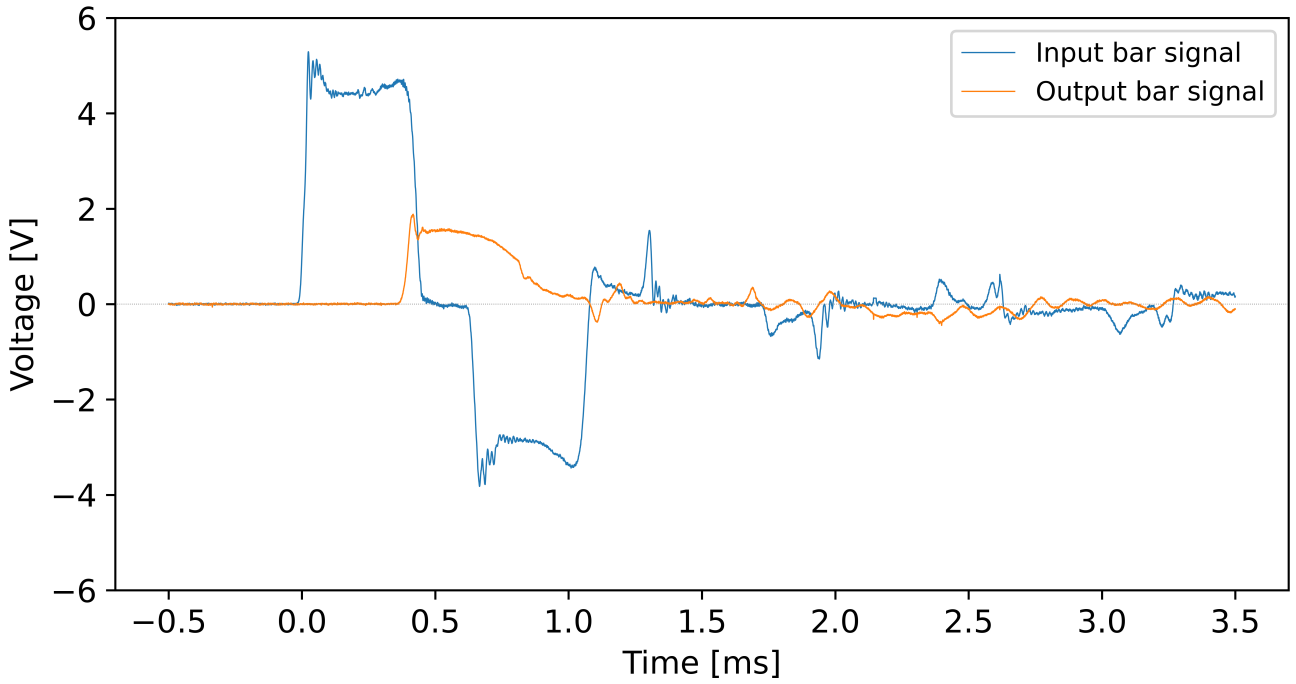

(a) Signals recorded from an interrupted test, M3, using full momentum trapping

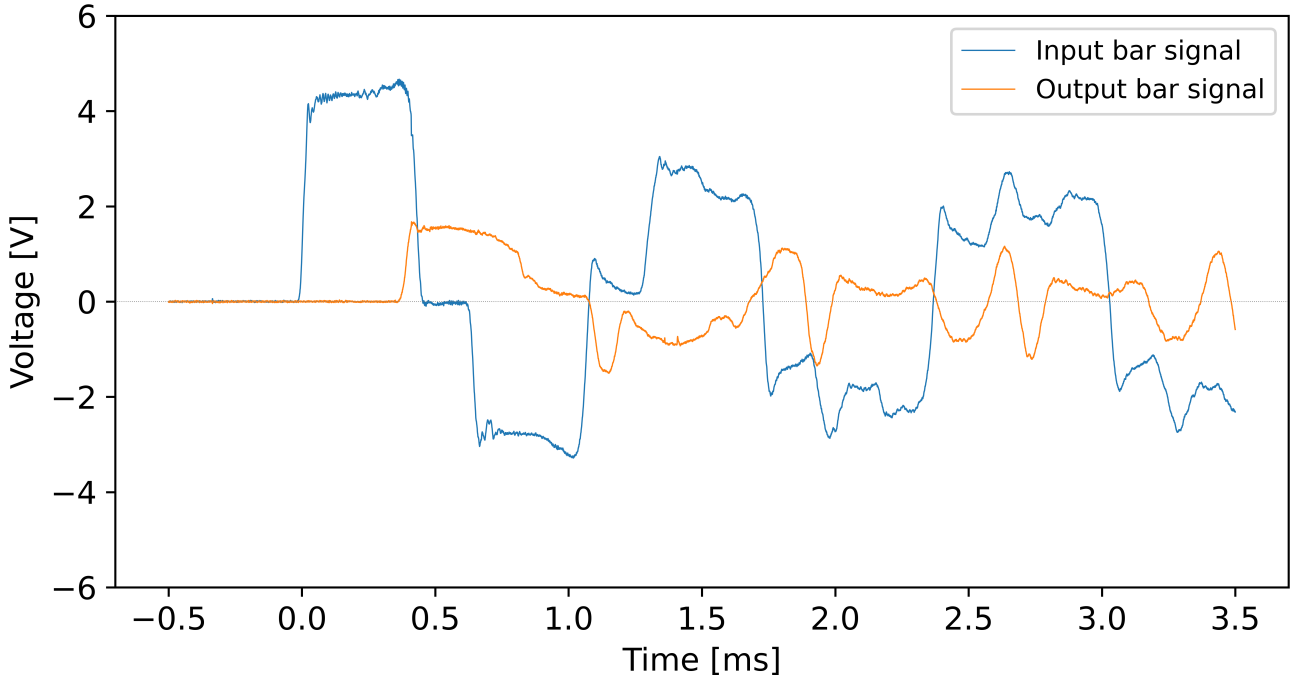

(b) Signals recorded from an uninterrupted test, M4, using only primary momentum trapping

Figure I.1 Comparison of the recorded signal for interrupted versus uninterrupted TSHB tests, at $v_0 = 11.5$ m/s

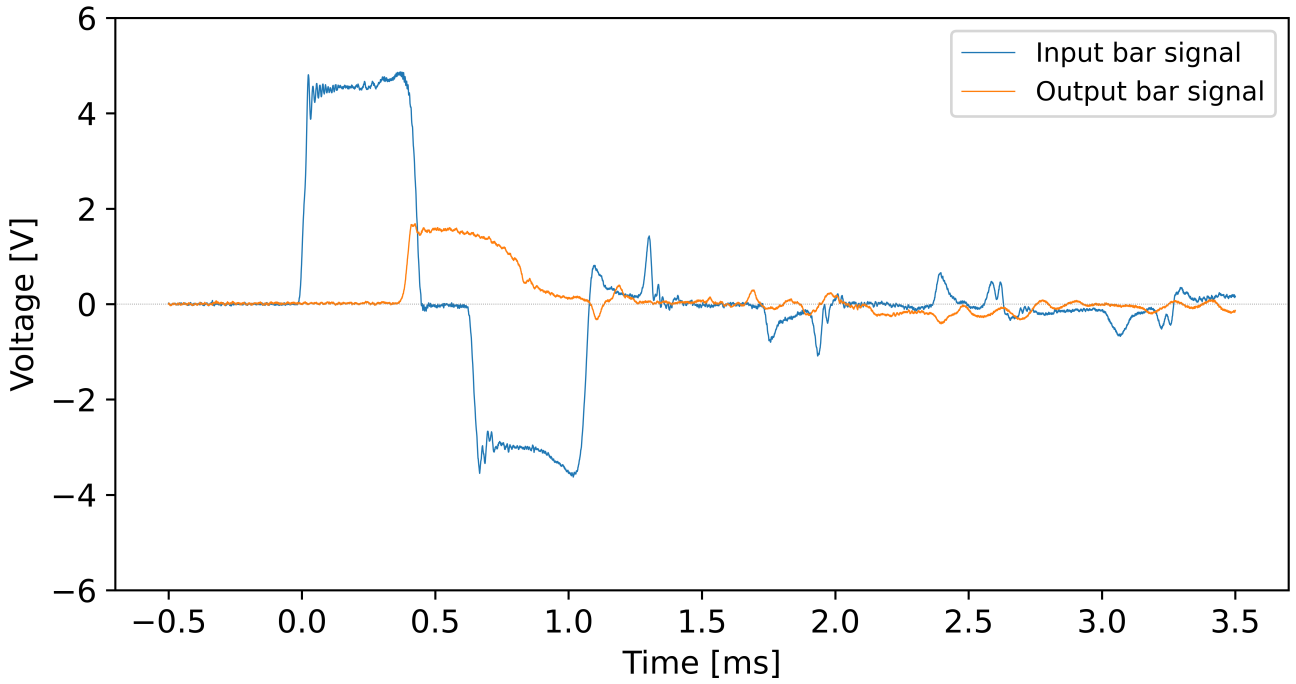

(a) Signals recorded from an interrupted test, M5, using full momentum trapping

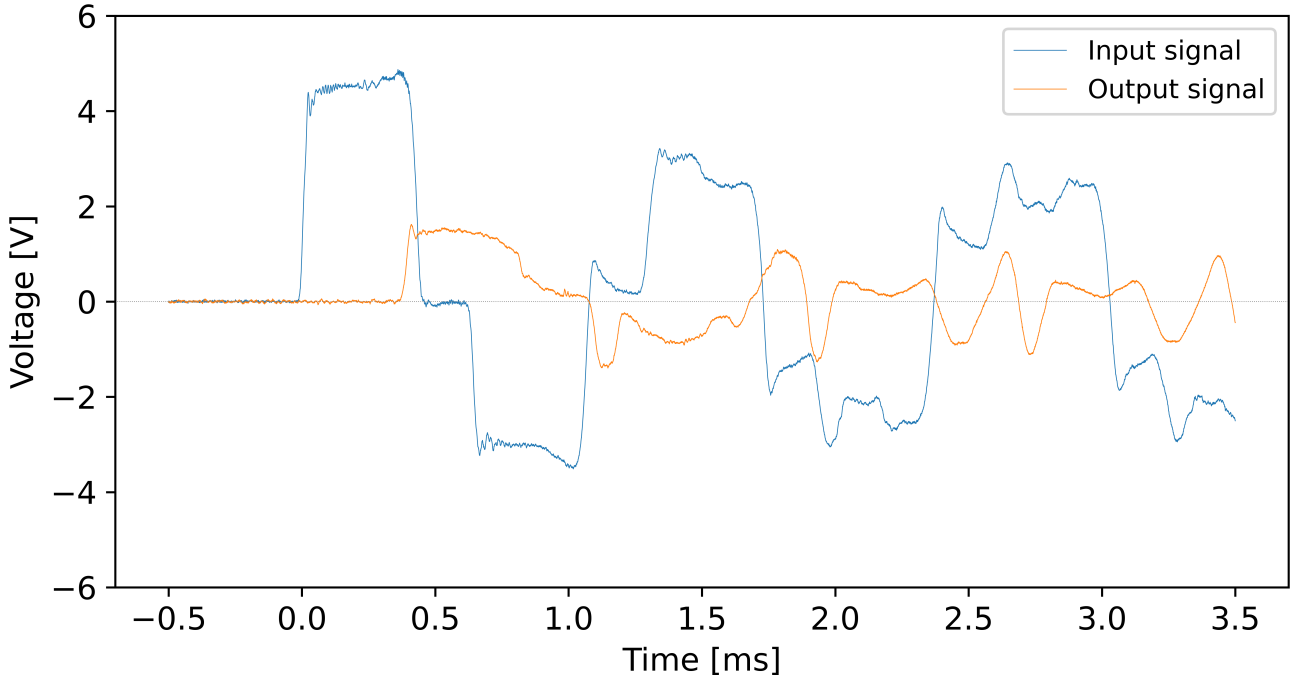

(b) Signals recorded from an uninterrupted test, M6, using only primary momentum trapping

Figure I.2 Comparison of the recorded signal for interrupted versus uninterrupted TSHB tests, at $v_0 = 12.0$ m/s

Appendix J

Damage to the Trap Sleeve

Figure J.1 displays the impact region of the TSHB. The striker input flange is removed and the striker tube is drawn back to show the input bar, primary momentum trap, and isolator sleeve. Since the striker impacts the incident flange in an upwards direction in this sketch, there needs to be a suitable gap in between the input bar and the isolator sleeve. The sleeve is a fixed part, and damage may occur of the input bar was to collide with it during testing.

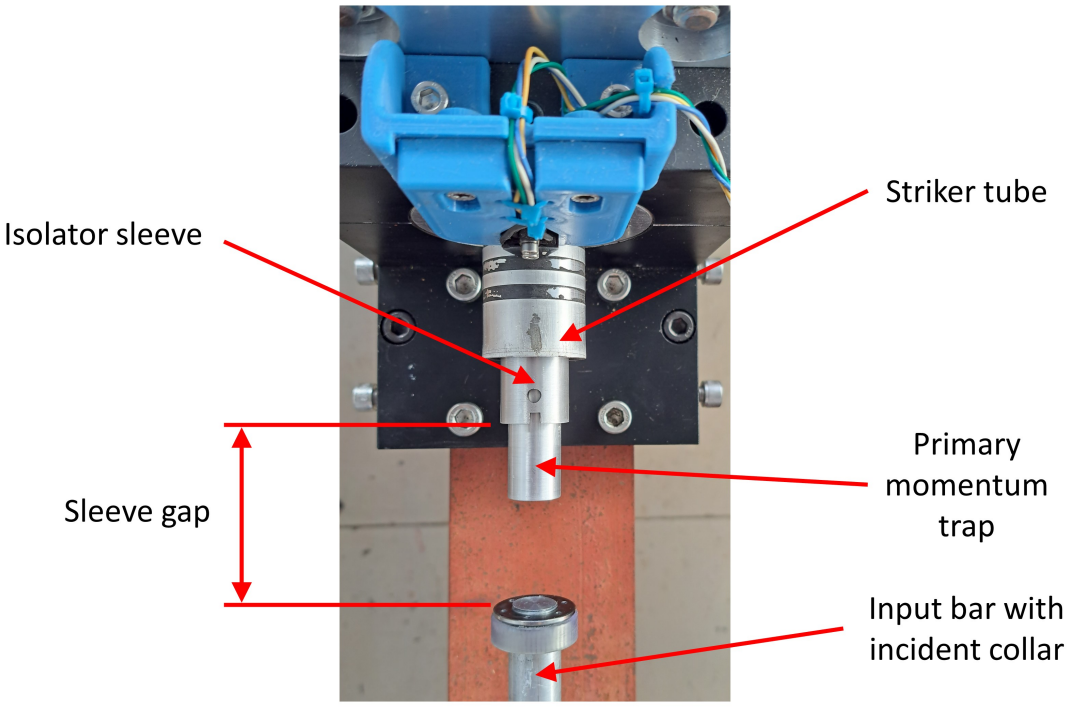

Figure J.1 Photograph showing the positioning of the isolator sleeve relative to the input bar

There was an incident where this did occur. The input bar and isolator sleeve collided forcefully and damaged the sleeve. The first version of the sleeve used venting slots as part of its compressive barrel function, and this impact caused it to buckle at that location. See Figure J.2 below illustrating this failure:

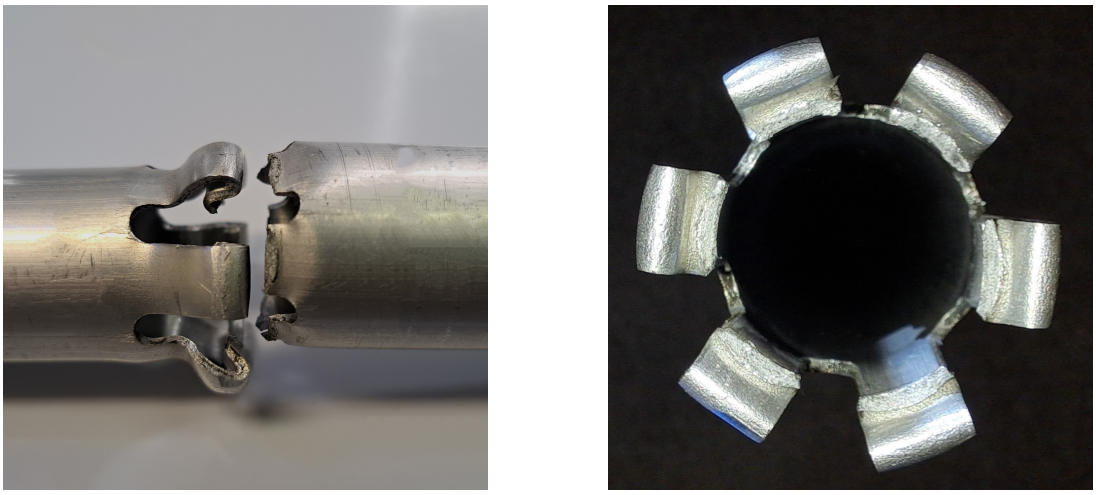

(a) A side view **(b)** An end view

Figure J.2 Photographs documenting the damage to the isolator sleeve

This happened as a result of accidentally firing a striker of this length too hard. The specimen fractured very easily, leaving a large quantity of kinetic energy still in the system. Despite the momentum trap being in place, the struck end of the input bar was displace enough to make contact with the sleeve. The sleeve had to be re-manufactured. The risk of this damage happening again was mitigated in four ways:

1. The venting slots in the sleeve were changed to a series of holes, and the tube used has a slightly thicker wall. These changes made the sleeve more robust.

2. The sleeve gap, as shown in Figure J.1, was widened slightly.

3. A shoulder of insulation tape was wrapped around the input bar behind on of its supports. This was positioned such the the tape would collide with the support bushing before the input bar collided with the sleeve. At the very least this would take some energy out of a catastrophic impact for the sleeve.

4. The striker was not fired as excessive speed. Speeds were increased only to the point where specimen fracture occurred.

Appendix K

Bill of Materials

Assembly	Description	Part Number	Quantity	Material/stock
Gas gun	Front flange	THMMAL006-006	1	6061 T6 aluminium
	Rear flange	THMMAL006-018	1	6061 T6 aluminium
	Pressure tube	THMMAL006-019	1	Aluminium barrel stock (S-ID160XOD170)
	Barrel tube	THMMAL006-007	1	Aluminium barrel stock (S-ID63XOD68)
	Barrel collar	THMMAL006-009	1	6061 T6 aluminium
	Barrel support	THMMAL006-008	1	6061 T6 aluminium
	Piston	THMMAL006-002	1	6061 T6 aluminium

Assembly	Description	Part Number	Quantity	Material/stock
Gas gun	Tie rod	THMMAL006-030	6	M12 threaded rod (E/G)
	Tie rod nut	TF:48709	12	M12 nut (E/G)
	Flange pin	THMMAL006-032	2	3D printed PLA
	Piston stopper	THMMAL006-033	1	3D printed PLA
	8mm Swivel stud elbow	MA150814	1	Purchased off-the-shelf
	12mm Swivel stud elbow	MA151212	1	Purchased off-the-shelf
	Internal circlip 70mm	TF:53115	1	Purchased off-the-shelf
	Nitrile O-ring 4mm x 160mm	RMT4X160	1	Purchased off-the-shelf
	Nitrile O-ring 4mm x 152mm	RMT4X152	2	Purchased off-the-shelf
	Nitrile O-ring 4mm x 72mm	RMT4X72	1	Purchased off-the-shelf
	Nitrile O-ring 4mm x 55mm	RMT4X55	1	Purchased off-the-shelf
	Nitrile O-ring 4mm x 48mm	RMT4X48	1	Purchased off-the-shelf
	⌀12mm Polyethelene tube	PE12BLACK	1.2 m	Purchased off-the-shelf
	⌀8mm Polyethelene tube	PE8BLACK	1.2 m	Purchased off-the-shelf

Assembly	Description	Part Number	Quantity	Material/stock
Barrel clamp	Barrel clamp	THMMAL006-087	1	Stainless steel
	M10 X 70 cap screws	TF:67866	2	Purchased off-the-shelf
	M10 hex nut	TF:48697	2	Purchased off-the-shelf
Tensile striker	Striker tube	THMMAL006-010	1	6061 aluminium
	Striker flange	THMMAL006-016	1	Ti-6Al-4V
	Striker pressure collar	THMMAL006-020	2	POM
Striker bushing	Striker bushing inner	THMMAL006-080	1	PTFE
	Striker bushing outer	THMMAL006-081	1	Brass
Input bar	Input bar	THMMAL006-005	1	7075 T6 aluminium
	Input flange	THMMAL006-003	1	Ti-6Al-4V
	Input flange bushing	THMMAL006-004	1	SLA printed resin
Output bar	Output bar	THMMAL006-014	1	7075 T6 aluminium
	Output flange	THMMAL006-023	1	Ti-6Al-4V
	Output trap bushing	THMMAL006-024	4	SLA printed resin

Assembly	Description	Part Number	Quantity	Material/stock
Isolator sleeve	Isolator sleeve	THMMAL006-011	1	6082 T6 aluminium
	Sleeve bushing	THMMAL006-001	2	PTFE
	Sleeve cap	THMMAL006-203	1	AISI 1020
	Sleeve mount	THMMAL006-202	1	Brass
	⌀12mm push-in connector	MA111212	1	Purchased off-the-shelf
	⌀12mm polyethelene tube	PE12BLACK	3 m	Purchased off-the-shelf
Gun support	Clamp base	THMMAL006-105	2	Mild steel
	Upper clamp half	THMMAL006-102	2	Mild steel
	Lower clamp half	THMMAL006-104	2	Mild steel
	Bed clamp	THMMAL006-106	2	Mild steel
	Thinned pin	THMMAL006-101	4	⌀6 x 30 dowel pins
	⌀6 x 30 dowel pins	TF:69199	4	Purchased off-the-shelf
	M10 X 30 cap screw	TF:67848	4	Purchased off-the-shelf
	M10 X 80 cap screw	TF:67870	4	Purchased off-the-shelf
	M10 X 90 cap screw	TF:67873	4	Purchased off-the-shelf
	M10 X 40 cap screw	TF:59190	16	Purchased off-the-shelf
	Jacking screw cap	THMMAL006-107	120	3D printed PLA

Assembly	Description	Part Number	Quantity	Material/stock
Tube striker	80mm tube striker	THMMAL006-206	1	6000 series aluminium
	30mm striker front bushing	THMMAL006-207	1	SLA printed resin
	30mm striker rear bushing	THMMAL006-208	1	SLA printed resin
100mm striker	100mm striker	THMMAL006-204	1	6082 T6 aluminium
	20mm striker front bushing	THMMAL006-211	1	SLA printed resin
	20mm striker rear bushing	THMMAL006-212	1	SLA printed resin
240mm striker	240mm Striker	THMMAL006-205	1	6082 T6 aluminium
	20mm striker front bushing	THMMAL006-211	1	SLA printed resin
	20mm striker rear bushing	THMMAL006-212	1	SLA printed resin
500mm Striker	Compressive Striker	THMMAL006-200	1	7075 T6 aluminium
	3/4” striker front bushing	THMMAL006-209	1	SLA printed resin
	3/4” striker rear bushing	THMMAL006-210	1	SLA printed resin
Miscellaneous parts	Solid trap bar	THMMAL006-013	2	6082 T6 aluminium
	Solid trap bushing	THMMAL006-015	4	SLA printed resin
	Hollow trap bar	THMMAL006-029	1	6000 series aluminium
	Trap cone	THMMAL006-025	1	3D printed PLA

Assembly	Description	Part Number	Quantity	Material/stock
Gun cap	Gun Cap	THMMAL006-201	1	AISI 1020
	⌀12mm push-in connector	MA111212	1	Purchased off-the-shelf
Flange spanner	Flange spanner	THMMAL006-040	1	K110 tool steel
	⌀2 x 16 dowel pins	TF:90486	4	Purchased off-the-shelf
Specimen clamp spanner	Specimen clamp spanner	THMMAL006-041	1	K110 tool steel
	⌀2 x 16 dowel pins	TF:90486	4	Purchased off-the-shelf
Bar bushings	Bushing outer	THMMAL006-501	22	6061 T6 aluminium
	30mm bushing inner	THMMAL006-500	2	PTFE
	20mm bushing inner	THMMAL006-500	2	PTFE
	3/4” bushing inner (W)	THMMAL006-500	5	PTFE
	3/4” bushing inner (S)	THMMAL006-500	5	PTFE
	19.6mm bushing inner (W)	THMMAL006-500	2	PTFE
	19.6mm bushing inner (S)	THMMAL006-500	2	PTFE
	30mm bushing inner (W)	THMMAL006-500	2	PTFE
	30mm bushing inner (S)	THMMAL006-500	2	PTFE

Assembly	Description	Part Number	Quantity	Material/stock
Pneumatic board	Face	THMMAL006-300	1	18mm pine board
	Side L	THMMAL006-301	1	18mm pine board
	Side R	THMMAL006-302	1	18mm pine board
	Brace	THMMAL006-303	2	18mm pine board
	50mm wood screw	1FE60U	20	Purchased off-the-shelf
	Valve handle spacer	THMMAL006-304	8	3D printed PLA
	1/4” valve housing L	THMMAL006-305	3	3D printed PLA
	1/4” valve housing R	THMMAL006-306	3	3D printed PLA
	1/2” valve housing L	THMMAL006-307	1	3D printed PLA
	1/2” valve housing R	THMMAL006-308	1	3D printed PLA
	1/4” face piece half	THMMAL006-309	4	3D printed PLA
	1/2” face piece half	THMMAL006-310	2	3D printed PLA
	Gauge housing	THMMAL006-311	2	3D printed PLA
	1/4” regulator 10bar	R55-2	1	Purchased off-the-shelf
	Gauge 10 bar panel mount 1/4 ”	PBGU63BB12QC3G	2	Purchased off-the-shelf

Assembly	Description	Part Number	Quantity	Material/stock
Pneumatic board	1/4” ball valve	BOSTON 1/4”	3	Purchased off-the-shelf
	1/2” ball valve	BOSTON 1/2”	1	Purchased off-the-shelf
	1/4” nipple	RA121414	4	Purchased off-the-shelf
	1/2” nipple	RA121212	1	Purchased off-the-shelf
	1/4” male stud banch tee	MA200814	1	Purchased off-the-shelf
	1/2” male stud banch tee	MA201212	1	Purchased off-the-shelf
	Male stud	MA130814	1	Purchased off-the-shelf
	Male stud	MA110614	1	Purchased off-the-shelf
	⌀8mm bulkhead	MA270808	1	Purchased off-the-shelf
	⌀12mm bulkhead	MA271212	1	Purchased off-the-shelf
	⌀8mm equal elbow	MA280808	1	Purchased off-the-shelf
	⌀12mm equal elbow	MA281212	1	Purchased off-the-shelf
	Female stud	MA170814	2	Purchased off-the-shelf
	Adapter	MB260812	1	Purchased off-the-shelf
	1/4” bulkhead	RA141412	2	Purchased off-the-shelf
	1/2” bulkhead	RA141434	1	Purchased off-the-shelf

Assembly	Description	Part Number	Quantity	Material/stock
Light trap	Light trap body	THMMAL006-400	1	3D printed PLA
	Strain relief clamp	THMMAL006-401	1	3D printed PLA
	Infrared LED	TSHG5410	2	Purchased off-the-shelf
	Infrared phototransistor	BPW85	2	Purchased off-the-shelf
	M6 x 20 cap screws	TF:59054	2	Purchased off-the-shelf
	M6 hex nut	TF:48661	2	Purchased off-the-shelf
	2.9 x 12 Self tapping screw	TF:42607	2	Purchased off-the-shelf
ROS	Fixed ROS mount	THMMAL006-402	1	3D printed PLA
	Sliding ROS mount	THMMAL006-403	1	3D printed PLA
	M6 x 16 cap screws	TF:59052	2	Purchased off-the-shelf
	M5 x 16 cap screws	TF:59006	2	Purchased off-the-shelf
	M3 x 10 cap screws	TF:58935	2	Purchased off-the-shelf
	M6 hex nut	TF:48661	2	Purchased off-the-shelf
	M5 hex nut	TF:48652	2	Purchased off-the-shelf
	M3 hex nut	TF:48637	2	Purchased off-the-shelf
	Reflective object sensor	QRB1113	1	Purchased off-the-shelf

Appendix L

Engineering Assembly Drawings

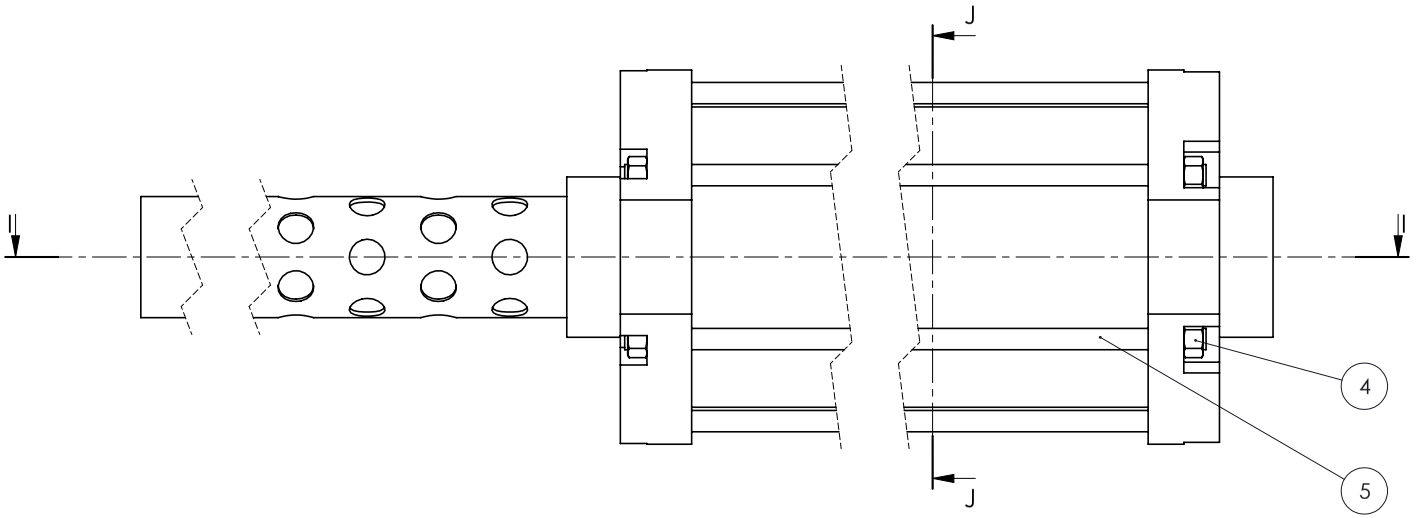

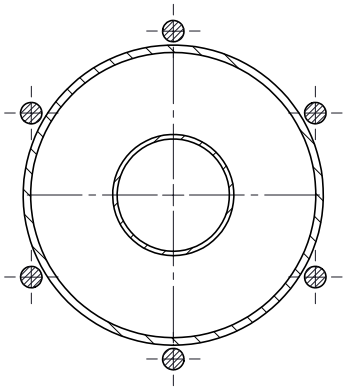

SLICE SECTION J-J

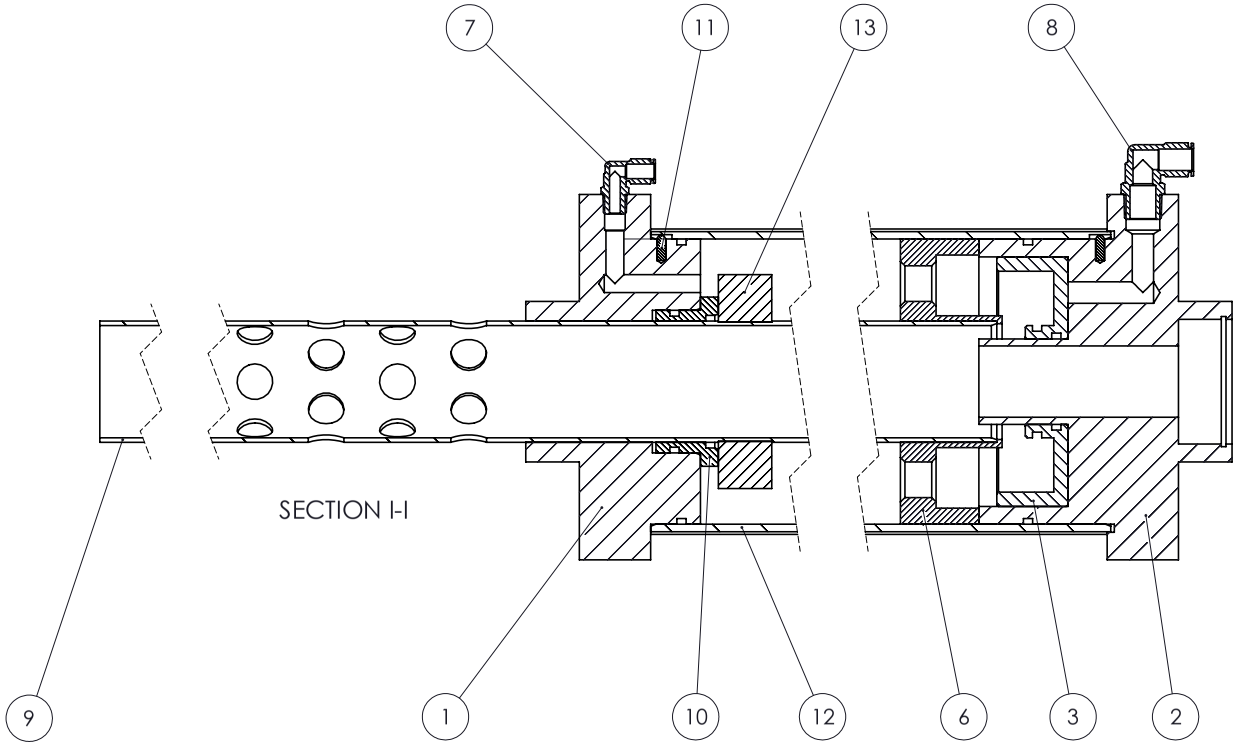

SECTION I-I

NO.	PART NUMBER	DESCRIPTION	SPECIFICATION	QTY
13	THMMAL006-087	Barrel Clamp	See DWG for details, Stainless steel	1
12	THMMAL006-019	Pressure Tube	See DWG for details, Provided 160 ID piston barreling	1
11	THMMAL006-032	Flange Pin	See DWG for details, 3D printed PLA	2
10	THMMAL006-009	Barrel Collar	See DWG for details, 6061 T6 aluminium	1
9	THMMAL006-007	Barrel Tube	See DWG for details, Provided 63 ID piston barreling	1
8	MA151212	Push-in Pneumatic Fitting, 90 Deg Swivel, 12mm	Brass Nickel Plated	1
7	MA150814	Push-in Pneumatic Fitting, 90 Deg Swivel, 8mm	Brass Nickel Plated	1
6	THMMAL006-008	Barrel Support	See DWG for details, 6061 T6 aluminium	1
5	THMMAL006-030	Tie Rod	See DWG for details, M12 threaded rod electro-galvanised	6
4	UCT-11109	Hex nut M12	ISO 4032 - M12, Carbon Steel Gr 8.8	12
3	THMMAL006-002	Piston	See DWG for details, 6061 T6 aluminium	1
2	THMMAL006-018	Rear Flange	See DWG for details, 6061 T6 aluminium	1
1	THMMAL006-006	Front Flange	See DWG for details, 6061 T6 aluminium	1

Scale: 1:3 on A3

University of Cape Town
Department of Mechanical Engineering

Drawn By: M THOMAS

All un-toleranced dimensions to adhere to ISO 2768-m

Title: Gas Gun Assembly

Checked :

Assembly drawing

Drawing Number :

Rev. : A

Sheet : 1 of 1

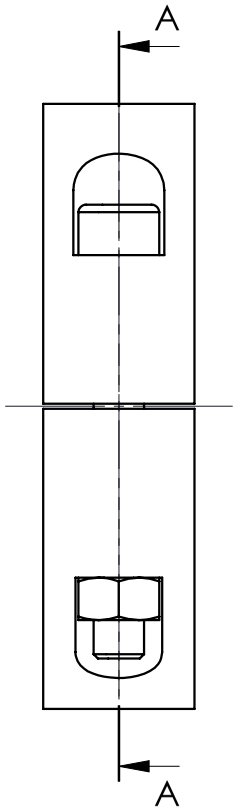

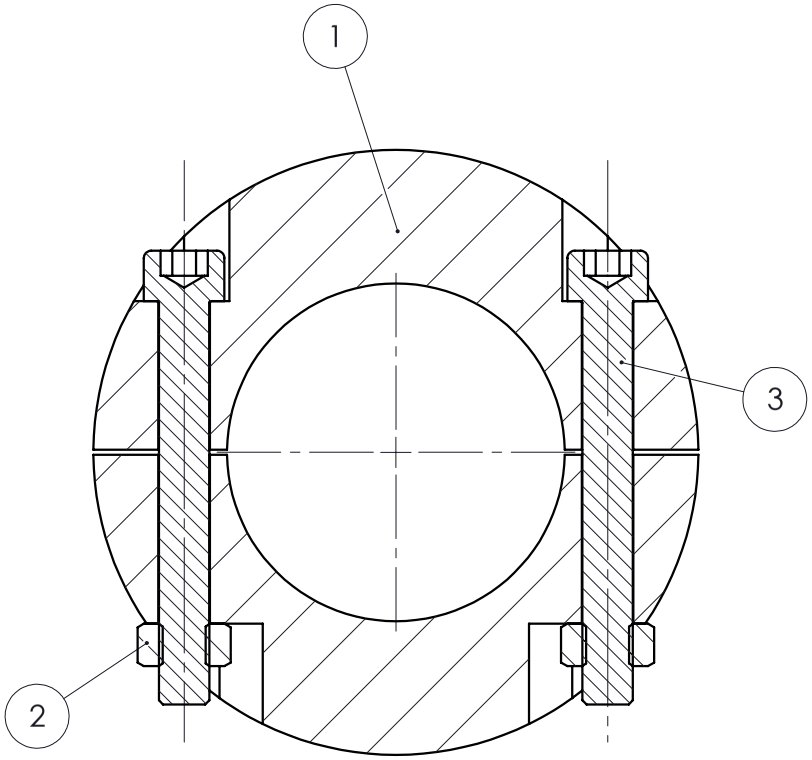

SECTION A-A

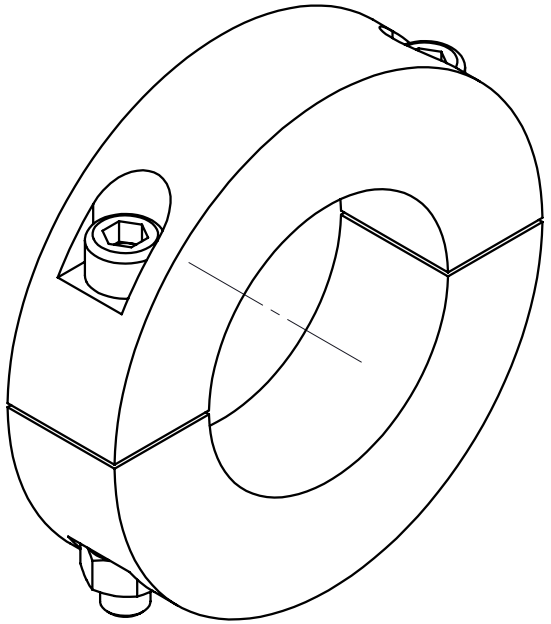

NO.	PART NUMBER	DESCRIPTION	SPECIFICATION	QTY
1	THMMAL006-087	Barrel Clamp	See DWG for details, Stainless steel	1
2	UCT-11108	Hex nut M10	ISO 4032 - M10, Carbon Steel Gr 8.8	2
3	UCT-05128	Socket HD Bolt M10	ISO 4762 - M10 X 80 x 32, Carbon Steel Gr 8.8	2

Scale: 2:3 on A4	University of Cape Town Department of Mechanical Engineering			
Drawn By: M THOMAS	All un-toleranced dimensions to adhere to ISO 2768-m	Title: Barrel Clamp Assembly		
Checked :	Assembly Drawing	Drawing Number :	Rev. : A	Sheet : 1 of 1

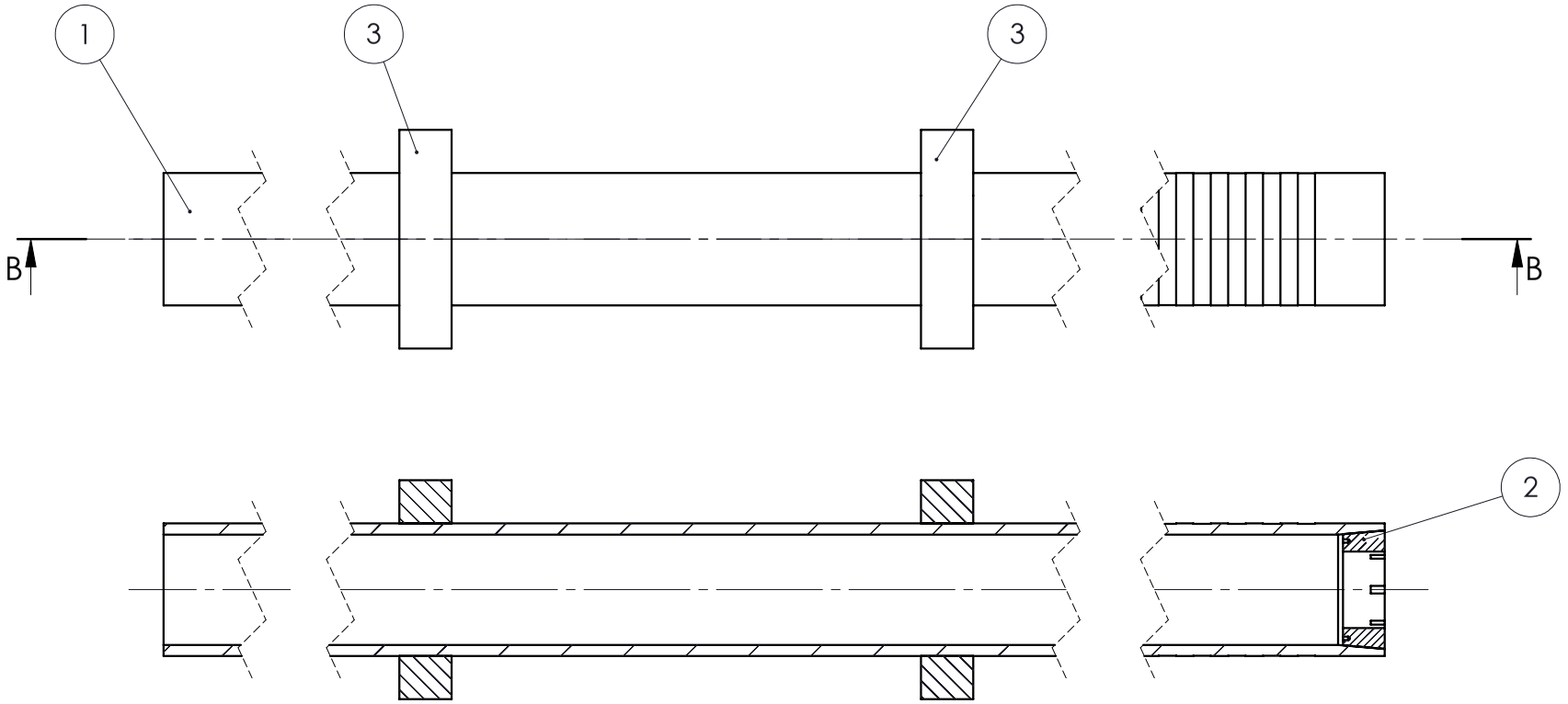

SECTION B-B

NO.	PART NUMBER	DESCRIPTION	SPECIFICATION	QTY
1	THMMAL006-010	Striker Tube	See DWG for details, 6061 aluminium	1
2	THMMAL006-016	Striker Flange	See DWG for details, Ti-6Al-4V	1
3	THMMAL006-020	Striker Pressure Collar	See DWG for details, POM	2

Scale: 1:2 on A4	University of Cape Town Department of Mechanical Engineering				
Drawn By: M THOMAS	All un-toleranced dimensions to adhere to ISO 2768-m	Title: Tensile Striker Assembly			
Checked :	Assembly Drawing	Drawing Number :	Rev. : B	Sheet : 1 of 1	

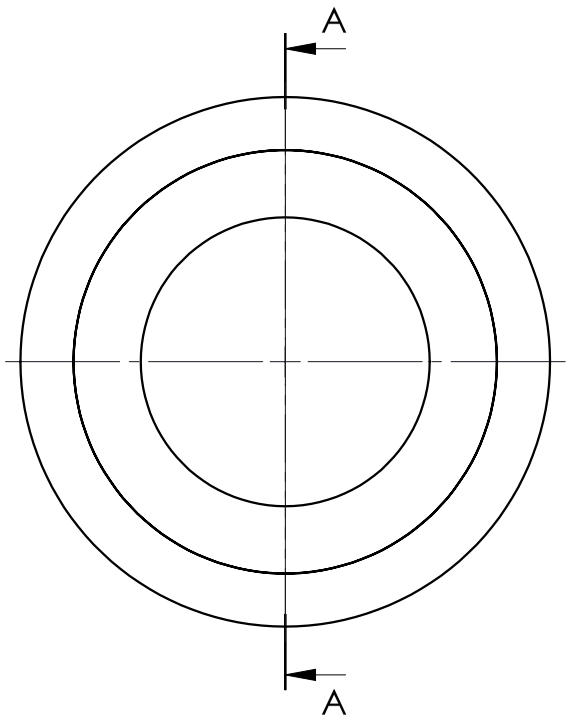

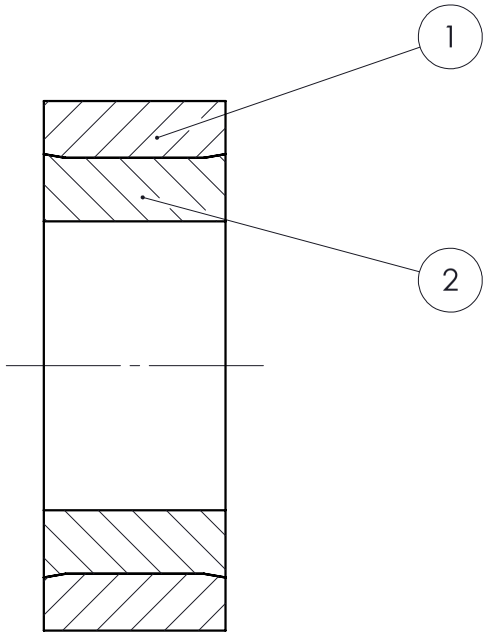

SECTION A-A

NO.	PART NUMBER	DESCRIPTION	SPECIFICATION	QTY
1	THMMAL006-081	Striker Bushing Outer	See DWG for details, Brass	1
2	THMMAL006-080	Striker Bushing Inner	See DWG for details, PTFE (general)	1

	Scale: 1:1 on A4	University of Cape Town Department of Mechanical Engineering			
Drawn By: M THOMAS		All un-toleranced dimensions to adhere to ISO 2768-m	Title: Striker Bushing Assembly		
Checked :		Assembly Drawing	Drawing Number :	Rev. : A	Sheet : 1 of 1

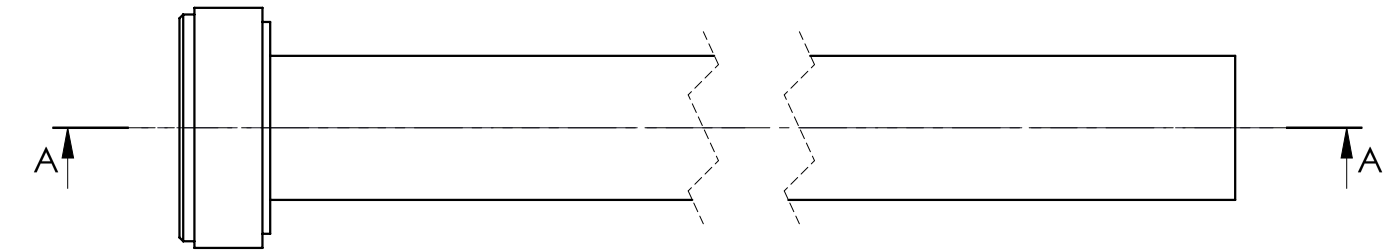

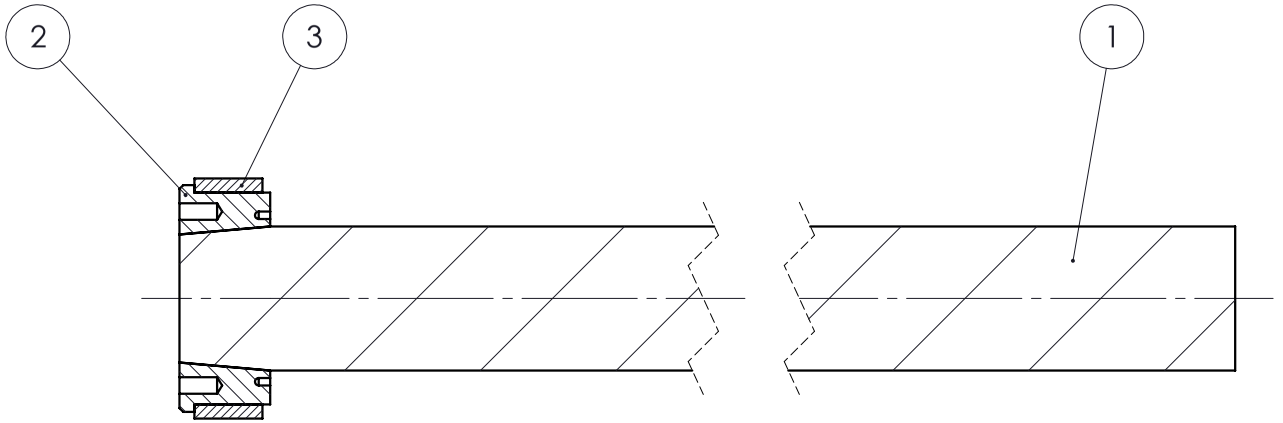

SECTION A-A

NO.	PART NUMBER	DESCRIPTION	SPECIFICATION	QTY
3	THMMAL006-004	Input Flange Bushing	See DWG for details, SLA printed resin	1
2	THMMAL006-003	Input Flange	See DWG for details, Ti-6Al-4V	1
1	THMMAL006-005	Input Bar	See DWG for details, 7075 T6 aluminium	1

Scale: 1:1 on A4	University of Cape Town Department of Mechanical Engineering			
Drawn By: M THOMAS	All un-toleranced dimensions to adhere to ISO 2768-m	Title: Input Bar Assembly		
Checked :	Assembly Drawing	Drawing Number :	Rev. : A	Sheet : 1 of 1

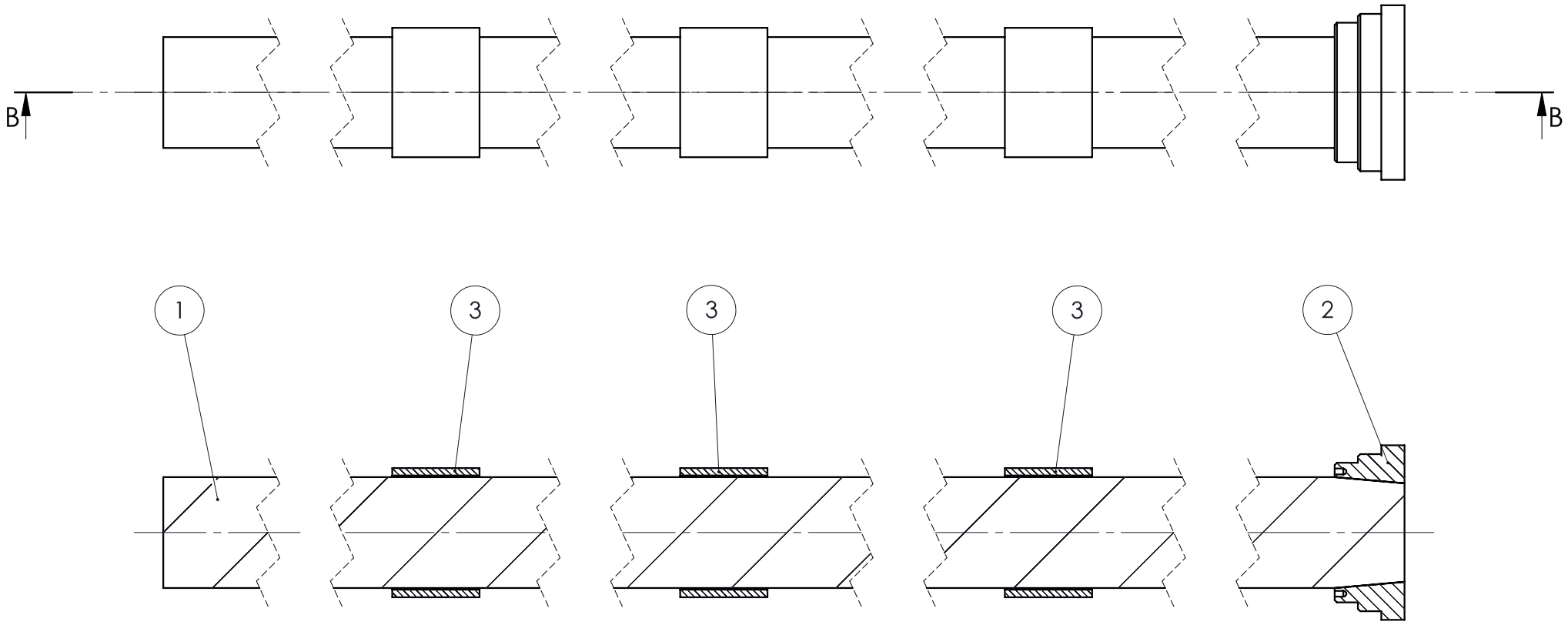

SECTION B-B

NO.	PART NUMBER	DESCRIPTION	SPECIFICATION	QTY
3	THMMAL006-024	Output Trap Bushing	See DWG for details, SLA printed resin	3
2	THMMAL006-023	Output Flange	See DWG for details, Ti-6Al-4V	1
1	THMMAL006-014	Output Bar	See DWG for details, 7075 T6 alumunium	1

Scale: 1:1 on A4	University of Cape Town Department of Mechanical Engineering			
Drawn By: M THOMAS	All un-toleranced dimensions to adhere to ISO 2768-m	Title: Output Bar Assembly		
Checked :	Assembly Drawing	Drawing Number :	Rev. : A	Sheet : 1 of 1

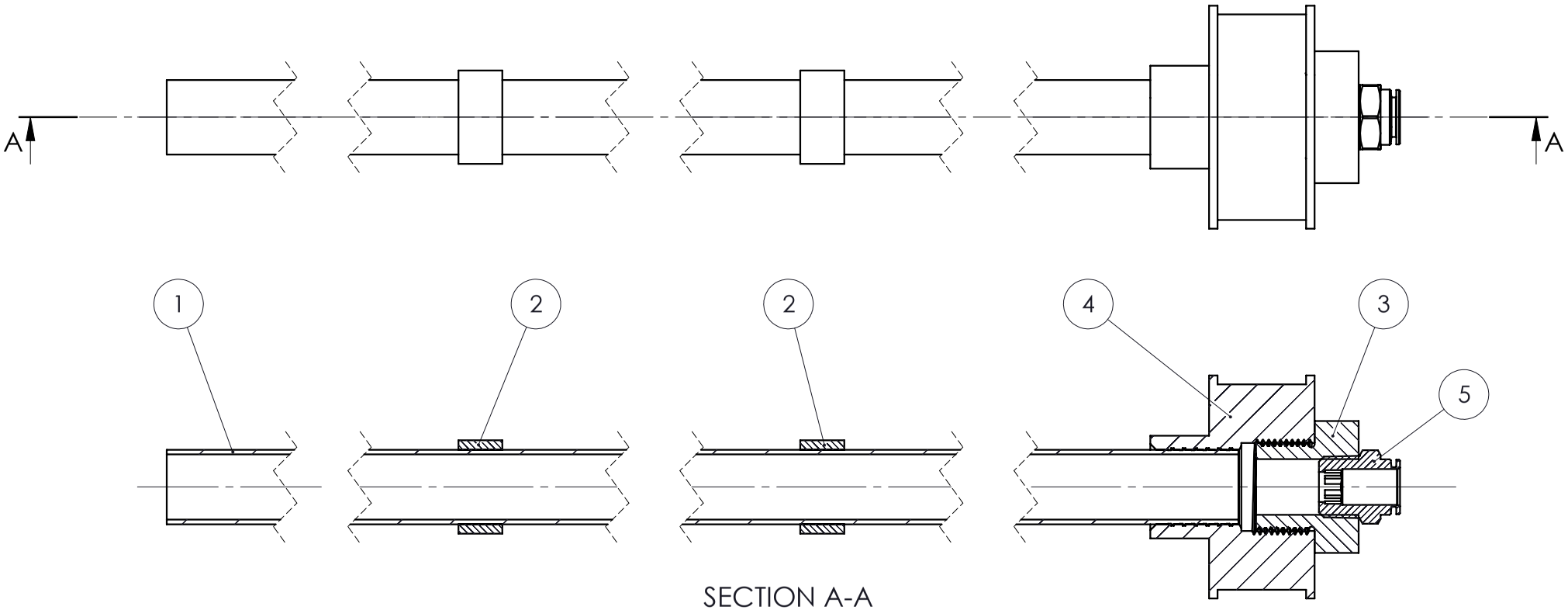

SECTION A-A

NO.	PART NUMBER	DESCRIPTION	SPECIFICATION	QTY
1	THMMAL006-011	Isolator Sleeve	See DWG for details, 6082 T6 aluminium	1
2	THMMAL006-001	Sleeve Bushing	See DWG for details, PTFE (general)	2
3	THMMAL006-203	Sleeve Cap	See DWG for details, AISI 1020	1
4	THMMAL006-202	Sleeve Mount	See DWG for details, Brass	1
5	MA111212	Push-in Pneumatic Fitting, Stud, 12mm	Brass Nickel Plated	1

	Scale: 1:2 on A4	University of Cape Town Department of Mechanical Engineering			
Drawn By: M THOMAS		All un-toleranced dimensions to adhere to ISO 2768-m	Title: Isolator Sleeve Assembly		
Checked :		Assembly Drawing	Drawing Number :	Rev. : C	Sheet : 1 of 1

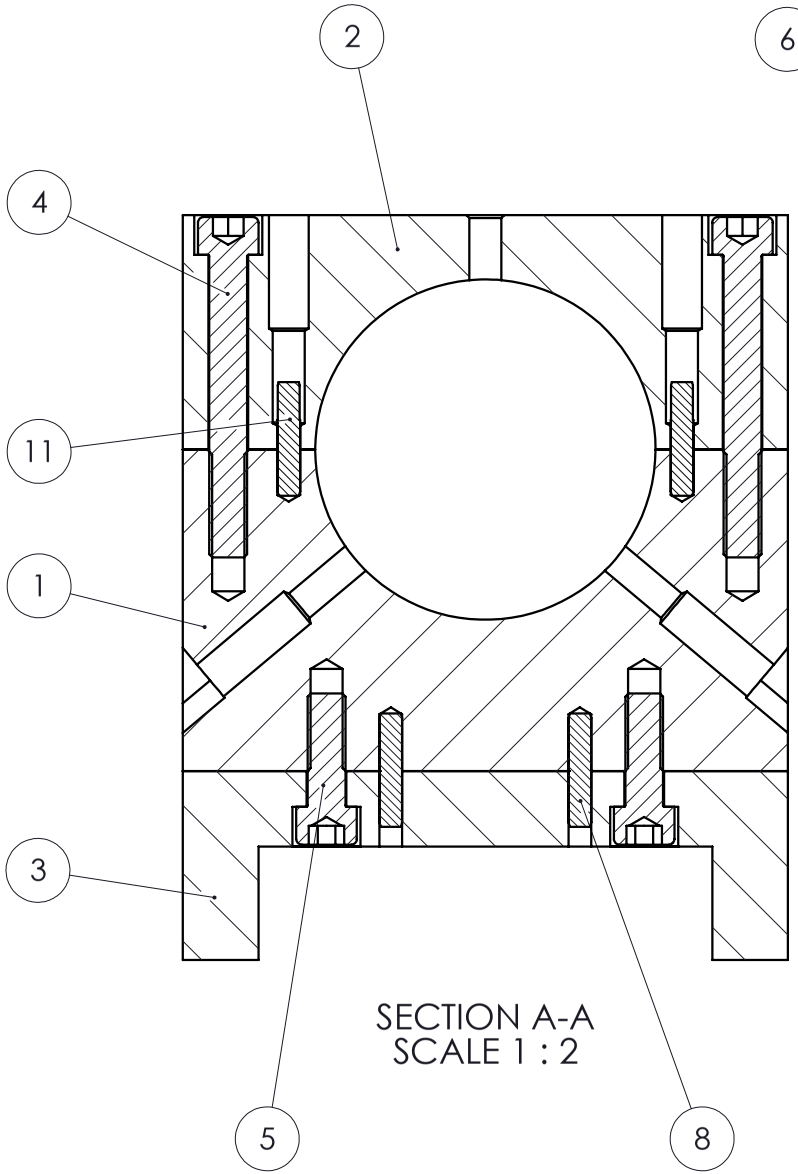

SECTION A-A
SCALE 1 : 2

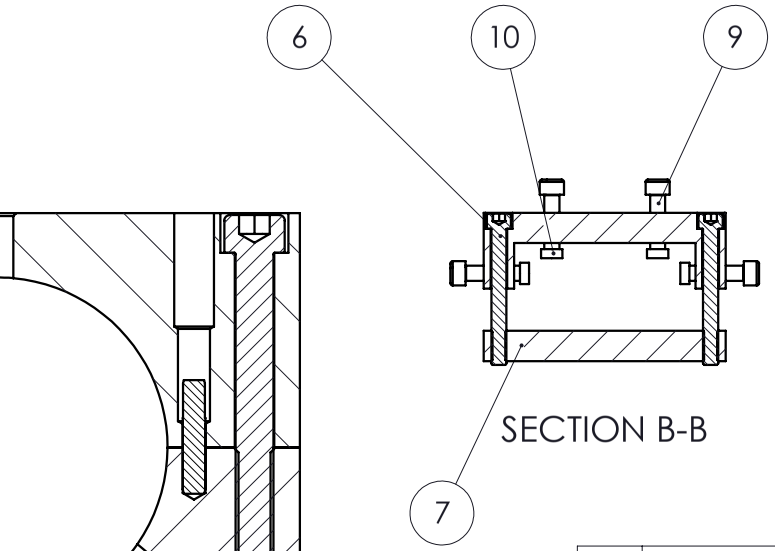

SECTION B-B

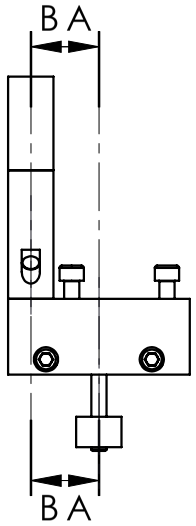

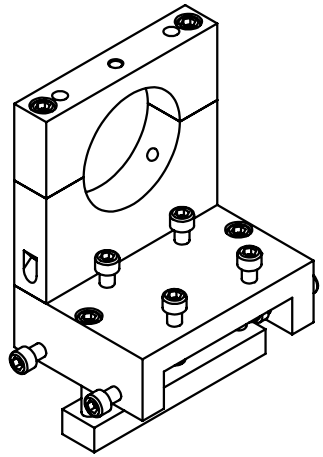

NO.	PART NUMBER	DESCRIPTION	SPECIFICATION	QTY
11	THMMAL006-101	Thinned Pin	ISO 8734 - 6 X 30 - A - St, ISO 8734 - 6 X 30 - A - St	2
10	THMMAL006-107	Jacking Cap	See DWG for details, PLA 3D printed	8
9	UCT-05114	Socket HD Bolt M10	ISO 4762 - M10 X 40 x 40, Carbon Steel Gr 8.8	8
8	UCT-12082	Parallel pin M6	ISO 8734 - 6 X 30 - A - St, Carbon Steel	2
7	THMMAL006-106	Bed Clamp	See DWG for details, Mild Steel	1
6	UCT-05130	Socket HD Bolt M10	ISO 4762 - M10 X 90 x 32, Carbon Steel Gr 8.8	2
5	UCT-05112	Socket HD Bolt M10	ISO 4762 - M10 X 30 x 30, Carbon Steel Gr 8.8	2
4	UCT-05128	Socket HD Bolt M10	ISO 4762 - M10 X 80 x 32, Carbon Steel Gr 8.8	2
3	THMMAL006-105	Clamp Base	See DWG for details, Mild Steel	1
2	THMMAL006-102	Upper Clamp Half	See DWG for details, Mild Steel	1
1	THMMAL006-104	Lower Clamp Half	See DWG for details, Mild Steel	1

Scale: 1:5 on A4	University of Cape Town Department of Mechanical Engineering			
Drawn By: M THOMAS	All un-toleranced dimensions to adhere to ISO 2768-m	Title: Gun Clamp Assembly		
Checked :	Assembly Drawing	Drawing Number :	Rev. : A	Sheet : 1 of 1

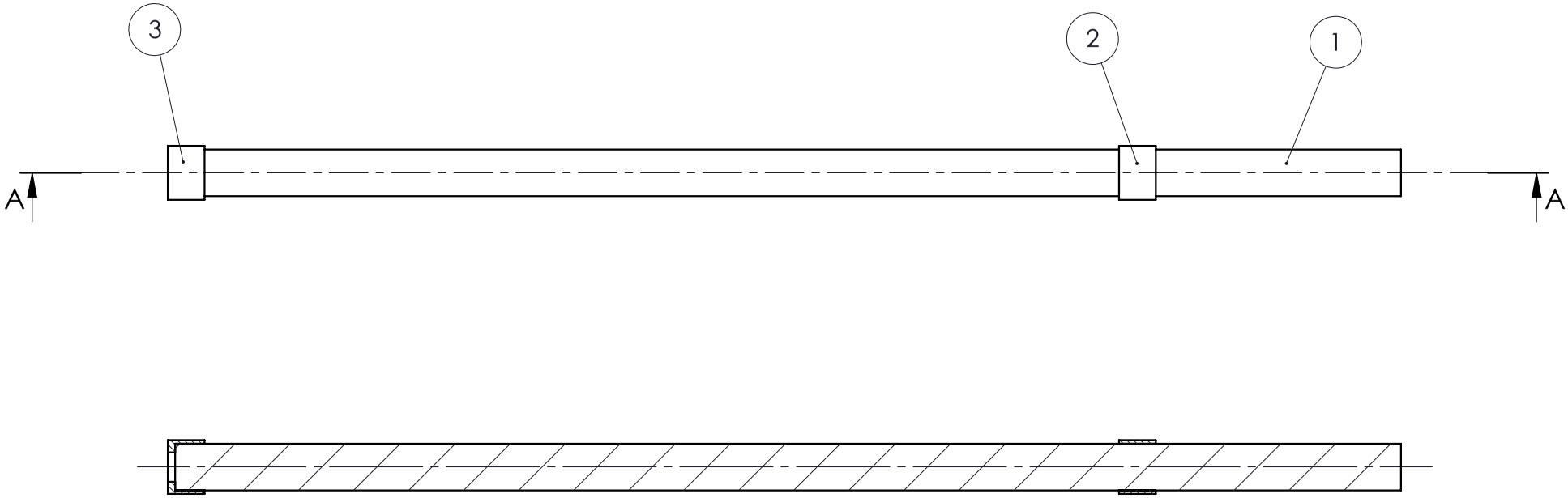

SECTION A-A

NO.	PART NUMBER	DESCRIPTION	SPECIFICATION	QTY
3	THMMAL006-210	3/4" Striker Rear Bushing	See DWG for details, SLA printed resin	1
2	THMMAL006-209	3/4" Striker Front Bushing	See DWG for details, SLA printed resin	1
1	THMMAL006-200	500mm Striker	See DWG for details, 7075 T6 aluminium	1

Scale: 2:5 on A4	University of Cape Town Department of Mechanical Engineering			
Drawn By: M THOMAS	All un-toleranced dimensions to adhere to ISO 2768-m	Title: 500mm Striker		
Checked :	Assembly Drawing	Drawing Number :	Rev. : A	Sheet : 1 of 1

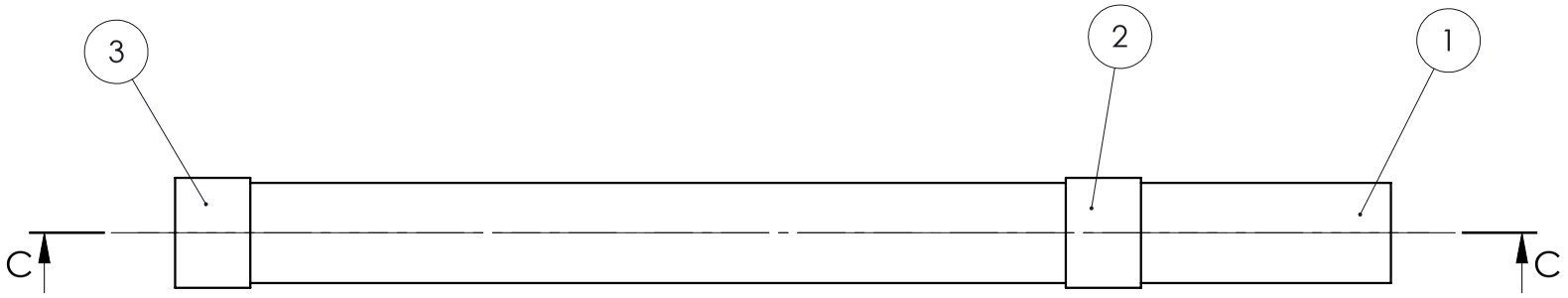

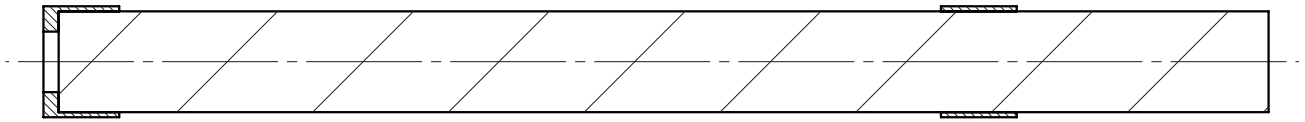

SECTION C-C

NO.	PART NUMBER	DESCRIPTION	SPECIFICATION	QTY
3	THMMAL006-212	20mm Striker Rear Bushing	See DWG for details, SLA printed resin	1
2	THMMAL006-211	20mm Striker Front Bushing	See DWG for details, SLA printed resin	1
1	THMMAL006-205	240mm Striker	See DWG for details, 6082 T6 aluminium	1

Scale: 2:3 on A4	University of Cape Town Department of Mechanical Engineering			
Drawn By: M THOMAS	All un-toleranced dimensions to adhere to ISO 2768-m	Title: 240mm Striker		
Checked :	Assembly Drawing	Drawing Number :	Rev. : A	Sheet : 1 of 1

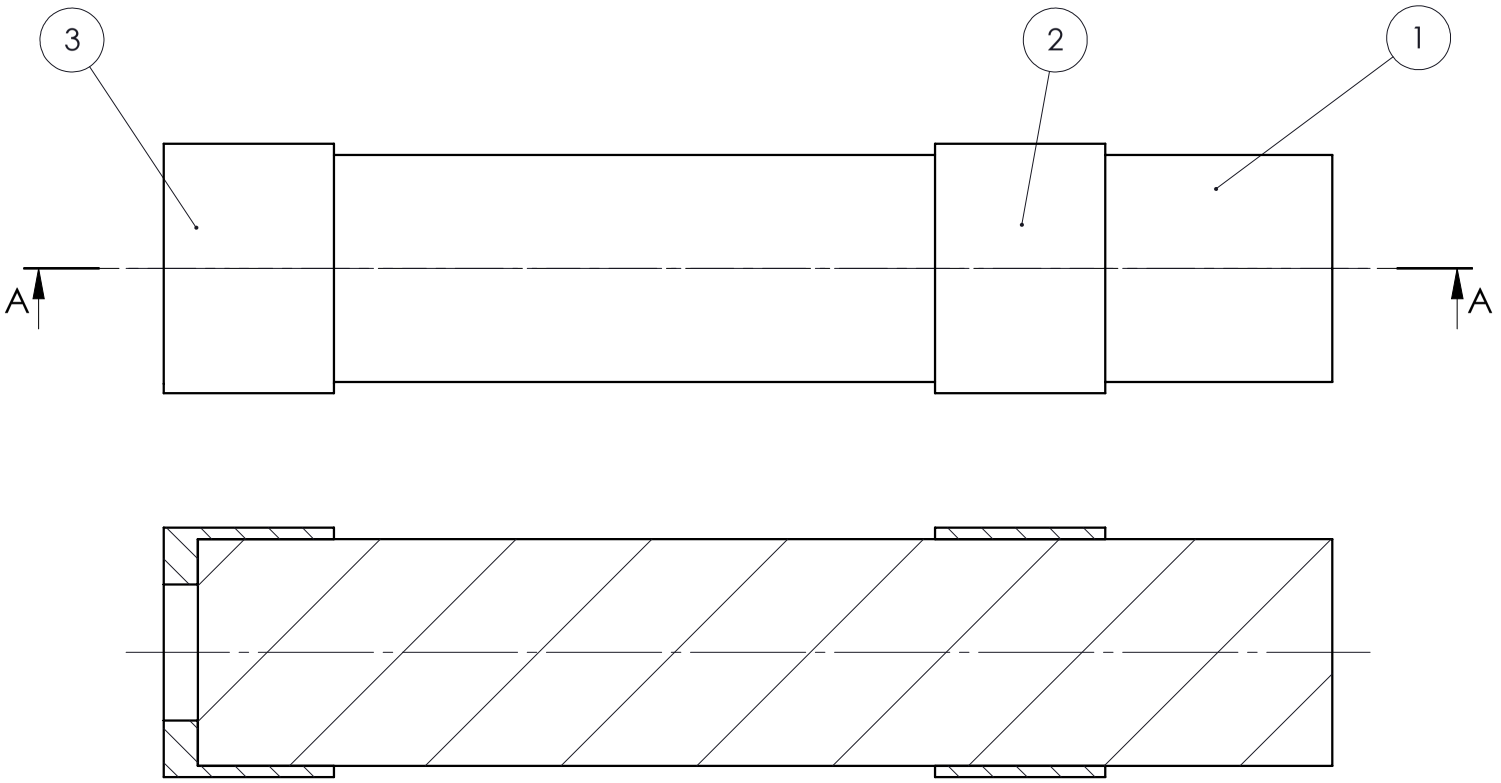

SECTION A-A

NO.	PART NUMBER	DESCRIPTION	SPECIFICATION	QTY
3	THMMAL006-212	20mm Striker Rear Bushing	See DWG for details, SLA printed resin	1
2	THMMAL006-211	20mm Striker Front Bushing	See DWG for details, SLA printed resin	1
1	THMMAL006-204	100mm Striker	See DWG for details, 6082 T6 aluminium	1

Scale: 3:2 on A4	University of Cape Town Department of Mechanical Engineering			
Drawn By: M THOMAS	All un-toleranced dimensions to adhere to ISO 2768-m	Title: 100mm Striker		
Checked :	Assembly Drawing	Drawing Number :	Rev. : A	Sheet : 1 of 1

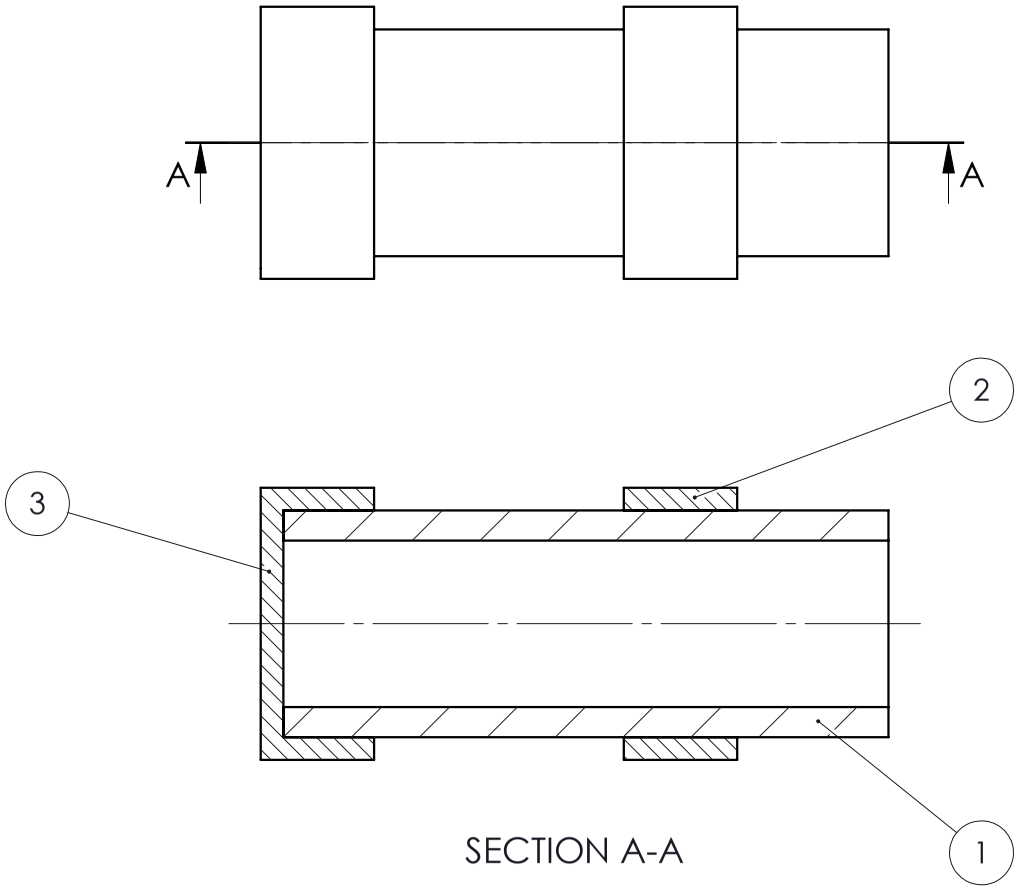

SECTION A-A

NO.	PART NUMBER	DESCRIPTION	SPECIFICATION	QTY
3	THMMAL006-208	30mm Striker Rear Bushing	See DWG for details, SLA printed resin	1
2	THMMAL006-207	30mm Striker Front Bushing	See DWG for details, SLA printed resin	1
1	THMMAL006-206	80mm Tube Striker	See DWG for details, 6000 series aluminium	1

Scale: 1:1 on A4	University of Cape Town Department of Mechanical Engineering			
Drawn By: M THOMAS	All un-toleranced dimensions to adhere to ISO 2768-m	Title: Tube Striker		
Checked :	Assembly Drawing	Drawing Number :	Rev. : A	Sheet : 1 of 1

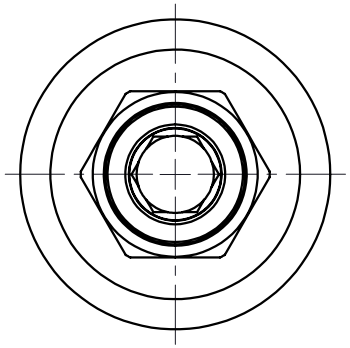

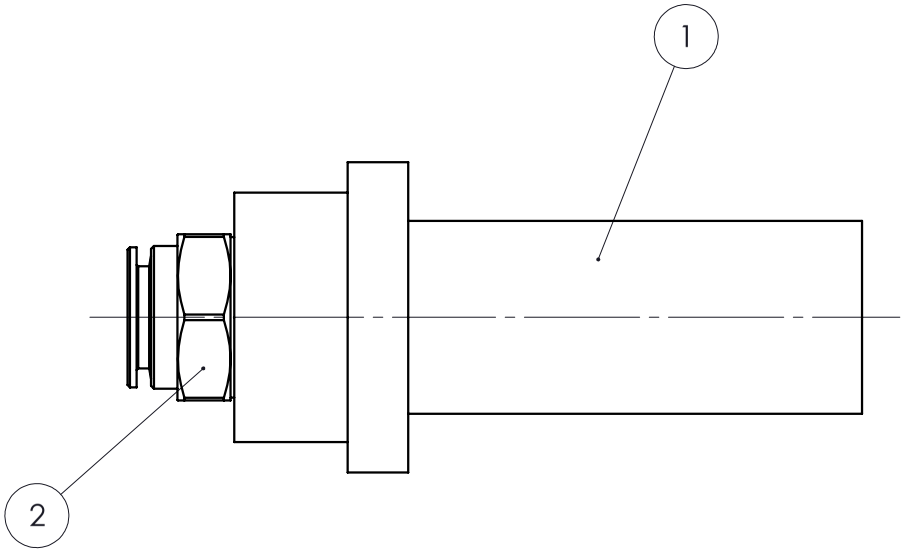

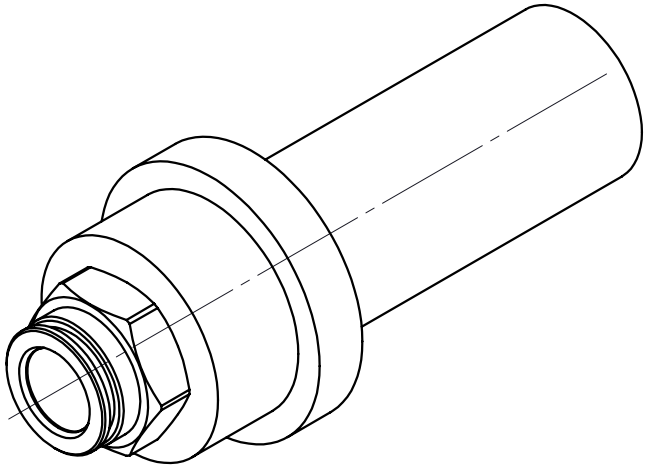

SCREW FITTING MA111212 INTO GUN CAP
USE PTFE TAPE FOR AIRTIGHT SEAL

NO.	PART NUMBER	DESCRIPTION	SPECIFICATION	QTY
1	THMMAL006-201	Gas Gun Cap	See DWG for details, AISI 1020	1
2	MA111212	Push-in pneumatic fitting	Brass Nickel Plated	1

Scale: 1:1 on A4	University of Cape Town Department of Mechanical Engineering			
Drawn By: M THOMAS	All un-toleranced dimensions to adhere to ISO 2768-m	Title: Gun Cap Assembly		
Checked :	Assembly Drawing	Drawing Number :	Rev. : A	Sheet : 1 of 1

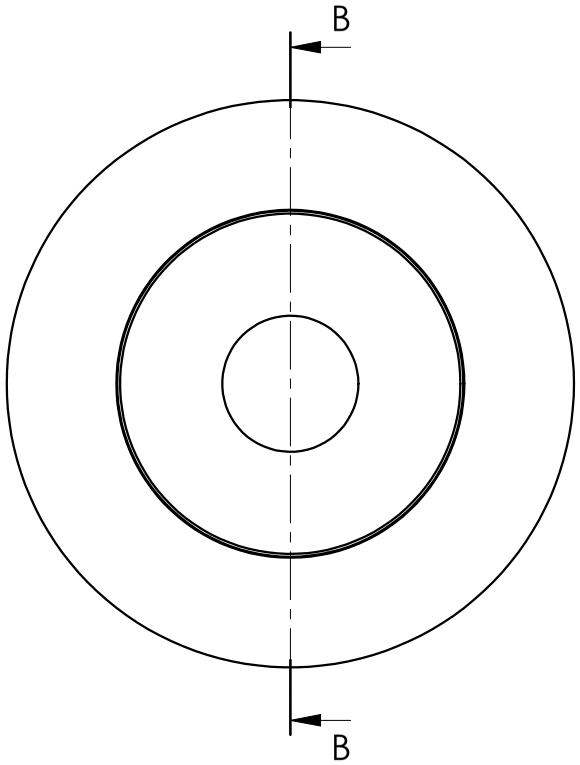

BAR BUSHING BLANK
QTY : 22

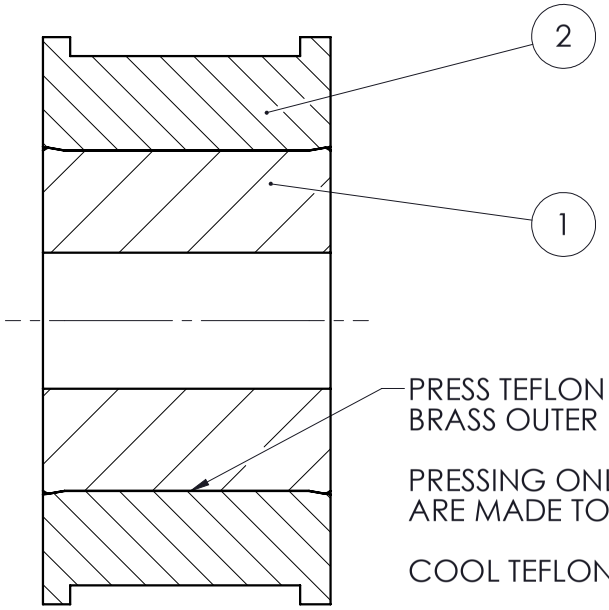

SECTION B-B

FITTING OF CENTRE BORE ONTO BARS (SLIDING FIT)			
NOMINAL DIAMTER OF CENTRE BORE	**BAR OVER WHICH THE BUSHING MUST FIT**	**QTY**	**AIR TEMP WHILE FITTING**
3/4"	INPUT BAR	5	< 16 °C
20MM	STOCK SOLID TRAP	2	< 16 °C
30MM	STOCK HOLLOW TRAP	2	< 16 °C
19.60MM	SOLID TRAP	2	< 16 °C
N/A	HOLLOW TRAP	2	< 16 °C
3/4"	INPUT BAR	5	> 24 °C
19.60MM	SOLID TRAP	2	> 24 °C
N/A	HOLLOW TRAP	2	> 24 °C

NO.	PART NUMBER	DESCRIPTION	SPECIFICATION	QTY
2	THMMAL006-501	Bushing Outer	See DWG for details, 6061 T6 aluminium	1
1	THMMAL006-500	Bushing Inner	See DWG for details, PTFE (general)	1

Scale: 1:1 on A4	University of Cape Town Department of Mechanical Engineering			
Drawn By: M THOMAS	All un-toleranced dimensions to adhere to ISO 2768-m	Title: Bar Bushing Assembly		
Checked :	Assembly Drawing	Drawing Number :	Rev. : B	Sheet : 1 of 1

Appendix M

Pre-screening Questionnaire regarding Ethics in Research

UNIVERSITY OF CAPE TOWN
IYUNIVESITHI YASEKAPA • UNIVERSITEIT VAN KAAPSTAD

PRE-SCREENING QUESTIONNAIRE OUTCOME LETTER

STU-EBE-2023-PSQ000272

2023/04/12

Dear Malcolm Thomas,

Your Ethics pre-screening questionnaire (PSQ) has been evaluated by your departmental ethics representative. Based on the information supplied in your PSQ, it has been determined that you do not need to make a full ethics application for the research project in question.

You may proceed with your research project titled:

A system for high strain rate interruptible tensile tests

Please note that should aspect(s) of your current project change, you should submit a new PSQ in order to determine whether the changed aspects increase the ethical risks of your project. It may be the case that project changes could require a full ethics application and review process.

Regards,

Faculty Research Ethics Committee